การออกแบบการจัดเรียงชั้นกระจกสำหรับเกราะใสที่ลามิเนตด้วยกระจกโซดาไลม์โดยการวิเคราะห์ทางไฟไนต์เอเลเมนต์

นางสาวยุคลธร ศรีลอย

จุฬาลงกรณ์มหาวิทยาลัย
Chulalongkorn University

บทคัดย่อและแฟ้มข้อมูลฉบับเต็มของวิทยานิพนธ์ตั้งแต่ปีการศึกษา 2554 ที่ให้บริการในคลังปัญญาจุฬาฯ (CUIR)
เป็นแฟ้มข้อมูลของนิสิตเจ้าของวิทยานิพนธ์ ที่ส่งผ่านทางบัณฑิตวิทยาลัย
The abstract and full text of theses from the academic year 2011 in Chulalongkorn University Intellectual Repository (CUIR)
are the thesis authors' files submitted through the University Graduate School.

วิทยานิพนธ์นี้เป็นส่วนหนึ่งของการศึกษาตามหลักสูตรปริญญาวิทยาศาสตรมหาบัณฑิต
สาขาวิชาเทคโนโลยีเซรามิก ภาควิชาวัสดุศาสตร์
คณะวิทยาศาสตร์ จุฬาลงกรณ์มหาวิทยาลัย
ปีการศึกษา 2558
ลิขสิทธิ์ของจุฬาลงกรณ์มหาวิทยาลัย

CONFIGURATION DESIGN OF SODA-LIME GLASS LAMINATED TRANSPARENT ARMOR BY FINITE ELEMENT ANALYSIS

Miss Yukolthorn Sriloy

A Thesis Submitted in Partial Fulfillment of the Requirements
for the Degree of Master of Science Program in Ceramic Technology
Department of Materials Science
Faculty of Science
Chulalongkorn University
Academic Year 2015
Copyright of Chulalongkorn University

Thesis Title	CONFIGURATION DESIGN OF SODA-LIME GLASS LAMINATED TRANSPARENT ARMOR BY FINITE ELEMENT ANALYSIS
By	Miss Yukolthorn Sriloy
Field of Study	Ceramic Technology
Thesis Advisor	Associate Professor Rojana Pornprasertsuk, Ph.D.
Thesis Co-Advisor	Ryan McCuiston, Ph.D.

Accepted by the Faculty of Science, Chulalongkorn University in Partial Fulfillment of the Requirements for the Master's Degree

.....Dean of the Faculty of Science
(Associate Professor Polkit Sangvanich, Ph.D.)

THESIS COMMITTEE

.....Chairman
(Associate Professor Nisanart Traiphol, Ph.D.)
.....Thesis Advisor
(Associate Professor Rojana Pornprasertsuk, Ph.D.)
.....Thesis Co-Advisor
(Ryan McCuiston, Ph.D.)
.....Examiner
(Sujarinee Sinchai, Ph.D.)
.....External Examiner
(Pavadee Aungkavattana, Ph.D.)

ยุคลธร ศรีลอย : การออกแบบการจัดเรียงชั้นกระจกสำหรับเกราะใสที่ลามิเนตด้วยกระจกโซดาไลม์โดยการวิเคราะห์ทางไฟไนต์เอเลเมนต์ (CONFIGURATION DESIGN OF SODA-LIME GLASS LAMINATED TRANSPARENT ARMOR BY FINITE ELEMENT ANALYSIS) อ.ที่ปรึกษาวิทยานิพนธ์หลัก: รศ. ดร. รจนา พรประเสริฐสุข, อ.ที่ปรึกษาวิทยานิพนธ์ร่วม: ดร. ไรอัน แมคคูสตัน, 177 หน้า.

จุดประสงค์ของงานวิจัยนี้เพื่อออกแบบเกราะใสลามิเนตชนิดกระจกโซดาไลม์/ฟิล์มพีวีบีที่มีน้ำหนักเบาและยังคงประสิทธิภาพการป้องกันกระสุนระดับ 3 ตามมาตรฐาน NIJ โดยใช้เทคนิคการวิเคราะห์ทางไฟไนต์เอเลเมนต์ ชิ้นงานเกราะใสและกระสุนที่ใช้สภาวะสมมาตรขนาดหนึ่งในสี่ส่วนจากขนาดจริง ถูกนำมาจำลองแบบทางไฟไนต์เอเลเมนต์แบบสามมิติ โดยกำหนดให้ความเร็วกระสุนเท่ากับ 853 เมตรต่อวินาที ขั้นตอนแรกผู้วิจัยได้ทำการปรับค่าตัวแปรในการเมชและในโมเดลวัสดุเพื่อให้ได้ผลการจำลองแบบทางไฟไนต์เอเลเมนต์ที่มีความแม่นยำและน่าเชื่อถือ แล้วทำการเปรียบเทียบลักษณะรอยแตกระหว่างผลการจำลองกับผลการยิงทดสอบเกราะใส

จากนั้นผู้วิจัยได้ศึกษาปัจจัยที่ส่งผลต่อประสิทธิภาพของเกราะใส ได้แก่ ความหนาของแผ่นปะทะโดยมีความหนาที่ 19 15 12 10 8 6 และ 3 มิลลิเมตร ความหนาของฟิล์มพีวีบีที่ 0.76 และ 1.52 มิลลิเมตร และลำดับการจัดเรียงของชั้นฟิล์มพีวีบีหนา 1.52 มิลลิเมตร และลำดับการจัดเรียงชั้นกระจกโซดาไลม์กับฟิล์มพีวีบีเพื่อการออกแบบชิ้นงานเกราะใสที่มีความหนารวมลดลงจากชิ้นงานมาตรฐานเชิงพาณิชย์ โดยใช้เทคนิคไฟไนต์เอเลเมนต์ในการคำนวณและวิเคราะห์ค่าเฉลี่ยความเสียหายต่อปริมาตร การกระจายพลังงานจลน์และพลังงานภายในของแต่ละชั้นของกระจกและฟิล์มในชิ้นงานลามิเนต ความลึกที่กระสุนเจาะทะลุ และ เส้นผ่านศูนย์กลางของหลุมกระสุน โดยค่าวิเคราะห์ที่กล่าวไปข้างต้นถูกนำไปใช้ในการออกแบบและประเมินประสิทธิภาพของชิ้นงานลามิเนตที่ออกแบบให้มีน้ำหนักเบาในการป้องกันกระสุนเปรียบเทียบกับชิ้นงานมาตรฐาน แล้วจึงคัดเลือกชิ้นงานที่คาดว่าจะผ่านการทดสอบไปทำการยิงทดสอบจริง พร้อมทั้งวิเคราะห์เปรียบเทียบความเสียหายของเกราะใสระหว่างผลการจำลองกับผลการทดสอบจริง

เกราะใสลามิเนตด้วยกระจกโซดาไลม์และฟิล์มพีวีบีที่ออกแบบในงานวิจัยนี้ สามารถลดความหนาและน้ำหนักลง 13.13 และ 13.62 เปอร์เซ็นต์ ตามลำดับ เทียบกับเกราะใสมาตรฐานทางการค้า โดยจากผลสำเร็จในการออกแบบเกราะใสที่บางและเบาที่ลดลงดังกล่าวแสดงให้เห็นว่าการจำลองแบบทางไฟไนต์เอเลเมนต์โดยโปรแกรม ANSYS explicitSTR® เป็นเครื่องมือที่มีประสิทธิภาพในการศึกษากลไกความเสียหายที่เกิดภายในชิ้นงานเกราะใสลามิเนต รวมทั้งใช้ในการออกแบบเกราะใสลามิเนตที่มีน้ำหนักเบาแต่ยังคงประสิทธิภาพการป้องกันกระสุนระดับ 3 ตามมาตรฐาน NIJ

ภาควิชา วัสดุศาสตร์	ลายมือชื่อนิสิต .....
สาขาวิชา เทคโนโลยีเซรามิก	ลายมือชื่อ อ.ที่ปรึกษาหลัก .....
ปีการศึกษา 2558	ลายมือชื่อ อ.ที่ปรึกษาร่วม .....

5572232023 : MAJOR CERAMIC TECHNOLOGY
KEYWORDS: SODA-LIME GLASS LAMINATES / LIGHTERWEIGHT-TRANSPARENT ARMOR / FINITE ELEMENT ANANLYSIS / BALLISTIC PERFORMANCE

YUKOLTHORN SRILOY: CONFIGURATION DESIGN OF SODA-LIME GLASS LAMINATED TRANSPARENT ARMOR BY FINITE ELEMENT ANALYSIS. ADVISOR: ASSOC. PROF. ROJANA PORNPRASERTSUK, Ph.D., CO-ADVISOR: RYAN MCCUISTON, Ph.D., 177 pp.

The goal of this research is to design a lighter weight soda-lime glass/polyvinyl butyral (PVB) laminated transparent armor capable of NIJ level III ballistic protection by finite element analysis (FEA) technique. The armor and projectile with impact velocity at 853 m/s was modeled in 3D using quarter symmetry. The meshing parameters and material model were calibrated to obtain the reliable accuracy in FEA results.

The effects of the striking glass thickness (19, 15, 12, 10, 8, 6 and 3 mm), PVB film (0.76 and 1.52 mm) thicknesses/ordering and the glass/PVB film configurations with reduced total target thickness on the ballistic performance were systematically examined. The FEA results were analyzed and compared to ballistic testing results in terms of the volumetric damage, the distribution of internal and kinetic energy in the laminates, the depth of penetration, and the crater diameter. These results will be subsequently used to evaluate the ballistic performance of laminated armor designs and to identify the optimal design for lighter weight laminated armor as compared to the reference design.

Lastly, the thinnest and lightest-weight soda-lime glass/PVB laminated transparent armor in this study could reach 13.13% and 13.62% of thickness and weight reductions, respectively, comparing to the commercial models. Thus, it could indicate that the FEA performed using ANSYS explicitSTR® software is a powerful tool for the study of the ballistic impact process, the damage propagation, as well as in optimizing the design of laminated transparent armor systems.

จุฬาลงกรณ์มหาวิทยาลัย
CHULALONGKORN UNIVERSITY

Department:	Materials Science	Student's Signature	.....
Field of Study:	Ceramic Technology	Advisor's Signature	.....
Academic Year:	2015	Co-Advisor's Signature	.....

ACKNOWLEDGEMENTS

I would sincerely like to express my profound thank Assoc. Prof. Dr. Rojana Pornprasertsuk, and Dr. Ryan McCuiston, my beloved advisor and co-advisor, respectively that always give me the valuable advice, encouragement during the research work and thesis writing until it succeed.

I deeply indebted to Dr. Sujarinee Sinchai as my beloved teacher and principal investigator of Fabrication and Development of Transparent Armor project for her concrete and warmly support, valuable advice, cheerful encouragement and generosity during the research work.

I gratefully thank Asst. Prof. Dr. Thanakorn Wassanapiarnpong and Dr. Karn Serivalsatit, as co-principal investigators for their helpful suggestions, discussions and encouragement.

I would like to thanks to Mr. Pavee Noonpakdee, Mr. Therdthai Thienthong and Mr. Sapha Pansanga from CAD-IT Consultants (Asia) Pte. Ltd. for useful training courses in ANSYS® ExplicitSTR Software for the beginners and technical support in simulation problems.

I would like to thank the Thai-German Specialty Glass Co., Ltd. for their strong collaboration on lab facilities, ballistic testing facilities and transparent laminates fabrication, The Naval Ordnance Department for their consistency provided the ballistic testing in this study

I would sincerely like to thank the Defense Science and Technology Policy, Ministry of Defense and the National Electronics and Computer Technology Center, Thailand that has been financially supported this study.

I would like to thank all of the transparent armor team members, that always help and support in ballistic testing, all my lovely colleagues and staff members in the Department of Materials Science, Faculty of Science, Chulalongkorn University that always kindly help, friendship and encouragement.

Furthermore, I really grateful thank to my most beloved mother, my sister, my grandmother, my uncle and aunt for their love and strong supports. Without all of you, this study could not be accomplished and I could not reach to this point.

CONTENTS

Page

จุฬาลงกรณ์มหาวิทยาลัย
Chulalongkorn University

Page

จุฬาลงกรณ์มหาวิทยาลัย
Chulalongkorn University

Page

จุฬาลงกรณ์มหาวิทยาลัย
Chulalongkorn University

Page

จุฬาลงกรณ์มหาวิทยาลัย
CHULALONGKORN UNIVERSITY

LIST OF TABLES

จุฬาลงกรณ์มหาวิทยาลัย
Chulalongkorn University

จุฬาลงกรณ์มหาวิทยาลัย
Chulalongkorn University

LIST OF FIGURES

CHAPTER 1
INTRODUCTION

1.1 Background and motivations

Laminated transparent armor is a multilayer armor system, which is composed of glass sheets laminated together by thin polymer films [1,2,3,4,5]. Soda-lime glass laminate systems have been widely used in military vehicles due to their low cost and durability. However a glass laminate system ordinarily requires a thick, transparent polymer layer on the back face to collect fragments from the damaged glass layers during a ballistic impact. The polymer backing layer has several disadvantages in practical application, such as laminate bulging and delamination after impact. Moreover, the polymer backing layer is mechanically soft and prone to scratching, can be deformed due to high temperature exposure and can become discolored over time. Therefore, this study has focused on a soda-lime glass backed laminate armor system. Since one of the main drawbacks of glass laminate armors is their overall weight, previously reported literatures [1,2,3,4] on the optimal design configurations for minimal armor weight, were focused on. This literature included investigations of new transparent materials with high hardness, compressive strength and stiffness, in order to obtain thinner and lighter laminated armor, while still maintaining the required ballistic protection.

The ballistic impact testing of laminated armor is a destructive technique, which has high cost in terms of material, labor and time. As a brittle material, glass generates a variety of damage under impact, due to such things as crack branching (bifurcation of a crack), crack path instability and crack curving, successive branching events, circumferential or ripple cracking, and micro-cracking. The damage patterns in the laminates are related with complex parameters such as crack and stress wave propagation, acoustic impedance mismatch, and energy dispersion, which are difficult to investigate experimentally. Furthermore, because soda-lime glass laminates have brittle failure behavior, it is difficult to repeat, collect and analyze the experimental results. Therefore, finite element analysis (FEA), through the use of an explicit dynamic solver, has been increasingly used to model the ballistic impact process. FEA plays a significant role in predicting the ballistic impact damage and optimizing laminate armor design, where the trial-and-error experimental technique alone would require too many resources. In addition, the modeling of light-weight, transparent, laminated armor for the NIJ level III protection, requires a large numbers of design variables to be optimized, such as the glass and film thicknesses, the glass/film layer configuration, the number of glass/film layers and the type of glass and polymer film. Thus, FEA can be an effective tool for the systematic optimization of light-weight laminated transparent armor.

This study focused on the FEA of the ballistic impact of soda-lime glass/polyvinyl butyral (PVB) laminated armor to gain insight into the design and optimization of laminated armor systems. The effects of soda-lime glass and PVB film thicknesses, glass/film layer configuration and the number of glass/film layers will be systematically studied and optimized to achieve the NIJ standard level III.

1.2 Objectives of this research

1. To investigate the effect of striking glass layer thickness, PVB film thickness/ordering and glass/film configurations on the ballistic protection performance of soda-lime glass/polyvinyl butyral (PVB) laminated armor using finite element analysis.

2. To design a lighter-weight configuration of soda-lime glass/polyvinyl butyral (PVB) laminated transparent armor capable of NIJ standard level III ballistic protection.

1.3 Expected Outcomes

Obtain the lighter-weight soda-lime glass/polyvinyl butyral (PVB) laminated transparent armor design with NIJ level III ballistic protection compared to the reference design.

จุฬาลงกรณ์มหาวิทยาลัย
Chulalongkorn University

CHAPTER 2

THEORY AND LITERATURE REVIEW

2.1 Transparent armors

Transparent armor is a system of functionally-integrated transparent materials whose main role is to provide blast/ballistic protection while retaining structural integrity and optical transparency of the constituent materials [1]. The application of transparent armor is not only for personal protection in case of non-combat face-shields for law-enforcement or security but also for military ground vehicles in the case of windshields and side-windows or explosion protection [1,6,7,8].

2.1.1 Traditional transparent armor components

Almost all transparent armors are laminated structures of hard ceramic materials (soda-lime glass) bonded together with polymeric films (polyvinyl butyral or polyurethane) [1,2,9,10]. The components of laminated armor have been categorized with regards to their role in the laminated system [1,9]. In this study we focused on transparent armor that was fabricated by the lamination of soda-lime glass with polyvinyl butyral (PVB) films. Soda-lime/PVB laminated, transparent armor is widely fabricated and used commercially because of its low cost and good ballistic performance.

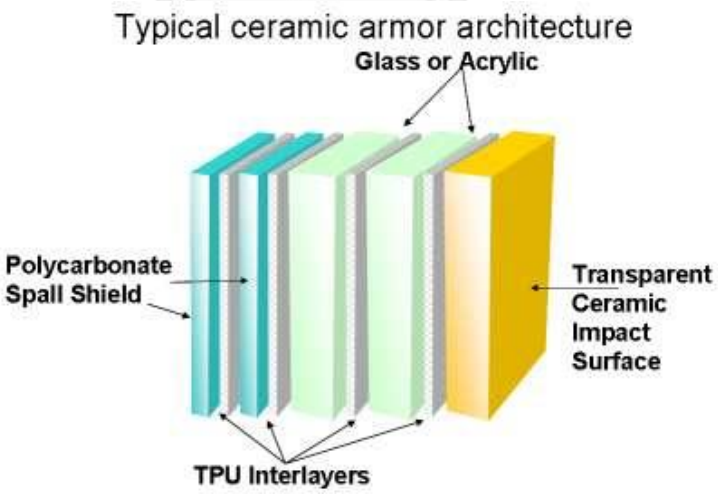

Figure 2.1 Example of a laminated, transparent armor structure[11].

2.1.1.1 Striking layer

The outermost layer of the laminate, i.e. the first layer that is impacted by the bullet/ thread with high velocity, is called the "striking layer" or "strike face". The striking layer is required to have high hardness and strength in order to destroy (e.g. blunting, erosion) the impacting bullet. This layer also performs as a kinetic energy absorption layer, in order to not pass much energy through to the adjacent layers. A good striking layer performance should completely defeat the impacting bullet. Furthermore, the transparency and other optical properties of the striking layer are also of concern because the main application is for use as vehicle windscreens or building windows. The layer must have optical clarity and be free from distortions. The striking layer should also have good durability to corrosive and thermally changing environments. Generally, the striking layer is made of glass or a transparent crystalline ceramic material, such as sapphire, aluminium-oxy-nitride (AlON^{TM}) or magnesium-aluminate spinel.

1. Soda-lime glass

As previously mentioned, soda-lime glass was selected as the striking layer for the laminated transparent armor. Soda-lime glass has been widely used as a striking layer because it is inexpensive, durable in various environments, has moderately high hardness and is widely available commercially. Soda-lime glass sheets come in various thicknesses, leading to flexible design of the transparent armor's configuration. The chemical, mechanical and optical properties of the soda-lime glass sheet use in this research (Siam Guardian Company) are shown in Table 2.1 and 2.2.

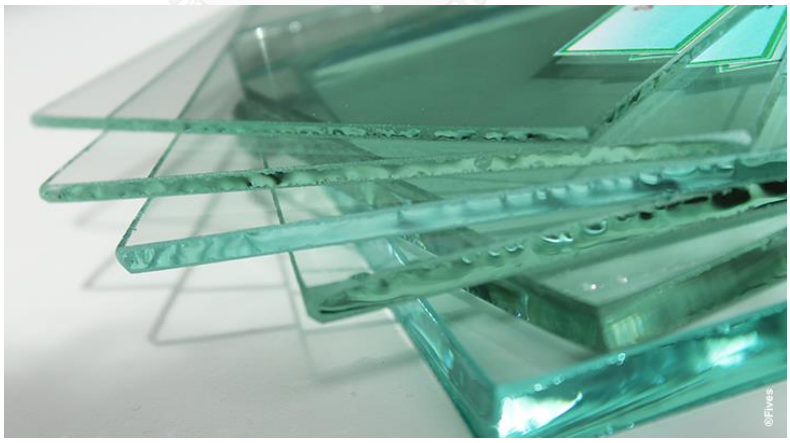

Figure 2.2 Example of soda-lime glass sheets[12].

Table 2.1 Chemical compositions of two different soda-lime glass sheets.

Substances	% Chemical Composition (%wt.)	
	Commercial[4]	Holmquist et.al.[13]
SiO_2	63-81	73.7
Na_2O	9-15	10.6
CaO	7-14	9.4
MgO	0-6	3.1
Al_2O_3	0-2	1.8
K_2O	0-1.5	1.1
Fe_2O_3	0-0.6	0.2

Table 2.2 Typical soda-lime glass sheet properties[14,15].

Mechanical Properties	
Density	2530 kg/m^3
Young's modulus	75 GPa
Poisson' Ratio	0.23
Hardness	5-6 Moh's scale
Tensile Strength	50 MPa
Thermal Properties	
Thermal Expansion Coefficient	86 x 10^{-7} / ^{0}C
Softening Point	715 ^{0}C
Optical Properties	
Refractive index	1.52

จุฬาลงกรณ์มหาวิทยาลัย
Chulalongkorn University

2.1.1.2 Adhesive / Polymeric interlayer

In laminated systems, the polymer interlayer plays an important role in kinetic energy absorption from the striking layer and in attaching adjacent fragmented glass layers together in order not to collapse the laminate armor after crack propagation through the whole structure. The interlayers can decrease crack propagation in the structure by acting as an energy dissipater, while still retaining as a good cohesion of the laminate system. Moreover, a good interlayer in transparent laminate systems needs high toughness and bending stiffness, optical transparency, undistorted optical properties and good environmental resistance. The well-known polymeric interlayers in laminates are polymethyl methacrylate (PMMA), polyvinyl butyral (PVB), polyurethane (PU), and ethyl vinyl acetate (EVA) [1,6,7,16].

1. Polyvinyl butyral film

Polyvinyl butyral (PVB), is a resin usually used for applications that require strong binding, optical clarity, adhesion to many surfaces, toughness and flexibility. It is an amorphous, random copolymer of vinyl butyral, vinyl alcohol and vinyl acetate with the general formula as shown in Figure 2.3. Because of its excellent adhesion to glass, energy mitigation and optical properties, PVB has become the most widely used interlayer for windshields in automobiles.

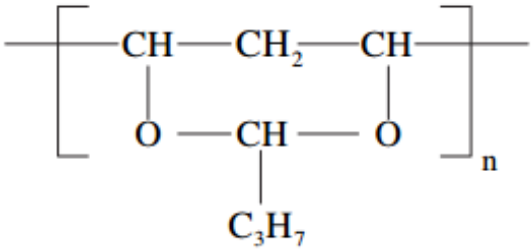

Figure 2.3 Molecular structure of polyvinyl butyral[3].

PVB films (DuPont™ Butacite® PVB interlayer) were chosen as the interlayer for the laminate structure in this study. The PVB films as used in the lamination process were the same dimensions as the glass sheets. The mechanical, thermal and optical properties of the PVB film are shown in Table 2.3.

จุฬาลงกรณ์มหาวิทยาลัย

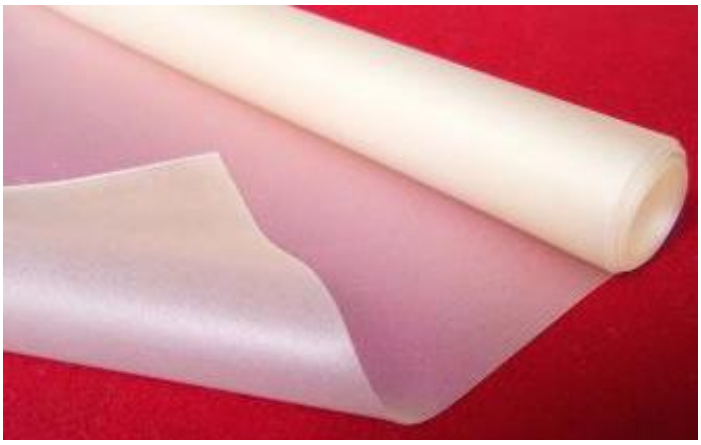

Figure 2.4 Example of Polyvinyl butyral (PVB) film[17].

Table 2.3 Typical Polyvinyl butyral (PVB) film properties[18,19,20].

Mechanical Properties	
Density	1066 kg/m^3
Young's modulus	11 MPa
Bulk modulus	2 GPa
Shear modulus	300 MPa
Tensile Strength	28.1 MPa
% Elongation (Failure)	275
Poisson' Ratio	0.49
Thermal Properties	
Specific Heat (C_p)	1973 J/kg ^{0}C
Thermal Expansion Coefficient	4.2 x 10^{-4} / ^{0}C
Softening Point	80 ^{0}C
Melting Temperature	200 ^{0}C
Glass Transition Temperature	15.4 ^{0}C
Optical Properties	
Refractive index	1.48

2.1.1.3 Backing layer

The last layer of the laminated, transparent armor has the role to collect and prevent any fragments from the projectile, striking layer and intermediate layers from entering in the vehicle cabin. Transparency is still an important factor of this layer, in addition to visual clarity, good scratch, chemical and environmental resistances. Normally, the backing layer is constructed from a thick, transparent polymer sheet, such as polycarbonate (PC), a popular backing material because of its high bending stiffness and toughness, which can perfectly accumulate and defeat the fragments. Nevertheless, PC-backed systems have been faced with problems such as delamination bulging. PC can also be degraded by thermal conditions leading to reduced optical clarity. Therefore, the laminated, transparent armor in this study was not backed with PC.

2.1.2 Autoclaving/lamination process

Transparent armor is generally fabricated by a lamination process in which soda-lime glass sheets are stacked with PVB films, layer by layer, as required by the configuration. Three to five optimized configurations will be chosen for the ballistic testing. The laminated transparent armor samples were fabricated by Thai-German Specialty Glass Co., Ltd. The lamination procedure is as follows. The soda-lime glass sheets are cut and washed with de-mineralized water at 25 ºC in an automatic washing machine, as shown in Figure 2.5.

Figure 2.5 The automatic washing machine used in the fabrication process [4].

Then, the clean glass sheets are stacked layer by layer of with the PVB film in the laminate structure as depicted in Figure 2.6.

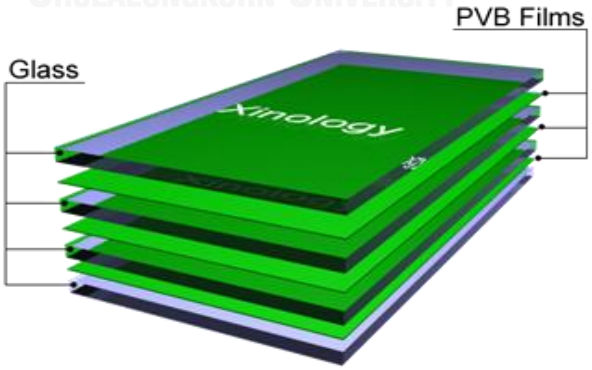

Figure 2.6 The typical laminate configuration[17].

During the assembly process, the environment of the assembly room is controlled to 20-25% relative humidity and a temperature of 20-30 ^{o}C. The stacked samples are passed through the pre-nip and de-airing process. The laminates are heated at 68 ^{o}C on the rolling machine as shown in Figure 2.7.

Figure 2.7 The rolling machine in the pre-nip and de-airing process[4].

Next, the laminates are put in the autoclave under a pressure of 13.5 bar (0.1 MPa) and a temperature of 135 ^{o}C. The autoclave process needs to maintain the proper pressure and heating conditions to strongly adhere the glass and PVB film by chemical bonding. Improper conditions can result in bubbles or other defects which will affect to the optical and strength properties of the laminated armor. Lastly, the finished samples are inspected before using.

Figure 2.8 The autoclave used in the laminate fabrication process[4].

2.2 Ballistic testing the NIJ standard level III[8]

The purpose of this standard is to establish minimum performance requirements and test methods for ballistically resistant, protective materials. The standard is applicable to all ballistically resistant materials (armor) intended to provide protection against gunfire, with the exception of police body armor and ballistic helmets, which are the topic of individual NIJ performance standards.

Many different types of armor are available that range in ballistic resistance from those designed to protect against small-caliber handguns to those designed to protect against high-powered rifles. The ballistic materials used to fabricate armor include metals, ceramics, transparent glazing, fabrics, and fabric-reinforced plastics; they are used separately or in various combinations, depending upon the intended threat protection level.

The ballistic threat posed by a bullet depends on its material composition, shape, caliber, mass, and impact velocity, among other things. Because of the wide variety of cartridges available in a given caliber, and because of the existence of hand loads, armors that will defeat a standard test round may not defeat other loadings in the same caliber. The test ammunitions specified in this standard represent common threats to the military and/or law enforcement community.

2.2.1 Requirements and setup

The level III testing according to the NIJ standard should protect against impact from a rifle or a test barrel chambered for 7.62 mm ball ammunition. The use of a rifle with a barrel length of 56 cm (22 in) is suggested. The test bullets should be 7.62 mm with a full metal jacket, and a nominal mass of 9.7 grams. The velocity of the bullet should be 838±15 m/s and should hit the target within a distance of 15 meters. An approved laminated, transparent armor must not produce any glass fragments which penetrate a witness plate set at 15 cm behind the target. In this study, the ballistic testing was performed at the Royal Thai Naval Ordnance Department, Sattahip, Chonburi, Thailand. The standard ballistic testing setup is shown in Figure 2.9. The target dimension is a square 305 mm x 305 mm and in a single hit test is impacted by 7.62 mm bullet in the target center.

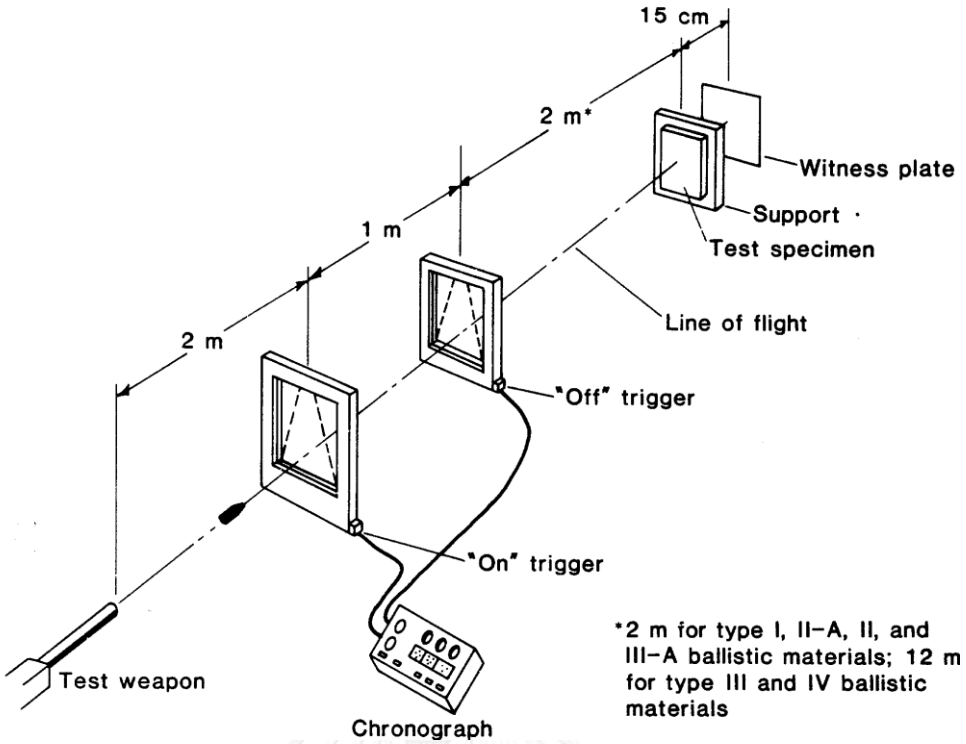

Figure 2.9 The ballistic testing setup diagram[8]

2.2.2 Criterions

Some technical terms are given definition to describe the criterion of ballistic testing approval.

- Witness Plate: A thin sheet of aluminum alloy placed behind a test specimen to determine the potential for an incapacitating injury from fragments.

- Penetration: Perforation of the witness plate by any part of the test specimen or test bullet, as determined by the passage of light when held up to a 60 Watt light bulb.

Practically, the witness plate is a 0.508 mm thick aluminum sheet, placed parallel to target and 150 mm behind the fixture test panel. For the testing of opaque armor (e.g. body armor), a thicker witness plate is used to mimic the uniform and skin of a soldier. In the present case of transparent armor, a thinner witness plate is used which acts as a surrogate for the soldiers' eye. Hence, any perforation of the witness plate signifies a potential eye injury for soldiers not wearing eye protection and is considered as a failure or a ''complete penetration'' of the tested transparent-armor system. Any other outcome of the armor testing qualifies as a ''partial penetration''. Figure 2.10 (a) shows the witness plate setup; (b) is the witness plate that shows an approved ballistic test. Figure 2.11(a), (b) and (c) show the witness plates from failed ballistic tests. The witness plates were impacted by the target fragments and which resulted in witness plate bulging and penetration.

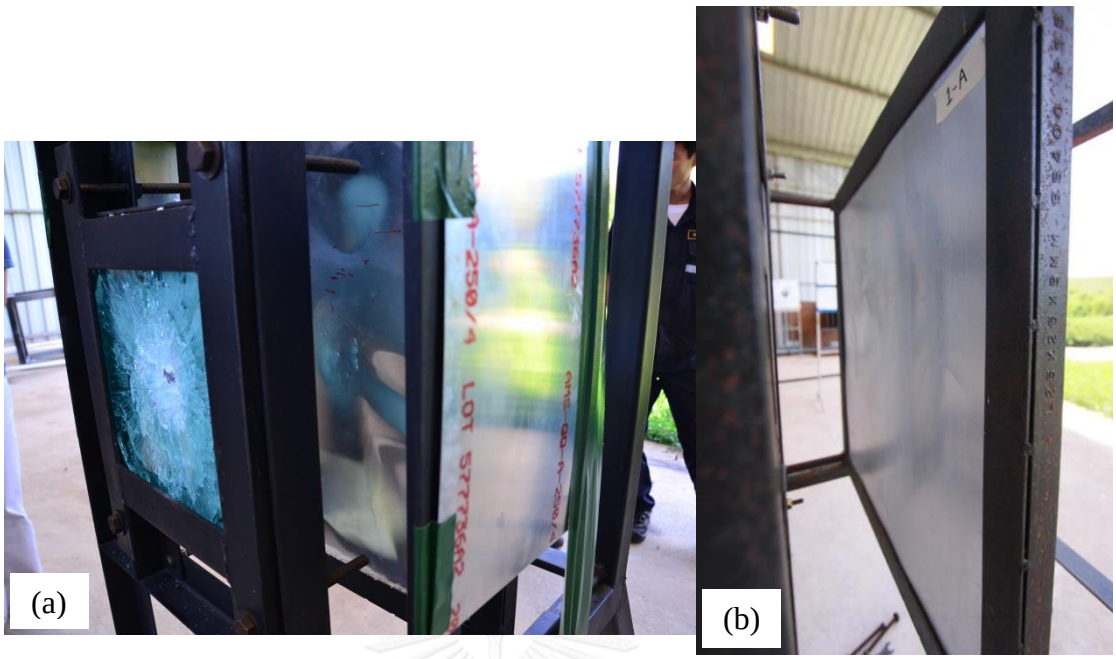

Figure 2.10 The witness plate setup used in ballistic testing (a) the witness plate setup was placed behind the target holder in ballistic testing and (b) the clear- surface of witness plate after finish testing.

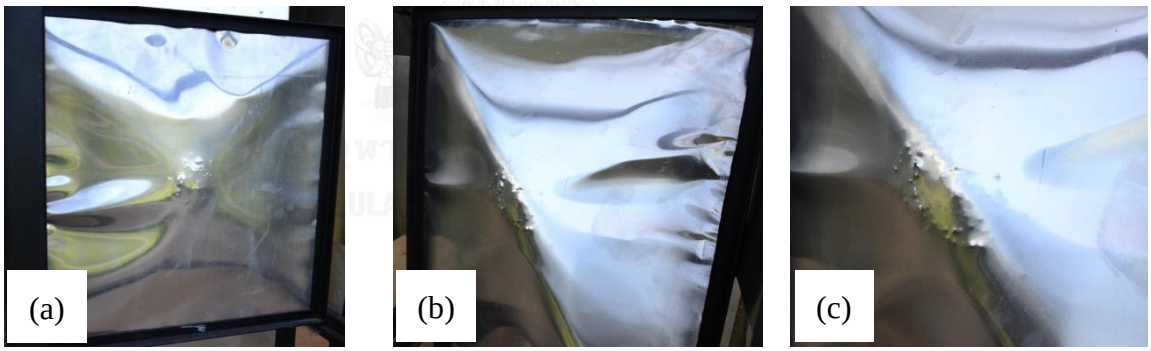

Figure 2.11 Examples of witness plates after ballistic testing (a) the scratched witness plate, (b) the bulged witness plate and (c) holes from glass fragments.

2.3 Finite Element Analysis principle

The basic idea of the finite element method is to apply mathematics to find the solution to a complicated mechanical problem by replacing it with a series of simpler ones. The solution will be only a very good approximation, rather than the exact solution. In the finite element method, the solution region is built up of many small, interconnected sub regions called 'elements'. Existing mathematical tools are not sufficient to find the exact solution to most practical problems in a reasonable amount of time. Thus, in the absence of any other convenient method to the finite element method is preferred. Moreover, with the finite element method, it will often be possible to improve or refine the approximate solution by spending more computational effort.

Although, the finite element method has been used extensively in the field of structural mechanics, it has also been successfully applied to solve several other types of engineering problems, such as heat conduction, fluid dynamics and electronics and magnetics. These applications have prompted researchers to use this technique for finding solutions to other complicated boundary value and similar types of problems. In fact, it has been established that the method can be used for the numerical solution of ordinary and partial differential equations. The general applicability of the finite element method can be seen by observing the similarities that exist between various types of engineering problems. For the illustrations as shown in Figure 2.12 (a) a given problem domain of a workpiece is divided in smaller subdomains, (b) a given problem domain with discrete finite elements corresponding to the curvature of the workpiece and (c) application of FEA to a complex geometry.

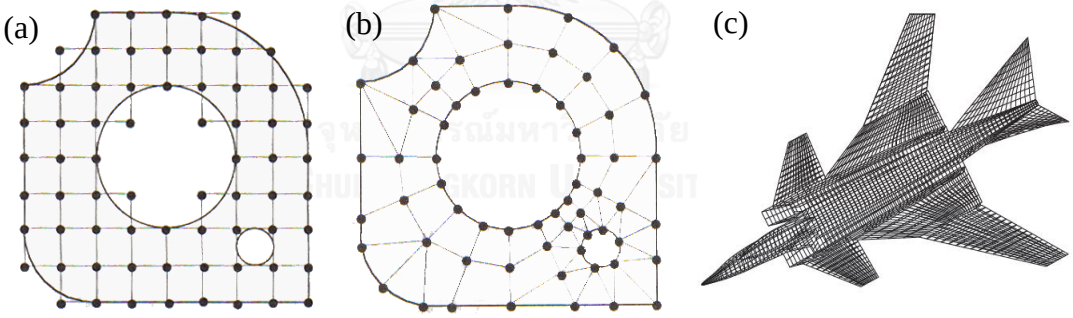

Figure 2.12 The finite element analysis concept in solving the given problems (a) Division subdomain of given problem, (b) The finished-mesh workpiece and (c) Finite Element mesh of a Fighter Aircraft[21].

There are widely-used commercial software packages for FEA numerical simulation, for instance, ANSYS®, ABAQUS® and MATLAB®. All of these software packages should be operated with a high performance computer in order to increase the efficiency of the mathematic calculation. Nevertheless, the chosen FEA program depends on the specific requirements or solutions desired.

2.3.1 ANSYS explicit dynamics

This research used the ANSYS explicit program, which enables the capture of short-duration events for the sample that undergo highly nonlinear, transient dynamic loading. With ANSYS explicit, researchers can gain insight into how a structure responds when subjected to severe loadings. Explicit finite element algorithms based on first principles accurately predict complex responses, such as large material deformations and failure, interactions between bodies, and environments with rapidly changing surfaces, structural mechanics, and other highly complex problems, especially ones with high strain rates and other complications. These types of problems are difficult to solve with general purpose, implicit finite element methods. The determination for whether a problem is implicit or explicit depends on the velocity and strain rate conditions, which are shown in Figure 2.13.

Solution	Impact Velocity (m/s)	Strain Rate (/s)	Effect
Implicit		$<10^{-5}$	Static / Creep
	< 50	10^{-5} - 10^{-1}	Elastic
	50 -1000	10^{-1} - 10^{1}	Elastic-Plastic (material strength significant)
	1000 - 3000	10^{5} - 10^{6}	Primarily Plastic (pressure equals or exceeds material strength)
	3000 - 12000	10^{6} - 10^{8}	Hydrodynamic (pressure many times material strength)
Explicit	> 12000	$> 10^{8}$	Vaporization of colliding solids

CHULALONGKORN UNIVERSITY

Figure 2.13 Mechanical responses of materials as a function of impact velocity[22].

The ANSYS explicit programs help researchers to explore a wide range of challenge problem, for example, high-speed and hypervelocity impacts, severe loadings resulting in large material deformation, material failure and fragmentation, penetration mechanics, and blast-structure interactions, etc. From this research, the ANSYS Explicit STR^{TM} software was selected to simulate the complex material behaviors under the ballistic testing conditions. The ANSYS explicit software products are summarized in Figure 2.14. In this case, the materials of interest are glass and polymeric films from static to dynamic conditions. The ANSYS Explicit STR^{TM} program is suitable for the simulation and design of products with highly nonlinear behavior. The target needs to survive impacts or short-duration high-pressure loadings.

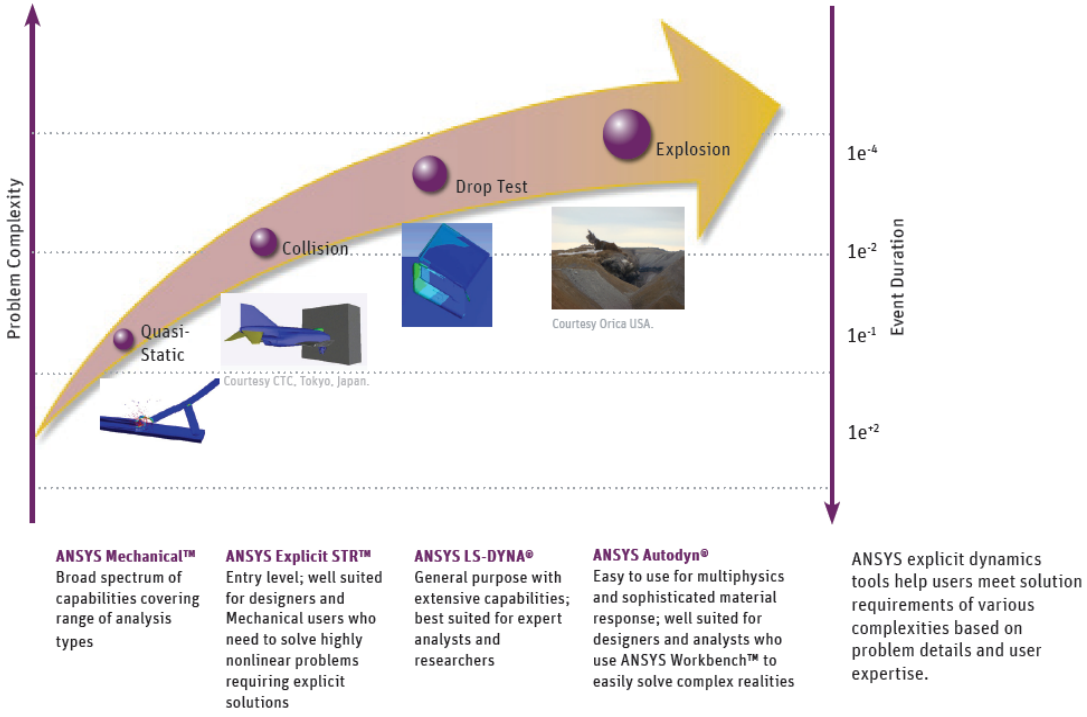

Figure 2.14 ANSYS software in dynamic case studies[22].

2.3.2 Meshing

Meshing is the process used to divide the problem's geometry into smaller pieces, known as elements. Mostly, in engineering problems, we need to find the values of a field variable such as displacement, stress, pressure, and velocity as a function of spatial coordinates (x, y, z). In the case of transient or dynamic-state problems, the field variable has to be found as a function of not only the spatial coordinates (x, y, z) but also time (t). The geometry of the problem is often irregular and complex [2]. For complex geometries, the given body often cannot be represented as an assemblage of only one type of element; therefore two or more types of elements may be used. The shapes, sizes, number, and nodal configurations of the elements have to be chosen carefully such that the original body or domain is simulated as closely as possible without increasing the computational effort needed for the solution.

2.3.2.1 Element shapes

Mesh types are mainly categorized as one of three types according to their dimension. Each element in a mesh is composed of at least one node (a point to create the shape of mesh) depending on element types. The first type is composed of one-dimensional elements used for a simple 1D analysis. In this case an element would have two nodes to form a line. The second type is composed of two-dimensional elements, which are planar, for instance, triangular, quadrilateral, rectangular and parallelogram, as shown in Figure 2.15. The third type is composed of three-dimensional elements, which are the solid elements, for more complex 3D geometry problems. Several examples of solid elements are shown in Figure 2.16.

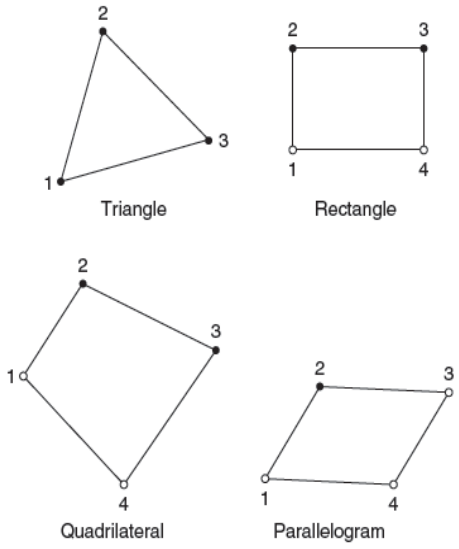

Figure 2.15 Two-dimensional elements[21].

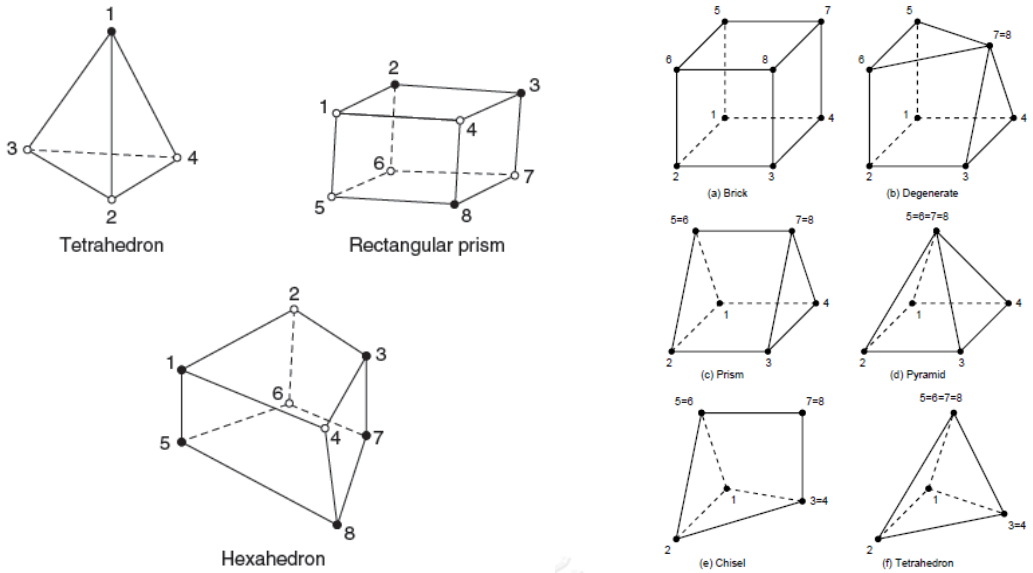

Figure 2.16 Three-dimensional elements[23]

This study focused on the simulation of three-dimensional geometries. The laminate structures were meshed with solid elements, mainly hexahedral or 'Hex' shaped elements. Normally, the automatic meshing tool in the ANSYS Workbench software will generate tetrahedral or 'Tet' shaped elements, which has the advantages of being able to fill an arbitrary volume very easily. A tet mesh can be generated quickly, automatically, and for complicated geometry. It is not well- suited for thin solids due to non-isotropy of the geometry and the nature of the element.

In explicit analyses, the locations of regions of high stress constantly change as the dynamic stress waves propagates throughout the entire mesh. Mesh refinement is usually used to improve solution accuracy. Mesh transitions should also be smooth for maximum accuracy. Hex meshing is preferred because it is more computationally efficient and sometimes more accurate for slower transients. While the hexahedral mesh is more efficient than a tetrahedral mesh, it is not always easy to generate for a given geometry. Laminated transparent armor is generally square or rectangular in shape. Due to this, hex meshing can uniformly fill the laminate geometry. There are several meshing methods that can be used to generate a hex element mesh in the laminate geometry. The 'hex dominant' mesh method creates mostly hex elements, but will also create some pyramid elements which are automatically split into two tetrahedral elements, if the geometry is irregular. The 'MultiZone' meshing method can produce excellent hex meshes if the mesher is able to identify and create a swept mesh for the geometry, and the element size is chosen carefully. The 'edge sizing' method is a general purpose way to mesh any geometry, but it can require significant setup on a part by part basis, and sometimes also requires a sliced geometry technique to be performed in ANSYS Design Modeler before meshing.

2.3.2.2 Element size and Numbers of elements

The element size is important for the several reasons, including the accuracy of stress levels, the damage that is captured, as well as the total simulation computational time. For example, the smallest element size controls the time step used to advance the solution in time. In explicit FEA, The element size should be controlled by the user throughout the meshing procedure, and not automatically. Therefore, the proper mesh size should be considered. The hexahedral mesh is more appropriate to use in this study than the tetrahedral mesh, as the tetrahedral mesh has a larger element and node counts. The time step for the tet mesh is also smaller than for a hex mesh.

The time step must be appropriate to ensure stability and accuracy of the solution. The size of the time step used in explicit time integration is limited by the CFL (Courant-Friedrichs-Levy) condition. This condition implies that the time step must be limited so that a stress wave cannot travel further than the smallest characteristic element dimension in the mesh, in a single time step. The smallest time step is calculated following equation 2.1.

$$\Delta t \leq f * \left[\frac{h}{c}\right]_{min} \quad \text{---------- Eq.2.1}$$

where, c is the material sound speed (m/sec)

f is the termination time (sec),

h is the element characteristic dimension, is calculated as follows: (Figure 2.17) Hexahedral = the volume of the element divided by the square of the longest diagonal and scaled by $\sqrt{2/3}$, Tetrahedral = the minimum distance of any element node to its opposing element face

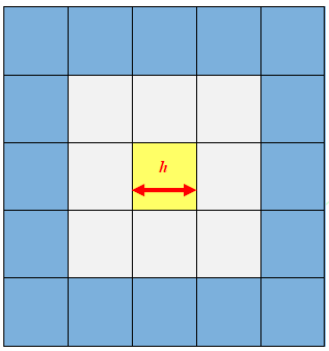

Figure 2.17 Diagram showing the 'h' value of a two-dimensional square element[22].

For example, a mesh with a characteristic dimension of 1 mm and a material sound speed of 5000 m/s would have a stable time step of 0.18 μsec; to solve this simulation to a termination time of 0.1 seconds, assuming no deformation, would require 555,556 time steps.

The meshing method determines the numbers of element and hence their size and the time step, as depicted in Figure 2.18. While the finer tet mesh ideally has more accuracy, the overall simulation time will be great due to the large number of elements. The hex dominant mesh has a smaller number of elements, but some of them are small, leading to the short time step and a long simulation time. In some cases, too small of a time step can result in an unfinished solution if the time step controls are improperly set. The swept hex mesh has a reasonable number of elements and longer time step, which is ideal.

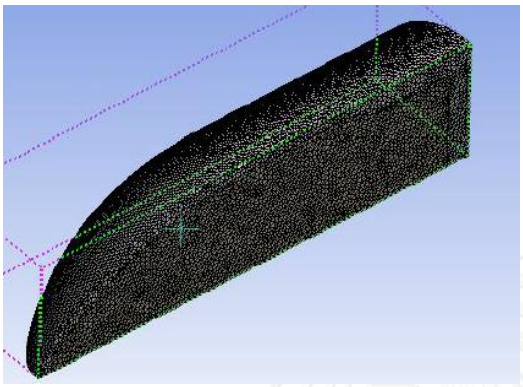

(a) Bullet was meshed by

2 mm Tet Mesh,

604,152 elements,

Time step = 3.346 E-5 ms

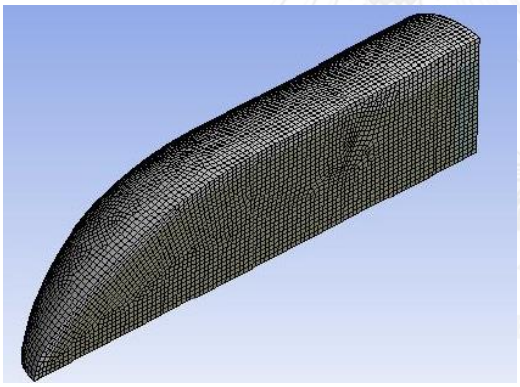

(b) Bullet was meshed by

2 mm Hex Dominant,

61,747 elements,

Time step = 3.1 E-6 ms

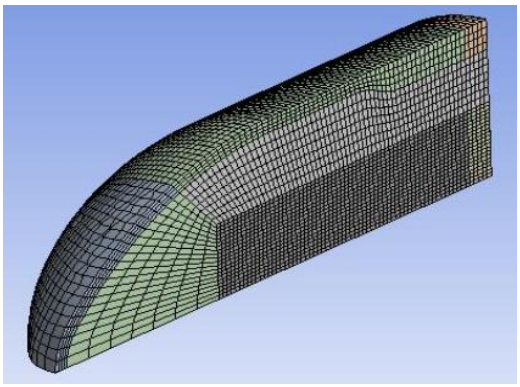

(c) Bullet was meshed by

2 mm Swept Hex Mesh,

44,000 elements

Time step = 5.668 E-5 ms

Figure 2.18 The projectile was meshed with different techniques obtained varied numbers of elements and time step in numerical setup[22].

2.3.2.3 Mesh Quality

A good quality mesh guarantees the best analysis results for the problem and minimizes the need for additional analysis runs. The mesh should be fine enough to resolve the primary features of the problem being analyzed. An all hexahedral mesh is preferred, but one minor drawback of an under-integrated hex element is an undesired deformation mode called “hourglassing”. If an element distorts in such a way that there is no net strain measured at the integration point (typically in the geometric center), no resistance forces are generated. As seen in Figure 2.19 on the left center, the two diagonals remain the same length even though the element distorts. If such distortions occur in a region of several elements, a pattern, such as that shown on the right, occurs and shows the reason for the name “hourglass instability”. In order to avoid such hourglass instabilities for hexahedral solid elements, a set of corrective forces are added to the solution, for example ‘AD standard’ which is the default setup for explicit ANSYS Explicit STR software.

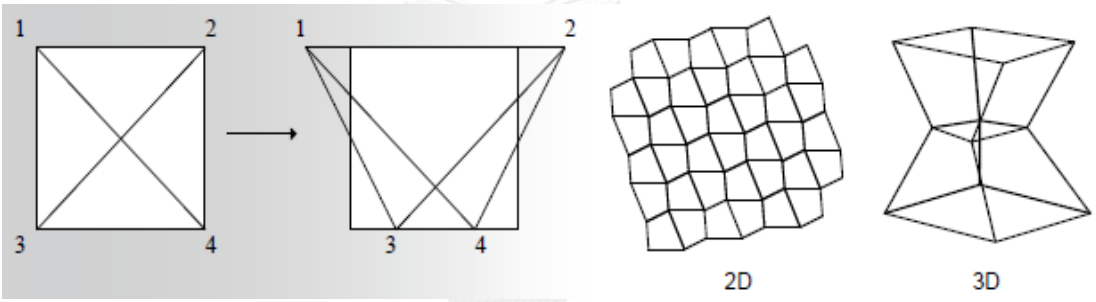

Figure 2.19 Illustration showing the “hourglass instability” in hexahedral mesh formulations[22].

Moreover, there are some mathematical calculations such as ‘skewness’ and ‘Element Quality’ which indicate the quality of the mesh. Skewness is one of the primary quality measures for a mesh. Skewness determines how close to ideal (that is, equilateral or equiangular) a face or cell is. According to the definition of skewness, a value of 0 indicates an equilateral cell (best quality) and a value of 1 indicates a completely degenerate cell as scaled in Figure 2.20. Highly skewed faces and cells should be avoided because they can lead to less accurate results than when relatively equilateral/equiangular faces and cells are used.

Skewness mesh metrics spectrum

Excellent	Very good	Good	Acceptable	Bad	Unacceptable
0-0.25	0.25-0.50	0.50-0.80	0.80-0.94	0.95-0.97	0.98-1.00

Figure 2.20 Skewness value range of meshing quality[22].

The normalized angle deviation method is widely used for 3D meshes, for such elements as hexahedral, prisms and pyramids; skewness is defined as equation 2.2

$$Skewness = \max\left[\frac{\theta_{max} - \theta_e}{180 - \theta_e}, \frac{\theta_e - \theta_{min}}{\theta_e}\right]$$ --------Eq.2.2

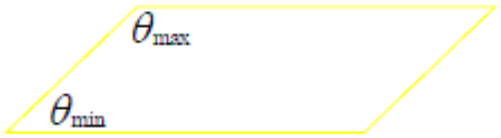

where, θ_{max} = largest angle in the face or cell,

θ_{min} = smallest angle in the face or cell,

θ_e = angle for an equiangular face/cell (such as 60 for a triangle, 90 for a quad, and so on).

The 'Element Quality' option in ANSYS provides a composite quality metric that ranges between 0 and 1 as shown in Figure 2.21. This metric is based on the ratio of the volume to the sum of the square of the edge lengths for 2D quad/tri elements, or the square root of the cube of the sum of the square of the edge lengths for 3D elements. A value of 1 indicates a perfect cube or square while a value of 0 indicates that the element has a zero or negative volume. The calculated formulations are shown in equation 2.3 for 2D elements and equation 2.4 for 3D elements.

Unacceptable	Bad	Acceptable	Good	Very good	Excellent
0-0.001	0.001-0.14	0.15-0.20	0.20-0.69	0.70-0.95	0.95-1.00

Chulalongkorn University

Figure 2.21 Meshing quality range[22].

$$Quality = C\left(\frac{area}{\sum(Edgelength)^2}\right)$$ --------Eq.2.3 (Quad/Tri elements)

$$Quality = C\left(\frac{volume}{\sqrt{[\sum(Edgelength)^2]^3}}\right)$$ --------Eq.2.4 (Brick elements)

where, the C constant for each type of element: Triangle = 6.928,

Quadrangle = 4.0, Tetrahedron = 124.708, Hexagon = 41.569,

Pyramid = 96.0 and Wedge = 62.354.

2.3.3 Lagrangian processor in three-dimensional FEA[21,22]

The history of the state of the material represented by a cell/element is known completely, so the implementation of sophisticated constitutive models is possible. The Lagrange coordinate system can accurately follow particle histories, and therefore accurately define material interfaces and also follow stress histories of material in elastic-plastic flow. The Lagrange processor operates on a structured (i-j-k) numerical mesh of brick-type element (3D). The vertices of the mesh move with material flow velocity. Material remains within its initial element definition with no transport of material from cell to cell. The Lagrange formulation tends to be faster computationally as no transport of material through the mesh needs to be calculated. Moreover, material interfaces, free surfaces, and history dependent material behavior are generally easier to follow in the Lagrange framework.

In the Lagrange method the coordinates move with the material, which is ideal for following the flow in regions of relatively low distortion, and possibly large displacement, where mesh tangling, if it does occur, will only occur at later times and in regions of low to moderate pressure gradients. A major disadvantage of Lagrange is if excessive material movement occurs, the numerical mesh may become highly distorted leading to an inaccurate and inefficient solution. Further, this may ultimately lead to a termination of the calculation, i.e. the model fails to complete. Rezoning the numerical mesh by remapping the distorted solution onto a more regular mesh so as to allow the calculation to continue to later times, is one approach to alleviate the mesh distortion problem, though this is often unavailable in commercial software, time consuming and comes with its own difficulties. Regardless, because of the inherit efficiency, the Lagrange method is typically used whenever the deformation and boundary conditions permit.

Through various contact algorithms it is possible for Lagrange grids to impact and slide along other Lagrange surfaces. These surfaces can be dynamically redefined as the surface changes due to erosion, etc. Erosion is a technique wherein the Lagrange cells are that are severally distorted are removed from the calculation before they become degenerate. These deformed element is some cases can be transformed into a free mass points not connected to the original mesh, but that retains the mass and momentum of the original element. These free nodes can further interact with other bodies or the original body from which they were eroded. This is a very powerful feature which allows the study of impact interaction problems including deep penetrations in the low to hypervelocity range using the Lagrange technique.

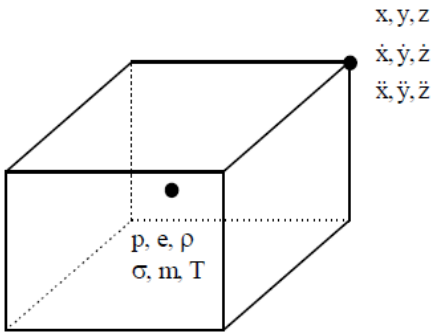

Figure 2.22 Location of variables in the Lagrange coordinate system [22].

2.3.3.1 Governing Equations

Lagrangian coordinate system used the partial differential equations to express the conservation of mass, momentum and energy calculations. Those equations are combined with the material models and a set of initial and boundary conditions to define the complete solution of the problem. As the material associated with a Lagrangian zone stays with that zone under any deformation, the *'conservation of mass'* is automatically satisfied. While, the density at any time can be determined from the current volume of the zone and its initial mass as seen in equation 2.5

$$\rho = \frac{\rho_0 V_0}{V} = \frac{m}{V} \text{ --------- Eq.2.5}$$

The partial differential equations which express the *'conservation of momentum'* relate the acceleration to the stress tensor σ_{ij} as shown in equation 2.6 below;

$$\begin{aligned} \rho\ddot{x} &= \frac{\partial\sigma_{xx}}{\partial x} + \frac{\partial\sigma_{xy}}{\partial y} + \frac{\partial\sigma_{xz}}{\partial z} \\ \rho\ddot{y} &= \frac{\partial\sigma_{yx}}{\partial x} + \frac{\partial\sigma_{yy}}{\partial y} + \frac{\partial\sigma_{yz}}{\partial z} \text{ -------Eq.2.6} \\ \rho\ddot{z} &= \frac{\partial\sigma_{zx}}{\partial x} + \frac{\partial\sigma_{zy}}{\partial y} + \frac{\partial\sigma_{zz}}{\partial z} \end{aligned}$$

The stress tensor is separated into a hydrostatic component p and a deviatoric component s as shown in equation 2.7.

$$\sigma_{xx} = -(p+q) + s_{xx}$$
$$\sigma_{yy} = -(p+q) + s_{yy}$$
$$\sigma_{zz} = -(p+q) + s_{zz} \text{ --------Eq.2.7}$$
$$\sigma_{xy} = s_{xy}$$
$$\sigma_{yz} = s_{yz}$$
$$\sigma_{zx} = s_{zx}$$

The negative sign for the hydrostatic pressure p follows from the usual notation that stresses are positive in tension and negative in compression (the opposite to that for pressure). In the actual equations solved the hydrostatic pressure p is augmented by a pseudo-viscous force, (q).

The strain tensor ε_{ij} is determined from the relation between the strain rates and the velocities $(\dot{x}, \dot{y}, \dot{z})$ as shown in equation 2.8;

$$\dot{\varepsilon_{xx}} = \frac{\partial \dot{x}}{\partial x}$$
$$\dot{\varepsilon_{yy}} = \frac{\partial \dot{y}}{\partial y}$$
$$\dot{\varepsilon_{zz}} = \frac{\partial \dot{z}}{\partial z} \text{ ---------- Eq.2.8}$$
$$\dot{\varepsilon_{xy}} = \frac{1}{2}\left(\frac{\partial \dot{x}}{\partial y} + \frac{\partial \dot{y}}{\partial x}\right)$$
$$\dot{\varepsilon_{yz}} = \frac{1}{2}\left(\frac{\partial \dot{y}}{\partial z} + \frac{\partial \dot{z}}{\partial y}\right)$$
$$\dot{\varepsilon_{zx}} = \frac{1}{2}\left(\frac{\partial \dot{z}}{\partial x} + \frac{\partial \dot{x}}{\partial z}\right)$$

and these strain rates are related to the rate of change of volume by:

$$\frac{\dot{V}}{V} = \dot{\varepsilon}_{xx} + \dot{\varepsilon}_{yy} + \dot{\varepsilon}_{zz} \text{ ---------- Eq.2.9}$$

จุฬาลงกรณ์มหาวิทยาลัย
Chulalongkorn University

For elastic behavior of a material, we relations between the deviatoric stress rates and the strain rates can be derived using equation 2.9 and Hooke's law, shown as shown in equation 2.10;

$$\dot{s}_{xx} = 2G\left(\dot{\varepsilon}_{xx} - \frac{1}{3}\frac{\dot{V}}{V}\right)$$

$$\dot{s}_{yy} = 2G\left(\dot{\varepsilon}_{yy} - \frac{1}{3}\frac{\dot{V}}{V}\right)$$

$$\dot{s}_{zz} = 2G\left(\dot{\varepsilon}_{zz} - \frac{1}{3}\frac{\dot{V}}{V}\right)$$

$$\dot{s}_{xy} = 2G\dot{\varepsilon}_{xy} \quad \text{---------- Eq.2.10}$$

$$\dot{s}_{yz} = 2G\dot{\varepsilon}_{yz}$$

$$\dot{s}_{zx} = 2G\dot{\varepsilon}_{zx}$$

The deviatoric variables will also be adjusted for other real effects, such as rigid body rotations, plastic flow, damage and failure as described more fully in "Material model".

The pressure (p) is related to the density (ρ) and the specific internal energy (e) through an equation of state as shown in equation 2.11, in the form described in the material models section.

$$P = f(\rho, e) \quad \text{---------- Eq.2.11}$$

This must be solved simultaneously with the equation expressing *'conservation of energy'*

$$\dot{e} = \frac{1}{\rho}\left(\sigma_{xx}\dot{\varepsilon}_{xx} + \sigma_{yy}\dot{\varepsilon}_{yy} + \sigma_{zz}\dot{\varepsilon}_{zz} + 2\sigma_{xy}\dot{\varepsilon}_{xy} + 2\sigma_{yz}\dot{\varepsilon}_{yz} + 2\sigma_{zx}\dot{\varepsilon}_{zx}\right) \text{------ Eq.2.12}$$

The explicit dynamics solver uses a central difference time integration scheme (Leapfrog method). After the forces have been computed at the nodes (resulting from internal stress, contact, or boundary conditions), the nodal accelerations are derived by dividing force by mass:

$$\ddot{x}_i = \frac{F_i}{m} + b_i \text{ ---------Eq.2.13}$$

where, x_i are the components of nodal acceleration (i=1,2,3), F_i are the forces acting on the nodes, b_i are the components of body acceleration and m is the mass of the node.

Chulalongkorn University

With the accelerations at time n - ½ are determined, the velocities at time n + ½ are found from

$$\dot{x}_i^{n+1/2} = \dot{x}_i^{n-1/2} + \ddot{x}_i^{n}\Delta t^{n} \quad \text{----------Eq.2.14}$$

Finally, the positions are updated to time n+1 by integrating the velocities

$$x_i^{n+1} = x_i^{n} + \dot{x}_i^{n+1/2}\Delta t^{n+1/2} \text{---------Eq.2.15}$$

For each time step, the equations are solved explicitly for each element in the model, based on input values at the end of the previous time step. Only mass and momentum conservation are enforced. However, in well posed explicit simulations, mass, momentum and energy should be conserved. Energy conservation is constantly monitored for feedback on the quality of the solution (as opposed to convergent tolerances in implicit transient dynamics) The series of calculations that are carried out in each incremental time step (or cycle) in a Lagrange mesh are shown schematically in Figure 2.23.

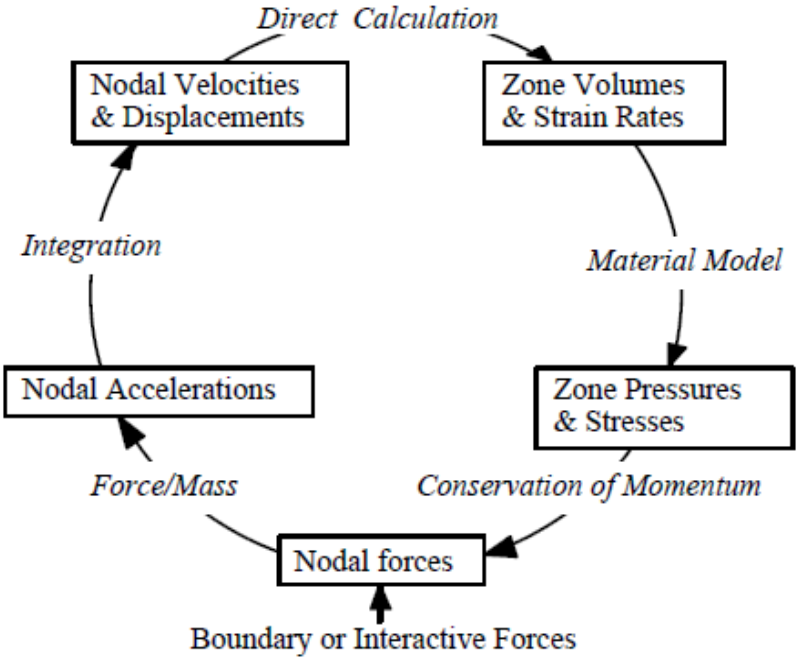

Figure 2.23 The Lagrange computation cycle [22].

The solution starts with a mesh having assigned material properties, loads, constraints and initial conditions. Integration in time produces motion at the mesh nodes. Motion of the nodes produces deformation of the elements. Element deformation results in a change in volume and density of the material in each element. The deformation rate is used to derive the strain rates (using various element formulations). Constitutive laws derive resultant stresses from the strain rates. Stresses are transformed back into nodal forces (using various element formulations). External nodal forces are computed from boundary conditions, loads and contacts. The total nodal forces are divided by the nodal masses to produce nodal accelerations.

At the bottom of the Figure 2.23, the boundary and/or interactive forces are updated and combined with the forces for inner zones computed during the previous time cycle. Then, for all non-interactive Lagrangian nodes, the accelerations, velocities and positions are computed from the momentum equation and a further integration. The accelerations are integrated explicitly in time to produce new nodal velocities. The nodal velocities are integrated explicitly in time to produce new nodal positions.

From these values the new zonal volumes and strain rates may be calculated. With the use of a material model, together with the energy equation, the zonal pressures, stresses and energies may be calculated, providing forces for use at the start of the next integration cycle. For the coupling of Lagrangian elements to other elements, there are addition calculations that are used to compute the interactive forces. The solution process (cycle) is repeated until the calculation end time is reached.

2.4 Material models in Explicit FEA[22]

According to the previous section, not only are the meshing methods important for the laminated target and the bullet, but the material models also play a key factor in the accuracy of the FEA of the ballistic impact damage of the armor. As explained in the Lagrange computation cycle, the individual nodes/mesh are defined with various variables that directly deal with the ‘material model’, and the data in the material models were used to perform the calculations in the Lagrange’s cycle. Explicit dynamic calculations utilize differential equations governing unsteady, dynamic material motion which express the local conservation of mass, momentum and energy. To calculate a complete solution, in addition to the appropriate initial and boundary conditions, it is necessary to define a further relation between the material flow variables. This can be done with a material model which relates stress to deformation and internal energy/temperature.

The material model is a specific material’s numerical function, which represents the characteristic behavior of the material under various loading conditions. For the dynamic response of a complex system, multiple models capturing brittle and ductile material behaviors were studied to determine the proper material model assignment and model variables. In almost all cases, the ‘stress tensor’ may be separated into a uniform ‘hydrostatic pressure’ (equal in three normal stress directions) and a ‘stress deviatoric tensor’ associated with the resistance of the material to shear distortion.

Material models are constructed with three main parts: (i) a strength model, (ii) an equation of state (EOS) and (iii) a failure model. The 'strength model' expresses the deviatoric component of a material's strength under loading to define the transition between elastic and plastic strain and relations between shear stress and strain, etc. The relation between the hydrostatic pressure, the local density (or specific volume) and local specific energy (or temperature) associated with the resistance of the material to shear distortion is known as an 'equation of state' and expresses the hydrostatic component of strength.

The 'failure model' describes the conditions under which the material is no longer capable of supporting stress or has otherwise failed. Failure models may be associated with a specific model or may be global conditions for the entire model to keep the calculations from terminating. The more accurate the material properties and the more suitable the material models that are input, the more efficient and reliable the FEA results that are obtained. Thus, significant amounts of research have been performed on calibrating and investigating strength and failure models for the ceramic, metal and polymer interlayer for FEA of the laminated armor systems.

2.4.1 Material model for Soda-lime glass

Holmquist et al. [13,24] established a well-known and widely use material model for describing the response of the high-energy ballistic impact or similar loading on brittle materials, referred to as the Johnson-Holmquist Ceramic Materials model or JH-1and JH-2, depending on the exact implementation. The model is capable of a wide range of loading conditions that produce large strains, high strain rates, and high pressures. The two models (JH-1 and JH-2) are based on two sets of curves of yield stress vs. pressure, i.e. intact and failed material curves. Each curve depends on the plastic strain and plastic strain rate. A damage variable, D, defines the level of fracture. For the JH-1 model, the intact material curve is used prior to fracture ($D < 1.0$). Once fracture has occurred ($D = 1.0$) the failed material curve is used. The JH-2 model also has an intact and failed material curve, but the model is gradually softened as damage accumulates. Cronin et al. [25] applied the JH-2 model for the FEA of a steel sphere impacting a silica-based glass plate to demonstrate the application of this model for impact simulation. Richards, et al. [26] conducted ballistic simulations using ANYSY AUTODYN to predict the ballistic protection performance and gain a correlated understanding, of 18-mm thick soda-lime glass/polyurethane interlayer/6mm polycarbonate backing layer laminates arranged at three different configurations. The ballistic limit and damage analysis results showed that the experimental and numerical models were in a good agreement.

Grujicic, et al. [27] also developed a material model for soda-lime glass, which treats glass as a stochastic brittle material in which damage dominated deformation and ultimate failure are controlled by the pre-existing flaws. The model was applied to predict the multi-hit performance of laminated targets consisting of five glass and five polycarbonate layers, respectively. Each of the glass laminates was tested with 4 shots and the computational results were compared to the final state of damage after each hit[7]. Although the simulation and experimental results were quite comparable, the material model is fairly different from the present study conditions. Thus, based on the

above observations, the JH-2 model was applied as the material model for soda-lime glass in this study.

2.4.1.1 Johnson-Holmquist model [13,28]

1. Strength model

The JH-2 constitutive model requires several material constants to completely describe to be elastic, with the stress state completely described by the elastic material properties (shear modulus) and equation of state. Based on the current material deformation, μ (equation 2.16) and corresponding pressure (equations 2.17 and 2.18) can be calculated. This is the equation of state for the material.

$$\mu = \frac{\rho}{\rho_0} - 1 \quad \text{---------- Eq.2.16}$$

$$P = K_1\mu + K_2\mu^2 + K_3\mu^3 + \Delta P_{n-1} \text{ (Compression) -------- Eq.2.17}$$

$$P = K_1\mu \quad \text{(Tension) ---------- Eq.2.18}$$

In equation 2.18, P corresponds to the bulking pressure of the material and is determined by the amount of accumulated damage. Under compressive loading, damage begins to accumulate within the material when the deviator stress exceeds a critical value. This damage accumulation is tracked via a damage parameter (ranging from 0 to 1.0), and the corresponding non-recoverable or plastic strain. Thus, the current material strength is determined by the damaged and undamaged strength curves as well as the current material damage. Figure 2.21 shows these curves for a ceramic material. Both the strength and pressure are normalized by the equivalent stress at the Hugoniot Elastic Limit (HEL) and the pressure at the HEL respectively. While, the normalized pressure is $P^* = P/P_{HEL}$, where P is the actual pressure and P_{HEL} is the pressure at the HEL. The normalized maximum tensile hydrostatic pressure the material can withstand. When subjected to tensile pressure, the material responds elastically until brittle failure at a specified effective stress value. This corresponds to complete instantaneous damage.

The intact material strength is defined as:

$$\sigma_i^* = A(P^* + T^*)^N (1 + C\ln \dot{\varepsilon}) \quad \text{---------- Eq.2.19}$$

And the fractured material strength as:

$$\sigma_f^* = B(P^*)^M (1 + C\ln \dot{\varepsilon}) \quad \text{---------- Eq.2.20}$$

Although the JH-2 model does account for strain rate effects, it has been noted that these effects are typically secondary compared the pressure effects. This has been noted experimentally, and is reflected in the typical values for the constants in the JH-2 model. The current material strength is then determined from equation 2.24.

$$\sigma^* = \sigma_i^* - D(\sigma_i^* - \sigma_f^*) \quad \text{---------- Eq.2.21}$$

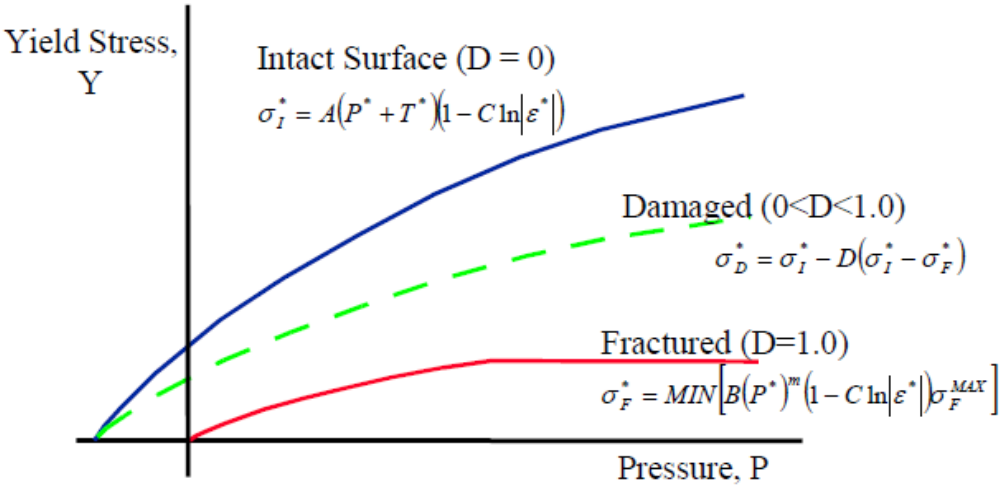

Figure 2.24 Graph of the intact and failed curves in the Johnson-Holmquist strength model[22].

จุฬาลงกรณ์มหาวิทยาลัย
Chulalongkorn University

2. Equation of State

The polynomial EOS is used with the Johnson-Holmquist model. This form of the polynomial EOS was adapted from the general Mie-Gruneisen EOS and has different analytical forms for the states of compression and tension. The model as implemented in Explicit STR requires several parameters such as the reference density (ρ_0), and constants A1, A2, A3, B0, B1, T1 and T2. If T1 is input as 0.0 it is reset to T1 =A1. The polynomial EOS then defines the pressure as;

For $\mu > 0$ (compression): $p = A_1\mu + A_2\mu^2 + A_3\mu^3 + (B_0 + B_1\mu)\rho_0 e$ -----Eq.2.22

For $\mu < 0$ (tension): $p = T_1\mu + T_2\mu^2 + B_0\rho_0 e$ --------Eq.2.23

3. Failure model

Based on the current strain and time increments, the current effective strain rate and total strains can be calculated. The current strength (equation 2.21) can be used to determine the current increment in plastic strain. From this, the current increment in damage can be determined as shown in equation 2.24.

$$\Delta D = \frac{\Delta \varepsilon_p}{\varepsilon_f},\ D = \sum \frac{\Delta \varepsilon_p}{\varepsilon_f} \quad \text{----------Eq.2.24}$$

where the plastic strain to fracture under a constant pressure is defined as:

$$\varepsilon_f = D_1 (P^* + T^*)^{D_2} \quad \text{----------Eq.2.25}$$

As previous indicated, an increment in the damage leads to material bulking. This can be described physically as the larger volume a fractured material occupies compared to the intact material. Constraint or confinement from the surrounding material results in a local increase in pressure.

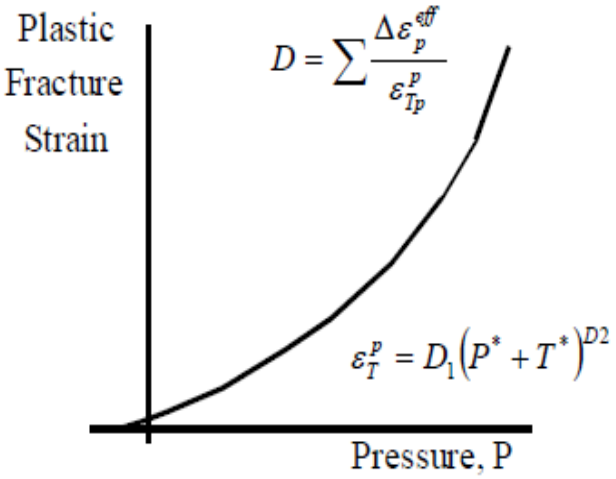

Figure 2.25 Graph of the Johnson-Holmquist failure model [22].

Chulalongkorn University

2.4.2 Material model for 7.62 mm Bullet

Hazell et al. [29] examined the penetration of a lead-antimony cored small-arms bullet (7.62 mm x 51 mm NATO Ball) against a glass face backed by elastomeric resin. A simple linear viscoelastic model was used for the resin, the Johnson and Cook model for the bullet and the JH-2 model for the float glass. The results showed that the thickness and configuration of the resin back support affected the energy absorption and the bullet penetration depth. Furthermore, their experimental and FEA results showed good agreement with regards to the failure patterns. Since this study use the same bullet (7.62 mm x 51 mm NATO ball), Hazell's material models for the bullet will be applied in this study.

2.4.2.1 Johnson-Cook model [29,30]

1. Strength model

The Johnson-Cook constitutive model aims to model the strength behavior of materials subjected to large strains, high strain rates and high temperatures. Such behavior might arise in problems of intense impulsive loading due to high velocity impact and explosive detonation. The model defines the yield stress σ as

$$\sigma = \left[A + B\varepsilon_p^n\right]\left[1 + Clog\varepsilon_p^*\right]\left[1 - T_H^m\right] \quad \text{--------Eq.2.25}$$

where, ε_p = effective plastic strain

ε_p^* = normalized effective plastic strain rate

T_H = homologous temperature = $(T - T_{room})/ (T_{melt} - T_{room})$

A, B, C, n and m = material constants

The expression in the first set of brackets gives the stress as a function of strain when $\varepsilon_p^* = 1.0\ sec^{-1}$ and $T_H = 0$. The constant A is the basic yield stress at low strains while B and n represent the effect of strain hardening. The expressions in the second and third sets of brackets represent the effects of strain rate and temperature, respectively. In particular the third relationship models the thermal softening so that the yield stress drops to zero at the melting temperature T_{melt}. The constants in these expressions were obtained by Johnson and Cook empirically by dynamic Hopkinson bar tensile tests over a range of temperatures and other mechanical tests and checked by calculations of Taylor tests of impacting metal cylinders on rigid metal targets which provided strain rates in excess of $10^5\ sec^{-1}$ and strains in excess of 2.0.

2. Equation of State

The Mie-Gruneisen form of the EOS is used to represent the relationship of pressure in terms of energy and volume and is expressed as a change in pressure dp which can be written as

$$dp = \left(\frac{\partial p}{\partial v}\right)_e dv + \left(\frac{\partial p}{\partial e}\right)_v de \quad \text{-------Eq.2.26}$$

and a given term, the Gruneisen Gamma is

$$\Gamma = v\left(\frac{\partial p}{\partial e}\right)_v \text{-------Eq.2.27}$$

The Gruneisen coefficient, Γ for the copper jacket and lead core of the 7.62 mm bullet in this study are shown in Table 2.4. The general form of the Mie-Gruneisen EOS is shown in equation 2.28;

$$p = p_r(v) + \frac{\Gamma(v)}{v}[e - e_r(v)] \text{ ---------Eq.2.28}$$

Table 2.4 The parameters of the Gruneisen EOS for the 7.62 mm bullet components[29].

	Notation	PRR (polyrubber)	Gilding metal (copper)	Core (lead)	Polycarbonate
Reference density (kg/m^3)	ρ	1010	8930	22340	1200
Bulk sound speed (m/s)	c_0	852	3940	2006	1933
Slope in U_s versus U_p diagram	S	1.865	1.489	1.429	2.65
Grüneisen coefficient	Γ	1.50	2.02	2.74	0.61

3. Failure model

The Johnson Cook failure model is used to model ductile failure of materials experiencing large pressures, strain rates and temperatures. It consists of three independent terms that define the dynamic fracture strain (ε_f) as a function of pressure, strain rate and temperature [29,31,32]. This failure model can only be applied to solid bodies.

The damage in the material is accumulated locally using a damage parameter, calculated as follows:

$$D = \sum_{t=0} \frac{\Delta\varepsilon}{\varepsilon_{JC}^f} \text{ ----------Eq.2.29}$$

where, $\Delta\varepsilon$ is the incremental strain and ε_{JC}^f is the equivalent failure strain. The value of ε_{JC}^f is recalculated using equation 2.30 for each time step giving the damage parameter its path dependency.

$$\varepsilon_{JC}^f = [D_1 + D_2 \exp D_3\sigma^*][1 + D_4 ln\dot{\varepsilon}^*][1 + D_5 T^*] \text{ --------Eq.2.30}$$

Here, $\sigma^* = p/\sigma$, where p is the pressure and σ is the von Mises equivalent stress. The material constants are D_1, D_2, D_3, D_4, and D_5. While, the first set of brackets shows the relationship of pressure dependence, the second one is the strain rate dependence and the last one is the temperature dependence.

2.4.3 Material model for PVB film

The mechanical properties of PVB, as an energy absorption interlayer material in a windshield etc., should be thoroughly studied, especially under impact scenarios. Although, PVB has served as an interlayer material in automotive windshields for over 70 years, little research has been reported on the mechanical properties of PVB, not to mention its dynamic behavior. However, there is some small amount of previous research that greatly enhances the understanding of the mechanical and dynamic behavior of PVB. The dynamic behavior of PVB interlayers in the laminates system has been studied by simulation. Various material models to represent the dynamic behavior that have examined include elastic, hyperelastic, viscoelastic and elastoplastic. From, experiments, it has been shown that the loading time has a big influence on the mechanical behavior of polyvinyl butyral (PVB). The long-time behavior of PVB is viscoelastic, while the short-time behavior is closer to elastoplastic or brittle. Like other plastic materials, PVB shows a failure with large strains (appr. 300%), which indicates the need of a hyperelastic material law in some cases.

2.4.3.1 Johnson-Cook model

Sun and Lai [10] examined the penetration depth of laminated transparent armor made of seven-layers of soda-lime glass, 2.12-mm thick PVB interlayers and 8 mm and 4.7 mm thick polycarbonate backing layers. The simulation results showed that by using the Johnson Cook strength model for PVB and the JH-2 model for soda-lime glass, that the penetration depth was only slightly over-predicted compared to those of experiment results. Thus, the Johnson Cook strength model will be used for PVB in this study.

1. Strength model

The Johnson-cook material model was used for the PVB film, as shown in equation 2.25;

$$\sigma = \left[A + B\varepsilon_p^n\right]\left[1 + Clog\varepsilon_p^*\right][1 - T_H^m] \quad \text{--------Eq.2.25}$$

As the PVB response is dependent on the strain rate and temperature, the expressions in the second and third sets of brackets, which represent the effects of strain rate constant (C) and temperature coefficient (m), respectively, were focused on. Due to there be lacking of sufficient dynamic property testing data of PVB films, there was a need to calibrate the material model to match the closest available results before numerical calculations.

2. Equation of State

The Mie-Gruneisen form of the EOS from section 2.4.2.1 was used.

3. Failure model

The experimental failure behavior of PVB film as interlayer in laminated target has rarely been observed. In practice, the percentage of elongation to failure can be up to 300 %. The principal strain failure model was applied to represent the failure of the PVB film interlayer. Principal strain failure was defaulted setup into two values in material model setup; the first value is Maximum Principal Strain (1E+20) and the second one is Maximum Shear Strain (1E+20). However, in this study, these two values were turn off in material model data, the failure characteristic of PVB would relate to the global erosion in initial FEA setup.

2.4.3.2 Mooney-Rivlin model

The Mooney-Rivlin hyperelastic model is popular for modeling the large strain, non-linear behavior of incompressible materials, i.e., rubber. It is important to understand that that the Mooney-Rivlin model does not give any special insight into material behavior. It is simply a curve-fit of various polynomials to the test data. The numerical values of coefficients resulting from the curve-fits are entered into FEA programs for use in mechanical analyses.

Yang and Zang [33] tested a hyperelastic material constitutive response model, based on the Mooney-Rivlin theorem, and presented an experiment device for testing PVB in tension under high strain rates. Uniaxial tensile experiments of PVB under high strain rates were conducted, and the corresponding experiment data were acquired. A strain rates range from 125.6 to 3768 s^{-1}, which is capable of covering the range of strain rates observed in the impact damage process of windshield at the speed 120 km/hr and below, were tested. After analyzing the features of the stress strain curves, the constitutive behavior of PVB at different strain rates were developed.

Xu et al. [34] conducted dynamic compression impact experiments on PVB specimens using the SHPB (Split Hopkinson Pressure Bar) method at strain rates of 700/s, 1200/s, 2200/s, 3500/s and 4500/s. After analyzing the characteristics of the stress-strain curves and energy absorption properties at the different strain rates, the constitutive behavior of the PVB was determined assuming the Mooney-Rivlin model. Parameters in these formulas are calibrated by fitting the experimental uniaxial stress-strain data.

The results showed that constitutive behavior was different in low speed impact versus high speed impact. The PVB absorbed three times more energy in high strain rate scenario than in the low strain rate case. The PVB behaved much under the strain rate 1200/s. The Mooney-Rivlin model was used to fit the stress-strain data obtained from the experiment because the curves were very similar to the rubber-like material studied previously. The fitting with the Mooney-Rivlin model were was found to describe the dynamic behavior appropriately.

The strain rate effect was then further studied. The results showed that PVB does behave rate-dependently under different strain rates. Furthermore, there was little difference between the models with and without a viscoelasticity effect. Thus, PVB can be treated as a material with little or no viscoelasticity.

The Mooney theory established a strain-energy function through careful experimentation to describe the large deformation of hyper-elastic materials. Rivlin gave the most general form of the strain-energy function in a purely mathematical way. On the basis of their research, the standard equation that describes the deformation characteristics of a hyperelastic material is as follows:

$$\sigma^e = p^e I + \alpha_1 B + \alpha_2 B^2 \text{----------Eq.2.31}$$

In the equation, σ^e is the Cauchy stress tensor, and I is unit tensor. p^e is pressure, which is introduced hypothetically because of incompressibility, and

$$\alpha_1 = \left(\frac{\partial W}{\partial I_1} + \frac{I_1 \partial W}{\partial I_2}\right), \alpha_2 = -\frac{2\partial W}{\partial I_2}, I_1 = tr(B), I_2 = \frac{|I_1^2 - tr(B^2)|}{2}$$

Where, W is the body strain energy, I_i is the invariant of B, and B is the Cauchy strain tensor.

Tschoegl[35] proposed that the Mooney–Rivilin model with higher-order terms could be better adapted to large deformation problems of the rubber-like material and gave the trinomial of the revised Mooney–Rivilin model as

$$W = A_1(I_1 - 3) + A_2(I_2 - 3) + A_3(I_1 - 3)(I_2 - 3) \text{ ------Eq.2.32}$$

In the equation, C_{10}, C_{01}, and C_{11} are material constants, which can be acquired through uniaxial tensile experiments. In uniaxial tension, elongation is represented by λ, so the Cauchy invariant can be expressed as

$$I_1 = \lambda^2 + 2\lambda^{-1}, I_2 = \lambda^{-2} + 2\lambda \text{ ----------Eq.2.33}$$

Inserting Eq.2.33 into Eq.2.31 and 2.32, under uniaxial tensile, the Mooney–Rivlin constitutive relation can be written as

$$\sigma = 2\lambda(1 - \lambda^{-3})(C_{10}\lambda + C_{01} + C_{11}(\lambda^2 + 2\lambda^{-1} - 3 + \lambda(\lambda^{-2} + 2\lambda - 3))) \text{ ----Eq.2.34}$$

จุฬาลงกรณ์มหาวิทยาลัย
Chulalongkorn University

In uniaxial tension, λ=1+ε, and ε is the tensile strain. Plugging λ=1+ε into Eq.2.34, the constitutive relation can be written as equation 2.35

$$\sigma = 2(1+\varepsilon)(1-(1+\varepsilon)^{-3})(C_{10}(1+\varepsilon) + C_{01} + 3C_{11}((1+\varepsilon)^2 - (1+\varepsilon) - 1 + (1+\varepsilon)^{-1}))$$ ----------Eq.2.35

Examples of C_{10} (A_1), C_{01} (A_2), and C_{11} (A_3) as a function of strain rate for the Mooney-Rivlin model shown in Table 2.5.

Table 2.5 Empirical material parameters fitted for the Mooney-Rivlin model[34].

Strain rate (s^{-1})	Mooney-Rivilin parameters		
	A_1	**A_2**	**A_3**
700	106.9032	-140.7256	-26.8505
1200	257.0411	-317.8733	-64.7156
2200	271.2663	-338.1145	-65.4526
3500	249.2075	-315.1729	-55.9025
4500	295.2272	-371.3073	-67.1798

จุฬาลงกรณ์มหาวิทยาลัย
Chulalongkorn University

2.4.3.3 Viscoelastic model

Viscoelastic materials are characterized by a combination of elastic behavior, which stores energy during deformation, and viscous behavior, which dissipates energy during deformation. The elastic behavior is rate-independent and represents the recoverable deformation due to mechanical loading. The viscous behavior is rate-dependent and represents dissipative mechanisms within the material. A wide range of materials (such as polymers, glassy materials, soils, biologic tissue, and textiles) exhibit viscoelastic behavior. Following are descriptions of the viscoelastic constitutive models, which include both small and large deformation formulations. Also presented is time-temperature superposition for thermo-rheologically simple materials and a harmonic domain viscoelastic model.

Amos and Bennison [36] investigated glass stress in two glass layers/ PVB film laminates using several methods, including finite element with a full polymer interlayer model. The soda-lime glass was modeled as a simple linear-elastic material with a Young's modulus of 72 GPa and a Poisson's ratio of 0.22. The PVB interlayer was modeled as a linear viscoelastic material with time and temperature effects. The resulted showed that the selection of the material model for the PVB interlayer still needed to be checked against code requirements in order to satisfy the individual simulation cases.

1. Strength model

To represent strain rate dependent elastic behavior, a linear viscoelastic model can be used. The long term behavior of the model is described by the long term or elastic shear modulus G_∞. Viscoelastic behavior is introduced via an instantaneous shear modulus G_0 and a viscoelastic decay constant β. The viscoelastic deviatoric stress at time increment n+1 is calculated from the viscoelastic stress at time increment n and the deviatoric strain increments at time increment n via

$$\sigma'_{vn+1} = \sigma'_{vn} e^{-\beta \Delta t_n} + 2(G_0 - G_\infty) \frac{(1-e^{-\beta \Delta t_n})}{\beta} \frac{\Delta \varepsilon'_n}{\Delta t_n} \text{ ---------Eq.2.36}$$

The deviatoric viscoelastic stress is added to the elastic stress to give the total stress at the end of each cycle.

2. Equation of State

In the ideal gas equation it is shown that p is a function of both specific volume v and specific entropy S. In many cases, especially if the material is a liquid or solid, the influence of changes in entropy is small or negligible so that p may be considered a function of only density (or specific volume). An alternative approach is to consider the initial elastic behavior expressed by an approximation to Hooke's Law which can be written as

$$p = K\mu \text{ ----------Eq.2.30}$$

where, $\mu = \frac{\rho}{\rho_0} - 1$ ---- Eq.2.16

and K is the material bulk modulus.

จุฬาลงกรณ์มหาวิทยาลัย
Chulalongkorn University

3. Failure model

Principal strain failure used the default setup for the two values in the material model; the first value is Maximum Principal Strain (1E+20) and the second one is Maximum Shear Strain (1E+20). But in this study setup both values were off in this material model.

2.4.4 Summary

From the overall literatures, the most widely-used material models of each component in dynamic loading condition in explicit material data are summarized in Table 2.6. However, in each material model needed to further adjust compulsory parameters that affect to the closet realistic in ballistic testing and damaged target. There are some important parameters would be calibrated because in reality material's parameters could not obtain from the experiment such as strain rate constant and thermal softening exponent in Johnson-Cook model.

Table 2.6 Material models for Soda-lime glass, PVB film and the 7.62 mm bullet.

Materials	Strength model	Equation of State	Failure model	References
Soda-lime glass	JH-2	Polynomial	JH Failure	[13,24,25]
PVB films	JC	No	Principal Strain	[30]
	Hyperelastic	No	No	[33,34]
	Viscoelastic	Linear EOS	Principal Strain	[36]
Lead core	JC	No	JC Failure	[29,32]
Copper alloy jacket	JC	No	JC Failure	[29,32]

จุฬาลงกรณ์มหาวิทยาลัย
Chulalongkorn University

2.5 Ballistic damage analysis

Practically, after ballistic testing of a laminate sample, the aluminum witness plate was observed to determine the pass/fail status. This was to the extent of characterization for many years. On the other hand, when there is a need to improve the ballistic performance of the laminate structures, the design must be iterated, often by studying the ballistic damage and the damage evolution of the laminate structures. This basic knowledge of how the laminates fail can lead to better ballistic performance of the laminated transparent armor.

Experimentally, ballistic damage characterization of laminate systems is done by the observation of the damage patterns and fragments of the target and projectile. The target can be cut in cross-section and photographs recorded to establish the damage pattern in the laminate structure. This type of characterization is a destructive technique, and the obtained data is just superficial surface data on the crack morphology. Other characterization methods can be applied to investigate the damage or damage evolution, for example, X-ray computed tomography (XCT) [37], flash X-ray and high–speed video camera [38]. While these methods generate desirable data, they still have limitations, chiefly the inability to provide insight into the stress or energy distributions in the laminate system. This type of mechanical data in the forms of the overall energy in system, the pressures, and the principal stress and strain of each layer are needed to estimate the ballistic strength. Therefore, FEA has been widely used to design and study the ballistic damage behavior of laminate systems [35,39,40,41].

2.5.1 Hertzian damage and ballistic crack patterns

When a high-speed projectile strikes a brittle material, such as glass, it will produce a characteristic damage, such as a conical crack and/or eroded impact crater, radial cracks, etc. The glass laminates produce concentric cracks in an approximately circular pattern around the point of impact[42]. They are usually in curved segments that terminate at radial cracks. At the impact location or crater there is typically a 'Hertzian cone' crack is a funnel-shaped area of damage caused by a high-velocity impact [43,44,45]. The ballistic damage pattern in glass laminated transparent armor was studied by Bless and Chen [20] for a 7 layer-glass laminate impacted by a 12.7 mm, 13.4 gram projectile at a velocity of 1,118±5 m/s. They investigated the damage in glass layer using an optical microscope (microscopic and macroscopic examination) and then sketched the observed damage patterns as shown in Figure 2.26.

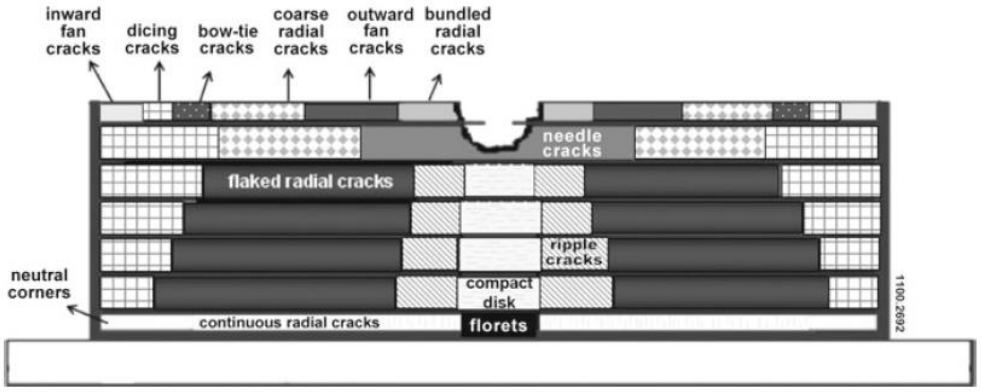

Figure 2.26 Sketch showing damage zones in a laminate target after ballistic impact [20].

The crack pattern in each layer of the laminate has a unique pattern. The strike layer showed the characteristic crack pattern as starting from the inner circle, these were the impact crater is located, bundled radial cracks, outward fan cracks, coarse radial cracks, a bow-tie region, dicing cracks, and inward fan cracks, as shown in Figure 2.27, and sketched in Figure 2.28. A similar damage pattern was seen in the second glass layer, when compared to the strike layer. The rearmost layer showed a different crack pattern, with florets, which are condensed cracks and very small asterisk-like features in the center of back plate, directly underneath the projectile impact site as shown in Figure 2.29.

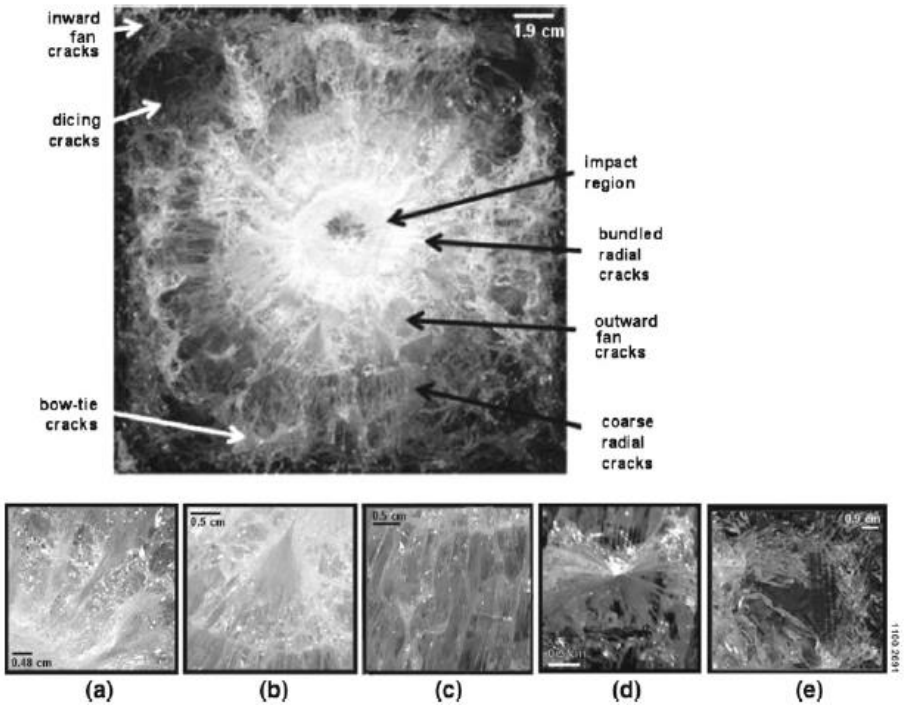

Figure 2.27 Details of damage in the strike plate: (a) bundled radial cracks, (b) fan crack, (c) coarse radial cracks, (d) bow-tie crack and (e) dicing crack [20].

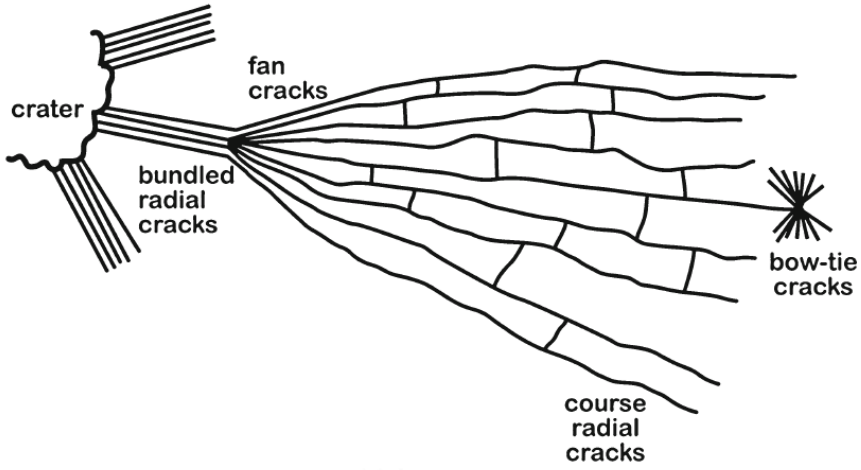

Figure 2.28 Drawing of crack features seen in the strike face (not to scale) [20].

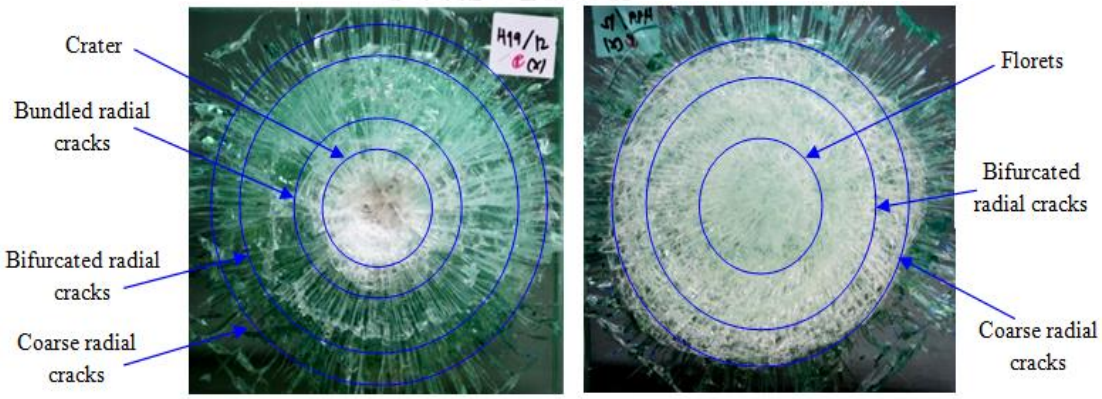

Figure 2.29 The damage of the strike face and the backing plate [9].

In the intermediate glass layers, there were compact central disks, surrounded by ripple cracks, coarse radial cracks, and dicing cracks, as shown in Figure 2.30. Around the central compacted column were ripple cracks, which were especially prominent in the first intermediate layer and decreased in extent in the deeper layers. However, the ripple crack fragments were coarser and harder to break loose than the needle crack fragments, and their axis was perpendicular to the radial direction. The coarse radial crack regions in the deeper glass layers were different from the corresponding regions in the first two layers. The glass between the radial cracks was composed of flakes that broke off in platelets parallel to the impact surface. More transverse cracks were found in the deeper layers than compared to the first two layers.

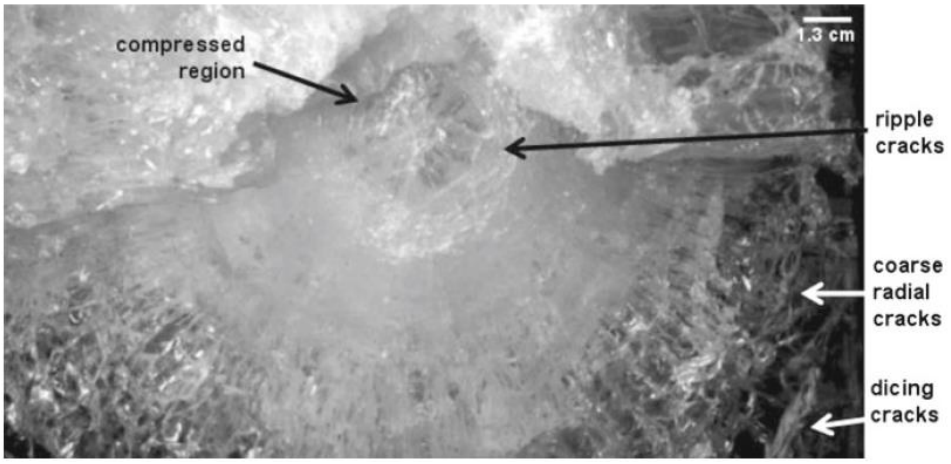

Figure 2.30 Compacted region in the intermediate layer, beneath where the projectile stopped, which transitions to ripple cracks and coarse radial cracks [20].

จุฬาลงกรณ์มหาวิทยาลัย
Chulalongkorn University

2.5.2 Ballistic failure mechanism

The projectile impact generates strong stress waves that propagate in the laminate structure, which are transmitted, absorbed and reflected in the structure. The stress waves interact with the boundaries and the interfaces between glass/film, glass/glass, and the crack surfaces where created. The stress/shock wave propagation within the laminate structures occurs during a very short duration in time and is very complex. Therefore, FEA simulation has been used to demonstrate the mechanism of bullet and target interaction leading to the failure of the target. Martin et.al had studied the failure mechanism of glass laminates under air blast loading. They observed that after the glass layers were failed, the polymer interlayer held the glass fragments together. The glass laminate failure process was divided into five phases in relation to the force versus displacement plot, as shown in Figure 2.31.

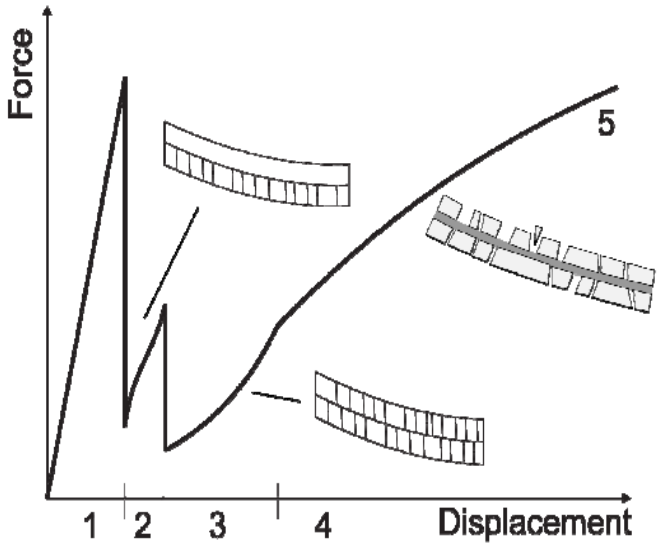

1st phase, elastic behavior of the glass plies.

2nd phase, the first glass ply is broken; the other glass ply is still intact. The interlayer is not damaged.

3rd phase, the second glass ply fails. The interlayer reacts elastically.

4th phase, the interlayer reacts plastically. The spalls are bonded to the interlayer.

5th phase, the interlayer fails by reaching failure strain or by cutting from the fragments.

While the 1st phase and its limit can be modelled with several analytical and numerical methods. The 2nd to 5th phases are more complex to simulate.

Figure 2.31 Failure mechanism of glass laminates [41].

2.5.3 Wave propagation and impedance mismatch

A significant factor influencing the failure of the glass laminates is stress wave propagation and interaction. Grujicic et al.[46] Investigated the stress wave propagation using an edge-on-impact (EOI) set up coupled with a high-speed 0.10 µs resolution Cranz-Schardin camera and a dynamic photo-elasticity technique, to visualize the propagation of stress waves in soda-lime glass sheet. The findings revealed that the propagation of the elastic longitudinal stress wave and transverse normal stress wave (the wave associated with the maximum principal stress) were found first, at 7.7 µs after impact of the spherical projectile at 440 m/s. The longitudinal stress wave traveled through the glass and then the transverse wave reflected backward from the elastic wave front, as visualized in Figure 2.32 (1) and (2) after 15 µs, and a coherent damage front and macro cracking was observed as shown in Figure 2.32 (3).

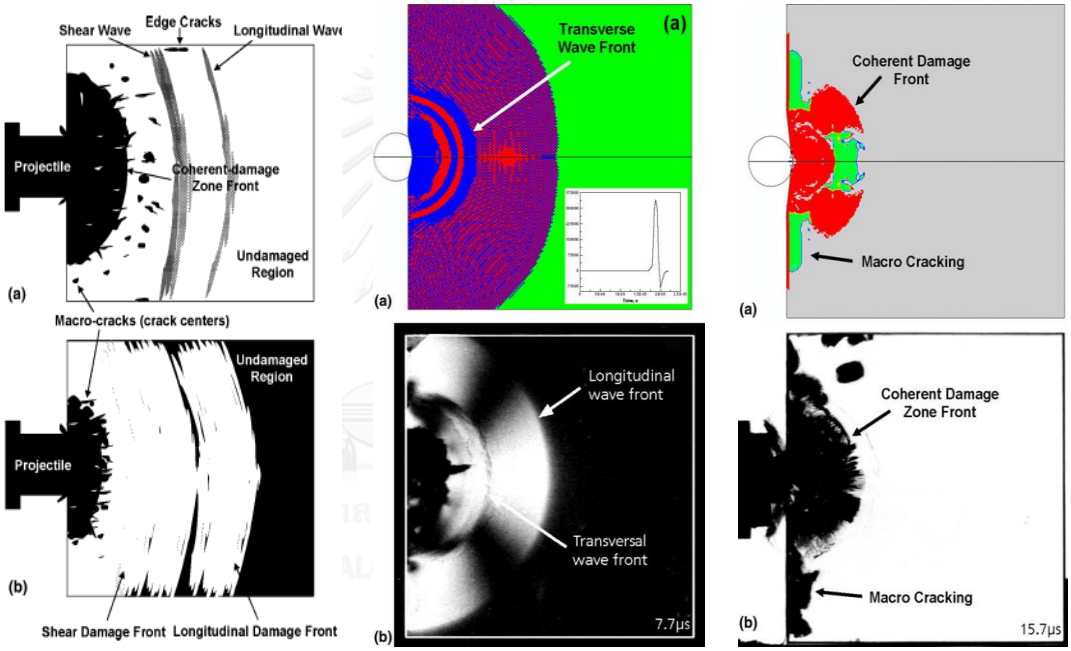

(1) Schematic of the typical
(a) shadowgraph and
(b) birefringence results obtained by Strassburger et al.

(2) A comparison of the transverse stress wave fronts obtained (a) computationally and (b) experimentally for post-impact time of 7.7 µs.

(3) A comparison of the coherent-damage zone fronts obtained (a) computationally and(b) experimentally for post-impact time of 15.7 µs.

Figure 2.32 The comparison of stress wave propagation between shadowgraph and simulation in a glass layer after spherical projectile impact at 440 m/s [46].

Furthermore, in multi-layer structures it is common that the materials might have widely different elastic moduli and (yield) strengths. The presence of a ceramic layer greatly increases the severity of the stress gradient at the interfaces. There is another factor which impacts the glass laminates' failure called 'impedance mismatch' [47,48,49,50,51,52], as shown Figure 2.33. Normally, each material has a specific acoustic impedance (Z) which is defined as the product of density (ρ) and acoustic velocity (C) of the material as shown in equation 2.31 [47].

$$Z = \rho C \quad \text{---------- Eq.2.31}$$

Acoustic impedance is important in the determination of acoustic transmission and reflection at the boundary of two materials having different acoustic impedances. Stress waves are reflected at boundaries where there are differences in acoustic impedance, Z. This is commonly referred to as impedance mismatch.

The formulation for acoustic reflection (R_{coef}) and transmission coefficient (T_{coef}) are given below for a wave-entering medium 2 from medium 1:

$$R_{coef} = \left(\frac{Z_2 - Z_1}{Z_2 + Z_1}\right)^2, \quad T_{coef} = 1 - R_{coef} \quad \text{--------- Eq.2.32}$$

The acoustic impedance of soda-lime glass and PVB films are 13.4 MRayl and 2.60 MRayl (1 Rayl = $kg.m^{-2}.s^{-1}$, S.I. unit of acoustic impedance is MRayl or Megarayls), respectively [53,54].

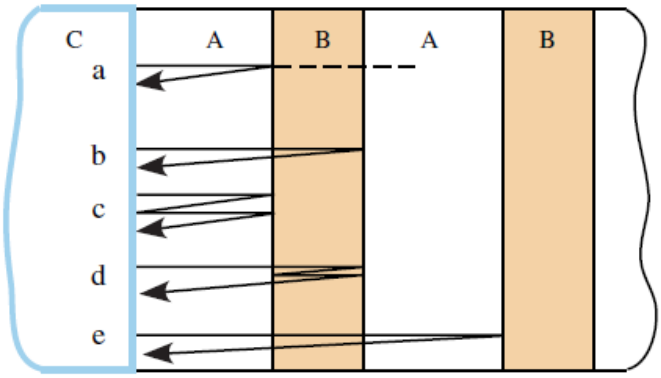

Figure 2.33 Multi-step loading method: the wave trains that reach the impact plane from inside of the target due to reflections [49].

Stress/shock wave propagation in multi-layer structures is significantly more complex than in monolithic materials and cannot be treated by simple superposition principles. Impact on multi-layer structures can produce severe stress heterogeneity at the interfaces as well as serious stress gradients within the layers themselves. Brittle layers have been shown to be highly susceptible to the formation of steep stress (strain) gradients and are, therefore, very likely to fracture. The ductile materials may be able to accommodate these gradients via plastic deformation. Zhuang, et al. [55] investigated the shock wave propagation in periodically layered polycarbonate/glass laminates that were impacted by aluminum plate at a velocity range 560 to 1100 m/s. The influence of the scattering effect induced by the internal interfaces on shock wave propagation in the heterogeneous laminates was studied. The role of interface heterogeneity, in terms of, impedance mismatch, the number of interfaces and the shock wave evolution with propagation distance was investigated.

The ratio of the acoustic impedance of glass (hard) layer to polycarbonate (soft) layer is approximately 8/1. It is apparent that the interface impedance mismatch has a very large effect on the heterogeneity of the interfaces. Therefore, it may be postulated that the interface impedance mismatch contributes to both the bulk and the deviatoric responses of the composite to shock compression.

If the total thickness of each component is kept constant, increasing the interface number (or the density of interfaces) of the laminates by reducing the layer thickness resulted in a steepening of the shock front slope and an increase in the amplitude of the oscillations in the shock profile. The former effect implies the increase in the nonlinearity of the laminates and the latter indicates that more of the kinetic energy has been transformed to internal energy and the dissipation of shock energy increased.

The effect of different propagation distances/ or specimen thickness revealed that the initial compression process of the structures (within the shock front) was independent of the propagation distance in the structures. For all cases, the difference between the laminates became important only after the initial compression. Two mechanisms may be responsible for this result. One is due to the dispersion resulting from the multiple reflections of the shockwave from the multiple interfaces. The other is due to the release wave originating from the rear (free) surface of the flyer and its interaction with the propagating shock wave in the structure.

By acoustic reflection and transmission, severe stress inhomogeneity may exist in multi-layer structures and these may have serious consequences for mechanical, as well as other properties. These research outcomes should serve as basic concepts for the design of multi-layered structures in order to optimize their energy dissipation and fracture characteristics.

2.5.4 Energy dissipation

As mentioned in the previous section, the failure mechanism of glass laminates is quite complicated to characterize and measure, particularly some information (stress wave, impact pressure, and acoustic impedance). Nevertheless, some research has been concerned with energy dissipation in laminate systems by mathematical calculation and experiment. Wilkins [56] studied the loss of bullet mass due to erosion from impact with a 15 mm thick ceramic plate at a velocity of 853 m/s. It was found that almost all of the kinetic energy was lost, with some being converted into internal energy in the target, and some being lost to plastic work/erosion of the bullet. The eroding mass of the bullet decreased the momentum of the bullet and reduced the penetration performance to the target. Figure 2.34 showed that approximately 30 percentage of the initial kinetic energy was absorbed via internal energy by the target.

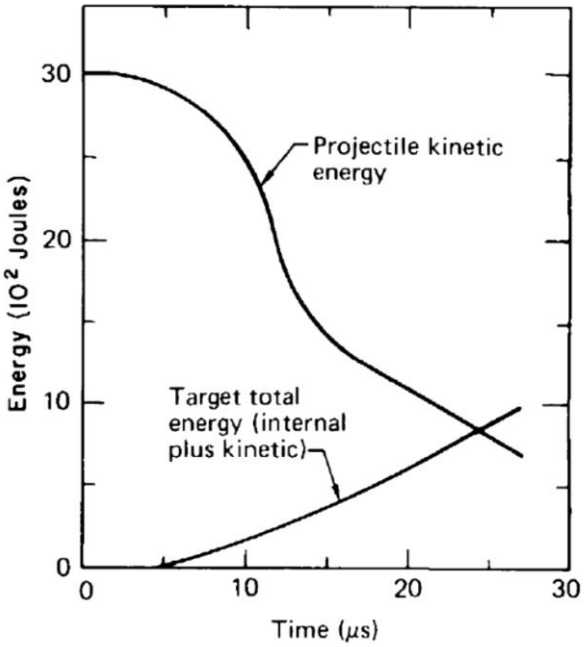

Figure 2.34 Graph showing the decrease in kinetic energy after bullet impact [44].

The ballistic limit of a material should be known in order to ensure a safe armor design. This limit is commonly defined as the minimum velocity at which a projectile consistently and completely penetrates a target of a given thickness and angle of obliquity. The energy required for complete penetration of the target material (E_p) is obtained from equation 2.33:

$$E_p = \frac{1}{2}m(v_i - v_f) \quad \text{---------- Eq.2.33}$$

where, m is the mass of the bullet, and v_i and v_f represent the impact and residual velocities, respectively. E_p typically depends on the velocity, shape and mass of the projectile and the composition of the impacted material, and indicates the extent of the damage. If the impact energy is below the threshold energy required for damage initiation, no damage occurs. With an increase in velocity above the threshold, a reduction in residual energy is accompanied by the spread of damage. In the ballistic range, a constant residual energy is observed as the impact energy exceeds the penetration threshold, thus localizing the damage to a neat perforation [57,58,59].

The internal dissipation of energy is one of the basic dynamic characteristics of a structural material and can be used for indirectly estimating its performance under loading. The energy absorption of composite components can be described in several ways. Most investigations of energy dissipation in glass and polymer materials have been carried out under time loading conditions[60]. Experimental data on the quantitative nature of the energy losses in polymers assumed that it was converted into heat. The measurement of energy dissipation under continuous loading is complicated. Therefore, FEA is one method to investigate these energy characteristics. As shown in Figure 2.35, FEA was used to simulate the energy dissipation and fracture propagation in the glass laminates. It was demonstrated that FEA can be a method for collecting data that cannot easily obtained by experiment.

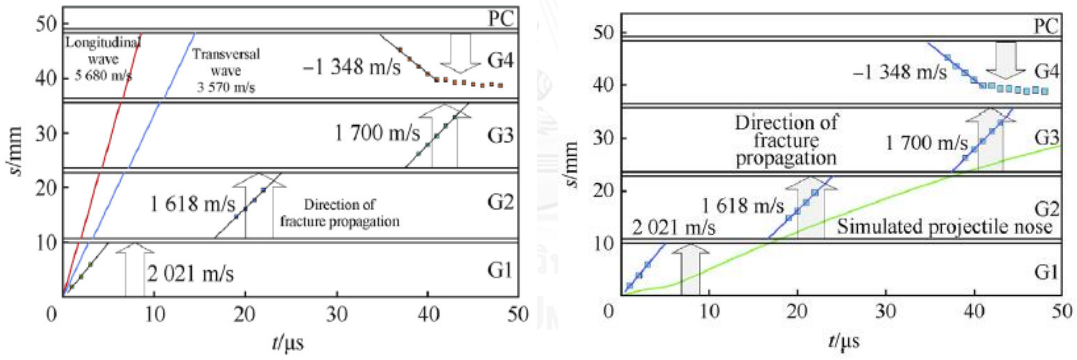

(a) Path-time history of wave and fracture propagation at an impact velocity of 805 m/s.

(b) Comparison of the experimental damage propagation and the computed position-time curve of the projectile.

Figure 2.35 Diagram of wave and fracture propagation within laminate samples [61].

The absorption capability of laminates structure is generally described in terms of internal energy absorption (energy per unit volume). Skvortsov et al. [62] postulated that the total energy absorbed by the target energy can be divided into the energy of damage and the energy of the elastic response of the target:

$$E_{absorb} = E_{damage} + E_{elastic}$$

The damage energy, E_{damage}, is associated with the energy of laminates damage/fracture and the energy of elastic response $E_{elastic}$, is related to the global deformation and kinematics of the target. In the case of laminates, the energy-dissipating mechanisms that contribute to E_{damage} are numerous. Quantification of the components of the energy of absorption is not an easy matter, though numerous attempts are known.

In this study, the FEA method was applied to investigate the kinetic energy (KE), internal energy (IE), and normalized energy (NormIE) by extracting the IE and KE results of each glass and PVB films layer using the ANSYS Explicit STR software. The energies absorbed in each glass layer were collected to evaluate the damage level of the overall laminates.

2.5.5 Volumetric damage calculations

All experimental studies of ballistic impact with penetration show that the absorption capabilities are increased with higher impact velocities, and that the energy of absorption, E_{abs} has its limit at the higher velocities. These phenomena are related to the damage response of the laminated structure, because deformation and kinematic motion of the target play an essential role in the energy dissipation. The deformation of the target improves its energy-absorbing capabilities [62]. In this study, it was assumed that the damage energy was directly transformed into damage in the glass layers. Normally, the damage in the glass layers is not measured because its inherit failure behavior is hard to measure in factual quantities. Glass laminates are comprised of a brittle material, glass, and a softer interlayer, often PVB. When the bullet impacts the glass layer, it results in the creation of numerous cracks within the glass layer. The Hertzian cone crack, the radial crack pattern, etc., in the laminates is very complicated, and it is extremely difficult to measure the number of cracks; it is highly prone to counting errors and generating false data[4]. Therefore, the FEA method is used to simulate the damage in three dimensions as a function of time, impact velocity, etc. This enables the determination of ballistic damage when combined with suitable material models and FEA setup. The calculated ballistic damage value is called ‘volumetric damage’ and it is the product of the elemental volume of each glass layer and the damage level that is obtained from the failure model of the soda-lime glass. Due to some of the present limitations of FEA, the volumetric damage may not exactly match when compared with experimental results, but it can use as a reasonable criterion to optimize the design of laminated, transparent armor.

2.6 Previous design laminated transparent armor configuration

A lighter-weight laminated, transparent armor design is challenging current research trend in transparent armor. The main drawback of the majority of laminated, transparent armor designs is their high weight. Though, these previous transparent armor configurations can serve as the basis for the fundamental design concept, in order to obtain a lighter weight, laminated, transparent armor design. It should be mentioned that the configurations are typically designed for testing of a specific bullet types or bullet velocity, etc.

Strassburger et al. [61] fabricated glass laminates which consisted of four layers of soda-lime glass, one with a thickness of 10 mm and three layers each with a thickness of 12 mm, and a 3 mm thick polycarbonate backing. PVB or PU bonding layers were used which had a thickness of 0.8 mm. The dimension of the laminates were 500 mm x 500 mm and they were tested against a 7.62 mm armor piercing (AP) projectile with a tungsten carbide core (total mass 11.1 g.) at an impact velocity range from 800 to 880 m/s, as shown in Figure 2.36. The results showed that this configuration could perform good bullet protection.

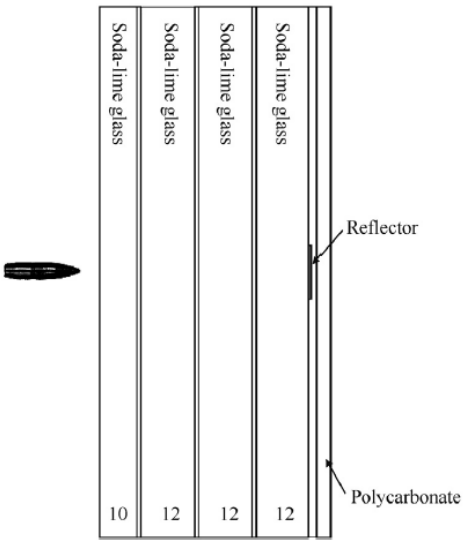

Figure 2.36 Glass laminate design for tests with 7.62 mm AP projectiles [61].

Bless and Chen [20] mimicked the transparent armor design of a military lightweight fighting vehicle. The surrogate armor had seven-layers of soda-lime glass sized 30 cm x 30 cm, a polycarbonate backing sized 36 cm x 36 cm and bonded with 0.6 mm thick polyurethane films. The target was impacted with a standard 12.7 mm (50 caliber) 13.4 grams, HRC30 steel fragment-simulating projectile (FSP) at a velocity of 1,118±5 m/s. Bobaru et al. [39] also adopted the same designed configuration of Bless and Chen in order to conduct an FEA study to compare the damage patterns of each layer of glass in the laminates. The glass laminate configuration is depicted in Figure 2.37.

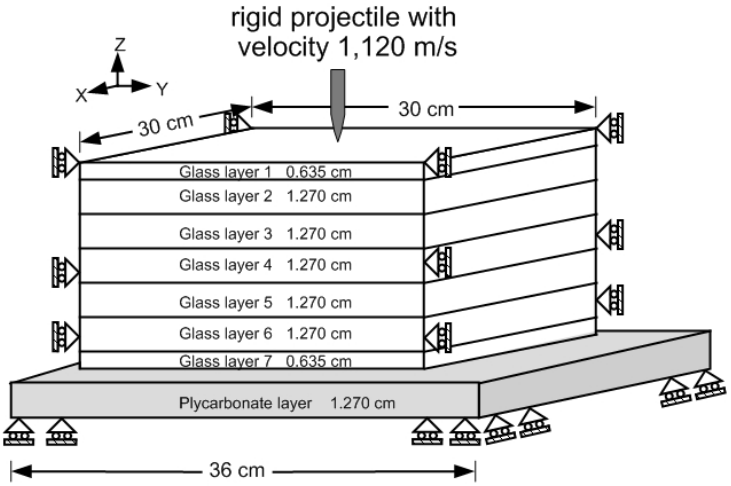

Figure 2.37 Sketch of the laminated glass target [39].

Grujicic et al. [7] FEA study used the same laminated target design, with dimensions of 304.8 mm x 304.8 mm x 73 mm. It consisted of five layers of 10.42 mm thick glass and five layers of 4.17 mm thick polycarbonate. The target was impacted with four 0.30-caliber M2 AP (armor piercing) bullets, as displayed in Figure 2.38, at a velocity range from 592 to 893 m/s. The targets were tested and evaluated for partial or complete penetration. The results showed that the simulations and Dolan's experimental results were in good agreement that the ballistic velocity limit for this configuration was 815 m/s.

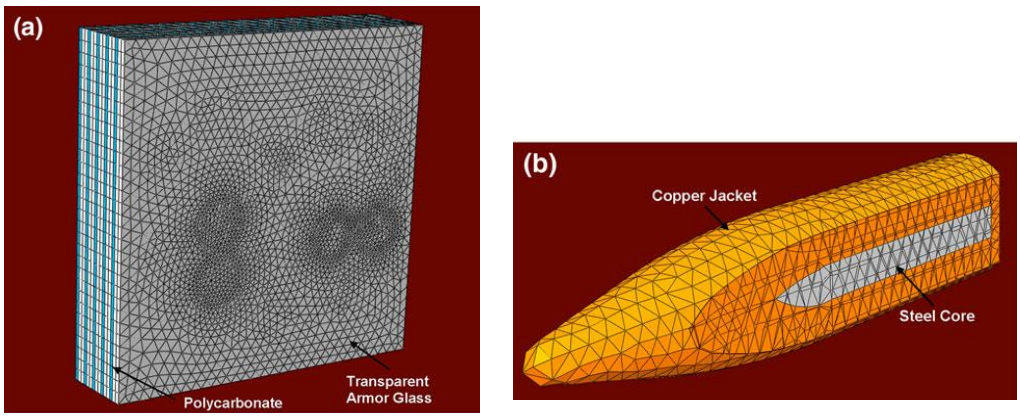

Figure 2.38 Typical finite element meshes used for discretization of (a) transparent-armor test sample and (b) projectile.

Chaichuenchob et al. [9] and Jantharat et al. [3] studied the crack evolution in various laminated target configurations by experimental and FEA simulation. The laminated targets were fabricated with soda-lime glass/PVB film with a size of 305 mm x 305 mm. The targets were shot with a 7.62 mm lead-cored bullet at a velocity of 838±15 m/s. The configurations that were tested are listed in Table 2.7. The effects of the different laminate configurations on the resulting glass damage after impact were studied. The post-test targets were delaminated, and the number of cracks in each glass layer was counted in order to estimate the damage level in each layer. Two laminate configurations with the same total thickness of 67.8 mm referred to as H-19 and I-12, with glass thickness arrangements of 19-12-12-12-6-3 mm and 12-19-12-12-6-3 mm, respectively, showed the lowest damage level among all of the laminate configurations that were examined. The crack analysis further showed that the I-12 model had the lowest number of cracks on the backing plate and was therefore the best glass/PVB configuration that was examined.

Table 2.7 Laminate armor configurations of test specimens [9].

Model	Thickness (mm)					
	H12	**H8**	**H6**	**I12**	**I8**	**I6**
1st layer	19	19	19	12	12	12
2nd layer	12	12	12	19	19	19
3rd layer	12	8	6	12	8	6
4th layer	12	8	6	12	8	6
5th layer	6	8	6	6	8	6
6th layer	3	6	6	3	6	6
7th layer	-	3	6	-	3	6
8th layer	-	-	3	-	-	3
Total Thickness (mm)	67.8	68.56	69.32	67.80	68.56	69.32
Areal density (kg/m^2)	165.99	166.80	167.61	165.99	166.80	167.61

According to the literature review, FEA has been shown to be able to successfully simulate ballistic impact results and should be able to provide beneficial guidance in this study. Thus, to gain more insight into the ballistic protection behavior of laminated, transparent armor systems, the FEA of soda-lime glass/PVB interlayer armor is performed in this study using ANSYS Explicit STR software. The effects of the soda-lime glass and PVB film thicknesses, the glass/film configuration and the number of glass/film layers will be systematically studied and the design optimized, to achieve a lighter-weight soda-lime glass/PVB laminated transparent armor model, with NIJ standard level III ballistic protection, as compared to the reference models. The optimized configuration will then be used as a new design for the soda-lime glass/PVB interlayer laminated transparent armor fabrication. The ballistic test (NIJ standard level III) will be performed in parallel, and the experimental results will be analyzed and compared with of the results of the FEA.

จุฬาลงกรณ์มหาวิทยาลัย
Chulalongkorn University

CHAPTER 3

EXPERIMENTAL PROCEDURES

In this chapter, the details of the 3D FEA simulations and experimental testing of the soda-lime glass/PVB laminated, transparent armor, for the design optimization studies are described.

3.1 Numerical Setup

In order to obtain reasonable results from the 3D FEA simulations, several design and material model calibrations must be performed, as well as the determination of the model parameters for the prediction of material deformation and failure. Material characterization such as the bullet construction and chemical composition were also performed to obtain sufficient information for the material model calibration.

3.1.1 Geometry design

For the FEA simulations of the ballistic impact event, the impact model for this study had two main components: (i) the 'Target', which is constructed of alternating layers of soda-lime glass and PVB film, and (ii) the 'Bullet', which is a 7.62-mm diameter bullet constructed of a copper metal jacket covering a lead core. These two components have specific details in their geometry and dimensions which were acquired in order accurately construct the CAD models for further FEA processing.

3.1.1.1 Target

The experimental targets consisted of soda-lime glass sheets bonded together with polyvinyl butyral (PVB) films using an autoclave process. Commercially-available soda-lime glass sheet thicknesses of 3, 6, 8, 10, 12, 15 and 19 mm were used. Based on the NIJ standard requirements, the glass sheets were cut into squares 305 mm x 305 mm. The initial target configurations were designed using multiple glass layers with the various glass thicknesses, bonded with 0.76 mm thick PVB films. In some models, two layers of PVB film were bonded between the glass layers to make a 1.52 mm thick PVB film. Before ballistic testing, the targets were inspected to assure that no bubbles occurred between the glass and PVB film layers. Examples of the finished targets are shown in Figure 3.1. As the laminated targets are square and the bullet impact was directly in the center, the target geometry for the FEA simulations was drawn with quarter symmetry in order to reduce the computational time.

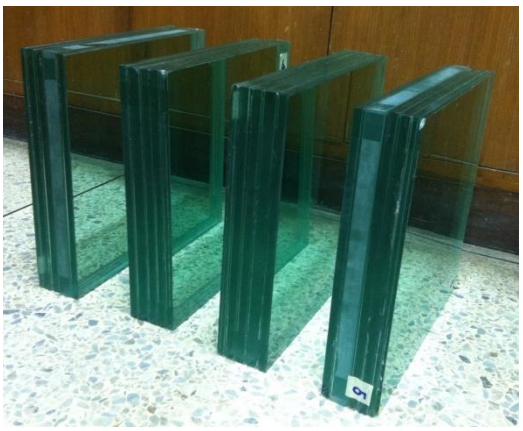

Figure 3.1 Soda-lime glass/PVB laminated transparent armor samples [4].

3.1.1.2 Bullet

In accordance with the NIJ level III testing requirement, the bullet used was a 7.62-mm full metal jacketed (FMJ) bullet. The bullet is made of a lead alloy core covered with a copper alloy jacket. For the FEA, the initial conditions of bullet were set to impact the target perpendicular to the strike face of the target at a velocity of 838 ± 15 m/s. The reference bullet used in this study is depicted in Figure 3.2.

In order to investigate the bullet geometry and chemical composition, the bullet was cut in a vertical cross section. The specimen's surface was ground with fine-sandpaper and polished with 1 μm diamond powder suspension. The chemical composition and dimensions of the 7.62 mm bullet were characterized with an Electron Probe Micro Analyzer (EPMA) (JEOL JXA-8100 EPMA). The chemical composition of the lead and copper alloys were compared with the respective material models available in the ANSYS™ material database and in the literature. Figure 3.3 shows images from the EPMA of the cross section of the bullet at 550X magnification. The bullet was composed of the expected core and jacket structure. Thickness dimensions of the jacket are given in Figure 3.3(a-b) as well.

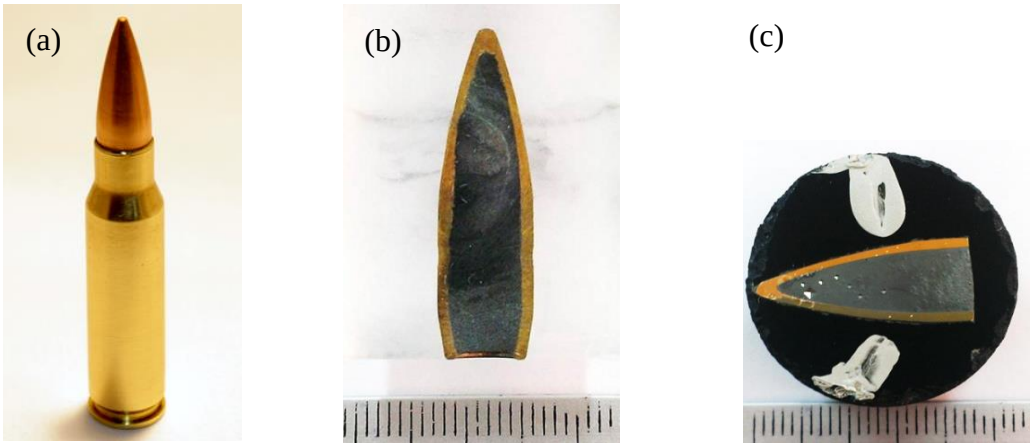

Figure 3.2 Representative 7.62mm FMJ bullet used in this study (a) 7.62 mm FMJ cartridge, (b) 7.62 mm FMJ bullet cross-section mounted in thermosetting resin, (c) 7.62 mm FMJ bullet tip mounted in conductive resin.

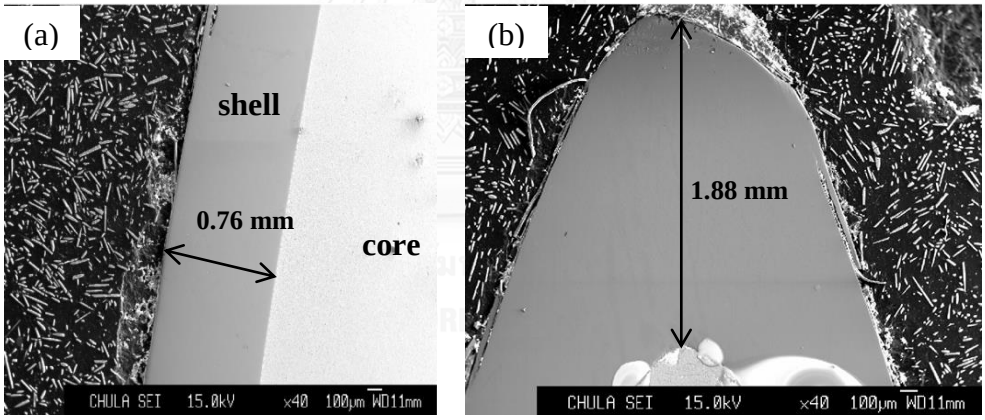

Figure 3.3 EPMA images of the 7.62 mm bullet cross section at 550X magnification (a) Copper jacket side and (b) Copper jacket tip.

3.1.1.3 Target and Bullet FEA Models by DesignModeler in ANSYS software

In this study, the commercial FEM software, ANSYS ExplicitSTR was used for the ballistic impact simulations of the laminated, transparent armors. The starting point of the FEA study was to draw the target and bullet geometry in three dimensions using ANSYS DesignModeler. Two, three and six-layer soda-lime glass/PVB laminated targets were created. The dimensions of the quarter symmetry targets were fixed at 152.5 mm x 152.5 mm for the square target, while for the round targets, the radius was fixed to 152.5 mm. The initial configurations for the calibration models are listed in Table 3.1 and depicted in Figure 3.4.

The reference models were approved, commercially-available transparent armor, capable of NIJ standard level III ballistic protection. The reference configurations, referred to as STD1 and STD2, were modeled to act as baselines for the assessment of the other configurations in terms of volumetric damage and ballistic damage characteristics. Additionally, the damage complexities in multiple-layer targets made it too difficult to properly calibrate the initial FEA conditions in the setup process. Thus, the six-layer targets from the previous study in Ref. [3,5] named A19 and B19 were also used to help calibrate the accuracy of the initial FEA setup of two-layer targets.

It was assumed that all bullets in practical testing had the same overall geometry as shown in Figure 3.5(c). This bullet sketch was adapted from the two-dimensional cross section of 7.62mm bullet in Hazell et al.'s research [27] and the measured bullet dimensions in this study.

The quarter symmetry two- and three -layer transparent armor systems were initially used for mesh adjustments and the FEA setup (Figure 3.4 and 3.5). All of the models simulated the ballistic impact within the time period of 300 microseconds. Moreover, initially, the material models that are widely used in FEA for soda-lime glass, PVB, and the bullet are listed in Table 3.2. These material models will be initially used in this study. Model adjustments may be subsequently evaluated and compared with the experimental results.

Table 3.1 Configuration of the laminated transparent armors used in the calibration models.

Model name / Order assembly	Thickness (mm)						
	STD1	**STD2**	**A19**	**B19**	**T1-S (square shape)**	**T1-R (round shape)**	**T2**
1st Glass	**Proprietary**	**Proprietary**	19	12	19	19	10
1st PVB			0.76	0.76	0.76	0.76	0.76
2nd Glass			12	19	19	19	10
2nd PVB			0.76	0.76			0.76
3rd Glass			12	12			10
3rd PVB			0.76	0.76			
4th Glass			12	12			
4th PVB			0.76	0.76			
5th Glass			6	6			
5th PVB			0.76	0.76			
6th Glass			3	3			
Total thickness (mm)	**67.8**	**68.56**	**67.8**	**67.8**	**38.76**	**38.76**	**31.52**

Table 3.2 The materials models used in initial setup of FEA in ballistic impact of soda-lime glass/PVB interlayer laminated transparent armor model.

Materials	Strength	Equation of State	Failure	References
Soda-lime glass	Johnson Holmquist 2	Polynomial	Johnson Holmquist 2	[4],[6]
PVB interlayer	Johnson Cook	No	Principal Strain	[10]
Lead core	Johnson Cook	Shock linear	Principal Strain	[9]
Copper alloy jacket				

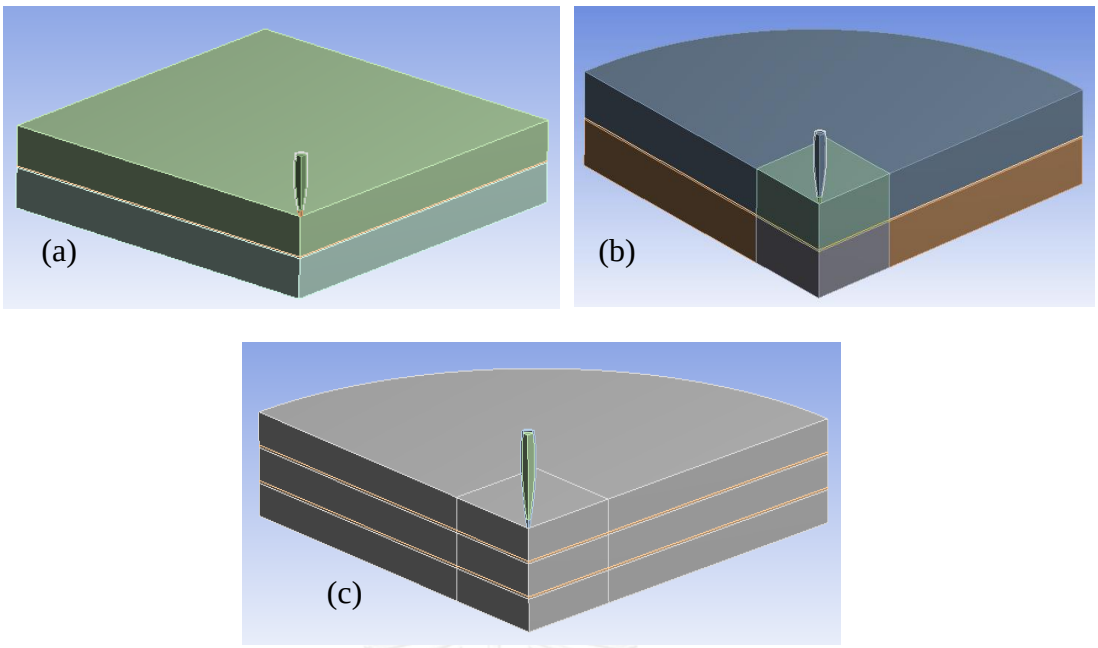

Figure 3.4 The quarter symmetry two and three layer FEA models of (a) T1-S square model, (b) T1-R round model with square cut at the impact corner and (c) T2 model.

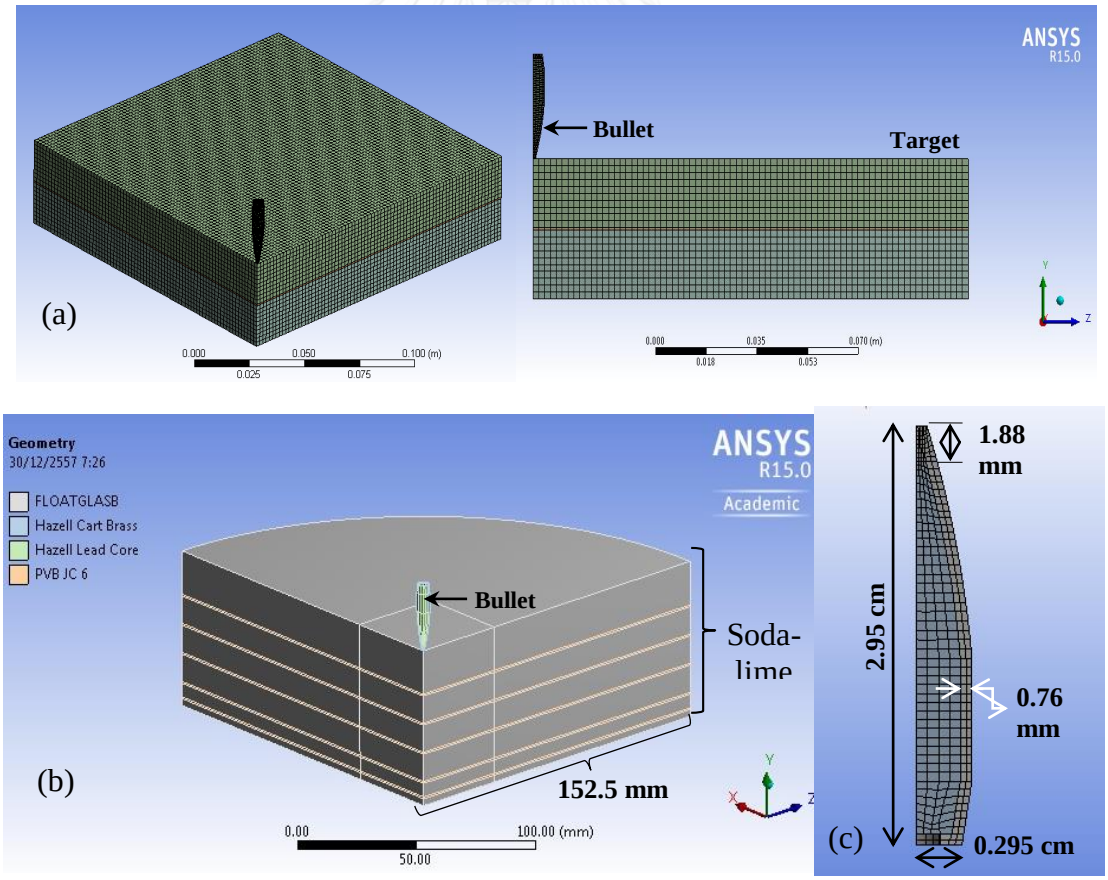

Figure 3.5 Setup of the quarter symmetry models depicting (a) meshed two-layer and (b) six-layer soda-lime glass/PVB armor and (c) a 7.62-mm bullet.

3.1.2 Model Calibration

Due to the lack of some existing material parameters for describing the dynamic deformation and failure conditions, the material model calibration was one of the most important steps in FEA simulation set-up. The complexity of the body interaction between the glass and bullet under high velocity impact conditions was another complicated step for the FEA simulation set-up. Since the individual part interactions also played a significant role in the damage behavior of the laminated target structure, the interaction assignments have to be systematically adjusted to obtain reasonable FEA results. Thus, the two and three-layer models of the soda-lime glass/PVB transparent armors were used for calibrating the larger six-layer models by comparing the damage patterns and crater sizes with experimental ballistic results.

Once the material model parameters and meshing methods were adjusted for the two and three-layer transparent armors, the FEA simulations were performed on the standard configuration of the six-layer soda-lime glass/PVB laminated targets. The initial parameters and meshing details are listed in Table 3.3 and were further adjusted to obtain a reasonable correlation with the experimental results.

In this section, the FEA calibration was focused on, in terms of the meshing method, mesh size, mesh shape, glass/films interface interaction and the material models for soda-lime glass and PVB film. These are the significant factors which can create closer outputs between FEA and experiments. The details of the FEA setup conditions are discussed below.

3.1.2.1 Mesh Size / Element Type / Body Interaction

A Lagrangian framework, which assumes that each element in the mesh is deformable, was used for the ballistic impact FEA simulations. In the Lagrangian method, meshing is an important step which partially determines the accuracy and the total computational time of the FEA simulation.

Good meshing techniques will lead to suitable contact surfaces between adjoining parts, while the element type and size, which affects the total number of nodes, controls the computational time. For example, the smaller the element size, the greater the number of calculation cycles required and the longer the computation time. Therefore, in this study the target and bullet were meshed with hexahedral elements with a size range of 0.4-1.25 mm. The two-layer target for both square and round target geometries, referred to as T1-S and T1-R, respectively (Table 3.1 and Figure 3.4), were used for comparison with the experimental results, while the three, five and six-layer targets only used the round target geometry for the better meshing and to obtain more realistic ballistic damage results (i.e. radial cracks).

As previously mentioned, the glass layers in the experimental targets were bonded together using PVB film. As no evidence of delamination was observed after the ballistic testing, the body interaction between the glass and PVB films in the FEA simulations were assumed to be perfectly bonded and unbreakable and as such the FEA target model was treated as a single part in ANSYS. The contact algorithm between the bullet and the target was set to trajectory contact and the impact was perpendicular with a velocity of 853 m/s, which is the upper limit of bullet velocity required in the NIJ standard Level III. The body interaction between the bullet and the target was either frictional or frictionless, in order to determine which could better duplicate the experimental results. The mesh calibration details are summarized in Table 3.3.

The two and three-layer laminated targets, referred to as T1-S, T1-R and T2, respectively (Table 3.1) were used as the initial calibration models. The conditions obtained after the calibration were used for damage analysis in the five and six-layer models, STD1, STD2, A19 and B19 (Table 3.1).

Table 3.3 Mesh calibration parameters

Conditions	
Target geometry	Square
	Round
Element type	Hexahedral
Target mesh size (mm)	1.25
	1.0
	0.65
	0.5
Bullet mesh size (mm)	0.75
	0.65
	0.4
Body Interaction	Frictional
	Frictionless

จุฬาลงกรณ์มหาวิทยาลัย
Chulalongkorn University

3.1.2.2 Material models

Another important factor in the FEA simulation is the material model which is selected for each material. Some calibrations for the material model parameters were performed to gain insight into the material deformation and failure behavior in the laminated targets.

1. Material Model for Soda-lime Glass

The Johnson-Holmquist (JH2) model, a well-known material model for brittle materials under dynamic loading conditions [3-5], was used for the soda-lime glass sheet. The initial JH2 parameters are listed in Table 3.4. These parameters were obtained from the previously reported literature for similar impact loading, but some of the parameters needed to be calibrated to better describe the soda-lime glass deformation behavior in this study. The hydrodynamic tensile limit value (T-value), the maximum dynamic tensile load capacity of soda-lime glass, is one of the important calibration parameters in the JH2 strength model. This value indicates the strength threshold of a brittle material under dynamic tensile loading. For example, if the tensile loading was higher than the T-value, then crack damage (ex. random radial cracks which were bifurcated throughout the material) would occur in material. Because the T value of soda-lime glass was highly dependent on the fabrication process and varied greatly in the previously reported works, in this study, the T-values were varied as shown in Table 3.5 for material model calibration process.

จุฬาลงกรณ์มหาวิทยาลัย
Chulalongkorn University

Table 3.4 Soda-lime glass properties according to Johnson-Holmquist model [13,25,28]

Johnson-Holmquist model	Units	Value
Density	kgm^{-3}	2530
JH Strength Continuous		
Failure Type		Gradual
Hugoniot Elastic Limit (HEL)	Pa	5.95E+09
Intact Strength Constant A		0.93
Intact Strength Exponent N		0.77
Strain Rate Constant C		0.003
Fracture Strength Constant B		0.35
Fracture Strength Exponent m		0.4
Maximum Fracture Strength Ratio SFMAX		0.5
Damage Constant D1		0.053
Damage Constant D2		0.85
Bulking Constant B		1
Hydrodynamic Tensile Limit T	Pa	**Varied**
Shear Modulus	Pa	3.04E+10
Polynomial EOS		
Parameter A1	Pa	4.54E+10
Parameter A2	Pa	-1.38E+11
Parameter A3	Pa	2.90E+11
Parameter B0		0
Parameter B1		0
Parameter T1	Pa	4.54E+10
Parameter T2	Pa	0

จุฬาลงกรณ์มหาวิทยาลัย
Chulalongkorn University

Table 3.5 Hydrodynamic tensile limit constant

Varied Value	Hydrodynamic Tensile Limit or T-Value (MPa)
JH-30	-30
JH-35	-35
JH-40	-40
JH-60	-60
JH-70	-70
JH-80	-80

2. Material Model for PVB

The modeling of the impact and deformation behavior of PVB films varies widely in the literature. Therefore, in this study, three material models, i.e. Johnson-Cook, Mooney-Rivlin and viscoelastic, were investigated. The model parameters are listed in Tables 3.6-3.9. Some of the experimentally determined parameters were unavailable and needed to be systematically varied in the calibration model to reasonably fit the experimental results.

For dynamic deformation problems, the Johnson-Cook (JC) material model proposes a semi-empirical constitutive model for elastic-plastic materials (e.g. metals, polymers) which describe the mechanical behavior at large strains, high strains rate, and high temperatures [6-8]. For each effect (strain hardening, strain rate hardening and thermal softening), an independent term is used in the mathematical equation, which in turn makes this model relatively easy to calibrate. As a result, the JC model was used to describe the PVB film mechanical behavior in laminated targets. The parameters for PVB with the JC model are listed in Table 3.6 and 3.7.

Table 3.6 Required parameters for the Johnson-Cook model of PVB [30]

Johnson-Cook model	Units	Value
Density	kgm^{-3}	1066
Specific Heat	$Jkg^{-1}C^{-1}$	1973
Johnson Cook Strength		
Strain Rate Correction		First-Order
Initial Yield Stress	Pa	7.58E+07
Hardening Constant	Pa	6.90E+07
Hardening Exponent		1
Strain Rate Constant		**Varied**
Thermal Softening Exponent		**Varied**
Melting Temperature	C	200
Reference Strain Rate (/sec)		1
Shear Modulus	Pa	3.00E+08
Bulk Modulus	Pa	2.00E+9
Shock EOS Linear		
Gruneisen Coefficient		1.55
Parameter C1	ms^{-1}	2486
Parameter S1		1.577
Parameter Quadratic S2	ms^{-1}	0

Table 3.7 Strain rate constant and thermal softening exponent of the Johnson-Cook model for PVB

Varied Value	Strain Rate Constant	Thermal Softening Exponent
PVBJC	0	1.85
PVBJC2	0.052001	1.85
PVBJC3	0.052001	0
PVBJC4	0.0843	0

The second material model used to describe the mechanical behavior of the PVB film in this study was the hyperelastic Mooney-Rivlin model. In this case, the PVB film is considered as an incompressible elastomer, which is rubber-like in short-time dynamics, with a high strain rate dependency that focused on strain rate at 1200 and 2200 s^{-1} as PVBMRS1 and PVBMRS2. The required parameters for the Mooney-Rivlin material model are as shown in Table 3.8.

Table 3.8 Required parameters for the Mooney-Rivlin model for PVB [34]

Mooney-Rivlin model	Units	PVBMRS1	PVBMRS2
Strain rate	s^{-1}	1200	2200
Density	kgm^{-3}	1066	1066
Mooney-Rivlin 3 Parameters			
Incompressibility Parameter	Pa^{-1}	1.0E-08	1.0E-08
Material Constant C10 (A_1)	Pa	-2.57E+08	-2.71E+08
Material Constant C01 (A_2)	Pa	3.18E+08	3.38E+08
Material Constant C11 (A_3)	Pa	6.47E+07	6.55E+07

จุฬาลงกรณ์มหาวิทยาลัย
Chulalongkorn University

Moreover, the mechanical behavior of the PVB film might be considered as linear viscoelastic, which follows the linear superposition principle and where the relaxation rate was proportional to the instantaneous stress. In this case, the instantaneous stress is proportional to the strain. The viscoelasticity can be isotropic or anisotropic. The required parameters for the viscoelastic material model are shown in Table 3.9.

Table 3.9 Required parameters for the viscoelastic material model for PVB [63]

Viscoelastic model	Units	PVBvis
Density	kgm^{-3}	1066
Viscoelastic		
Instantaneous Shear Modulus (High Rate) G0	Pa	3.30E+08
Viscoelastic Decay Constant	s^{-1}	12.6
Bulk Modulus	Pa	2.0E+10
Shear Modulus	Pa	6.9E+05

The criterion for the PVB material model selection depended significantly on the damage propagation between the glass interfaces and the damage in the last glass layer of the STD1 and STD2 models and as well as the damage distribution in the A19 and B19 models. The JC model which could best replicate the damage results was applied in this study.

The erosion of failed bullet and target elements in the simulation was controlled by a geometric strain limit, which was set at 1.5 or 150% deformation. This element erosion is performed to avoid the generation of severally distorted elements which can slow or even halt a simulation. The eroded elements were converted into point masses which retain the mass and inertia of the eroded elements. This point masses were able to continue interacting with the model.

จุฬาลงกรณ์มหาวิทยาลัย
Chulalongkorn University

3. Material Model for Bullet

The 7.62-mm bullet is composed of a copper alloy jacket and a lead-antimony core. The Johnson-Cook material model was used to describe the mechanical behavior for both material components of the bullet. The required mechanical parameters of the Johnson-Cook model for the lead and copper alloys are summarized in Table 3.10.

Table 3.10 Required parameters for the Johnson-Cook model for the 7.62-mm bullet [29]

Johnson-Cook model	Units	Hazell Lead core	Hazell Cart Brass
Density	kgm^{-3}	11340	8930
Specific Heat	$Jkg^{-1}C^{-1}$	124	385
Johnson Cook Strength			
Strain Rate Correction		First-Order	First-Order
Initial Yield Stress	Pa	4.00E+07	5.75E+08
Hardening Constant		0	0
Hardening Exponent		0	0
Strain Rate Constant		0	0
Thermal Softening Exponent		1	1.09
Melting Temperature	C	251.85	1049.9
Reference Strain Rate(/sec)		1	1
Shear Modulus	Pa	7.00E+09	4.40E+10
Shock EOS Linear			
Gruneisen Coefficient		2.74	2.02
Parameter C1	ms^{-1}	2006	3940
Parameter S1		1.429	1.489
Parameter Quadratic S2	ms^{-1}	0	0
Principal Strain Failure			
Maximum Principal Strain		0.2	0.05
Maximum Shear Strain		1.00E+20	1.00E+20

3.2 Ballistic damage comparisons

To validate the FEA results, the depth of penetration and impact crater diameter from the experimental and simulation results were compared. Practically, the new designed configurations (target) were tested with two samples in order to repeat and confirm the approval criterion as in Chapter 2, section 2.2.2. The successful approval model should be passed both samples in the testing. Furthermore, this study focused on analyzing the average volume fraction of damaged glass (i.e. volumetric damage) in each layer from the numerical results, as shown in Figure 3.6. As the glass layers experienced brittle failure, the damage was accumulated and lowered the overall strength of the target.

The JH2 damage model was developed for the simulation of brittle materials subjected to high pressure, larges stresses and strain rates. The JH2 constitutive model requires several material constants to completely describe the elastic stress state of the material, such as the shear modulus and density. Based on the current material deformation, μ (equation 3.1), the corresponding pressures (equations 3.2a and 3.2b) can be calculated. This is the equation of state for the material.

$$\mu = \frac{\rho}{\rho_0} - 1 \quad \text{---------- Eq.3.1}$$

$$P = K_1\mu + K_2\mu^2 + K_3\mu^3 + \Delta P_{n-1} \quad \text{(Compression) ---------- Eq.3.2 a}$$

$$P = K_1\mu \quad \text{(Tension) ---------- Eq.3.2 b}$$

In equation (3.2 a), P corresponds to the bulking pressure of the material and is determined by the amount of accumulated damage.

Under compressive loading, damage begins to accumulate within the material when the deviator stress exceeds a critical value. This damage accumulation is tracked via a damage parameter (ranging from 0 to 1.0), and the corresponding non-recoverable or plastic strain. Thus, the current material strength is determined by the damaged and undamaged strength curves as well as the current material damage. Both the strength and pressure are normalized by the equivalent stress at the Hugoniot elastic limit (HEL) and the pressure at the HEL respectively. When subjected to tensile pressure, the material responds elastically until brittle failure at a specified effective stress value. This corresponds to complete instantaneous damage.

Based on the current strain and time increments, the current effective strain rate and total strains can be calculated. The damage level (D) is calculated as the ratio of incremental plastic strain over the pressure dependent fracture strain. The current strength can then be used with the radial return method to determine the current increment in plastic strain. From this, the current increment in damage can be determined as shown in equation 3.3.

$$\Delta D = \frac{\Delta \varepsilon_p}{\varepsilon_f},\ D = \sum \frac{\Delta \varepsilon_p}{\varepsilon_f} \quad \text{---------- Eq.3.3}$$

Where the plastic strain to fracture under a constant pressure is defined as:

$$\varepsilon_f = D_1 (P^* + T^*)^{D_2} \quad \text{---------- Eq.3.4}$$

The numerical damage of the glass is indicated by D in a range of 0 (undamaged material) to 1 (fully damaged material) as shown in Figure 3.6.

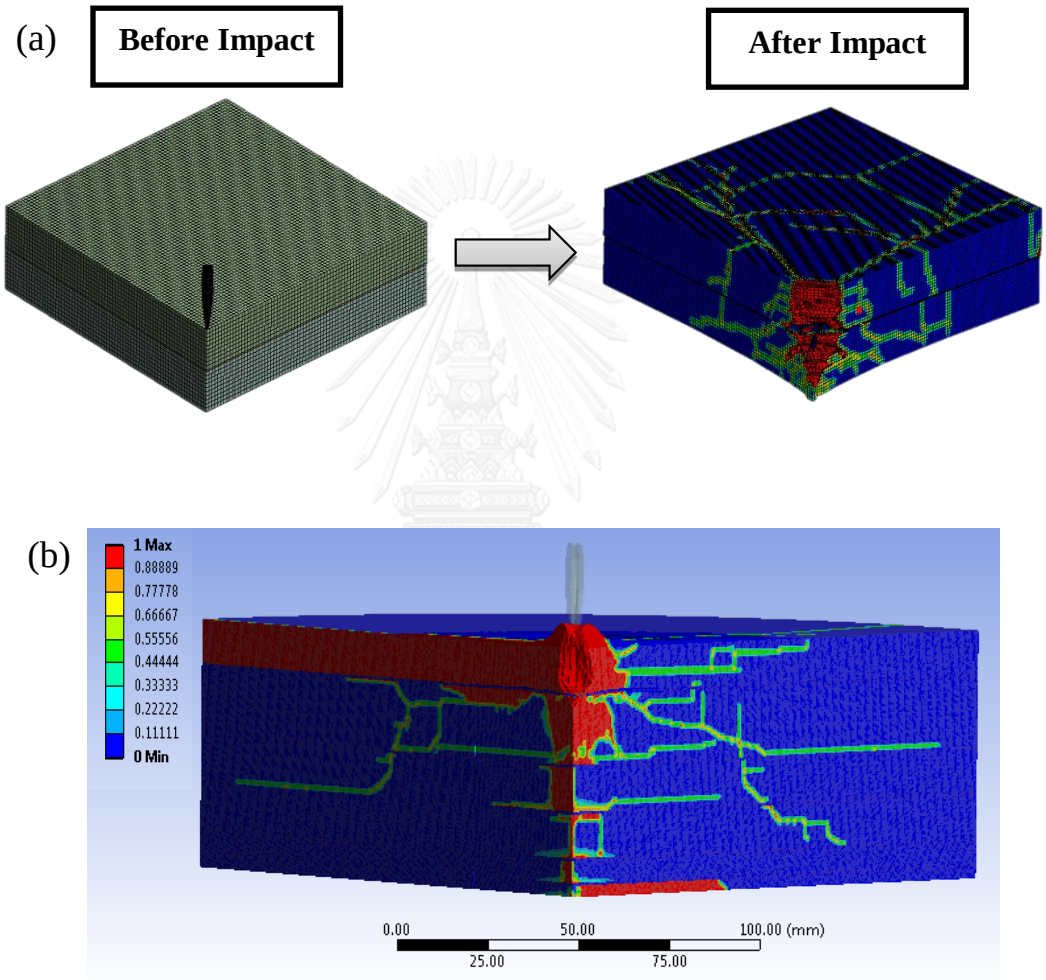

Figure 3.6 Damage of soda-lime glass/PVB film laminated transparent armor (a) numerical model before and after bullet impact and (b) after bullet impact at 300 microseconds (The legend indicates the damage level of the soda-lime glass).

3.2.1 DOP and crater diameter

Examples of the bullet penetration depth and the crater diameter of the models are shown in Figure 3.7. The simulation results were compared to the experimental results. The bullet penetration depth was measured using digital Vernier calipers and averaged from five locations, while the crater diameter (which excluded the dense bifurcated radial crack area) was averaged from ten locations. The FEA and experimental results should ideally show a reasonable agreement for all of the armor models. These comparisons thus validated that the numerical setup and the material models used in the FEA study.

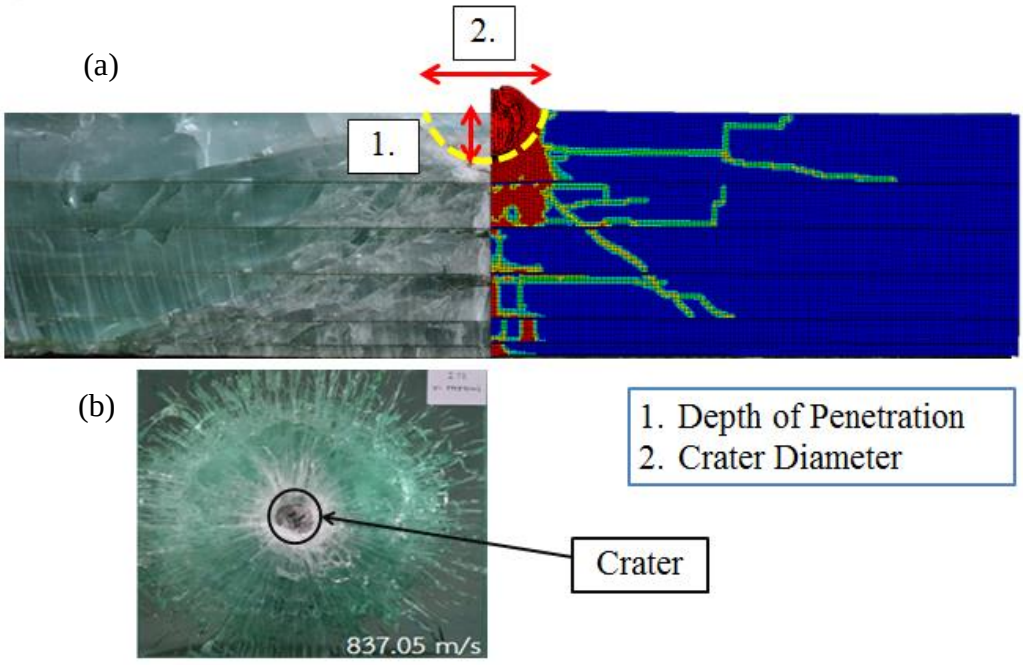

Figure 3.7 Ballistic damage for a soda-lime glass/PVB film laminated target (a) comparison between FEA and experimental result and (b) the crater from an experimental sample.

3.2.2 Volumetric damage

The volumetric damage (VD) was used to assess the damage level at the simulation end time in each glass layer, and was calculated using Eq. 3.5.

$$\%\ \mathrm{VD} = \frac{\text{Damage level} * \text{Elemental volume}}{\text{Total elemental volume in each layer}} \times 100 \quad \text{-------Eq.3.5}$$

where 'Damage level' was extracted from the D (damage level) value in the JH2 model for each element at the end time, and 'Elemental volume' was calculated from the total mass of each element divided by the element density at the start time. Ideally, the volumetric damage (VD) in the last layer (G6 in six-layer and G5 in five-layer target) of the non-reference models should be less than or equal to the equivalent volume damage of the reference models, STD1 and STD2, and therefore will be used as the crucial criterion to optimize the configuration design of the laminated targets in this study.

Furthermore, if we assumed that the glass with the damage level in a range of 0.75-1.00 was the severe damage glass (due to approximately 75% decrease in its strength), the VD for the damage level in a range of 0.75-1.00 (VDMax) were also calculated for the consideration. In most cases, the VDMax in turn suggesting that overall damage occurred in the severe range.

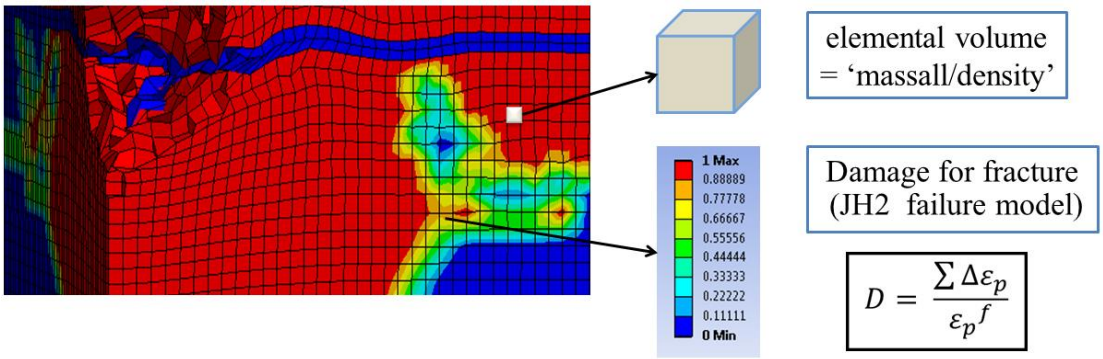

Figure 3.8 Volumetric damage calculation procedures of soda-lime glass/PVB film laminated target.

3.2.3 Energy comparisons

The amount of internal energy in each glass and PVB layer was collected every $1x10^{-3}$ seconds until the simulation end time was reached. The internal energy and internal energy density, with respect to time in each layer, for all models were compared. The results were then correlated with the observed simulation damage and the experimental results from Ref.[3,4,64]. The normalized internal energy of each glass and PVB layer was subsequently calculated by dividing the internal energy by the total volume of each layer. Additionally, the kinetic energy of each glass layer was collected for comparison because some residual kinetic energy from the eroded elements of the bullet, which are converted to small particles (point masses) are able to transfer the kinetic movement to the glass layer. Internal energy, kinetic energy and normalized internal energy of each layer are referred to as IE, KE and NormIE, respectively. For example, the internal energy of the first to last glass layer was named as IE_G1, IE_G2, IE_G3, IE_G4, IE_5 and IE_G6, respectively. While the internal energy of PVB interlayer from the first to the last was represented as IE_P1, IE_P2, IE_P3, IE_P4 and IE_P5, respectively. The energy of all the designed models was compared to the reference STD1 and STD2 models in order to study the ballistic damage mechanism in the laminated systems.

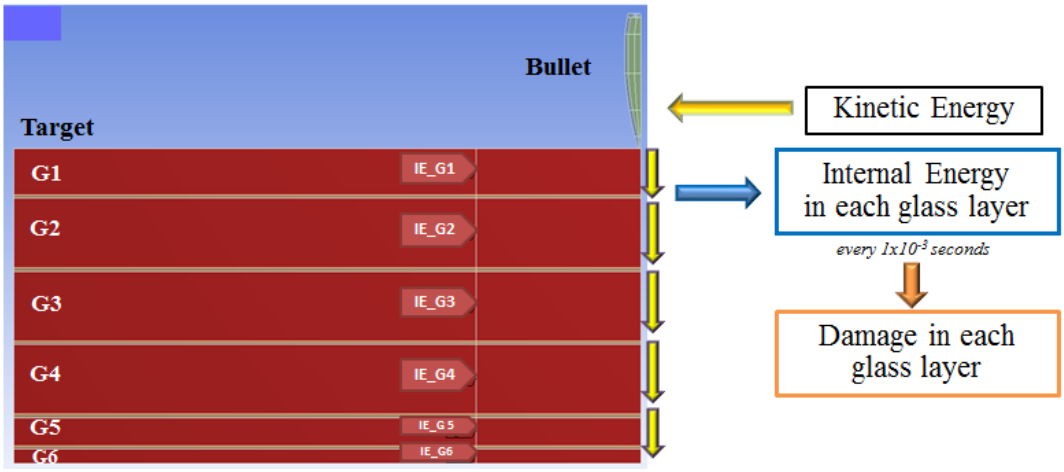

Figure 3.9 Diagram of internal and kinetic energy collection within the soda-lime glass/PVB film laminated targets.

3.3 Study on the effect of configuration design in soda-lime glass/PVB laminated transparent armor

3.3.1 Effect of striking-layer glass thickness

The striking-layer glass plays an important role in the process of eroding and defeating the bullet. Therefore, this first group of armor models aimed to study the effect of the striking-layer glass thickness on the ballistic protection performance of the laminated armors. The striking-layer glass thicknesses considered in this study were 19, 15, 12, 10, 8, 6 and 3 mm, for which the models were referred to as A19, A15, A12, A10, A8, A6 and A3, respectively. The model configurations are summarized in Table 3.11. These configurations were adapted from the A19 model in the previous study in order to compare the resulting ballistic performance to the reference models, STD1 and STD2, of which the glass thickness configurations are proprietary to the manufacturer. However, some configurations were already tested by the NIJ standard level III according to previous research [3,4,64].

Table 3.11 Laminate configurations for the study of striking-glass layer thickness

Model name / **Order assembly**	**Thickness (mm)**						
	A19	***A15***	***A12***	***A10***	***A8***	***A6***	***A3***
G1	**19**	**15**	**12**	**10**	**8**	**6**	**3**
P1	0.76	0.76	0.76	0.76	0.76	0.76	0.76
G2	12	12	12	12	12	12	12
P2	0.76	0.76	0.76	0.76	0.76	0.76	0.76
G3	12	12	12	12	12	12	12
P3	0.76	0.76	0.76	0.76	0.76	0.76	0.76
G4	12	12	12	12	12	12	12
P4	0.76	0.76	0.76	0.76	0.76	0.76	0.76
G5	6	6	6	6	6	6	6
P5	0.76	0.76	0.76	0.76	0.76	0.76	0.76
G6	3	3	3	3	3	3	3
Total thickness (mm)	67.8	63.8	60.8	58.8	56.8	54.8	51.8
%Reduced Thickness	*1.11*	*6.94*	*11.32*	*14.24*	*17.15*	*20.07*	*24.45*

3.3.2 Effect of PVB Thickness and Ordering

The second group of model configurations was designed in a previous study in Ref. [3] in order to determine the effect of PVB thickness and PVB thick-film ordering on the ballistic performance. The thicknesses of the PVB film in this section are referred to as 'normal PVB' with a thickness of 0.76 mm and 'thick PVB' with a thickness of 1.52 mm. In this design group, the glass thicknesses were fixed to the F15 model at 15, 12, 12, 12, 6 and 3mm, respectively. The sequence of the thick PVB layer substituted for the normal PVB film is summarized in Table 3.12.

Table 3.12 Laminate configurations for the study of PVB thickness and ordering (underline means thick PVB film insertion)

Model name / Order assembly	Thickness (mm)					
	A15-1TP	***A15-2TP***	***A15-3TP***	***A15-4TP***	***A15-5TP***	***A15-AllTP***
G1	15	15	15	15	15	15
P1	**1.52**	0.76	0.76	0.76	0.76	**1.52**
G2	12	12	12	12	12	12
P2	0.76	**1.52**	0.76	0.76	0.76	**1.52**
G3	12	12	12	12	12	12
P3	0.76	0.76	**1.52**	0.76	0.76	**1.52**
G4	12	12	12	12	12	12
P4	0.76	0.76	0.76	**1.52**	0.76	**1.52**
G5	6	6	6	6	6	6
P5	0.76	0.76	0.76	0.76	**1.52**	**1.52**
G6	3	3	3	3	3	3
Total thickness (mm)	64.56	64.56	64.56	64.56	64.56	67.6
%Reduced Thickness	*5.83*	*5.83*	*5.83*	*5.83*	*5.83*	*1.40*

3.4 Configuration Optimization

The objective of this study aims to design a lighter-weight soda-lime glass/PVB laminated armor with NIJ standard level III ballistic protection.The overall armor thickness (i.e. more or thicker glass layers) is a significant factor toward the overall weight of the armor. Since the ballistic performance of the target might be affected by too severe by decrease in thickness, in this section, the optimal thickness of laminated transparent armor, capable NIJ level III protection, was investigated. Targets with some percentage of thickness reduction were compared with the reference STD2 model, while the percentage of volumetric damage in the last glass layer were compared to

volumetric damage in both the STD1 and STD2 reference models. These criteria were significant results used to predict the ballistic performance for further design configurations. The results from Section 3.3 were used as a guideline for the optimization of the laminate configuration in this section.

3.4.1 Configuration optimization at the reduced thickness of 61.8 mm

Two different 6-layer armor configurations were designed to have a total thickness of 61.8 mm, by varying the glass layer thicknesses. The configurations in this section were systematically adapted from the F19 model, and only the G2, G3 and G4 layers were adjusted accordingly. The effects of the different glass configurations on the damage and energy distribution were investigated. Details of the configurations studied in this section are shown in Table 3.13.

Table 3.13 Laminate configurations for reducing the total thickness to 61.8 mm

Model name / Order assembly	Thickness (mm)	
	RT1-1	***RT1-2***
G1	19	19
P1	0.76	0.76
G2	12	10
P2	0.76	0.76
G3	10	10
P3	0.76	0.76
G4	8	10
P4	0.76	0.76
G5	6	6
P5	0.76	0.76
G6	3	3
Total thickness (mm)	61.8	61.8
%Reduced Thickness	*9.86*	*9.86*

3.4.2 Configuration optimization at the reduced thickness of 59.8 mm

The next goal was to set the total target thickness at 59.8 mm, to again decrease the overall weight of the target. The model configurations in this section were also designed to verify the effect of the thickest-glass layer location on the ballistic performance by varying the location between G1 and G2. The G4-layer thickness were also varied from 6-8 mm, while the thickness of the G3, G5 and G6 layers were kept constant at 10, 6 and 3 mm, respectively. Details of the configurations studied in this section are summarized in Table 3.14.

Table 3.14 Laminate configurations for reducing the total thickness to 59.8 mm

Model name / **Order assembly**	**Thickness (mm)**			
	RT2-1	***RT2-2***	***RT2-3***	***RT2-4***
G1	**19**	**12**	**19**	**10**
P1	0.76	0.76	0.76	0.76
G2	**12**	**19**	**10**	**19**
P2	0.76	0.76	0.76	0.76
G3	10	10	10	10
P3	0.76	0.76	0.76	0.76
G4	6	6	8	8
P4	0.76	0.76	0.76	0.76
G5	6	6	6	6
P5	0.76	0.76	0.76	0.76
G6	3	3	3	3
Total thickness (mm)	59.8	59.8	59.8	59.8
%Reduced Thickness	*12.78*	*12.78*	*12.78*	*12.78*

3.4.3 Configuration optimization at the reduced thickness of 58.8 mm

In this section, the total target thickness was reduced to 58.8 mm with the configurations shown in Table 3.15. The thickest glass layer of 19 mm was moved from the G1 to the G4 layer. These configurations were then used to investigate the glass ordering effect on the ballistic performance. Additionally, the configurations were designed to determine whether or not the thick glass layer should be arranged between thinner glass layers.

Table 3.15 Laminate configuration for reducing the total thickness to 58.8 mm

Model name / **Order assembly**	**Thickness (mm)**			
	RT3-1	***RT3-2***	***RT3-3***	***RT3-4***
G1	**19**	**15**	**15**	**15**
P1	0.76	0.76	0.76	0.76
G2	**15**	**19**	6	6
P2	0.76	0.76	0.76	0.76
G3	6	6	**19**	6
P3	0.76	0.76	0.76	0.76
G4	6	6	6	**19**
P4	0.76	0.76	0.76	0.76
G5	6	6	6	6
P5	0.76	0.76	0.76	0.76
G6	3	3	3	3
Total thickness (mm)	58.8	58.8	58.8	58.8
%Reduced Thickness	*14.24*	*14.24*	*14.24*	*14.24*

3.4.4 Additional design studies of RT3-2 Thick PVB insertion

As mentioned in Section 3.3.2, the use of a thick PVB film tended to increase the ballistic performance in the A15-1TP, A15-2TP, A15-3TP and A15-AllTP models. Therefore, in this section, the thick 1.52 mm PVB film was substituted for the regular 0.76 mm PVB film in some PVB layers of the RT3-2 models as shown in Table 3.16. The effect of the thick PVB film on the ballistic performance was subsequently studied and analyzed.

Table 3.16 Laminate configurations for RT3-2 thick PVB film insertion study (underline means thick PVB film insertion)

Model name / **Order assembly**	**Thickness (mm)**				
	RT3-2	***RT3-2-1TP***	***RT3-2-2TP***	***RT3-2-3TP***	***RT3-2-AllTP***
G1	15	15	15	15	15
P1	0.76	**1.52**	0.76	0.76	**1.52**
G2	19	19	19	19	19
P2	0.76	0.76	**1.52**	0.76	**1.52**
G3	6	6	6	6	6
P3	0.76	0.76	0.76	**1.52**	**1.52**
G4	6	6	6	6	6
P4	0.76	0.76	0.76	0.76	**1.52**
G5	6	6	6	6	6
P5	0.76	0.76	0.76	0.76	**1.52**
G6	3	3	3	3	3
Total thickness (mm)	58.8	59.56	59.56	59.56	62.6
%Reduced Thickness	*14.24*	*13.13*	*13.13*	*13.13*	*8.69*

3.5 Research procedures

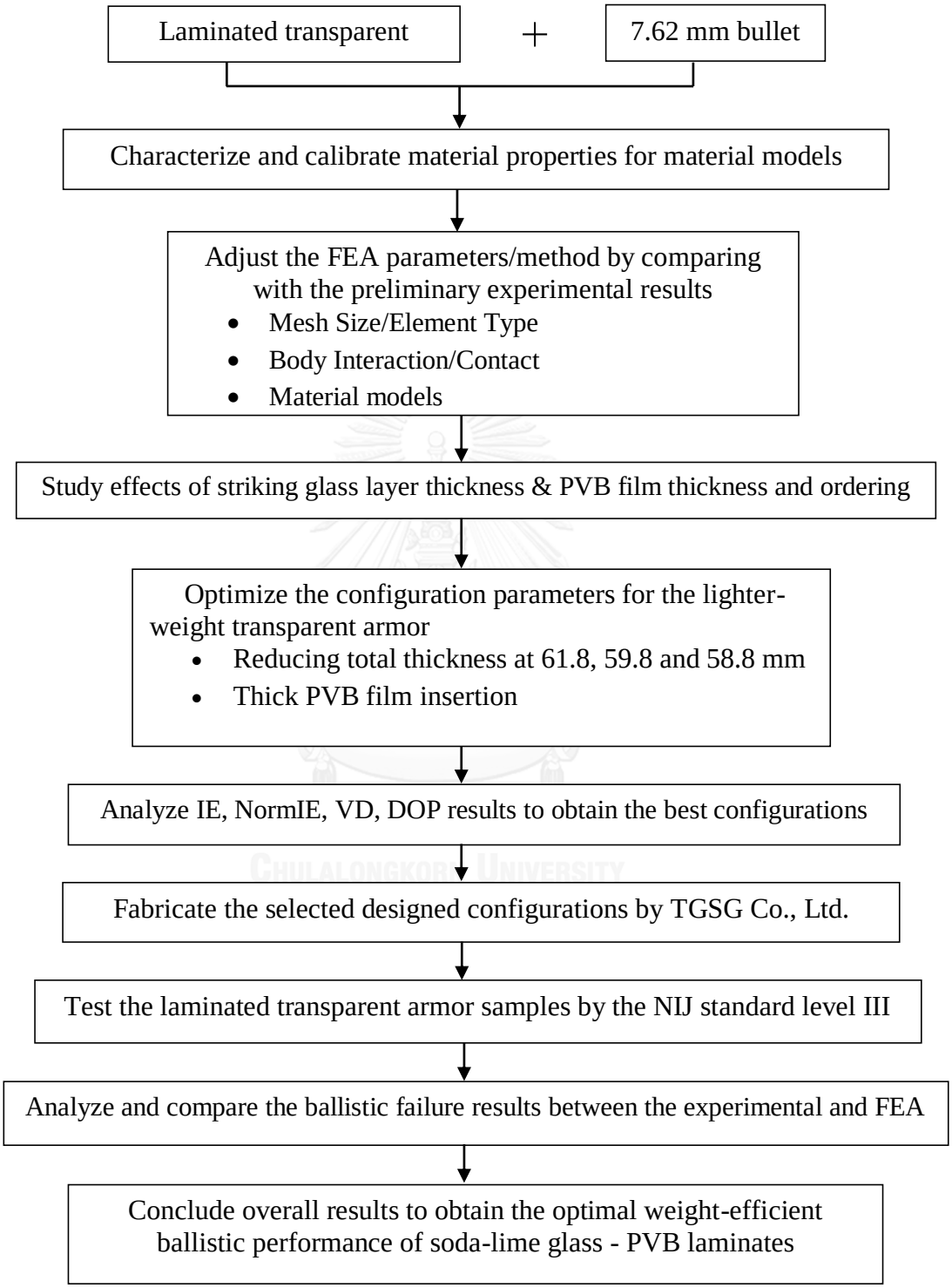

CHAPTER 4
RESULTS AND DISCUSSION

4.1 Model Calibration Results

The model calibration was the most crucial part in the numerical setup. In this study, the model calibration was divided into two main parts, (i) meshing and (ii) material model effects.

4.1.1 Mesh size / Element Type /Body Interaction results

As mentioned in Chapter 2, the hexahedral element shape is preferred in 3D explicit simulations; therefore, the meshing was performed by specifying the edge sizing and using the sweep method to obtain the uniform mesh size and reasonable simulation time. The two-layer configurations (19-19 mm) were initially used to calibrate the meshing in the numerical as shown in Figure 4.1.

Figure 4.1 presents the hexahedral mesh for each component (i.e. bullet part which had complex details on the tip and target which had just a square geometry). The target was easily fit with a hexahedral mesh due to its simple geometry. Since the thickness of the PVB interlayer was only 0.76 mm, to obtain more accurate FEA result, each PVB layer contained at least two layers of elements. Furthermore, in the initial calculation, the material model from the explicit material model database in 'Engineering Data' in ANSYS Explicit STR® Library was assigned for each component as discussed in Chapter 3 (Table 3.2).

The experimental results from the ballistic samples in Figure 4.2 showed the ballistic damage with an impact crater and radial crack patterns. In Figure 4.2 (a), the T1 target displayed the Hertzian crack pattern in the striking layer, and cracks propagated throughout the whole body. The rear plate was severely damage with a hole along the impact area and direction. Additionally, some kinetic energy was converted into heat causing the PVB film to be partially melted and solidified on the back plate. The T2 sample showed more overall damage on the target than T1 due to the lower thickness. Finer bifurcated cracks were created in the striking layer and there was a complete penetration hole through the rear plate of the target. All PVB interlayers were completely melted around the bullet impact zone. The rear plate also showed the hole and mirror image pattern due to the backward direction of the impact wave. The experimental results from T1 and T2 samples were subsequently used as a comparison with our FEA models for the meshing calibration.

As mentioned in Chapter 2-3, the simulation time depends on the elemental size, the number of elements and the mesh size. In case of mesh sizing, the bullet and target discretion methods used in T1-S and T1-R sample were listed in Table 4.1. The average skewness and element quality of each meshing method were used as a criterion for the quality of element meshing before simulation solving as summarized in Table 4.1. Moreover, the numerical calculation results of each condition was summarized in Table 4.2 whether which condition could be the most suitable meshing to further calibration with six-layer targets.

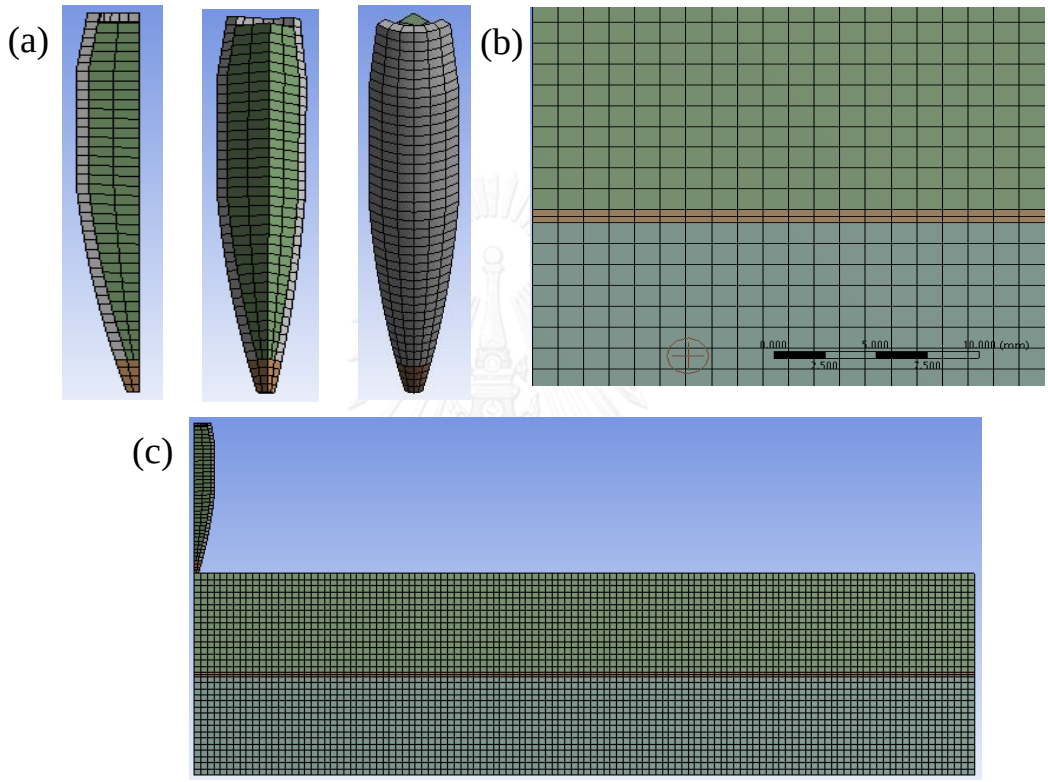

Figure 4.1 The hexahedral meshing of bullet and target in Explicit FEA: (a) Bullet meshing for tip, core and jacket with hexahedral mesh shape, (b) Target with the uniform-size hexahedral meshing on the glass layers and two-layer hexahedral meshing on each PVB interlayer, and (c) the overall meshing of the target and bullet with the hexahedral mesh shape.

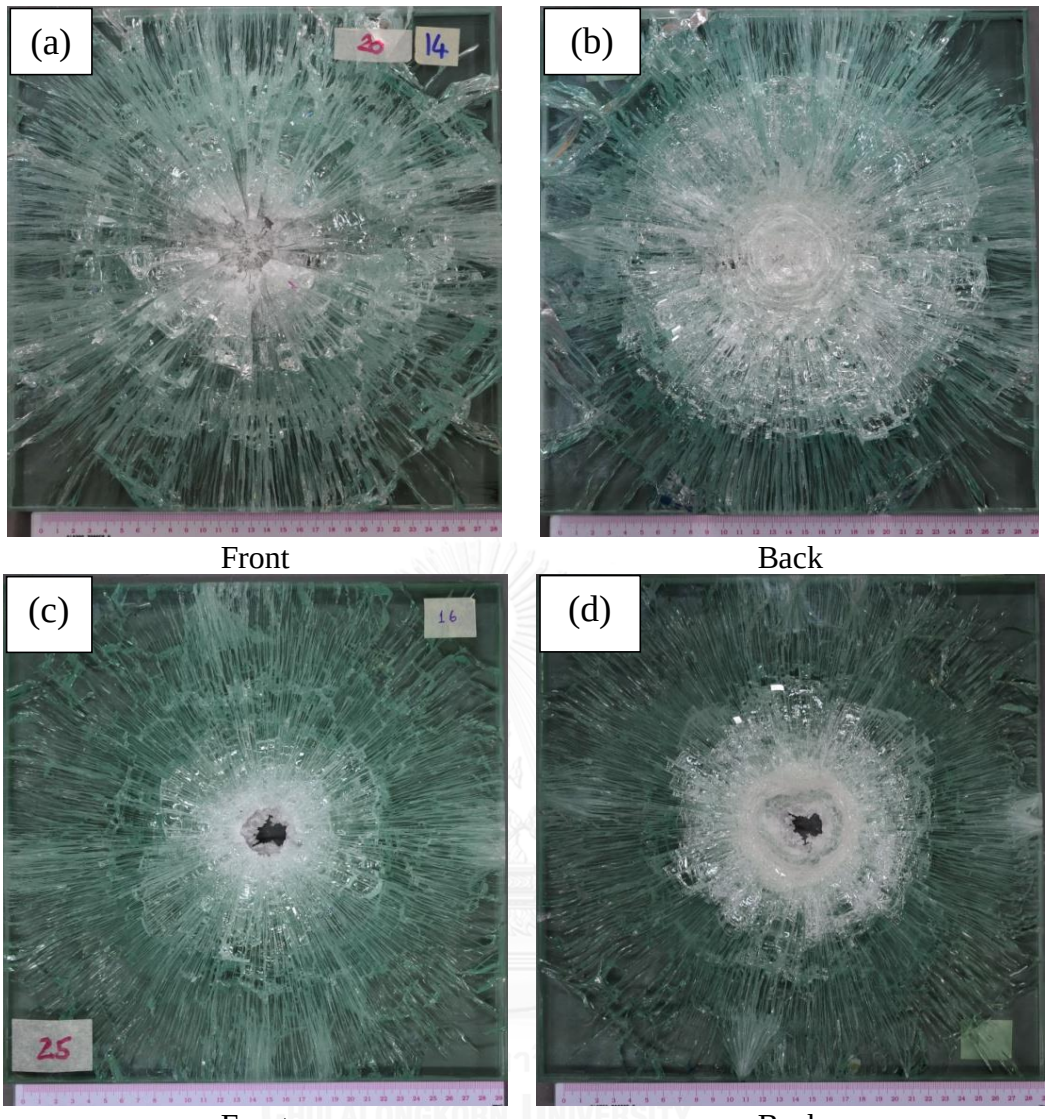

Figure 4.2 Striking and backing plates images of (a-b) T1-19-19 and (c-d) T2-10-10-10 targets after the ballistic testing at impact velocities of 844.01 m/s and 839.14 m/s, respectively.

Table 4.1 Summary of the meshing conditions and body interactions of T1 and T2 samples and the meshing criterion determination

Model name	Target Shape	Mesh size (mm)		Body Interaction (bullet/ target)
		bullet	target	
T1-S (A)	Square	0.4	1.25	N/A
T1-S (B)	Square	0.75	1.25	N/A
T1-S (C)	Square	0.75	1.0	N/A
T1-R (A)	Round	0.75	1.25	N/A
T1-R (B)	Round	0.75	1.0	N/A
T1-R (C)	Round	0.75	0.5	N/A
T1-R (D)	Round	0.75	0.65	N/A
T2 (A)	Round	0.75	0.65	Frictionless
T2 (B)	Round	0.75	0.65	Frictional

Model name	Number of Elements	Number of Nodes	Average Skewness	Average Element Quality
T1-S (A)	491,928	516,313	6.75×10^{-4}	0.97
T1-S (B)	490,062	513,432	2.09×10^{-4}	0.97
T1-S (C)	576,462	601,278	1.77×10^{-4}	0.95
T1-R (A)	355,708	372,456	6.42×10^{-2}	0.76
T1-R (B)	427,868	447,300	6.64×10^{-2}	0.71
T1-R (C)	3,287,868	3,360,958	6.31×10^{-2}	0.74
T1-R (D)	1,571,154	1,615,694	6.40×10^{-2}	0.73
T2 (A)	1,346,858	1,388,759	6.40×10^{-2}	0.70
T2 (B)	1,346,858	1,388,759	6.40×10^{-2}	0.70

Chulalongkorn University

Table 4.2 The summary of FEA running process of T1-S, T1-R and T2 models

Cases	End time (ms)	Progression	Time Increment	Problem
T1-S (A)	0.20	100%	8.92×10^{-9} s	N/A
T1-S (B)	0.50	100%	1.19×10^{-8} s	N/A
T1-S (C)	0.50	100%	3.32×10^{-8} s	N/A
T1-R (A)	0.15	63.9%	2.00×10^{-8} s	Too large energy error
T1-R (B)	0.15	100%	1.81×10^{-8} s	N/A
T1-R (C)	0.15	42.5%	Varied (1.52×10^{-8} -3.02×10^{-10} s)	Too small time step
T1-R (D)	0.15	100%	2.96×10^{-8} s	N/A
T2 (A)	0.15	35.5%	2.17×10^{-8} s	Too large energy error
T2 (B)	0.60	100%	7.27×10^{-9} s	N/A

จุฬาลงกรณ์มหาวิทยาลัย
Chulalongkorn University

The damage/ crack pattern obtained from FEA were represented by the color scale of damage level from 0 to 1.0 (JH2-failure model). The damage level of glass from 0.1 to 1.0 was shown from light blue to red color in the simulated target. The undamaged glass was shown in dark blue color zone as depicted in Figure 4.3 below. The damage or crack pattern in experimental and simulated results was compared by the damage color zone estimation.

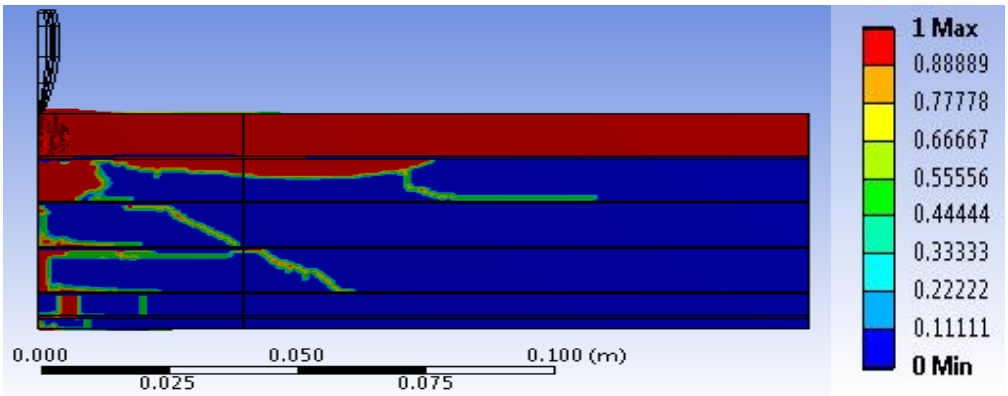

Figure 4.3 The color scale to indicate the cross-sectional damage level of the target after the bullet impact.

For T1-S (A) case, the average element sizes of bullet and target were set 0.40 and 1.25 mm, respectively. The total number of elements in T1-S (A) was 491,928 elements (Table 4.1). The overall skewness was 6.75×10^{-4} indicating the excellent mesh (in range of 0-0.25). The element quality value was 0.97, which also indicated as the excellent mesh (in a range of 0.95-1.00). The end time in ballistic impact phenomena was initially set at 0.2 ms. Moreover, after analyzing the simulation results on the ballistic damage of T1-S (A) model (Table 4.2), the end time and the number of elements were subsequently adjusted to better match the crack propagation observed in the experimental results.

For T1-S (B) model, the element size of bullet was adjusted to 0.75 mm, and the end time was prolonged to 0.5 ms. The average skewness and element quality were still in the range of excellent mesh. The clock time spent about 46 hours to finish calculation compared to 24 hours in T1-S (A) model due to the longer end time setting. According to the FEA results of T1-S (B) in Table 4.3, the damage in striking plate (G1) showed more crack propagation through the back side of the target (G2). This result suggested that the end time was long enough to simulate the crack propagation towards the outermost of the rear plate. However, the difference in the element size between the bullet and target in T1-S (B) model could cause the inconsistent damage propagation along the element region. Thus, the finer element size of target at 1.0 mm at the same end time of 0.5 ms was then applied to T1-S (C) model.

Table 4.3 Comparison of the ballistic damage propagation in the first and second glass layers of T1-S (A-C) model using different bullet/target element size.

Bullet /Target Element size	Damage in each glass layer	
T1-S (A) 0.4/1.25 mm	G1	G2
	Front / Back	Front / Back
	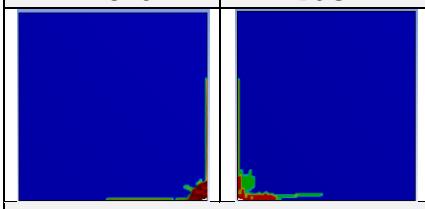	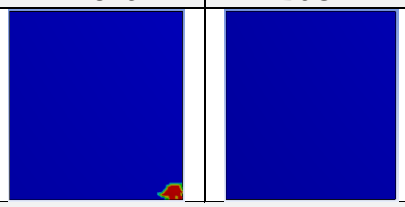
	Left	Right
	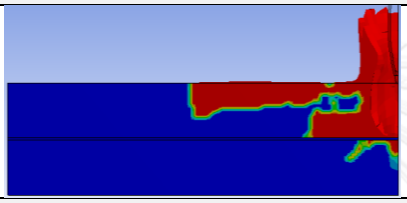	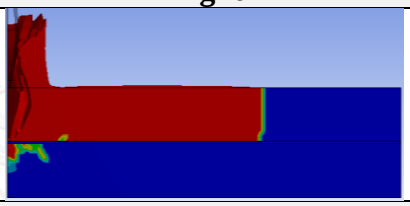
T1-S (B) 0.75/1.25 mm	G1	G2
	Front / Back	Front / Back
	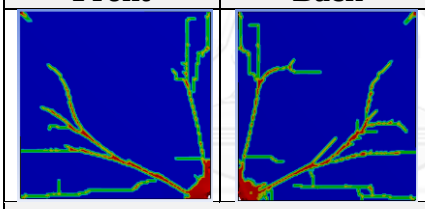	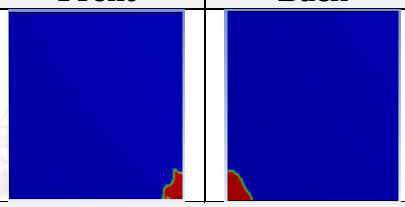
	Left	Right
	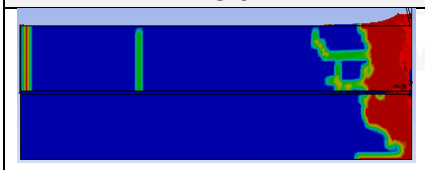	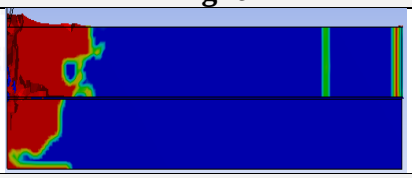
T1-S (C) 0.75/1.0 mm	G1	G2
	Front / Back	Front / Back
	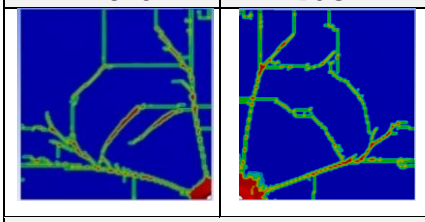	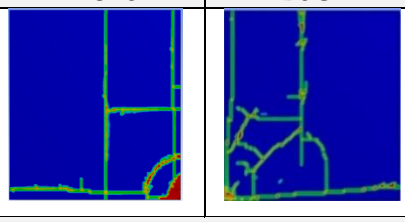
	Left	Right
	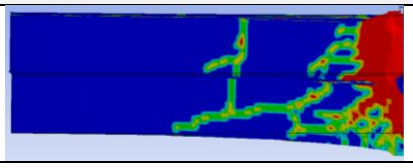	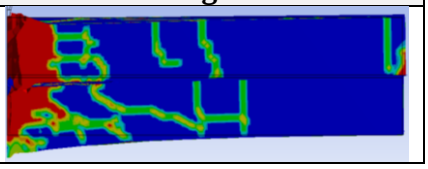

For T1-S (C) model, the average skewness and element quality were still in the range of excellent mesh. However, due to the larger time step, the calculation time for T1-S (C) was then reduced to 24 hours. The damage propagation on striking layer showed some radial crack propagation in both front and back sides. Damage crack was primarily propagated along the element orientation toward the edge of the targets, and some fragments of glass layer were bulged outwards on the back side of the target. The FEA damage pattern between layers was also quite similar to the Hertzian damage pattern observed experimentally.

According to T1-S (A-C) results, the utilization of square targets did not well represent the radial cracks propagation in glass target of ballistic simulation (Figure 4.4). Since the damage calculation was mesh dependent in Lagrange system, the cracks could only propagate along the element alignments and might not effectively transfer to the adjacent element due to element shape restriction.

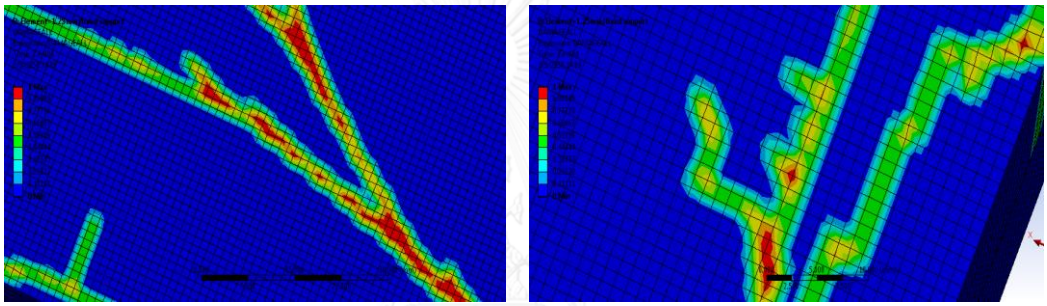

Figure.4.4 The crack propagation along the element alignment with the bifurcated crack on the striking plate.

Owing to lacking of radial crack propagation along the square target, the round targets (T1-R (A-D) models) were employed in FEA instead. To investigate the effect of element size on the damage pattern, the round targets at different element sizes as listed in Table 4.1. The end time was initially set at 0.15 ms in order to reduce the total computational time.

For T1-R (A) model, the bullet and target element sizes of 0.75 mm and 1.25 mm, respectively, was employed. The skewness was increased to 6.42e-2, and the element quality was 0.76, still indicating good element quality (in level of 0.70-0.95). However, the calculation process was not completed due to too larger energy error arising from the eroded elements transformed into mass points with too high kinetic energy. Therefore, the target element size was adjusted to 1.0 mm, referred to as T1-R (B) model (Table 4.1), of which the skewness was in the excellent range, while the element quality was in a good level (Table 4.1). The damage on the striking layer (G1) was shown as radial cracks (Table 4.4) without any bifurcated cracks, suggesting that some more adjustment may be required to better match the FEA results with the experimental results.

For T1-R (C) model, the finer mesh size of 0.5 mm was then employed to obtain better and smoother damage propagation in the glass layers. The skewness and element quality were still same range as shown previous cases (Table 4.1). However, the calculation could not be completed due to the problem of 'too small time step", arising from too small deformed elements close to the center of the round target. Thus, in the T1-R (D) model, the coarser mesh size of 0.65 mm in the target was set to be closer to the bullet element size. The average element quality and skewness of elements met the satisfied criterion. The FEA results shown in Table 4.4 demonstrated the relatively good agreement of the FEA damage propagation on targets with the experimental results (Figure 4.2a). We could obviously observe the radial or bifurcated cracks in both front and back sides of the striking and rear plates, together with the similar Hertzian crack pattern between glass layers.

In summary, the round target with the bullet and T1-target element sizes of 0.65 mm and 0.75 mm, respectively, provided the most stable calculation and good agreement with the experimental data. In addition, because the brittle materials under the high dynamic impact loading could form abundant fragments with high deformation, elements in different parts of model could interact, distort and contact one another. Thus, the effect of body interaction between different parts in the model on the damage propagation was investigated in the next step.

จุฬาลงกรณ์มหาวิทยาลัย
Chulalongkorn University

Table 4.4 The ballistic damage propagation in T1-R models obtained from FEA

Bullet/ Target Element size	Damage in glass layer	
T1-R (A) 0.75/ 1.25 mm	G1	G2
	Front / Back	Front / Back
	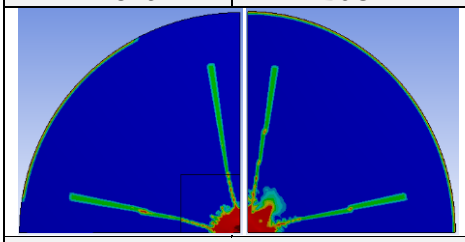	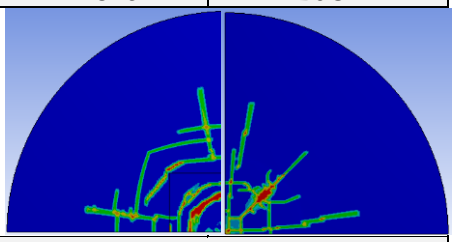
	Left	Right
	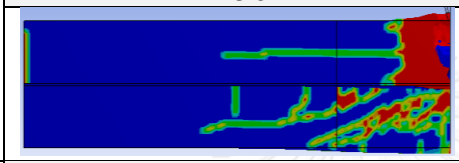	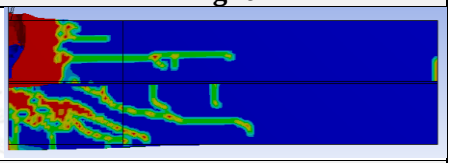
T1-R (B) 0.75/ 1.0 mm	G1	G2
	Front / Back	Front / Back
	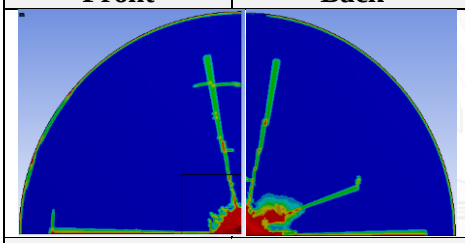	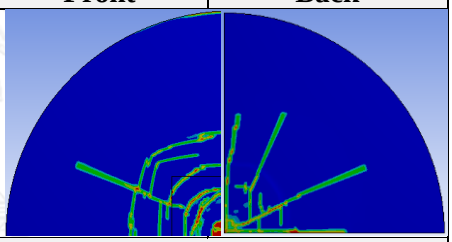
	Left	Right
	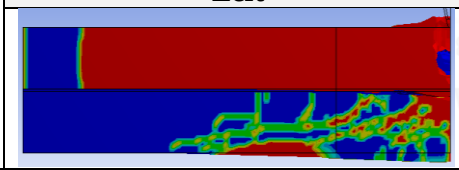	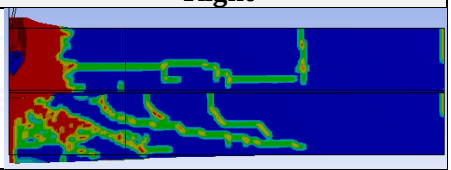
T1-R (C) 0.75/ 0.5 mm	G1	G2
	Front / Back	Front / Back
	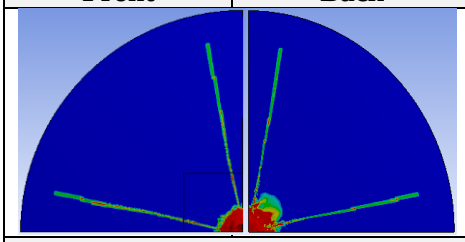	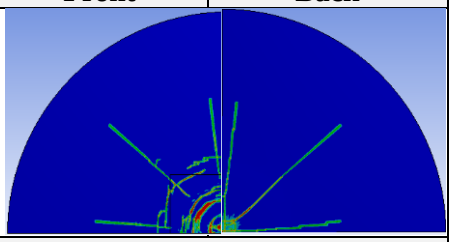
	Left	Right
	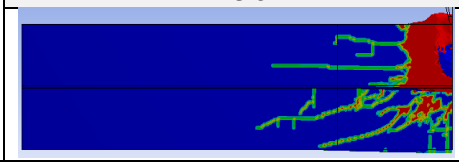	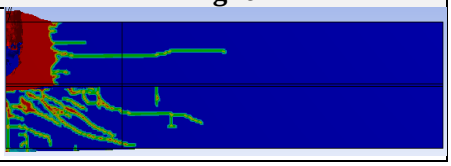

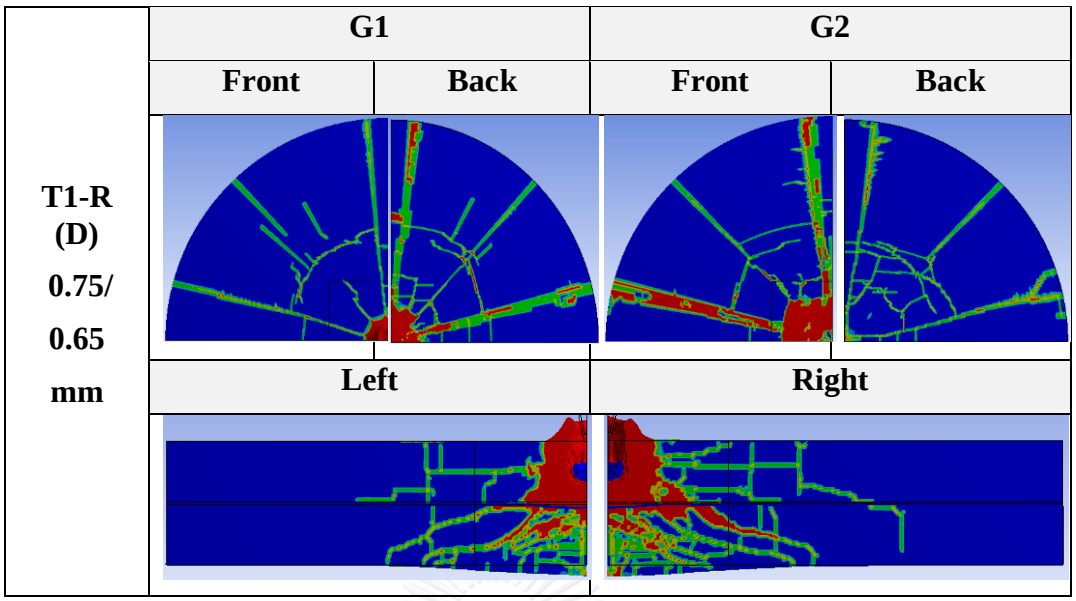

In T1-S and T1-R model, the body interaction between soda-lime glass and PVB film was set as bonded interaction, while the bullet and target interaction were set as frictionless which all components are freely cashed without inertia effect. Therefore, in this T2 models, the local region between target and bullet interaction were set as frictionless (T2 (A)) and frictional (T2 (B)) with a static frictional coefficient of 0.5, a dynamic coefficient of 0.3 and a decay constant of 0.01. In all T2 models, the meshing conditions similar to T1-R (D) were applied.

The damage analysis of T2 models from FEA were shown in Table 4.5. Similar to T1-R (A) model, the calculation of T2 (A) model could not be completed through the end time due to too large energy error, likely caused by the frictionless interaction between the eroded elements without the inertia effect. Too high kinetic energy was observed in some eroded elements. On the contrary, T2 (B) model could complete the calculation up to the end time of 0.6 ms. With the frictional interaction, the eroded/distorted elements scratched or hit the others with the inertia effect. Hence, the damage analysis of T2 (B) showed the higher level of damage propagation through the target, which was in the better agreement with the experimental results in Figure 4.2(c-d). Therefore, the best meshing and body interaction conditions for T1 and T2 model were (i) the round target with the hexahedral mesh size of 0.65 mm, (ii) the bullet with the hexahedral mesh size of 0.75 mm, (iii) the frictional body interaction between target and bullet and (iv) the bonded body interaction between soda-lime glass and PVB films, while keeping the body interaction of the rest as frictional. After finish the meshing step, the other important adjustment was material model calibration of each component to get the most reliable numerical setup.

Table 4.5 The ballistic damage propagation in T2 model

Body Interaction	Damage in each glass layer					
	G1		G2		G3	
	Front	Back	Front	Back	Front	Back
T2 (A) Frictionless	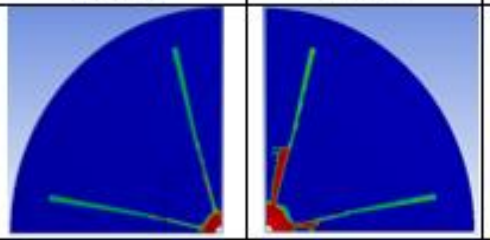		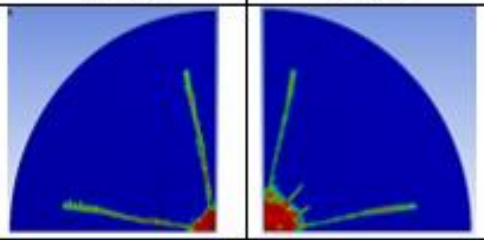		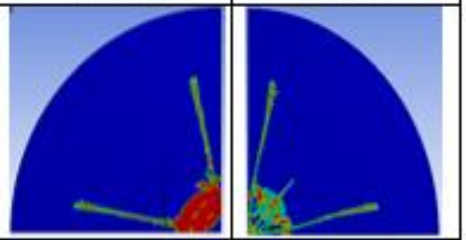	
T2 (B) Frictional	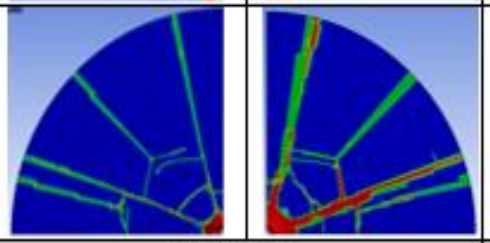		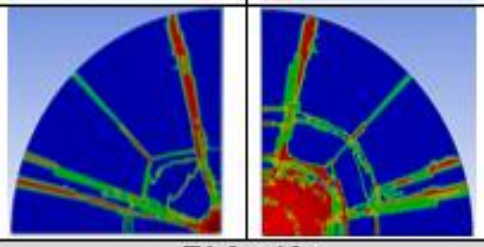		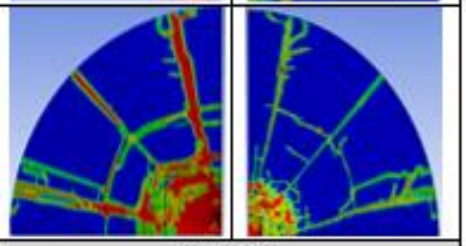	
	Left side		Right side		Overall	
T2 (A) Frictionless					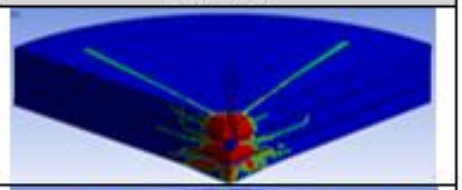	
T2 (B) Frictional	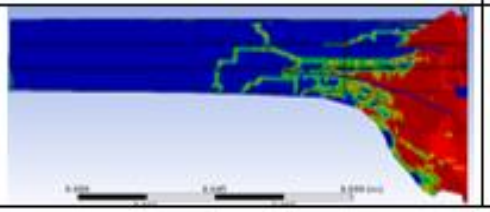		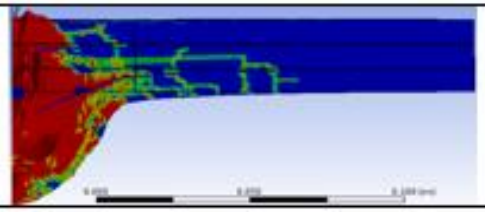		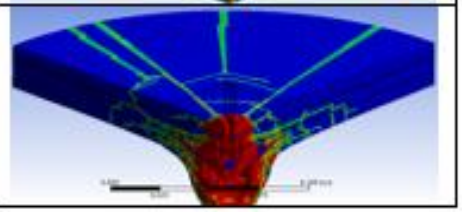	

4.1.2 Material model calibration results

The material model adjustment was focused in this section in order to get the more accurate material behavior prediction under explicit dynamic impact. Due to lacking of some experimental materials data under dynamic loading, we need to adjust and study the effects of some material parameters in the FEA numerical setup on the damage behavior of the FEA model. The numerical adjustments were thus performed in the six-layer target models, using the same target geometry, meshing method and element sizes optimized from the previous section.

4.1.2.1 Effect of material model calibration in Soda-lime glass

In Chapter 3, we explained the importance of hydrostatic tensile limit (HTL) towards the strength of glass material. STD2 model, the commercial six-layer target model, was first performed FEA to investigate the damage behavior and compare with the experimental results. According to the experimental damage analysis of STD1 and STD2 models after ballistic testing, the rear plate of both models contained no visible cracks. This result could be the initial guideline to adjust the material parameters of soda-lime glass in the FEA setup. Therefore, the FEA was performed on STD2 models with HTL of soda-lime glass in a range of 30 to 80 MPa, referred to as JH-30 to JH-80 model, respectively.

According the FEA result in Table 4.6, the HLT apparently affected the damage propagation on each glass layer. For JH-30, the damage crack propagated throughout the whole target from layer to layer. Especially, on the back side of rear plate (G6) showed the highest amounts and the most severe level (red color zone) of cracks comparing to other cases in Table 4.6. When increasing the HLT-values from 30 to 35, 40, 60, 70 and 80, the damage level of cracks were obviously declined. This means that the higher HLT-value, the higher impact strength of glass layers was obtained.

Even though the crack propagation in G1 to G5 of JH-30, JH-35 and JH-40 was well-distributed and closed to the experimental results, the severe damage of G6 was unlikely found in the experiment. Thus, HLT-values in range of 30-40 MPa were neglected from further calculation due to the deviation from experiment.

For JH-60 and JH-70, G1 to G3 showed the similar radial crack patterns as JH-30 and JH-40, but the lower fraction of damage (red color) zone was obtained. While, G4 to G6 showed the different crack pattern from JH-30 and JH-40 due to the lower bifurcated cracks observed at HLT-values higher than 40 MPa. A few radial cracks were still observed on G5 and G6 in JH-60 and JH-70 models. For JH-80 model, G2 of JH-80 model showed the lower amount of cracks compared to others. On the other hand, G6 of JH-80 contained the bifurcated cracks more than G6 of JH-70. In conclusion, JH-2 model with HLT-value of 70 MPa could match the damage pattern of glass failure of FEA and experimental results because crack pattern in G1 to G4 show the reasonable agreement , while the crack patterns in G5 and G6 showed the lowest amount of crack, which best match with the experiment. This model was subsequently used to in the further calibration steps.

Table 4.6 Damage analysis of G1 to G6 in the STD2 model at various HLT-values (30-80 MPa), referred to as JH-30 to JH-80 models.

Glass Model	Damage in glass layer (STD2)					
	G1		G2		G3	
	Front	Back	Front	Back	Front	Back
JH-30	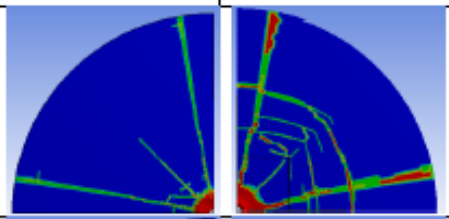		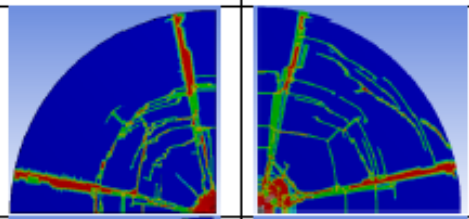		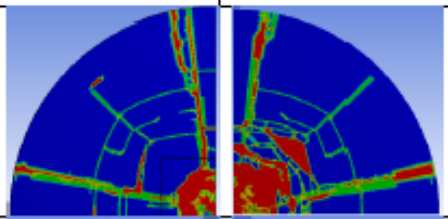	
JH-35	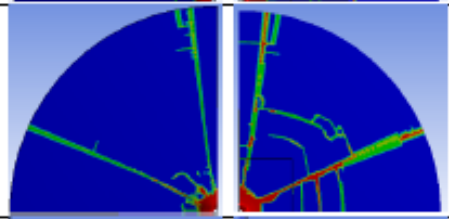		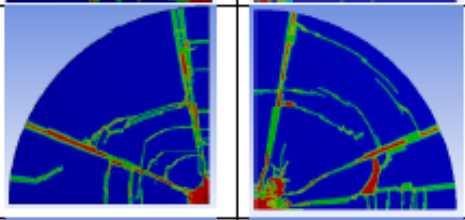		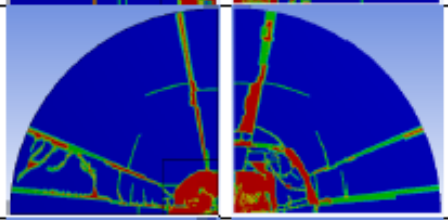	
JH-40	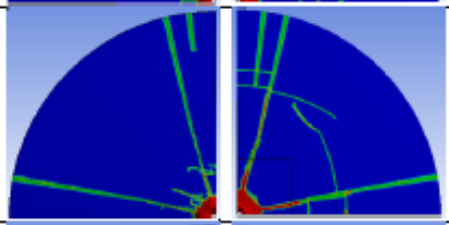		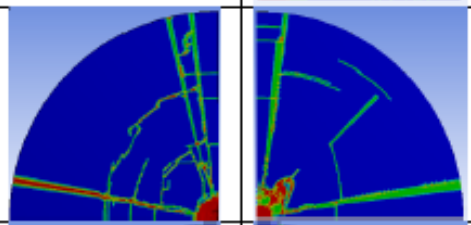		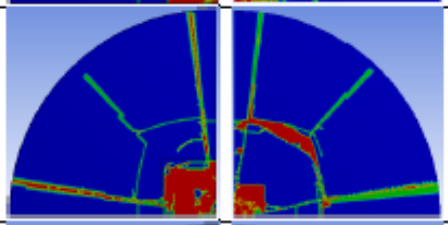	
JH-60	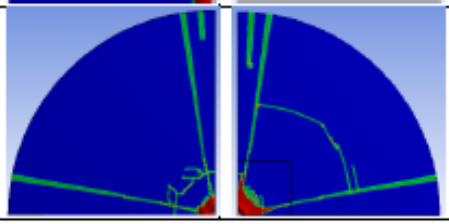		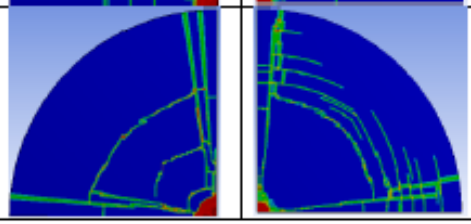		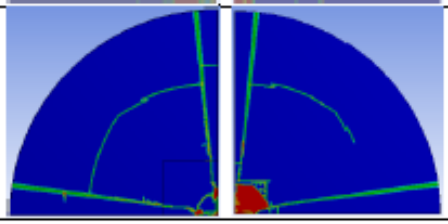	

Glass Model	Damage in glass layer (STID2)					
	G4		G5		G6	
	Front	Back	Front	Back	Front	Back
JH-30						
JH-35						
JH-40						
JH-60						

Glass Model	Damage in glass layer (SID2)					
	G1		G2		G3	
	Front	Back	Front	Back	Front	Back
JH-70						
JH-80						
	G4		G5		G6	
JH-70						
JH-80						

4.1.2.2 Effect of material model calibration for PVB

In Chapter 2, within laminates structure, the PVB interlayer may play a crucial role in accumulating and distributing the internal energy from the bullet impact. However, the material properties of PVB films were mostly available in static testing conditions, and not much available in the dynamic condition (under the high impact velocity) due to the requirement of more complex testing facilities. Therefore, in this study, several material models for PVB interlayers (i.e. Johnson-Cook, hyperelastic Mooney-Rivilin, and viscoelastic models, referred to as, PVBJC (Table 3.6-3.7), PVBMRS (Table 3.8) and PVBvis (Table 3.9), respectively) were investigated in the FEA studies. The STD2 model was once again used for the PVB material model calibration calculations.

Typically, due to different mechanical behavior description in the material models, the damage value of PVB interlayer was not available in the FEA; therefore, the damage in each glass layer was considered and compared with the experimental results instead. All the damage level of each glass layer within STD2 models using various PVB material models were summarized in Table 4.7.

In Table 4.7, the STD2 model with PVBJC and showed the radial crack propagation across glass layer till in G3, while PVBMRS1, PVBMRS2, and PVBvis did not shown good enough radial crack propagation in G3. While comparing the number of crack and crack patterns on G5 and G6, PVBMRS1 and PVBMRS2 models showed the highest number of cracks with some bifurcation, while PVBJC and PVBvis model showed only non-bifurcated cracks along the corner. From these observations, PVBJC model likely performed better radial crack propagation through the whole target than other material models. Thus, PVBJC material model was subsequently optimized in terms of strain rate constant and thermal softening exponent in the next section.

From Chapter 2 to 3, under the dynamic loading condition, Johnson-Cook (JC) material model proposed a semi-empirical constitutive model for elastic-plastic materials which described the mechanical behavior at large strains, high strains rate, and high temperatures [6-8]. The strain rate hardening and thermal softening in this model were then calibrated to obtain more precise PVB interlayer behavior in the laminates system of this study. All damage in the laminates obtained from JC parameter calibration (Table 3.7) was summarized in Table 4.8.

Table 4.7 Damage patterns in each glass layer of STD2 model with different material models.

PVB Model	Damage in glass layer (STD2)					
	G1		G2		G3	
	Front	Back	Front	Back	Front	Back
PVBJC	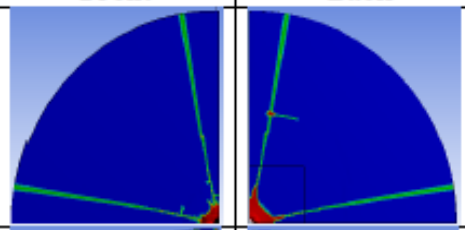					
PVBMRS1	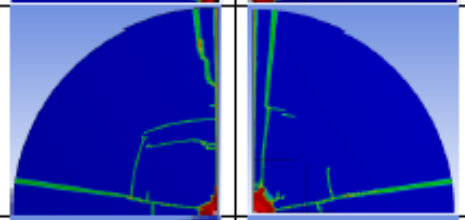					
PVBMRS2	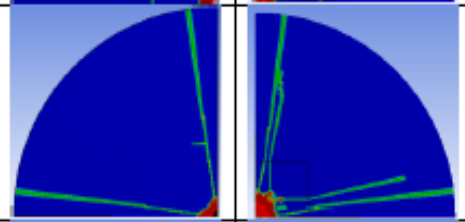					
PVBvis	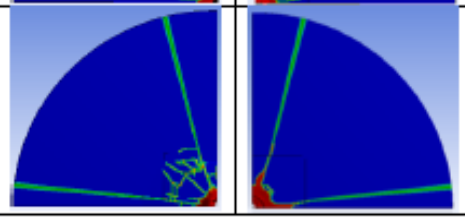					

PVB Model	Damage in glass layer (SID2)					
	G4		G5		G6	
	Front	Back	Front	Back	Front	Back
PVBJC						
PVBMRS1						
PVBMRS2						
PVBvis						

From the FEA results in Table 4.8, PVBJC2 with the strain rate constant of 0.052 (at strain rate 700 s^{-1}) coupling with thermal softening exponent of 1.85 showed the lower number of radial cracks in G2 than PVBJC results, while in G6, the bifurcated cracks were observed. On the other hand, once the thermal softening exponent term was set to 0 in PVBJC3, the crack propagation in G6 consequently showed lower bifurcated cracks, while the other layers depicted the similar crack pattern and amount compared to PVBJC2. Furthermore, if the strain rate constant was set to the higher strain rate (1200 s^{-1}) as in PVBJC4 model, the lower damage propagation was observed in G6 and more radial crack propagations were observed in all layers from G1 to G4. These results in turn showed that the thermal softening exponent mainly affected the crack bifurcation, while the strain rate constant affected toward the radial crack propagation. Thus, the selected material model for PVB interlayer in this study is PVBJC4, which employed JC model with strain rate constant of 0.084 and without thermal softening exponent effect.

จุฬาลงกรณ์มหาวิทยาลัย
Chulalongkorn University

Table 4.8 Damage patterns in each glass layer of STD2 model with varied parameter in JC model.

PVB Model	Damage in glass layer (STD2)					
	G1		G2		G3	
	Front	Back	Front	Back	Front	Back
PVBJC	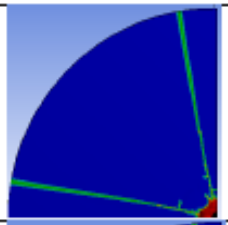	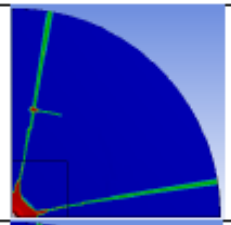	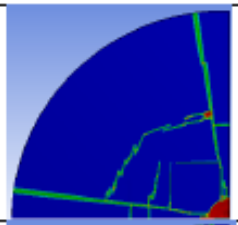	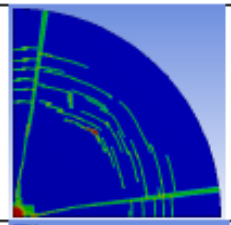	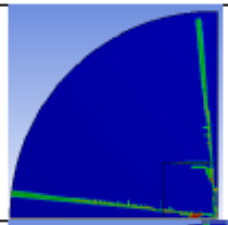	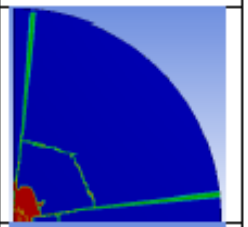
PVBJC2	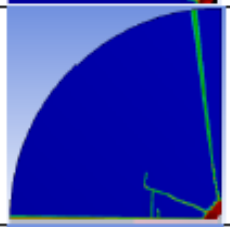	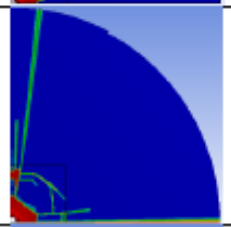	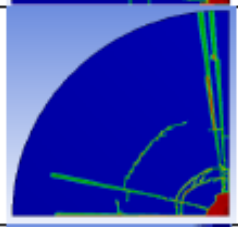	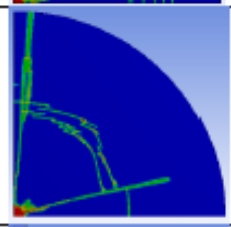	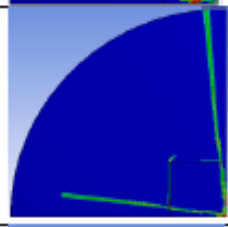	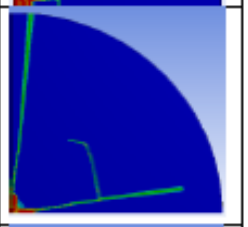
PVBJC3	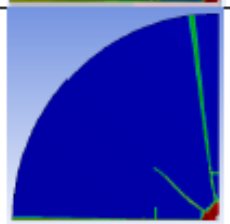	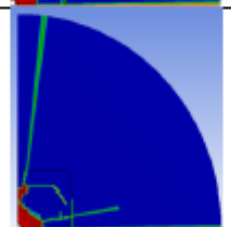	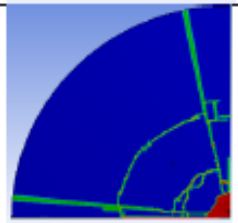	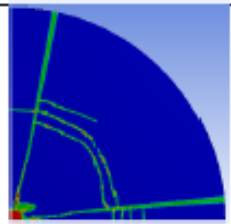	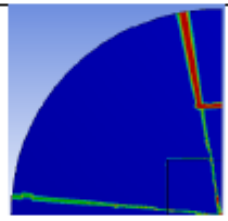	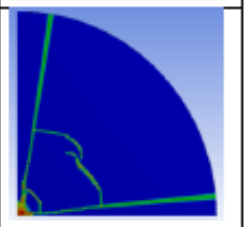
PVBJC4	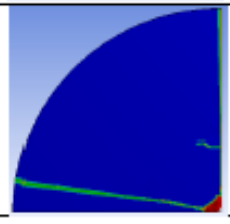	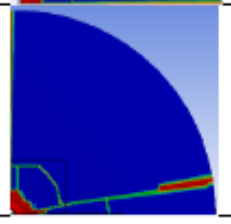	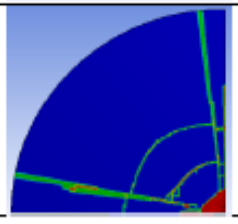	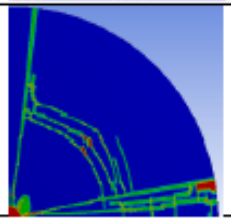	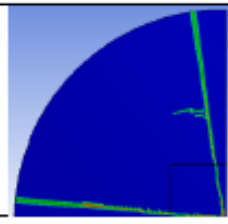	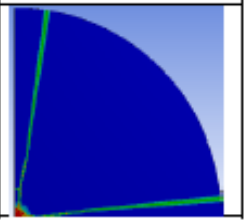

PVB Model	Damage in glass layer (STD2)					
	G4		G5		G6	
	Front	Back	Front	Back	Front	Back
PVBJC						
PVBJC2						
PVBJC3						
PVBJC4						

Additionally, we further adapted all calibrated conditions (i.e. the meshing method, element-size and material model calibrations for targets) to other models (for example, STD1, A19 and B19 models). Since the experimental analysis of damage in each glass layer of A19 and B19 models were intensively investigated in Ref. 1, the FEA results of A19 and B19 models were compared to those previously reported in Ref.1 for the final calibration of target. The results were thus summarized in Table 4.9-4.12.

The FEA and experimental results of STD1 model in each glass layer were in good agreement. The damage in G5 and G6 are the similar between STD1 and STD2. This result in turn confirmed that the meshing conditions and material model calibration could be used in STD1 model (Table 4.9-4.10). The comparisons of FEA and experimental results of A19 and B19 models were shown in Table 4.12 and 4.13, respectively. The FEA damage result of A19 and B19 model were in an agreement with the experimental results in term of the radial crack propagation pattern in the cross-section, but were quite different in term of the numbers of radial crack in each glass layer. This result deviation was arising from the Lagrange calculation system, where the materials were represented with elements at finite sizes. Therefore, the crack lines were tentatively exaggerated due to the limitation of the element size used in the models.

จุฬาลงกรณ์มหาวิทยาลัย
Chulalongkorn University

Table 4.9 Summary of damage pattern in each glass layer of STD1 and STD2 models using JH-70 and PVBJC4 material models.

Model	Damage in glass layer					
	G1		G2		G3	
	Front	Back	Front	Back	Front	Back
STD1	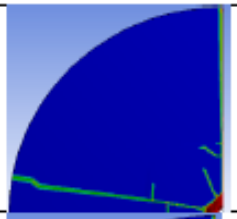	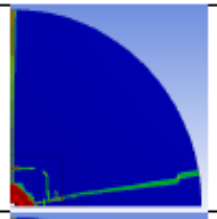	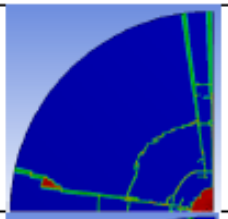	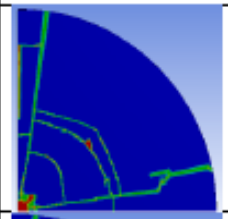	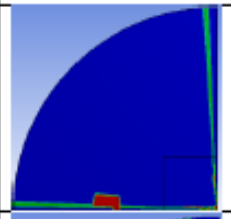	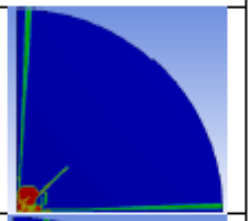
STD2	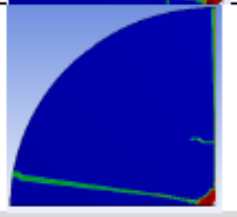	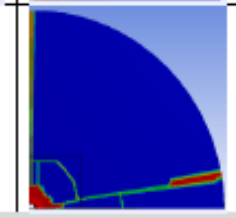	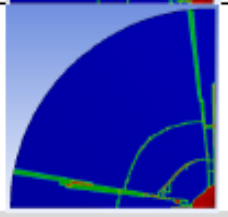	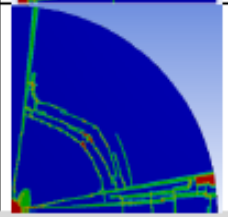	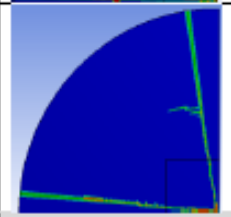	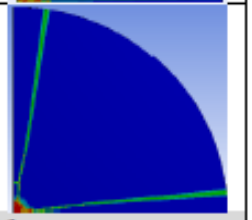
	G4		G5		G6	
STD1	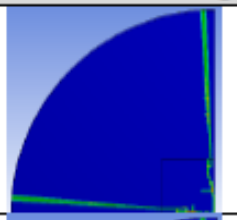	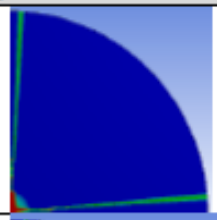	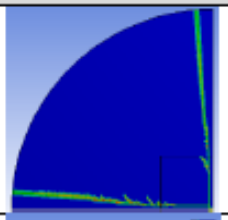	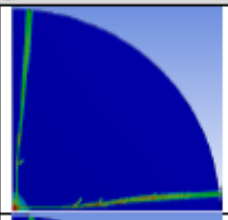	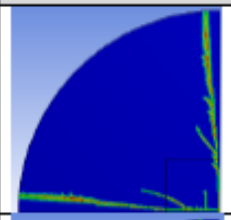	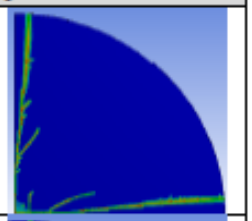
STD2	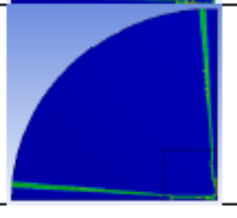	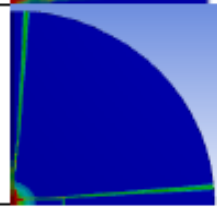	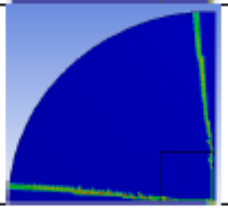	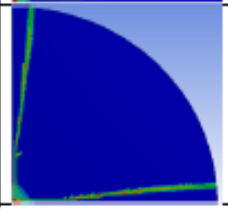	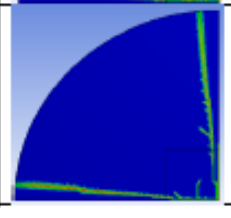	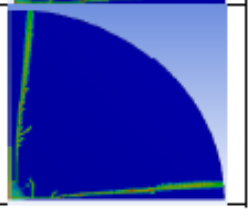

Table 4.10 Cross-sectional view of damage propagation in STD1, STD2, A19 and B19 models

Model	Damage in glass layer	
	JH-70 / PVBJC4	
	Left side	Right side
STD1	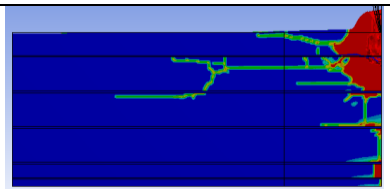	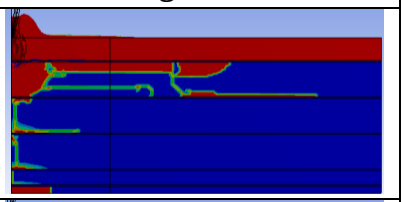
STD2	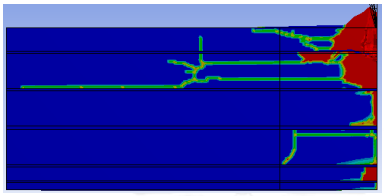	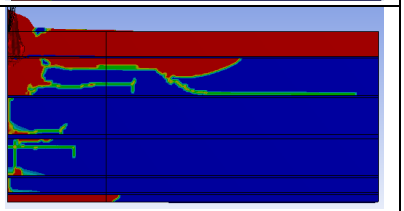
A19	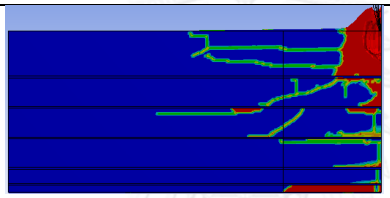	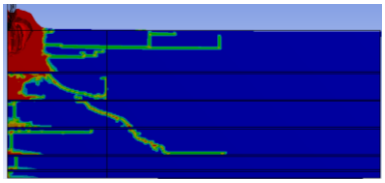
B19	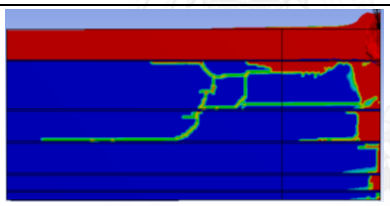	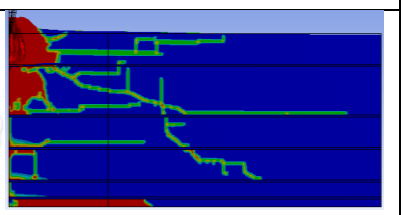

จุฬาลงกรณ์มหาวิทยาลัย
Chulalongkorn University

Table 4.11 Numerical and experimental results comparison of A19 models in each glass layer with JH-70 and PVBJC4 material model.

Glass Layer	Damage in glass layer A19				
	Experiment	FEA		Experiment	FEA
G1	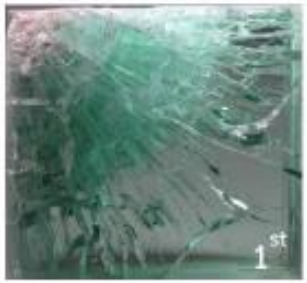	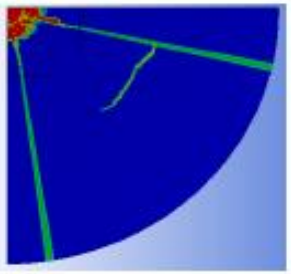	G4	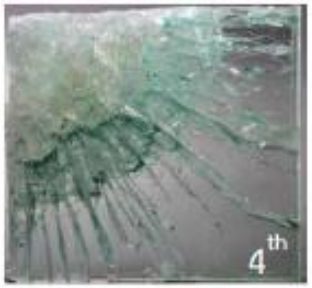	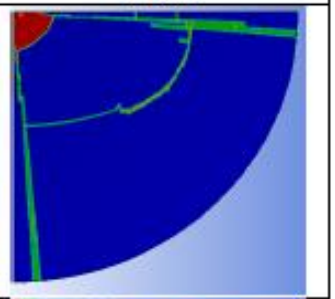
G2	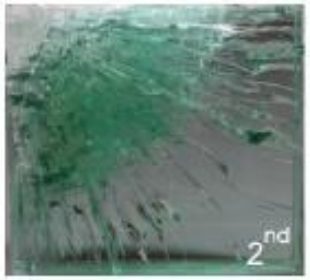	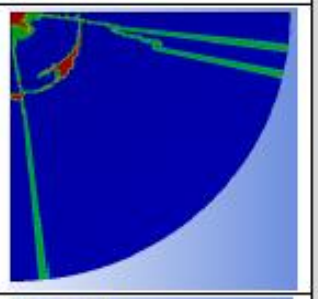	G5	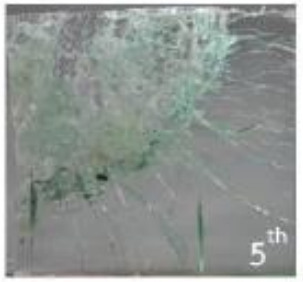	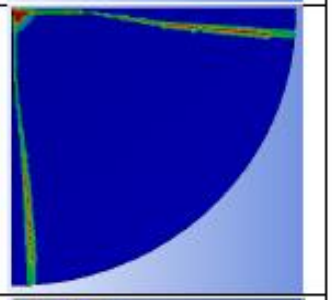
G3	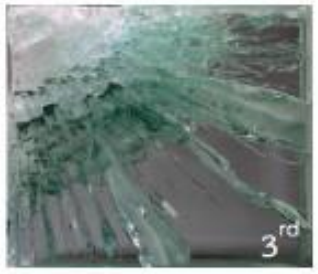	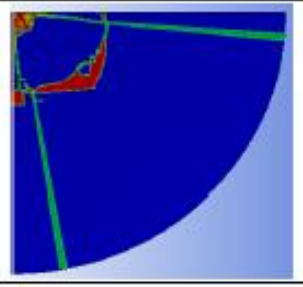	G6		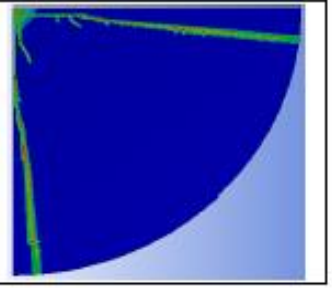

Table 4.12 Numerical and experimental results comparison of B19 models in each glass layer with JH-70 and PVBJC4 material model.

Glass Layer	Damage in glass layer B19				Glass Layer
	Experiment	FEA	Experiment	FEA	
G1					G4
G2					G5
G3					G6

4.1.2.3 Effect of Material model for Bullet

The Johnson-Cook model was applied with all bullet components following by Hazell et.al [29]. JC model could perform the perfect match with the real bullet that was almost eroded after hitting with target. All numerical models setup was perfectly interact with the target.

4.2 Results on the effect of configuration design in soda-lime glass/PVB laminated transparent armor

After obtaining the calibrated material models from the previous section, the study on the effect of configuration design in the soda-lime glass/PVB laminated system was performed. Each component of the laminates had influence toward the overall ballistic performance of targets. The ballistic damage characteristic of FEA and experimental results were analyzed and compared. The overall damage estimation of each model was subsequently compared to the maximum damage level of STD1 and STD2 models, which was used as a prediction criterion whether the target would pass the ballistic test.

4.2.1 Effect of Striking glass thickness

Striking layer played an important role in the bullet erosion. With the glass thickness available commercially, more than thousand configurations of six-layer transparent armors could be designed. Therefore, in this section, the study of striking glass thickness effect on the ballistic protection performance was first focused. To reduce the numbers of feasible configurations, the glass thickness other layer of G2 to G6 layers were kept similar to those in A19 (19-12-12-12-6-3) model. The striking glass thickness was then reduced from 19 mm to 12, 10, 8, 6 and 3 mm (referred to as A12, A10, A8, A6 and A3, respectively). Depth of penetration (DOP), crater diameter, volumetric damage and energy of each glass layer in all above models were subsequently analyzed and compared with respect to the striking glass thickness (G1) and also with the experimental results.

4.2.1.1 DOP and Crater diameter

The DOP and crater diameters from FEA results were summarized in Table 4.13. The results showed that the models with thinner G1 than G2 had the higher bullet penetration depth. According to, for A19, B19 and A15 models (see configurations in Table 3.11), B19 (12-19-12-12-6-3) with the thinner striking layer thickness of 12 mm showed the deeper but smaller crater diameter than those of A19. Therefore, initial estimation of ballistic performance of A19 was higher than B19 in case of crater diameter occurred and G6 damage in experimental. When compared A19 and A15, the bullet was stopped at the same G1 layer, while crater diameter of A19 was larger than A15. For the lower striking glass thickness in A12 to A3 models, the crater diameters were in a same range as those in A19 and A15 but the DOP was much higher than A15.

Table 4.13 Depth of penetration, the layer that bullet stopped and crater diameter in all configurations of striking layer thickness effect from FEA

Model	DOP (mm)	Bullet stopped	Crater diameter (mm)
STD1	14.30	G2	26.19 ± 2.71
STD2	13.89	G2	28.52 ± 5.58
A19	13.93	G1	31.31 ± 4.58
B19	14.66	G2	27.89 ± 3.15
A15	14.38	G1	28.04 ± 0.99
A12	15.29	G2	26.88 ± 1.80
A10	15.18	G2	29.41 ± 5.69
A8	14.87	G2	26.01 ± 4.35
A6	12.44	G2	31.22 ± 3.84
A3	16.48	G2/P2	29.73 ± 3.04

4.2.1.2 Energy comparisons

In Chapter 2, Wilkins[56] studied the loss mass of bullet due to the erosion from ceramic plate interaction and found that the kinetic energy lost from bullet was not only through the internal energy absorption by target. Only 60% of initial kinetic energy was absorbed in the internal target, while the rest was caused by heat, the erosion of bullet and other types of energy loss. The losing mass of bullet in turn reduced momentum of bullet while hitting the target, and thus reduced its penetration ability into the target.

จุฬาลงกรณ์มหาวิทยาลัย
Chulalongkorn University

1. Kinetic Energy and Internal Energy

The kinetic and internal energy distribution in the targets at the end time of 0.3 ms was shown in Figure 4.5-4.6. The kinetic energy of the target was decreasing with the impact time due to the energy transformation to internal energy, contact energy and heat. Some kinetic energy may still remain in various parts of the target and gradually decreased to the final values as shown in Figure 4.5. At the end of FEA simulation time, the highest kinetic energy was remained in G2 of STD2, A8, A6 and A3 models, in G2 for all other models. However, the remaining kinetic energy was considered negligible compared to the internal energy of each layer in the target in Figure 4.6.

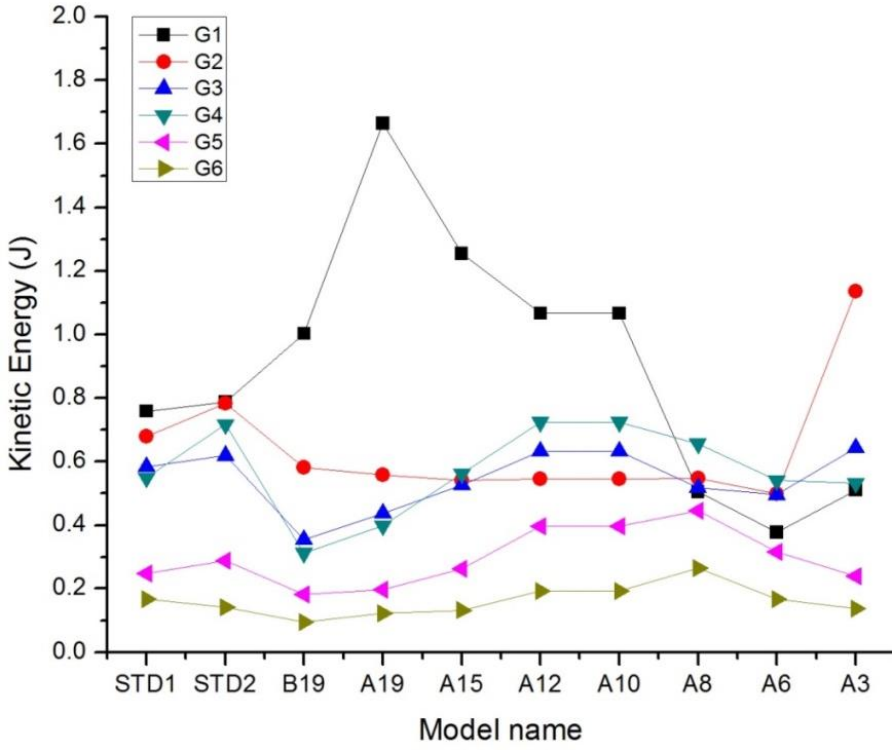

Figure 4.5 Kinetic energy distribution in each glass layer of all configurations used in striking glass thickness study.

The internal energy (IE) distribution in all glass and PVB layers was shown in Figure 4.6. Since the glass layers were much thicker than PVB films, the IE absorbed in the glass layers were much higher in that in each PVB interlayer. According to the results in Figure 4.6, the IE was absorbed by glass layers, in the following orders: (i) G1 > G2 > G3 > G4 > G5 > G6 for A19, B19, A15, A12 and A10 models and (ii) G2 > G1 > G3 > G4 > G5 > G6 for A8, A6 and A3 models.

From Figure 4.6(a), the IE absorbed in G1 in A-series was in the following order: A19 > A15 > A12 >A10 > A8 > A6 > A3 respectively. These results can conclude that the absorbed IE was proportional to G1 thickness. In Figure 4.7(c), the IE in P1 showed the following order: A12 > A10 > A15 > A8 > A6 > A19 > A3. According to the configuration with thick G1 (A19 and A15), the large fraction of IE were absorbed by G1, while the remaining IE was dissipated to P1 layer and caused only minimal amount of IE absorption in P1. However, once the G1 thickness decreased in the range of 3-12 mm (A3-A12 models), the bullets were penetrated to G2 layer; therefore, kinetic energy was directly absorbed in P1 and G2 and converted to the IE. Higher IEs were subsequently observed in P1, G2 and also P2 for the thinner A3-A8 models.

These results thus confirmed that the amount of IE accumulation in each glass layer and PVB film interlayer was related to striking glass thickness. We could conclude into three groups of configurations as followed:

(1) A19 and A15 models with the striking layer thickness as 19 and 15 mm, respectively, had the highest IE in G1 and lowest IE in P1. The striking glass layer played the important role in IE absorption and dissipation in this group of configurations.

(2) A12 and A10 models with striking layer thickness as 12 and 10 mm, respectively, had the medium IE in G1 and highest IE in P1. The G1, P1 and G2 all played the important role in IE absorption and dissipation in this group of configurations.

(3) A8, A6 and A3 models with striking layer thickness as 8, 6, and 3 mm, respectively, had the lowest IE in G1 and P1, and highest IE in G2 and P2. The G2 and P2 played the important role in IE absorption and dissipation in this group of configurations.

จุฬาลงกรณ์มหาวิทยาลัย
Chulalongkorn University

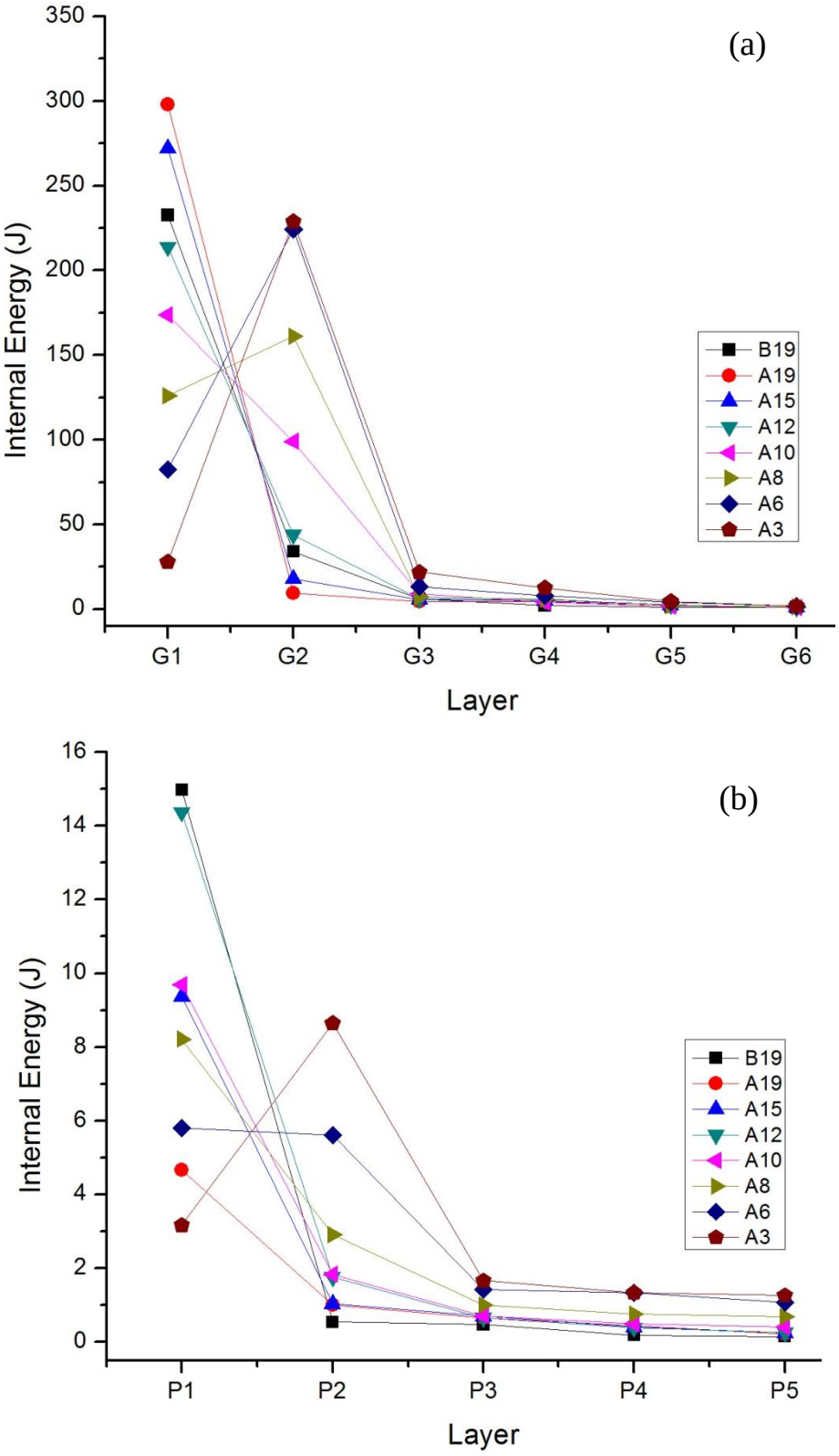

Figure 4.6 Internal energy distributions in (a) all glass layers and (b) all PVB layers used in the study of effect of striking glass thickness.

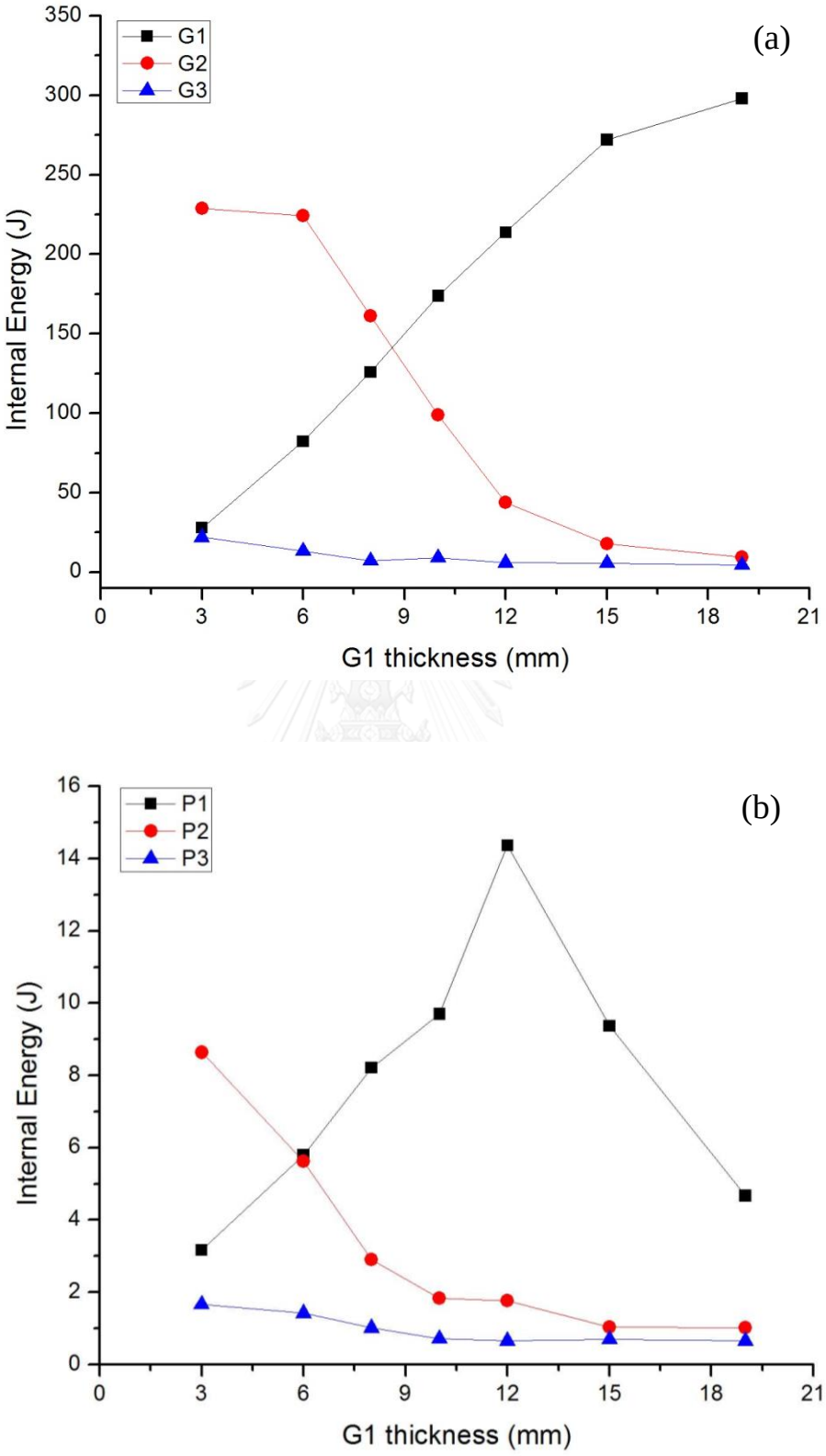

Figure 4.7 Comparison of IE of (a) G1, G2 and G3 and (b) P1, P2 and P3 with respect to G1 thickness.

2. Normalized Internal Energy

Since the amount of internal energy absorbed on target was dependent on the volume of each layer, in this section, the internal energy was then normalized with the total volume of each layer referred to as 'normalized internal energy (NormIE)' and compared between different models (Figure 4.8). The highest values of NormIE were still observed in either G1 or G2 if considering only glass layers and in either P1 or P2 for the PVB interlayers in all A-series. As shown in Fig.4.8, the NormIEs with respect to the glass thickness for all models were still similar those of IE except that the IE accumulations in G2, P1 and P2 were more pronounced, and the decreasing trend of NormIE was first observed at the higher G1 thickness than 15 mm (i.e. A19 model).

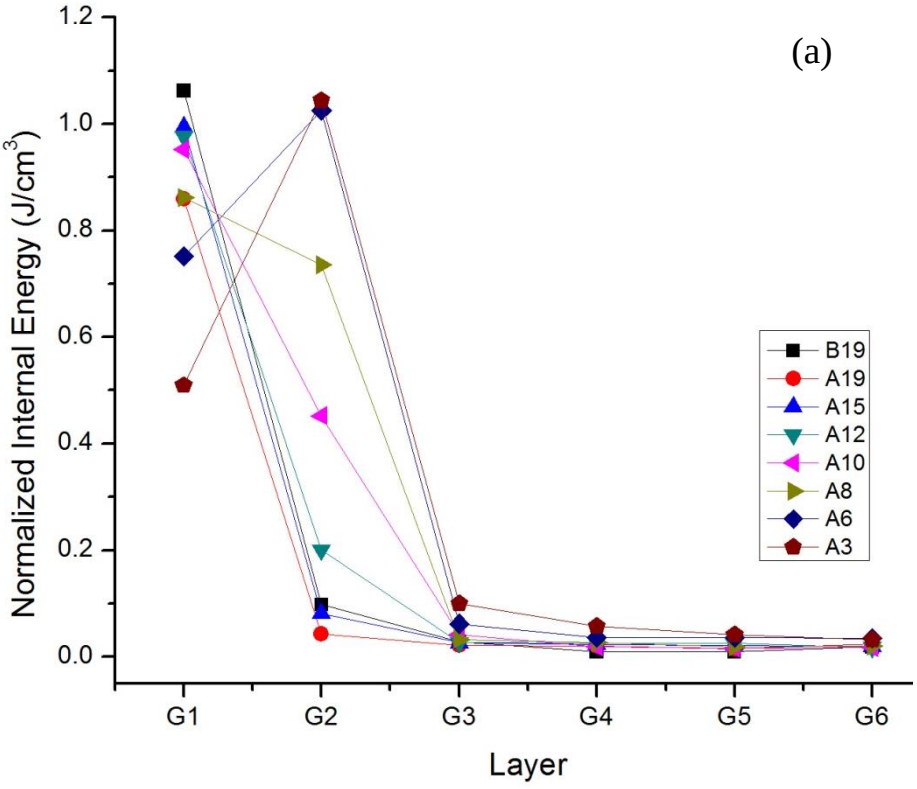

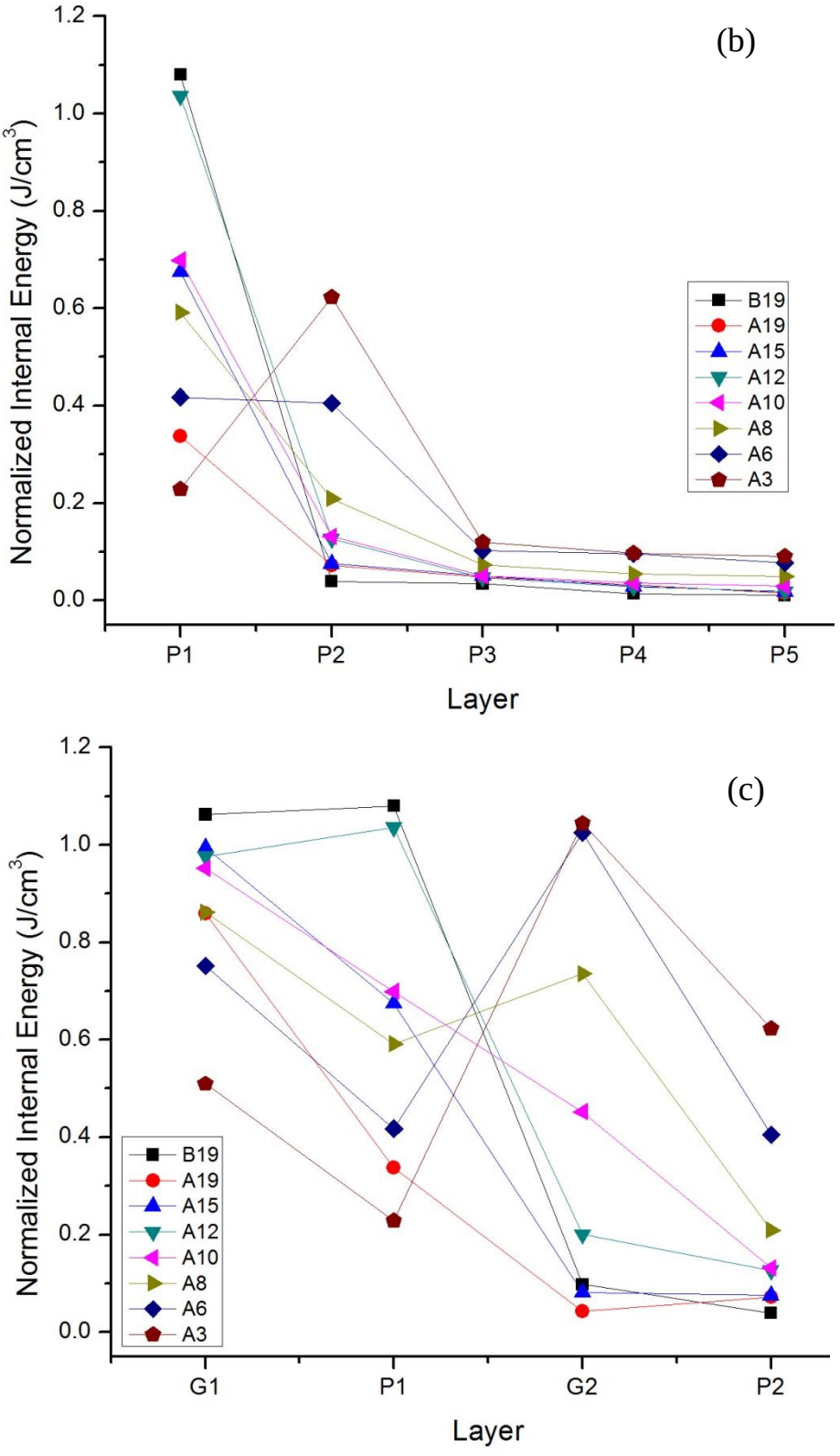

Figure 4.8 Normalized Internal energy distributions in (a) all glass layers, (b) all PVB interlayers and (c) G1, P1, G2 and P2 of configurations of design group by varied striking layer thickness.

The results in Figure 4.8 suggested that G1 and P1 together with G2 and P2 were absorbed similar internal energy densities, but due to much lower PVB film thickness, the lower total internal energy was accumulated in PVB layers as discussed earlier. According to Figure 4.9, the stress wave propagated mostly from G1 to P2 and started to level down below P2 Layer. Therefore, not only the G1 thickness could affect the ballistic performance, the G2, P1 and P2 thicknesses were also important factors in design the laminated configuration.

By considering glass and PVB layers separately as shown in Figure 4.8, in almost all models (except A6 and A3) , the NormIEs were highest in G1 and P1 were and then gradually declining in G2 and P2, respectively, while for A6 and A3 models, G2 and P2 showed the highest NormIEs. The NormIE of G3 to G6 and P3 to P5 were nearly constant, which indicated that below P3 layer, the internal densities of all layers were dramatically decreasing and were stable till the last glass layer (G6) in all models.

By comparing the change of NormIE in both glass and PVB layers together as shown in Figure 4.8-4.9, the trends of NormIE could be categorized into three groups:

(1) B19 and A12 models: Both had the same thickness of the striking glass of 12 mm and showed the similar NormIE in both G1 and P1 layers. Below P1, the NormIE was in the decreasing trend. Due to the high NormIE in P1, this could indicate that the PVB interlayer could significantly absorbed and dissipated the internal energy through the below layers in soda-lime glass/PVB laminates depended on the order of layer and glass thickness in the configurations.

(2) A19, A15 and A10 models: The highest NormIE was observed on G1, and the decreasing trend in the NormIE along each layer below the striking glass was found. Most of internal energy was absorbed in G1 and passed the rest in the adjacent layers. The depth of penetration was observed only in the G1 (except A10); thus these could indicate that the thick striking layer (G1) performed the stress wave propagation throughout the laminates structure.

(3) A8, A6 and A3 models: These were the models with thinner G1 compared to, G2. The models in this group showed the higher NormIE on G2 than that of P1. This was likely that the depths of bullet penetration were very high and the bullets were stopped at G2. Stress wave transferred through the G1 and P1 through G2 rapidly, and was absorbed in G2. Thus, the internal energy could distribute directly through G2 of these models.

The effect of G1 thickness on the NormIE distribution of all A-models were compared in Figure 4.8.-4.9. The results showed that the IE of G1 was increasing with G1 thickness up to 19 mm, while the NormIE of G1 was increasing with G1 thickness only up to 15 mm and started to decline after. Thus, the G1 had the maximum internal energy density at the thickness of 15 mm.

The different trends of IE and NormIE of P1 with respect to G1 thickness were observed. The IE and NormIE of P1 were increasing with G1 thickness up to 12 mm and declined after. At G1 of 15-19 mm, the bullet penetrated to only G1, while at the G1 thickness of 3-12 mm, the bullet could penetrate to G2. Therefore for the G1 thickness of 15-19 mm, the IE from G1 transferred directly to P1. The thicker G1 led to the lower IE energy dissipated to P1. However, at the G1 thickness of 3-12 mm, beside the IE from G1 transferred directly to P1, the remaining kinetic energy from bullet after penetration through G1 would also be transformed into IE in P1 and G2. As a result, the thinner G1, the higher IE and NormIE were accumulated in both P1 and G2.

On the other hand, the IE and NormIE of G2, G3, P2 and P3 were decreased with increasing G1 thickness. In A-models, the G1 and P1 layers took crucial roles to absorb and evenly distribute the energy through the layers below; therefore, the internal energy accumulated in the G2, P2, G3 and P3 were decreasing with increasing G1 thickness. This was caused by the lower amount of energy was transferred to G2, G3, P2 and P3 as G1 thickness increased.

จุฬาลงกรณ์มหาวิทยาลัย
Chulalongkorn University

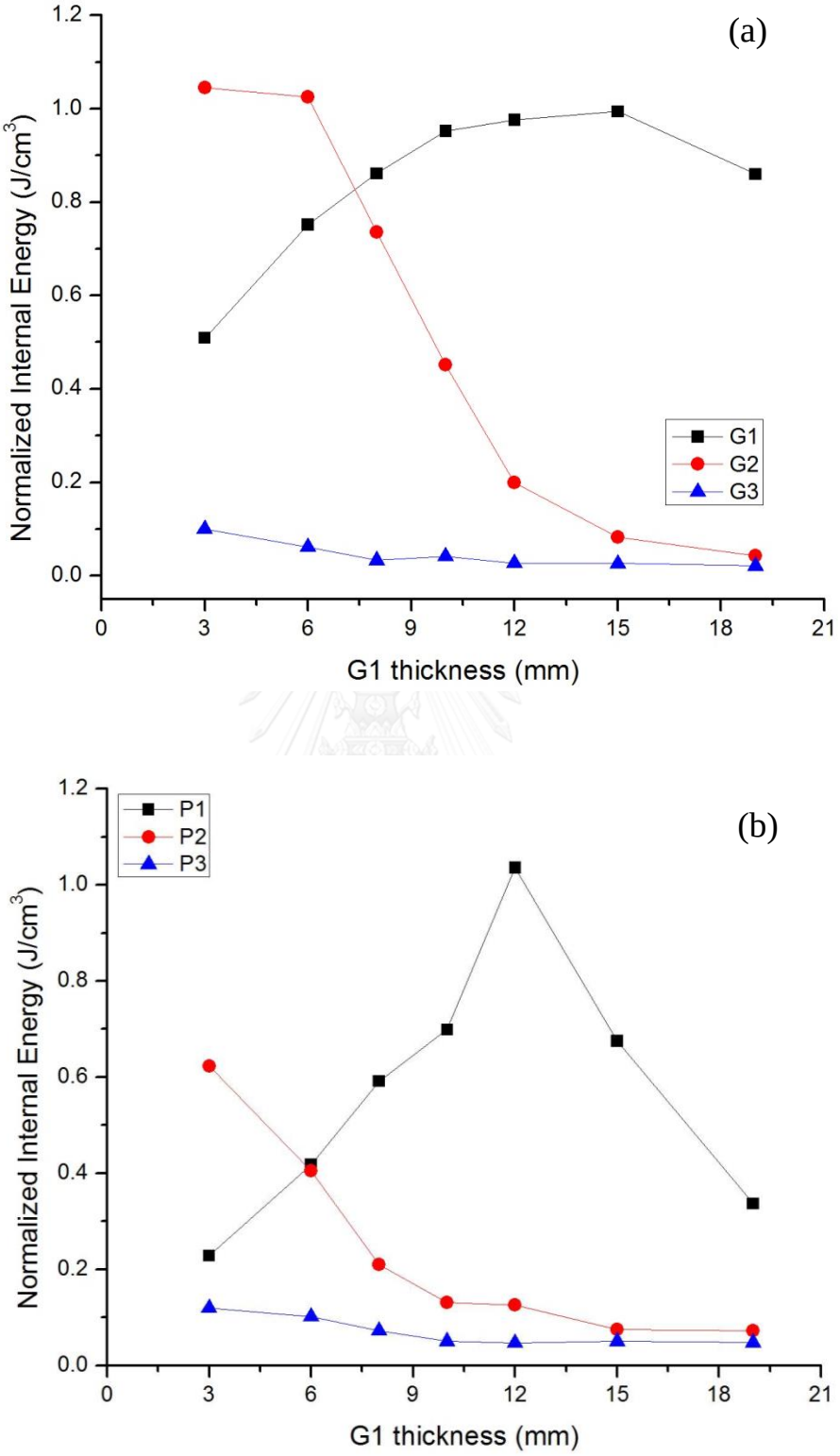

Figure 4.9 Comparison of NormIE of (a) G1, G2 and G3 and (b) P1, P2 and P3 with respect to G1 thickness.

4.2.1.3 Volumetric Damage

In this section, the percentage of volumetric damage (VD) in each glass layer for STD1, STD2, B19 and all A-models were compared as shown in Table 4.14 and Figure 4.10. The VD reported in this thesis was the average amount of damage per unit volume of each glass layer. For example, 5% VD could mean either the glass consisted of severe damage cracks (damage level = 1) at the 5% volume fraction or the moderate damage cracks (damage level = 0.5) at 10% volume fraction. However, in this study, we assumed that the higher VD represented the higher probability of having severe damage cracks.

The VD in G6 and the average VD on the overall target were used as criteria to select the target configurations for the ballistic performance test throughout this study. Those model which had higher overall VD than STD1 and/or STD2 models were considered unlikely to pass the NIJ standard level III test in this study. Thus, according to Table 4.13, the acceptable VD of G6 in each configuration should be in a range of 3.28 to 3.67% (from STD2 and STD1, respectively). The overall average VD of STD1 and STD2 were in a range of 3.83-4.02%, which could be used as another criterion for configuration evaluation.

Furthermore, if we assumed that the glass with the damage level in a range of 0.75-1.00 was the severe damage glass (due to approximately 75% decrease in its strength), the VDs of G1, G2 and G6 for the damage level in a range of 0.75-1.00 (VDMax) were also calculated for the consideration. In most cases, the VDMax in G1, G2 and G6 were about 84-98% of the VD values, which in turn suggesting that 84-98% of overall damage occurred on G1, G2 and G6 were in the severe range. However, for some models such as B19 and A3, the VDMax of G2 were only 57% and 40% of the overall VD; therefore, 43% and 60% of the VD occurred in G2 were bifurcated cracks and the build-in stress energy, respectively. According to these results, we could assume that more than 84% of the VD in G6 was the severe damage which could result in the glass fragments and the low performance of the target.

Chulalongkorn University

Table 4.14 Summary of VD for the study of striking glass thickness effect (STD1, STD2, B19 and A19-A3 models).

Model name	VD (%)						
	G1	G2	G3	G4	G5	G6	Average
STD1	4.18	**7.28**	2.30	**2.16**	2.72	**3.67**	**3.83**
STD2	4.25	**7.73**	2.64	**2.15**	2.81	**3.28**	**4.02**
B19	5.72	**8.20**	5.73	2.80	**2.62**	3.99	5.06
A19	**5.50**	4.51	3.41	3.80	**2.83**	**3.44**	**4.26**
A15	**5.57**	5.17	4.83	5.49	3.15	**2.72**	4.94
A12	**3.34**	**12.46**	3.75	4.04	4.67	3.62	5.65
A10	5.50	**7.55**	5.12	3.56	**2.99**	**3.43**	5.05
A8	4.89	**9.27**	**3.15**	4.58	3.28	**3.46**	5.15
A6	5.14	5.06	**5.25**	**4.05**	4.57	5.10	4.82
A3	4.96	**3.23**	5.79	**7.85**	5.90	4.83	5.57
Model name	**VDMax (%)**						
	G1	**G2**				**G6**	
STD1	4.07	7.09				3.15	
STD2	4.17	7.51				2.77	
B19	5.60	4.73				3.48	
A19	5.35	4.31				2.97	
A15	5.45	4.99				2.28	
A12	3.25	12.19				3.17	
A10	5.40	7.34				3.00	
A8	4.75	9.05				3.03	
A6	5.03	4.92				4.68	
A3	2.43	1.26				2.22	

By comparing the VDs of all A-models, the VD in G6 and average VD were in the following order A6> A3> A12> A8 > A19> A10>A15 and A12> A3> A8> A10> A15> A6> A19 (Table 4.14). These results thus indicated that A19 and A15 models had both the low VD in G6 and the low average VD, which were close to those in STD1 and STD2. Thus, it was likely that A19 and A15 models could pass the ballistic testing of NIJ standard level III.

B19 model, consisted of 12-mm G1 and 19-mm G2, showed the higher VD of G2 than that of A19, while the VD of G1 was similar (Table 4.14). Although the VD of G6 and the average of VD were slightly higher than STD1, STD2, A19 and A15, the VDMax in G6 of B19 was relatively close to that of A19. The higher VD of B19 than A19 was mainly caused by the higher number of bifurcated cracks and build-up stress energy. The result thus suggested that B19 model might not perform as well as A19 and A15 in the ballistic testing.

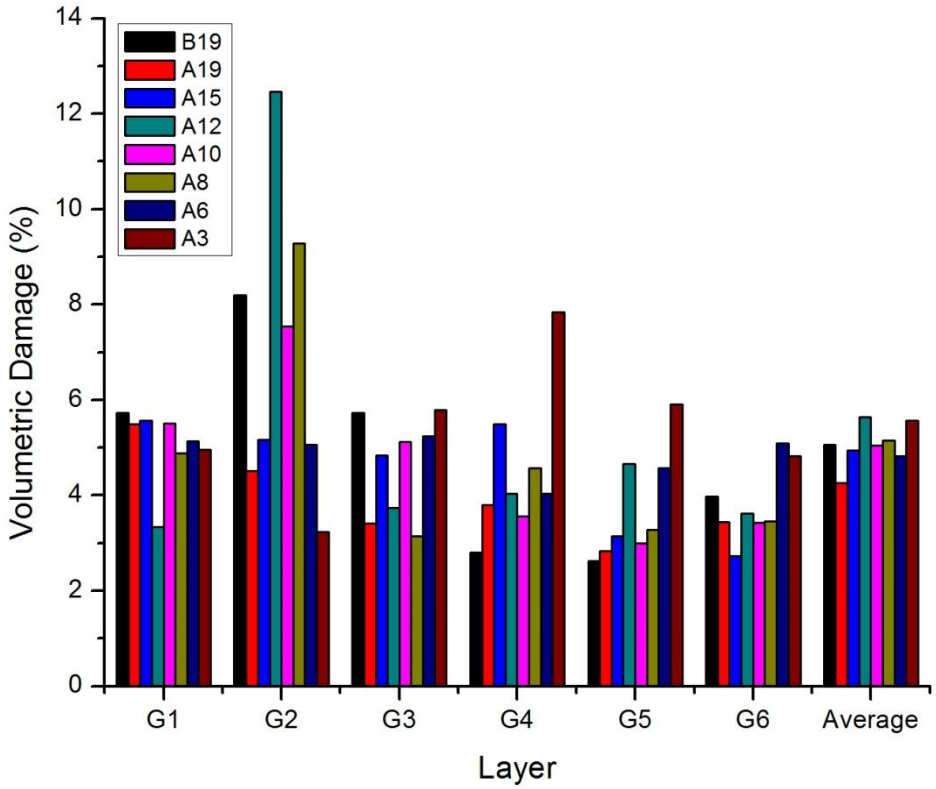

Figure 4.10 The VD of G1 to G6 and the average VD of all A-models and B19 used in the study of striking glass thickness effect.

Figure 4.10 showed the trend of VD in G1 to G6 of all configurations. The VD in G1 was in the following order: A15> A19> A10> A6> A3> A8> A12, while the order of VD in G2 was: A12 > A8 > A10> A15 > A6 >A19 > A3. According to Figure 4.10, the overall VD distribution was not in a direct relation with G1 thickness. The VD of G1 was relatively similar in all A-models, while some deviation was observed in the VD of G2. By comparing VD percentage of G1 and G2, the models could be separated into three groups which was slightly difference from IE observation:

(1) A19 and A15 models: These models showed the slightly higher VD in G1 than that in G2. Because the bullet penetrated within G1 in these models, most IE was accumulated in G1 layer and only low IE was transferred to G2, which in turn tentatively causing high damage in G1. These models showed the VD in G6 within the range of the standard models.

(2) B19, A12, A10 and A8 models: These models showed different trend from the previous case due to their higher VD of G2 than that of G1. Since the bullets penetrated rapidly through G1 and stopped at G2 together with the higher IE accumulation in G2 (Section 4.2.1.2), the higher VD in G2 of these models were observed. These models showed the VD in G6 was within the range of the standard models, while their average VDs were higher than those of A19, A15 and standard models.

(3) A6 and A3 models: Although these models also show high IE accumulation in G2, and also the high bullet penetration depth, the VD in G1 was still relatively similar to G2. This might cause by the low G1 thickness which may be more sensitive to the change in strength during bullet impact. Due to low G1 thickness, the IE accumulated in G1 might be enough to lower strength in A6 and A3 models; therefore, the damage was observed in G1 and G2. These models showed the similar VD in all glass layers and their VD in G6 and average VD were higher than the range of standard models.

The VD in each glass layer might not be directly proportional to its IE accumulation due to the more complexity in the combination of the range of damage level, the change of glass strength with increasing damage, together with the dynamic of impact and the stress wave propagation. However, the summation G1 to G2 in each configuration (Figure 4.11) could provide some interesting insights which could be used as another indicator and explanation for the VD of G6 in various models (Figure 4.10). The IE summation either from G1 to G3 or G1 to G6 still showed the similar pattern as those IE summation from G1 to G2 (Figure 4.11b), thus suggesting that IE of the top two glass layers could be the crucial part in the consideration of overall IE in the target. The trend of IE summation from G1 to G2 somewhat corresponded with the variation of VD in G6 as shown in Figure 4.10. The results suggested that the higher IE accumulations on the top glass layers likely lower the damage on the back plate (i.e. lower VD was likely observed in G6). Thus, to predict the failure of the target toward the ballistic testing, we should consider the VD in G6 and average VD together with the IE information and the summation of the internal energy in the top glass layers.

Therefore, according to our FEA results, the models that likely passed the NIJ standard level III should be A19 and A15. Although B19 showed slightly higher VD in G6 and average VD than the standard models, its VDMax values in all glass layers were quite similar to those of A19. Therefore, B19 model had some probability in passing NIJ standard level III, but were likely contained more damage on G6 than A19 and A15. On the contrary, A3-A12 models were not selected for the ballistic test due to their high average VD and VD in G6, which suggested some high possibility of failing the ballistic test. Furthermore, A8-A12 models showed very high VD in G2, which could potentially cause the problem for the re-shooting test and target stability during impact.

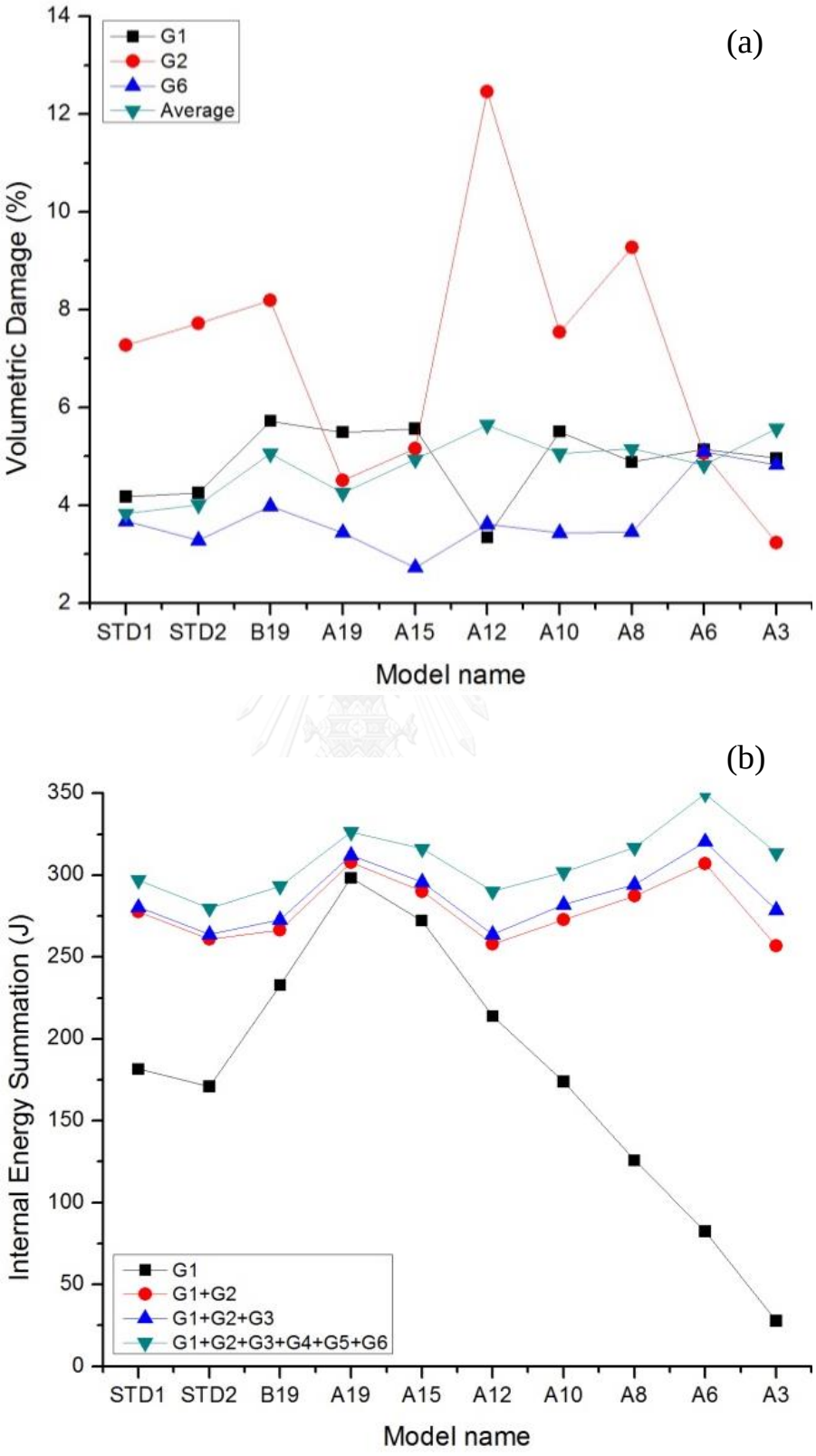

Figure 4.11 Plots of (a) the VD in G1, G2 and G6 and average VD, (b) the summation of internal energy in each model.

4.2.1.4 Comparison with Experimental Results

To compare the FEA and experimental results, the ballistic testing results by Chula Armor Research Unit [64], Chaichuenchob [4] and Jantharat [3] , were used for the comparison of DOP, the layer that bullet stopped and the crater diameter in each model compared between FEA and experimental results were compared in Table 4.15. The comparison was also necessarily used for re-confirming the accuracy level of our numerical calculations.

Table 4.15 Depth of penetration, the layer that bullet stopped and Crater diameters for all models in the study of striking layer thickness effect.

Model name	Depth of Penetration (mm)		Bullet stopped at		Crater Diameter (mm)	
	FEA	Expt	FEA	Expt	FEA	Expt
STD1	14.30	10.57 ± 0.24	G2	G1/P1	26.19 ± 2.71	30.64 ± 3.44
STD2	13.89	10.86 ± 0.37	G2	P1/G2	28.52 ± 5.58	28.00 ± 1.25
A19	13.93	10.55 ± 1.42	G1	G1	31.31 ± 4.58	35.49 ± 7.99
B19	14.66	11.37 ± 0.67	G2	G1/P1	27.89 ± 3.15	25.30 ± 2.59
A15	14.38	13.50 ± 0.51	G1	G1	28.04 ± 0.99	30.59 ± 6.74

Remarks: *Expt = Experiment results*

1. STD1 and STD2 models were tested by Chula Armor Research Unit [64]

2. A19 and B19 models were tested by, Chaichuenchob [4]

3. A15 model was tested by Jantharat [3]

By comparing FEA and experimental results of STD1, STD2, B19, A19 and A15 models, the DOP from FEA were slightly overestimated, while the layer that bullet stopped in each model was relatively closed to the experimental results. The slight deviation from experimental results could arise from the limitation of the element size used in Lagrange calculation. However, both outputs were considered as in acceptable range.

According to Table 4.15, the crater diameters were measured and compared between FEA and experimental results. FEA results were slightly underestimated the crater size. However, it must be noted that the crater had abundant glass fragments and bifurcated cracks, which might lead to some deviation in the measurement by digital Vernier calipers. Overall, the FEA and experimental results were in reasonable agreement in terms of DOP, the layer that bullet stopped and crater diameter. Therefore, the numerical setup calibrated from the previous sections was reasonable and feasible to further design a lighter-weight laminated transparent armor.

By considering the damage of the back of G6 layer, the STD1, STD2, B19, A19 and A15 models passed the NIJ standard level III (Table 4.16), which was in a good agreement with our FEA prediction. Thus, in some cases, our criteria on the VD in G6 to be lower than the standard models might be too restricted. However, thus far the results still showed that if the VD in G6 and average VD were within those of standard models, the models were most likely passed the ballistic test under the NIJ standard level III, thus confirmed the potential of using FEA in predicting the ballistic performance of soda-lime glass/PVB film laminates.

Furthermore, the results also revealed that the G1 thickness of at least 15 mm was required to totally destroy the bullet in the G1 layer. However, in the case of B19, due the thin G1 of 12-mm, the thick G2 layer of 19-mm must be required in order to completely stop the bullet in G2 and lower the energy dissipation to the below layers to be capable for bullet protection under NIJ standard level III.

Table 4.16 Ballistic damages of STD1, STD2, A19, B19 and A15 models in on the front side of G1 and back side of G6

Model Name	Front side	Back side	Bullet velocity (m/s)	NIJ level III result
STD1			833.92	Pass [64]
STD2			843.49	Pass [64]
A19	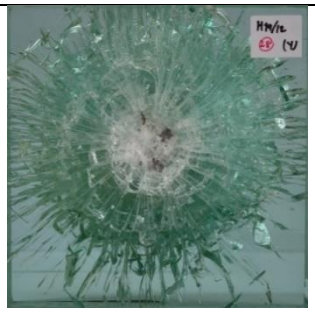		835.53	Pass [4]

B19	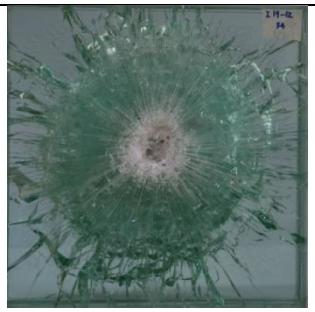		837.05	Pass [4]
A15			847.38	Pass [3]

จุฬาลงกรณ์มหาวิทยาลัย
Chulalongkorn University

4.2.2 Effect of PVB thickness and thick PVB ordering

From the previous section, A15 model was the thinnest target that could pass the ballistic test. Therefore, in this section, we studied the effect of PVB thickness and ordering in the modified A15 model. In some previously reported works[3,4], the effect of PVB film thickness and ordering played an important role in the ballistic protection performance. Therefore, in this study, the 0.76- and 1.52-mm thick PVB interlayer films were used at different ordering in A15 models as summarized in Table 3.12. The 3D-FEA technique was adopted to study the effect of PVP thickness or ordering to acquire the new laminated transparent armor design with the ballistic protection of the NIJ standard level III.

4.2.2.1 DOP and Crater diameter

The DOP, the layer that bullet stop and crater diameter of all models obtain from FEA were summarized in Table 4.17. By inserting thick PVB into the target, the DOP and crater diameter were increased in all models as compared to those in A15 model. The highest DOP was observed in A15-AllTP where the bullet could penetrate to G2.

Table 4.17 Depth of penetration, the layer that bullet stopped and crater diameter in all design configurations used in the study of PVB thickness/ordering effect

Model Name	DOP (mm)	Bullet stopped	Crater Diameter (mm)
A15	14.38	G1	28.04 ± 0.99
A15-1TP	15.13	G1/P1	30.11 ± 3.33
A15-2TP	15.59	G1/P1	30.48 ± 2.80
A15-3TP	14.84	G1	29.63 ± 3.02
A15-4TP	15.38	G1/P1	30.34 ± 2.48
A15-5TP	15.46	G1/P1	30.19 ± 2.63
A15-AllTP	16.56	G2	28.30 ± 3.23

4.2.2.2 Energy comparisons

1. Kinetic Energy and Internal Energy

The same velocity of bullet impact of 853 m/s was used in this study; therefore, the initial kinetic energy of the system was the same as those reported in the previous section. The kinetic energy in each glass layer at various thick-PVB film ordering was summarized in Figure 4.12. The highest kinetic energy was observed in G1 in all configurations, and similar trend of the change of kinetic energy from G1 to G6 were observed in all models except A15-AllTP. The kinetic energy of A15-AllTP showed a gradual declining from G1 to nearly zero in G6, while other models showed the relatively constant kinetic energy in G2-G4 layers. This might due to the deeper DOP of A15-AllTP, and the thick PVB might slow down the stress wave propagation and lead to the more gradual kinetic energy distribution through the layers below G1. However, the kinetic energy in each glass layer was considered negligible compared to that of internal energy in Figure 4.13. Therefore, we now proceeded to the internal energy analysis.

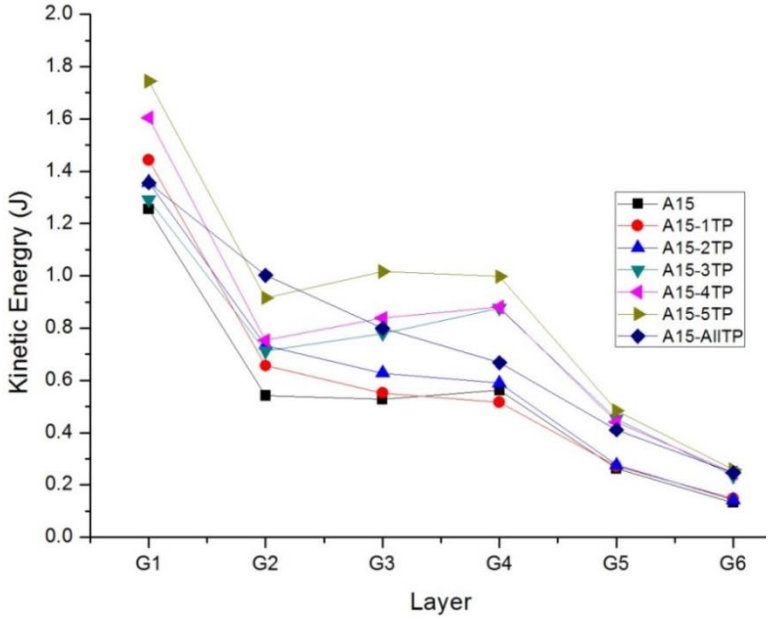

Figure 4.12 Kinetic energy distributions in each glass layer of all configurations used in the study of PVB thickness/ordering effect.

Figure 4.13 demonstrated the internal energy distribution in all layers. All models revealed the same pattern of internal energy distribution from G1 to G6. The IE was highest in G1 and drastically decreasing in P1 layer, which suggesting the highest deformation or stress energy accumulation in G1. The IE of G2 was only slightly higher than that of P1, and IE approached a constant value below G3 layer.

Table 4.18 IE distributions in all glass layers and PVB interlayers of all design configurations used in the study of PVB thickness/ordering effect.

Model name		Internal Energy (J)						
		A15	**A15-1TP**	**A15-2TP**	**A15-3TP**	**A15-4TP**	**A15-5TP**	**A15-AllTP**
Glass layer	**G1**	272.17	**280.64**	273.46	270.84	272.68	277.34	**284.31**
	G2	17.93	20.24	**21.24**	18.45	18.67	18.75	**20.20**
	G3	5.70	7.09	4.42	**7.88**	6.44	6.49	**5.90**
	G4	5.06	5.82	4.10	5.17	**5.52**	5.59	**6.06**
	G5	2.43	1.21	1.72	2.62	2.67	**1.66**	**2.37**
	G6	1.04	0.92	1.15	1.47	1.23	1.30	**1.06**
PVB layer	**P1**	9.37	**15.61**	9.36	9.74	9.23	10.05	**14.48**
	P2	1.04	0.99	**1.81**	0.98	0.98	1.21	**1.24**
	P3	0.70	0.61	0.74	**0.82**	0.53	0.60	**1.33**
	P4	0.40	0.43	0.59	0.36	**0.58**	0.30	**0.77**
	P5	0.25	0.20	0.26	0.34	0.27	**0.34**	**0.40**

จุฬาลงกรณ์มหาวิทยาลัย
Chulalongkorn University

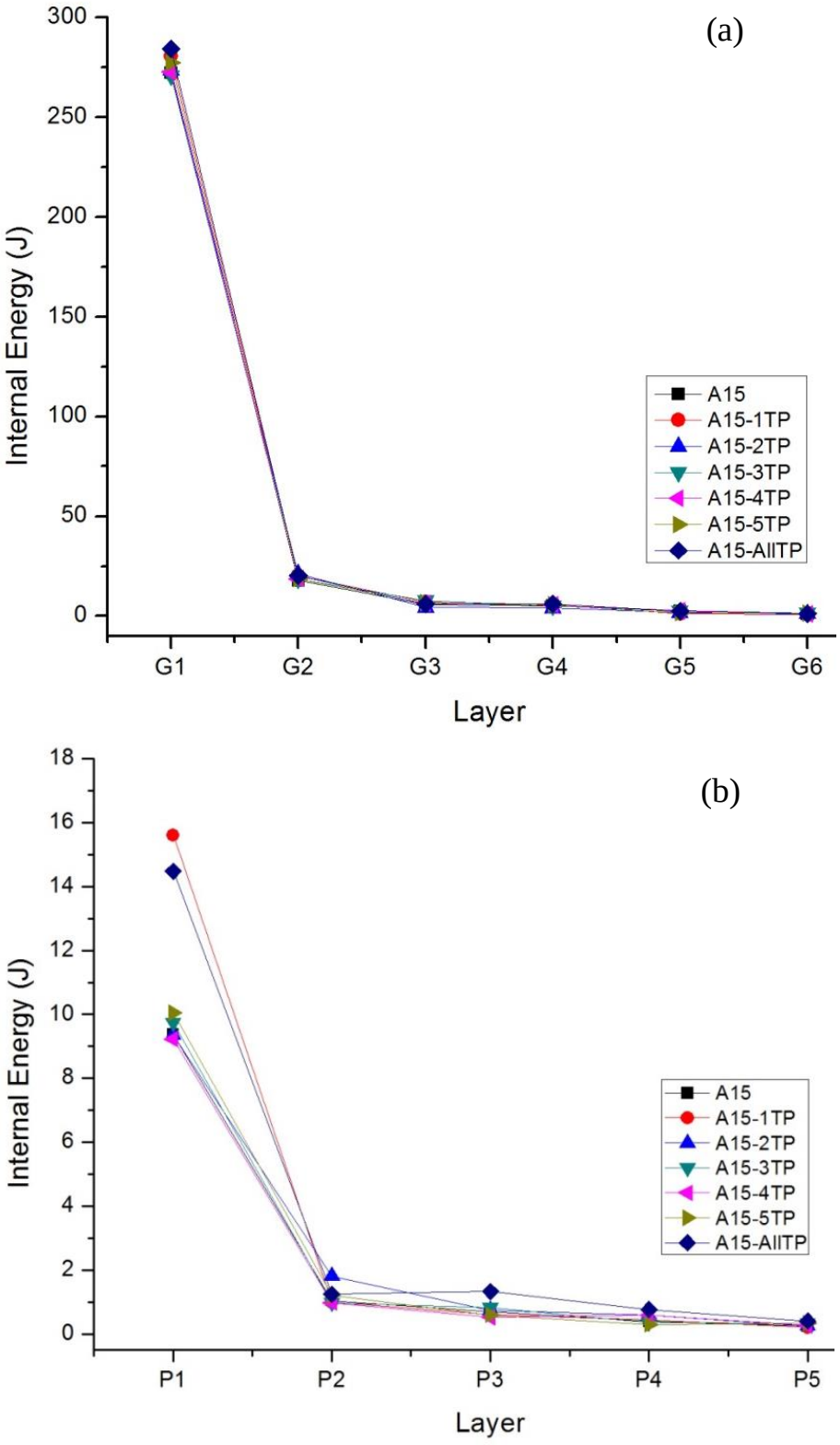

Figure 4.13 Internal energy distributions in (a) only glass layers and (b) only PVB interlayers of all design configurations used in the study of PVB thickness/ordering effect

By comparing the internal energy of glass and PVB interlayers separately as shown in Figure 4.13(b-c), the IEs of the glass layers in all models showed the same tendency. However, the IE distribution in P1 of A15-1TP and A15-AllTP models was considerably higher than other models. By excluding A15-AllTP, the highest IE on P1, P2, P3, P4 and P5 were observed in A15-1TP, A15-2TP, A15-3TP, A15-4TP (~A15-2TP), and A15-5TP (~A15-3TP), respectively. If the A15-AllTP model was included, the highest IE on P3, P4 and P5 were observed in A15-AllTP model. Comparing IE in the glass layers, similar trend was also observed. Without A15-AllTP, the highest IE on G1, G2, G3 were also observed in A15-1TP, A15-2TP, A15-3TP, respectively. However, for the highest IE on G4, G5, G6, no clear trend was found. Therefore, the glass layer above the thick PVB film trended to have higher IE accumulations than A15 model.

These results could confirm the role of thick PVB in the laminated structure that the thicker PVB layer could absorbed higher internal energy and thus contributed to the slightly different in IE distribution in glass layers. However the amounts of internal energy absorbed in PVB was not directly proportional to the PVB thickness. By comparing to A15, although the PVB thickness increased twice, the absorbed IE on the thick PVB was only slightly increased.

2. Normalized Internal Energy

As shown in Figure 4.14 (a), the NormIE of G1 to G6 showed the same distribution pattern as the IE plot discussed in the previous section because all models used the same glass thickness arrangement. However, the NormIE of P1 to P5 showed the opposite trend to those reported in the IE section (Figure 4.14). If excluding A15-AllTP, the lowest NormIE of P1, P2, P3, P4 and P5 were observed in A15-1TP, A15-2TP, A15-3TP, A15-4TP, A15-5TP, respectively. Thus, the thicker PVB contributed to the highest IE but the lowest NormIE distribution in that layer. As discussed earlier, the distribution of IE in PVB layer was not proportional to the volume of PVB films. Therefore, the result suggested that the increase in PVB thickness might assist the IE distribution into polymer layer but with the lower IE absorbed per unit volume.

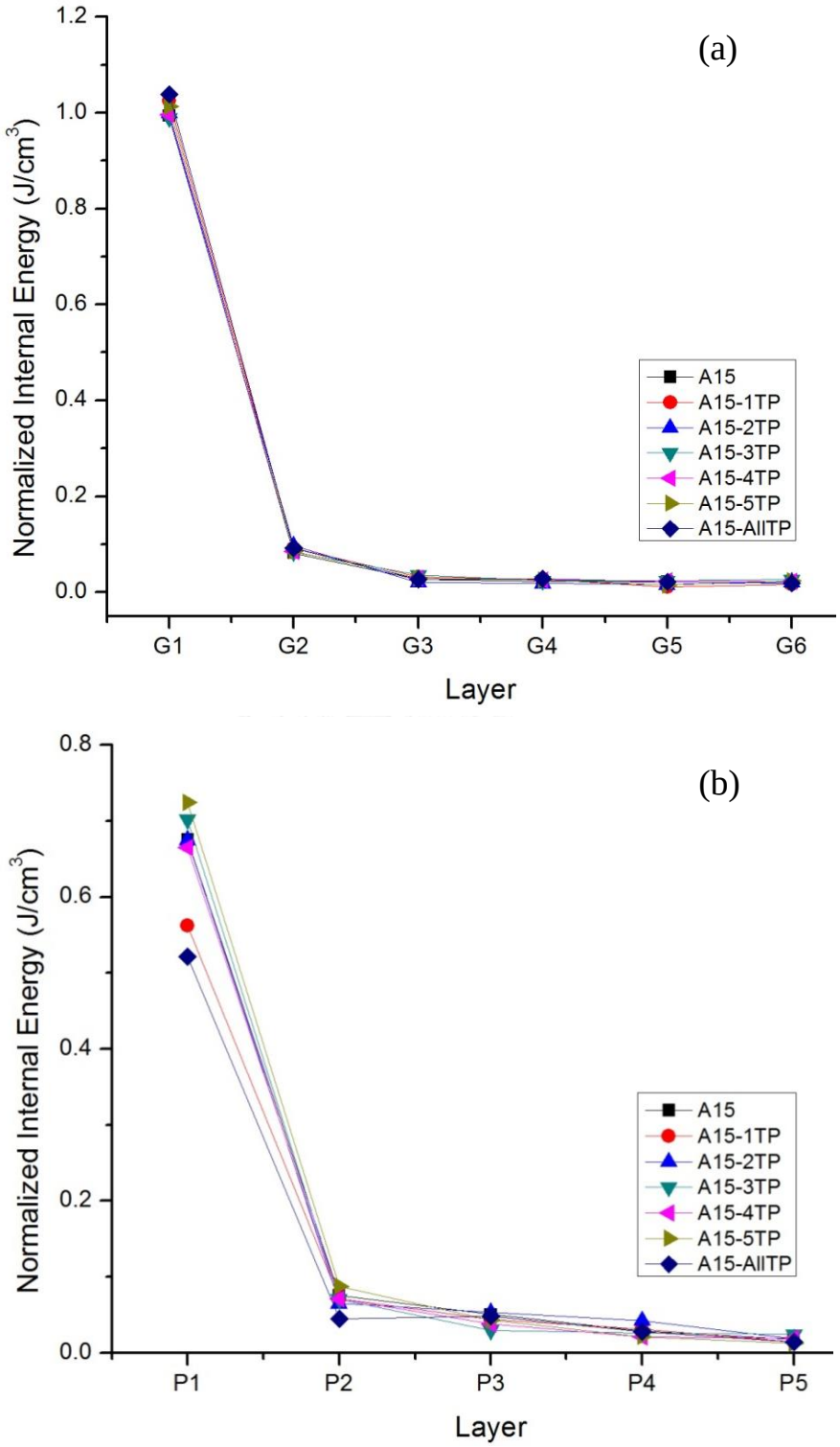

Figure 4.14 Normalized Internal energy distributions in (a) all glass layers and (b) all PVB interlayers for all configurations used in the study of PVB thickness/ordering effect.

Table 4.19 Normalized Internal energy distributions in all glass and PVB interlayers of all design configurations used in the study of PVB thickness/ordering effect.

Model name		Normalized Internal Energy (J/cm^3)						
		A15	A15-1TP	A15-2TP	A15-3TP	A15-4TP	A15-5TP	A15-AllTP
Glass layer	G1	0.99	**1.02**	1.00	0.99	1.00	1.01	**1.04**
	G2	0.08	0.09	**0.10**	0.08	0.09	0.09	**0.09**
	G3	0.03	0.03	0.02	**0.04**	0.03	0.03	**0.03**
	G4	0.02	0.03	0.02	0.02	**0.03**	0.03	**0.03**
	G5	0.02	0.01	0.02	0.02	0.02	**0.02**	**0.02**
	G6	0.02	0.02	0.02	0.03	0.02	0.02	**0.02**
PVB layer	P1	0.68	**0.56**	0.67	0.70	0.67	0.72	**0.52**
	P2	0.08	0.07	**0.07**	0.07	0.07	0.09	**0.04**
	P3	0.05	0.04	0.05	**0.03**	0.04	0.04	**0.05**
	P4	0.03	0.03	0.04	0.03	**0.02**	0.02	**0.03**
	P5	0.02	0.01	0.02	0.02	0.02	**0.01**	**0.01**

4.2.2.3 Volumetric Damage

The VD of all glass layers of each model was summarized in Table 4.20 and Figure 4.15. In most models the highest VD was observed on G1 which were in a good agreement with the observed IE in the previous section, except A15-3TP model had the highest VD on G3. The VD results in Figure 4.15 also revealed that wherever we added the thick PVB films, the adjacent glass layer above would show the higher VD to than the adjacent layer below. For example, in A15-1TP model, the thick PVB was inserted in P1, the VD in G1 was 6.292% which was higher than VD in G2 of 4.52%. In A15-3TP model, where the thick PVB layer was inserted in P3, the VD in G3 was also higher than the VD in G4. This might be due to the higher IE accumulation and slower stress wave propagation in the thick PVB leading to the lower energy transferred to the adjacent glass layer below. In case of A15-AllTP, since all interlayers were thick PVB, the gradual decrease of VD within glass laminates was observed. As shown in Table 4.20, the VDMax values revealed that the 93-98% of VD in G1 and G2 was in the damage level of 0.75-1.00; while the 86-90% of VD in G6 was in the high damage level for all models. According to the VDMax and VD from Section 4.2.1.3 and this section, in the next sections, the 85-90% of VD arose from the severe cracks would then be presumed.

Table 4.20 The VD and VDMax in all configurations used in the study of PVB thickness/ordering effect.

Model name	VD (%)						
	G1	G2	G3	G4	G5	G6	Average
STD1	4.18	7.28	2.30	2.16	2.72	**3.67**	**3.83**
STD2	4.25	7.73	2.64	2.15	2.81	**3.28**	**4.02**
A15	5.57	5.17	4.83	5.49	3.15	**2.73**	4.94
A15-1TP	**6.29**	4.52	5.33	5.44	2.42	**2.56**	5.00
A15-2TP	6.72	**5.55**	3.54	3.76	2.78	**2.68**	4.66
A15-3TP	5.68	4.67	**5.91**	4.62	4.47	**4.29**	5.02
A15-4TP	6.04	4.79	5.13	**4.78**	4.21	**3.77**	5.06
A15-5TP	5.59	4.78	5.46	5.00	**3.47**	4.35	5.01
A15-AllTP	**6.63**	**5.29**	**3.58**	**4.71**	**4.44**	**3.29**	4.98
Model name	**VDMax (%)**						
	G1	**G2**				**G6**	
A15	5.45	4.99				2.28	
A15-1TP	6.07	4.35				2.21	
A15-2TP	6.52	5.32				2.31	
A15-3TP	5.55	4.45				3.86	
A15-4TP	5.89	4.60				3.30	
A15-5TP	5.47	4.58				3.84	
A15-AllTP	6.43	4.92				2.86	

From Table 4.20 and Figure 4.15, the VD in G1 of all models could be arranged the following order: A15-2TP> A15-AllTP>A15-1TP > A15-4TP > A15-3TP > A15-5TP >A15. Also in Figure 4.15, the VD in G6 of all models was in the following decreasing order: A15-5TP > A15-3TP > A15-4TP > A15-AllTP > A15 > A15-2TP > A15-1TP, while the average VD was in the following order: A15-4TP > A15-3TP> A15-5TP > A15-1TP> A15-AllTP> A15> A15-2TP. These results thus revealed that the higher VD in G1 and G2 led to the lower VD in G6. Furthermore, by comparing to VD in G6 layers of STD1 and STD2, the results showed that A15, A15-1TP and A15-2TP models had the lower VD than those in STD1 and STD2 (for G6), while VD of G6 in A15-AllTP was slightly higher than STD2 but lower than STD1. The average VD in all models in this section was higher than those observed in STD1 and STD2 due to the lower total target thickness. Based on this result, the models that likely passed the ballistic test in the NIJ standard level III were A15, A15-1TP, A15-2TP and A15-AllTP.

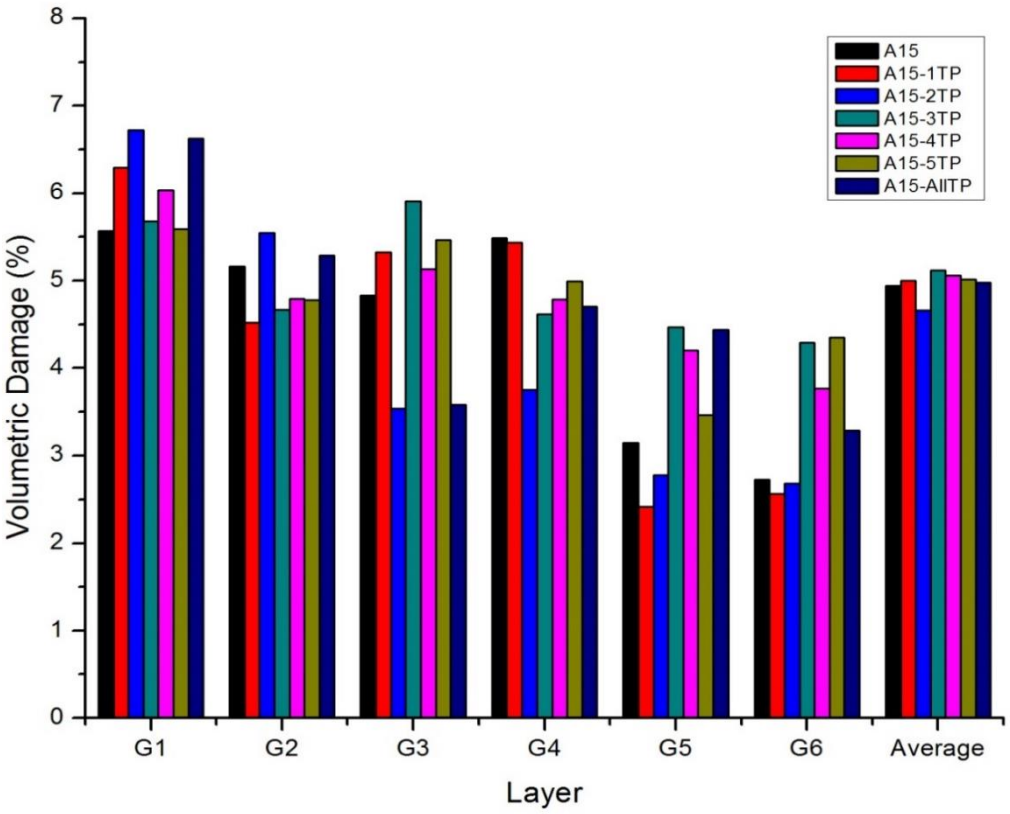

Figure 4.15 Summary of VD in all glass layers for all configurations used in the PVB thickness/ordering effect

As discussed in Section 4.2.1.2, the summation of internal energy in the top glass layers (G1 and G2) corresponded well with the VD in G6. The similar trend was also observed in this section as shown in Figure 4.16. If high IE was accumulated on the top glass layers, it was likely that lower VD in G6 should be observed. Thus, the high IE accumulations in the top layers of model A15-1TP, A15-2TP and A15-AllTP lead to the lower VD in G6 in all these models.

In conclusion, the thick PVB and ordering played an important role in the ballistic performance. The average VD in all models in this section were nearly the same, but the difference in VD in G6 (Figure 4.16(a)), and the summation of IE in top glass layers (Figure 4.16 (b)) could also be used as a criteria for selecting the high ballistic protection design. In this study, the higher ballistic performance of laminates structure was achieved when the damage propagation in glass laminates slowly down before reaching G3 layer. The thick PVB could eventually obstruct the damage propagation in the structure and increased the stress wave oscillation within the laminates by reflected the stress wave backwards to the above glass layer. Thus, A15-1TP, A15-2TP and A15-AllTP were likely passed the NIJ standard level III test. To further verify our FEA results, the laminates of all configurations studied in this section were fabricated Thai-German Specialty Glass Co., Ltd. and performed the ballistic testing under the NIJ standard level III. The FEA and experimental results were then compared in the next section.

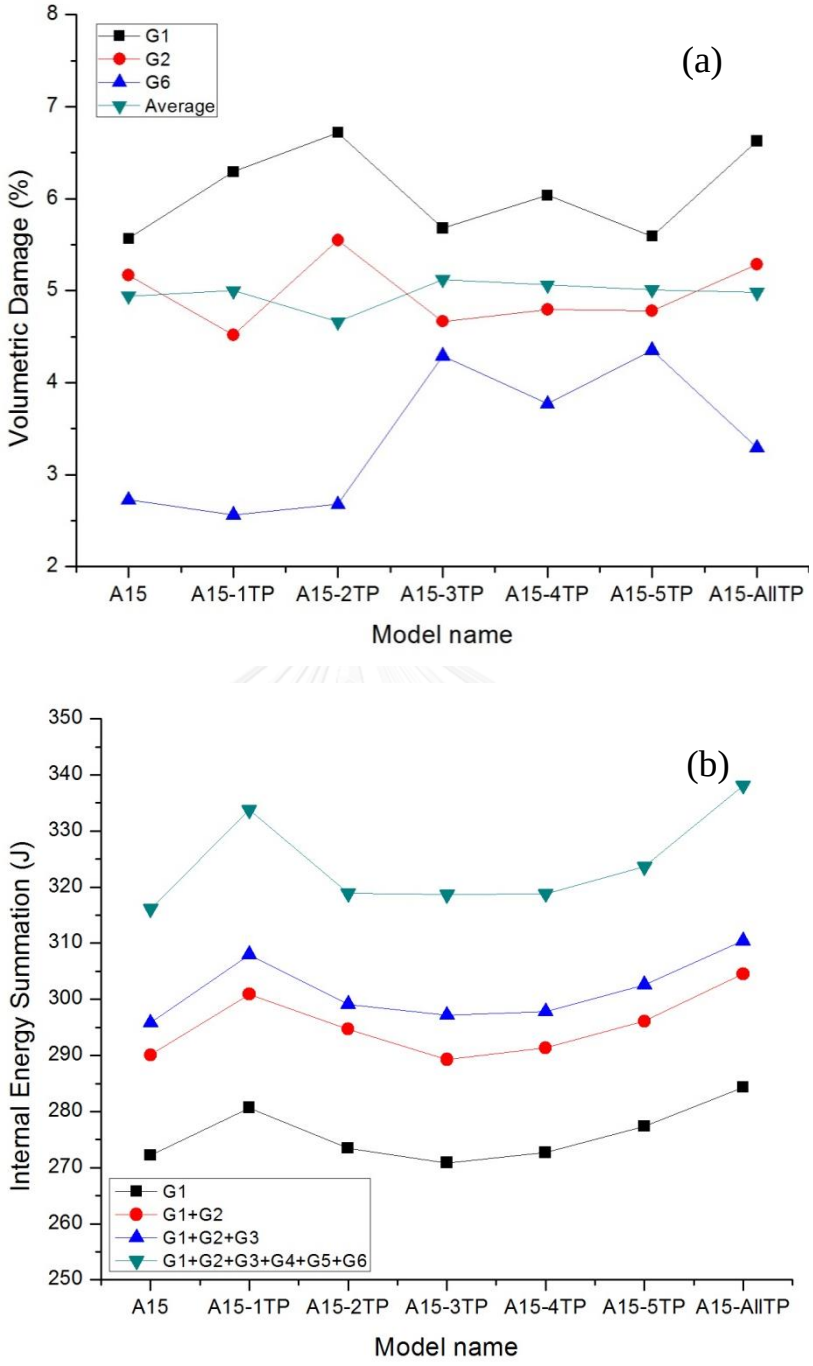

Figure 4.16 Comparison of (a) VD in G1, G2 and G6 and (b) summation of internal energy in glass layers for all design configurations used in the study of PVB thickness/ordering effect.

4.2.2.4 Comparison with Experimental Results

The DOP, the layer that bullet stopped and crater diameter of all models obtained from FEA and experiments were compared in Table 4.21. The FEA results revealed the good agreement with the DOPs and crater diameters.

Table 4.21 Depth of penetration and the layer that bullet stopped in design configurations of PVB thickness/ordering effect

Model name	Depth of Penetration (mm)		Bullet stopped		Crater Diameter (mm)	
	FEA	Expt	FEA	Expt	FEA	Expt
A15	14.38	13.50 ± 0.51	G1	G1	28.04 ± 0.99	30.59 ± 6.74
A15-1TP	15.13	14.47 ± 0.37	G1/P1	G1	30.11 ± 3.33	27.87 ± 2.42
A15-2TP	15.59	14.44 ± 0.36	G1/P1	G1	30.48 ± 2.80	27.44 ± 2.44
A15-3TP	14.84	14.43 ± 0.20	G1	G1	29.63 ± 3.02	29.89 ± 3.87
A15-4TP	15.38	15.95 ± 0.73	G1/P1	G1	30.34 ± 2.48	25.13 ± 5.11
A15-5TP	15.46	15.35 ± 0.90	G1/P1	G1/P1	30.19 ± 2.63	31.28 ± 3.41
A15-AllTP	16.56	14.76 ± 0.27	G2	G1	28.30 ± 3.23	27.88 ± 1.93

Remarks: *A15, A15-1TP, A15-2TP, A15-3TP, A15-4TP, A15-5TP and A15-AllTP models were tested by Jantharat* [3]

จุฬาลงกรณ์มหาวิทยาลัย

According to the experimental results, all models with thick PVB films showed higher DOPs and crater diameters than those of A15, which were in good agreement with the FEA results. However, the DOP variation observed in the experimental results, where A15-1TP, A15-2TP, A15-3TP and A15-AllTP showed lower DOP than those in A15-4TP and A15-5TP models were slightly different from those obtained from FEA.

According to Table 4.21, all models showed the Hertzian damage patterns but with various sizes of crater diameters as summarized in Table 4.19. By observing the back side of G6 of each model, A15-4TP and A-5TP models clearly showed the bulge out on the back of G6 with small pieces of glass fragments. The A15, A15-1TP, A15-2TP, A15-3TP and A15-AllTP model also showed the similar results, and only some dust of glass fragments on the back of G6 was observed.

Table 4.22 Ballistic damage of all configurations used in the study of PVB thickness/ordering effect.

Model Name	Front side	Back side	Bullet velocity (m/s)	NIJ level III result
A15			847.38	Pass (2) [3]
A15-1TP			843.26	Pass (2) [3]
A15-2TP	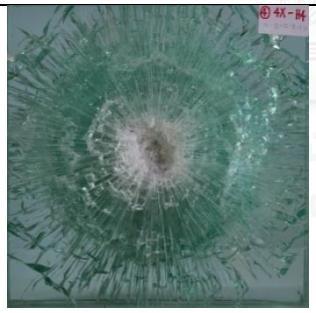	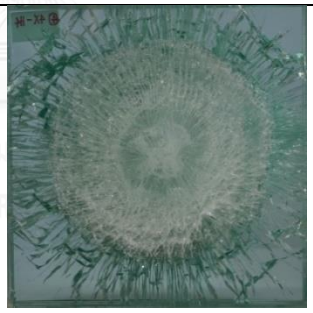	846.67	Pass (2) [3]
A15-3TP	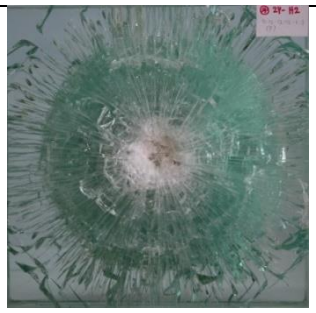		845.38	Pass (2) [3]

A15-4TP	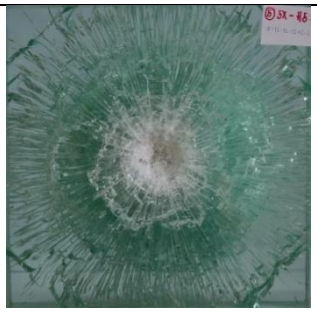	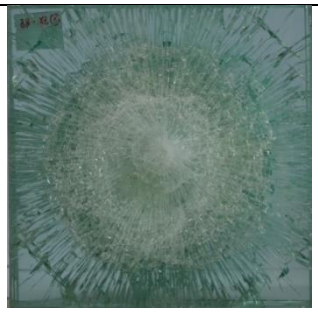	851.97	Fail (2) [3]
A15-5TP		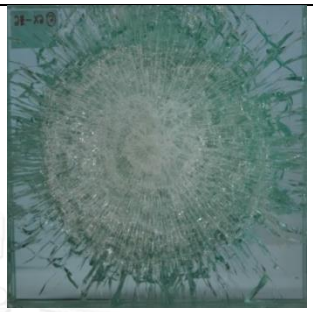	840.46	Fail (2) [3]
A15-AllTP			850.91	Pass (2) [3]

Hence, the models that passed the ballistic test in this section were A15, A15-1TP, A15-2TP, A15-3TP and A15-AllTP (Table 4.20). All models except A15-3TP showed the good agreement between FEA and experimental results, which also indicated that our FEA overestimated the damage of A15-3TP. The slight deviation from experimental results could arise from the limitation of the element size used in Lagrange calculation or the failure description of the PVB material model might still need some adjustment. However, the overall FEA results were still good enough for the prediction of the ballistic failure.

To design a lighter-weight laminates transparent armor, thick PVB films insertion could help in energy dissipation and slow down the stress wave propagation, but it might not be a necessary component for this A15 configuration. The thicker PVB films not only added the fabrication cost and weight to the target, it also did not show the significant better improvement toward to ballistic protection compared to A15 model. However, the thick PVB might be beneficial in other configurations, where the higher energy dissipation and slower stress wave propagation were essential. With the more insight understanding of the G1 thickness effect and thick PVB ordering effect, the optimization of the lighter-weight 6-layer soda-lime glass/PVB configurations was subsequently performed in the next section. The initial configurations for the

optimization would be starting from A19 and A15 configurations. The normal PVB thickness of 0.76 mm was initially employed in order to lower the total thickness of the armor.

4.3 Results of configuration optimization

In this section, we aimed to design a lighter-weight soda-lime/PVB laminated armor capable of ballistic protection under the NIJ standard level III. Since the total thickness of laminates was directly related to the overall weight of laminates, we aimed to design the lower-thickness armors by initially adapting A19 (67.8 mm) and A15 (63.8 mm) configurations into lower overall thickness of 61.8, 59.8, and 58.8 mm. The G1 thicknesses in all optimization studies were either 19 or 15 mm due to their high ballistic protection observed in the previous sections. The first part of this section will discuss the configurations with thickness of 61.8 mm (RT1 series), 59.8 mm (RT2 series) and 58.8 mm (RT3 series), followed by the addition of thick PVB film.

The summary of DOP, the layer bullets stopped and crater diameters of all models used in the configuration optimization studies with FEA technique was listed in Table 4.23. These results were then analyzed and discussed in the following energy analysis and the comparison with experimental sections.

จุฬาลงกรณ์มหาวิทยาลัย
Chulalongkorn University

Table 4.23 Depth of penetration, the layer that bullet stopped and crater diameter in all configurations used in the configuration optimization studies

Model Name	DOP (mm)	Bullet stopped	Crater Diameter (mm)
A19	13.93	G1	31.31 ± 4.58
A15	14.38	G1	28.04 ± 0.99
RT1 Series (Target thickness of 61.8 mm)			
RT1-1	10.45	G1	41.71 ± 8.92
RT1-2	11.08	G1	50.45 ± 5.92
RT2 Series (Target thickness of 59.8 mm)			
RT2-1	13.72	G1	36.28 ± 4.91
RT2-2	14.45	G2	39.61 ± 6.04
RT2-3	13.51	G1	37.01 ± 5.51
RT2-4	15.19	G2	33.24 ± 6.53
RT3 Series (Target thickness of 58.8 mm)			
RT3-1	11.61	G1	37.78 ± 6.45
RT3-2	15.72	G1/P1	37.60 ± 1.22
RT3-3	16.16	G2	39.65 ± 1.58
RT3-4	17.16	G2	39.63 ± 8.98
RT3-2 Thick PVB insertion			
RT3-2-1TP	16.60	G2	40.77±12.88
RT3-2-2TP	15.80	G2	40.21±10.73
RT3-2-3TP	12.90	G1	41.86 ± 2.56
RT3-2-AllTP	17.80	G2	38.05 ± 9.66

4.3.1 Results of RT1 series with the target thickness of 61.8 mm

Two configurations were considered in this RT1 series: (1) RT1-1 (19-12-10-8-6-3) and (2) RT1-2 (19-10-10-10-6-3). Both configurations had the same G1, G5 and G6 thicknesses while changing the G2-G3-G4 thicknesses and keeping the total thickness of these three layers to be at 30 mm. The internal energy and VD for all RT1 model series were then analyzed in the following sections.

4.3.1.1 Internal energy and normalized internal energy comparisons

The internal energy distribution of RT1 series were displayed in Table 4.24 and Figure 4.17. Both configurations show similar IE distribution pattern, which showed the maximum IE on G1 and drastically decreased in the glass and PVB layers below. RT1-2 showed slightly higher IE in G1 and lower IE in G6 than RT1-1. However, no significant difference in IE distribution in glass layers were observed in both configurations, which suggested that the variation in glass thickness in the G2-G4 layers did not significantly change the IE distribution in glass layers, but instead affected the IE distribution in PVB interlayers (Figure 4.17 (b)).

RT1-1 model showed higher IE accumulation in P1 but lower IE in other PVB layers than those of RT1-2 model. RT1-1 that have various intermediate glass layer thicknesses which could cause more variation in backward stress propagation compared to that of RT1-2. This could eventually cause the higher IE in P1 of RT1-1. The NormIE also showed the exact same distribution pattern as the IE results as shown in Figure 4.18.

Table 4.24 Internal energy in all glass layers and PVB interlayers of all configurations in RT1 series

Model name		Internal Energy (J)	
		RT1-1	RT1-2
Glass layer	G1	295.76	297.77
	G2	9.91	9.35
	G3	5.34	5.14
	G4	4.12	3.87
	G5	2.92	2.02
	G6	1.02	0.79
PVB layer	P1	4.66	1.64
	P2	0.77	1.07
	P3	0.60	0.83
	P4	0.41	0.47
	P5	0.26	0.24

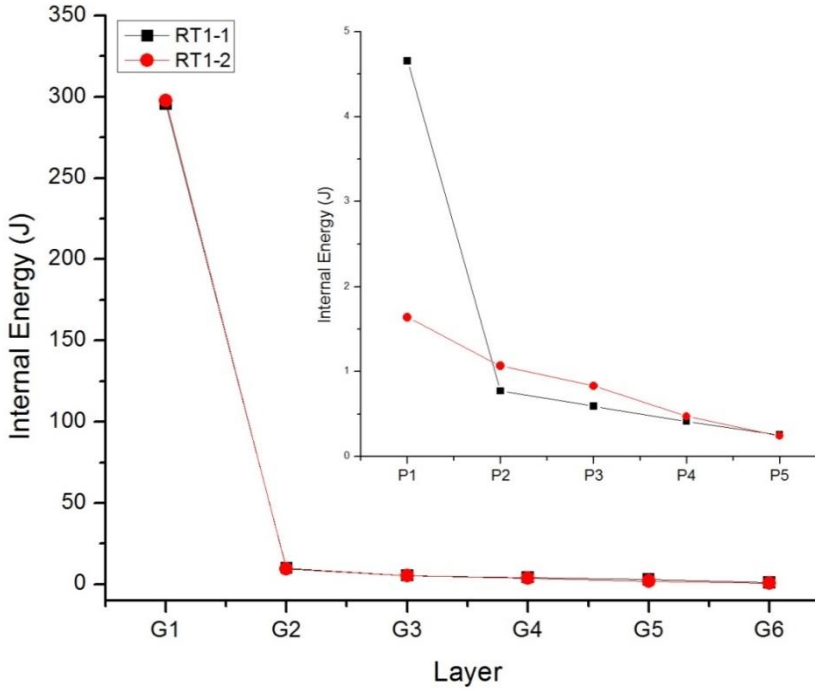

Figure 4.17 IE distributions in all glass layers (inset: IE distribution of only PVB layers) of all configurations in RT1 series.

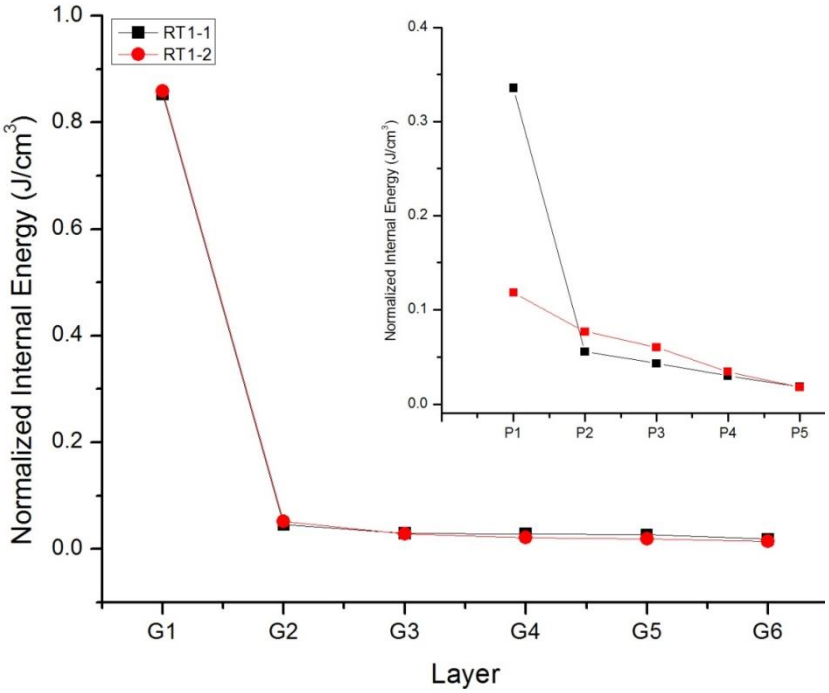

Figure 4.18 NormIE in all glass layers (inset: NormIE distribution of all PVB layers) of all configurations in RT1 series.

4.3.1.2 Volumetric Damage

The VD of RT1 series were summarized in Table 4.25 and Figure 4.19. The results showed that RT1-1 had relatively low VD variation in all glass layers, while RT1-2 showed higher VD variation especially in G1 layer. Despite the difference in glass thickness arrangement in G2-G4, their VDs were about the same in those layers. Instead, the difference in the G2-G4 configurations resulted in the higher VD in G1 and much lower VD in G6 of RT1-2 model (Figure 4.19). According to IE results, slightly higher IE accumulation in G1 and lower IE in G6 could indicate the higher VD in G1 and lower VD in G6 of RT1-2.

From Table 4.25, the VD comparison of RT1 series with STD1, STD2 and A19 models, the RT1-1 showed the average VD closed to STD1 and lower than STD2 and A19 models. Although VD in G6 was slightly higher than those of standard models, RT1-1 could still have high bullet protection capability and the high possibility of passing the ballistic test. On the contrary, RT1-2 showed the much lower VD in G6, while its average VD was higher than STD1, STD2, A19 and RT1-1. Thus, based on our criteria, RT1-2 also showed the high potential for the bullet protection and the capability of passing the ballistic test under the NIJ standard level III. As a result, the RT1-1 and RT1-2 were selected for the ballistic test under the NIJ standard level III to confirm the accuracy of our FEA prediction.

Table 4.25 Percentage of Volumetric Damage of all glass layer in all configurations RT1 series.

Model name	VD (%)						
	G1	G2	G3	G4	G5	G6	Average
STD1	4.18	**7.28**	2.30	**2.16**	2.72	**3.67**	**3.83**
STD2	4.25	**7.73**	2.64	**2.15**	2.81	**3.28**	**4.02**
A19	**5.50**	4.51	3.41	3.80	**2.83**	3.44	4.26
RT1-1	**3.71**	3.77	4.06	4.31	**4.76**	3.79	3.98
RT1-2	**6.52**	3.93	4.45	4.02	3.56	**2.58**	4.78

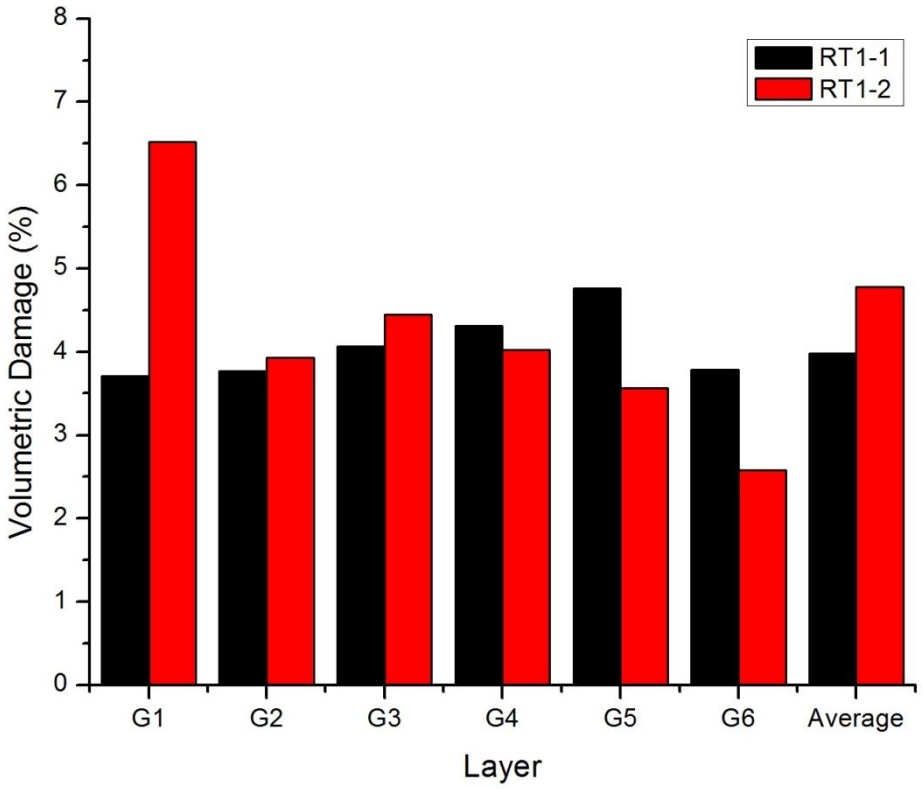

Figure 4.19 Volumetric damage distribution in all glass layers of all configurations in RT1 series.

4.3.2 Results of RT2 series with the target thickness of 59.8 mm

The total target thickness was aimed to be 59.8 mm in this section; therefore, the design of thinner configurations was adjusted based on the RT1-1 and RT1-2 models as followed: (i) RT2-1 (19-12-10-6-6-3) (ii) RT2-2 (12-19-10-6-6-3) (iii) RT2-3 (19-10-10-8-6-3) (iv) RT2-4 (10-19-10-8-6-3). The RT2-1 and RT2-3 models were adapted the same G1-G3 and G5-G6 configurations of RT1-1 and RT1-2 models with the lower G4 thicknesses. In RT2-2 and RT2-4 models, G1 and G2 were switched from RT2-1 and RT2-3, respectively, while keeping other layers the same. RT2-2 and RT2-4 models were used to verify the effect of thickest glass layer location (either as G1 and G2) on the ballistic protection performance.

4.3.2.1 Energy comparisons

1. Internal Energy

The IE distribution of RT2 series were shown in Figure 4.20(a-c) and Table 4.26. As expected, among all glass layers, the highest IE was observed in G1 and drastically decreased from G2 to the below layers (Figure 4.23a). Among the PVB interlayers, P1 also show the highest IE accumulation, while the IE in P2 to P5 was almost reaching the zero value (Figure 4.20(b)).

Table 4.26 Internal energy in all glass and PVB interlayers of all configurations in RT2 series

Model name		Internal Energy (J)			
		RT2-1	RT2-2	RT2-3	RT2-4
Glass layer	G1	292.28	229.73	312.10	181.20
	G2	8.89	41.39	9.11	97.48
	G3	4.91	7.22	5.40	6.08
	G4	4.10	4.11	4.74	2.04
	G5	3.26	2.22	2.38	1.10
	G6	1.00	0.72	0.82	0.75
PVB layer	P1	4.54	14.22	4.74	10.87
	P2	0.82	0.89	0.92	0.67
	P3	0.68	0.41	0.68	0.32
	P4	0.49	0.25	0.51	0.17
	P5	0.36	0.21	0.34	0.12

จุฬาลงกรณ์มหาวิทยาลัย
Chulalongkorn University

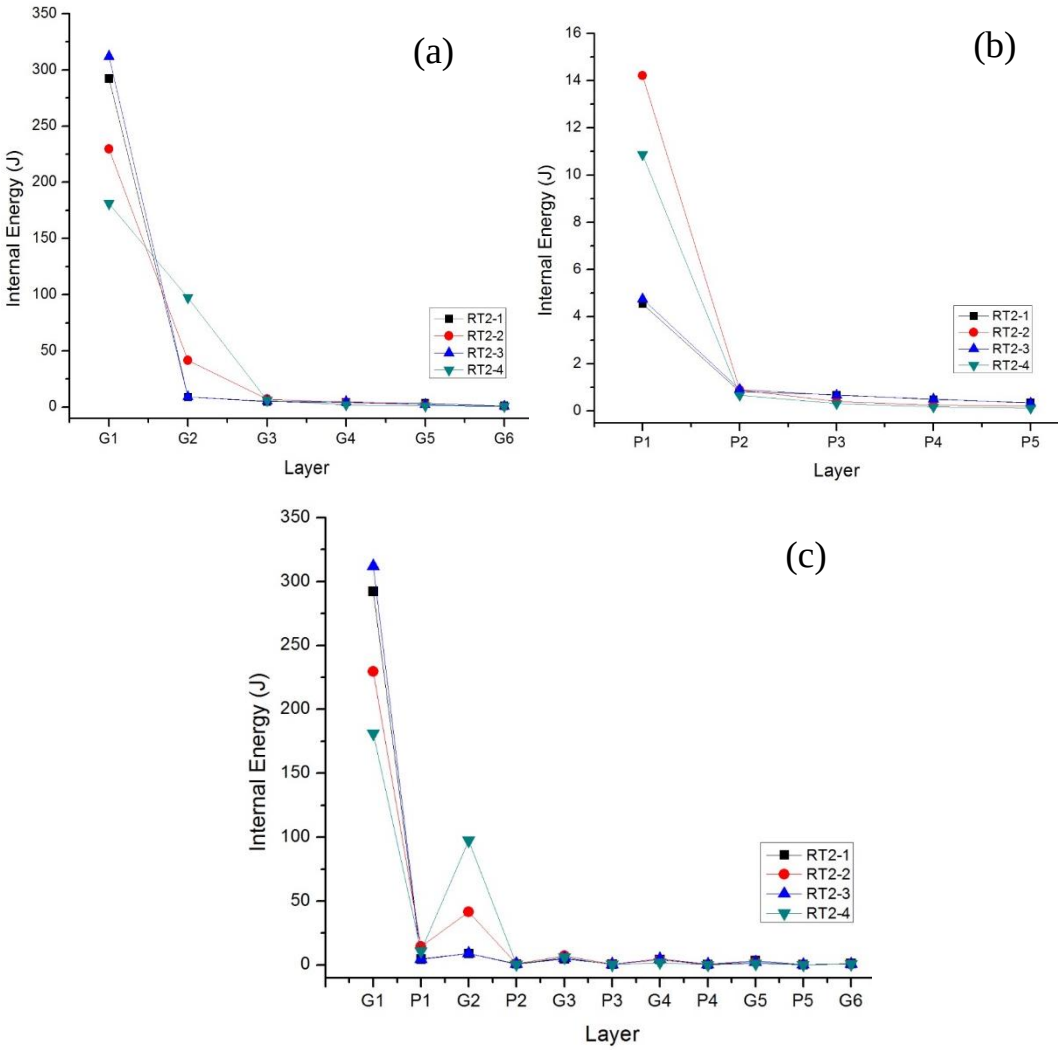

Chulalongkorn University

Figure 4.20 Internal energy distributions in (a) G1 to G6, (b) P1 to P5 and (c) all glass and PVB interlayers of all configurations in RT2 series.

The IE in G1 of RT2 series were decreased in the following order: RT2-3> RT2-1> RT2-2> RT2-4, while for IE in G2, the opposite trend of RT2-4 > RT2-2> RT2-3~RT2-1 was found. The results revealed that for RT2-1 and RT2-3 models (with 19-mm G1), the stress wave was mainly accumulated on G1 and gradually transferred to the below layers. However, for RT2-2 and RT2-4 models, due to the bullet penetration to G2 (Table 4.23), the kinetic energy of the bullet was directly transferred to G2 layer. Thus, the higher IEs in G2 of RT2-2 and RT2-4 than those of RT2-1 and RT2-3 models were observed.

2. Normalized Internal Energy

Since very low IE was observed in G3-G6 layers of RT2 series, NormIE of G1, G2 and P1 layers were analyzed and compared in this section. Figure 4.21 showed the NormIE in G1, G2 and P1 of RT2 series. The results showed that the NormIE was decreased in the following order: G1 > P1 > G2 in all models, and RT2-2 and RT2-4 showed the higher NormIE than RT2-1 and RT2-3 in all three layers. By comparing NormIEs of all three layers with those of RT1 series, the RT2-1 showed similar NormIE compared to RT1-1, while the rest of the RT2 models showed higher values than those in RT1 series.

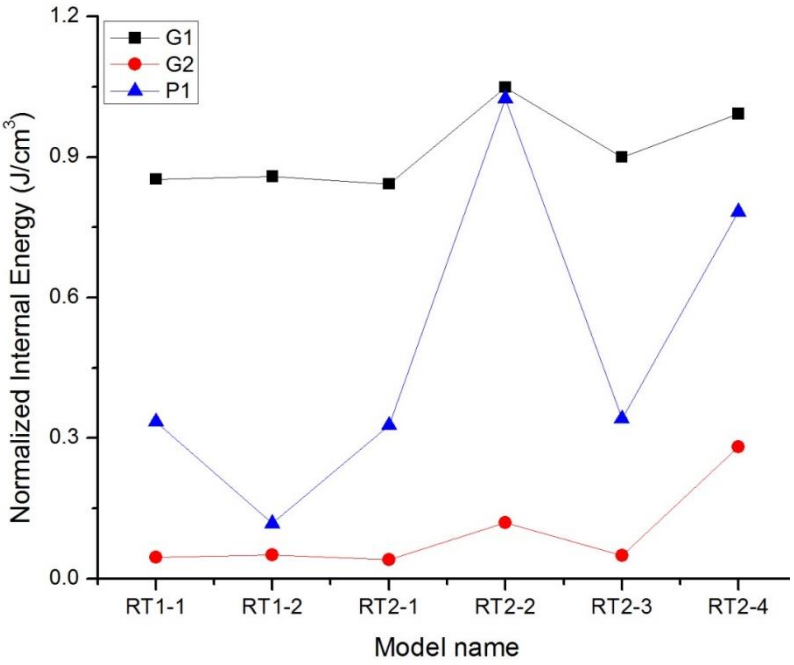

Chulalongkorn University

Figure 4.21 NormIE distributions in G1, G2 and P1 of all configurations in RT2 series.

4.3.2.2 Volumetric Damage

The VD in all layers of RT2 series were summarized in Table 4.27 and Figure 4.22. All RT2 configurations had the VD in G6 within the lower-upper bound of two standard models, but with much higher average VD compared to RT1 series and standard models, especially in RT2-2 model. Both RT2-1 and RT2-3 models showed the highest VD in G1 (their thickest glass layers), while the RT2-2, RT2-4 models with the thinner G1 of 12 and 10 mm, respectively, showed the highest VD in G2 and G3 layers with the higher VD variation. Due to their thin G1 layers, the high VD in G2 and G3 of RT2-2 and RT2-4 were caused by the bullet penetration into G2 layer. However, even though the higher VD in G2-G3 were observed in RT2-2 and RT2-4, the VD in G6 of all RT2 series were almost the same, suggesting the equivalent ballistic protection.

By comparing with standard models, all RT2 series showed much higher average VD, especially RT2-2 which showed very high average VD of 7.07% with the high VD in G2 and G3 due to high bullet penetration depth. The VDs in G6 in all RT2 models were lower than that of STD1, but higher than that of STD2. Therefore, the RT2-1, RT2-3 and RT2-4 models were chosen for ballistic testing.

Table 4.27 Percentage of Volumetric Damage of all glass layers in all configurations in RT2 series

Model name	VD (%)						
	G1	G2	G3	G4	G5	G6	Average
STD1	4.18	**7.28**	2.30	**2.16**	2.72	**3.67**	**3.83**
STD2	4.25	**7.73**	2.64	**2.15**	2.81	**3.28**	**4.02**
RT1-1	**3.71**	3.77	4.06	4.31	**4.76**	3.79	3.98
RT1-2	**6.52**	3.93	4.45	4.02	3.56	**2.58**	4.78
RT2-1	**5.63**	3.97	4.33	4.29	5.18	**3.36**	4.73
RT2-2	**2.98**	**10.55**	10.16	5.56	4.11	**3.19**	7.07
RT2-3	**6.54**	5.39	3.78	4.95	4.34	**3.10**	5.19
RT2-4	4.64	5.56	**7.61**	3.20	**2.59**	**3.03**	4.97

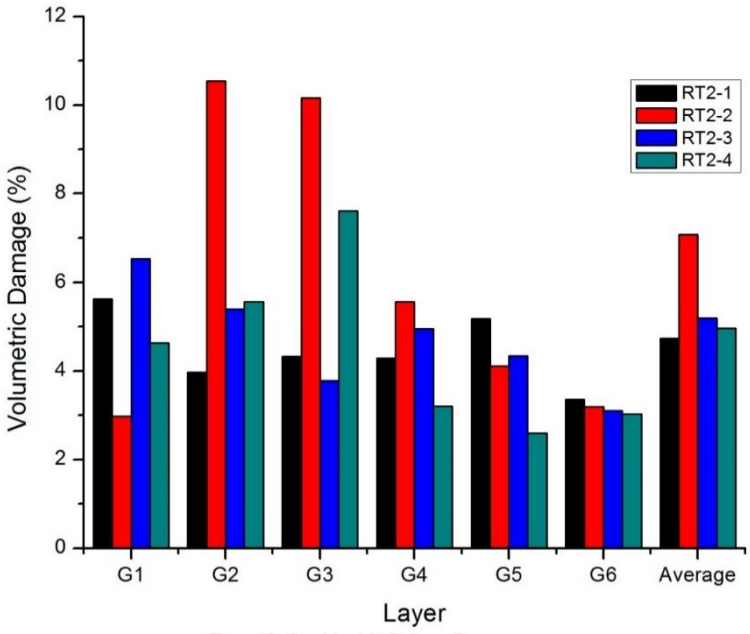

Figure 4.22 Volumetric Damage distribution in each glass layer of all configurations in RT2 series.

To study the effect of decreasing thickness from 61.8 to 59.8 mm, RT1 and RT2 series were compared (Figure 4.23-4.24). By decreasing G4 thickness from RT1-1 (19-12-10-8-6-3) model, RT2-1 (19-12-10-6-6-3) model showed higher VD in G1, G2, G3 and G5 and lower VD in G4 and G6 than those of RT1-1 (Figure 4.23). The thinner G4 could result in lower IE absorption capability leading to the backscatter of the stress wave and also the higher magnitude of stress wave transferred to G5 and G6. This in turn caused the VD scattered throughout the laminates mostly in the upper glass layer, and higher damage in G5. Similarly, by decreasing G4 thickness from RT1-2 (19-10-10-10-6-3), RT2-3 (19-10-10-8-6-3) model showed higher VD in all glass layers except G3 as shown in Figure 4.24. The thinner G4 in RT2 series thus resulted in higher damage in almost throughout the whole target.

In the next section, the target thickness was reduced to 58.8 mm. Due to the high average damage obtained from this series, we therefore did not proceed with the thickness reduction from this RT2 series. Since G1 and G2 layers were the most important layers to stop the bullet penetration and lower the magnitude of stress wave, the thick glass layers of 19-mm and 15-mm were used G1 and G2 in the next section.

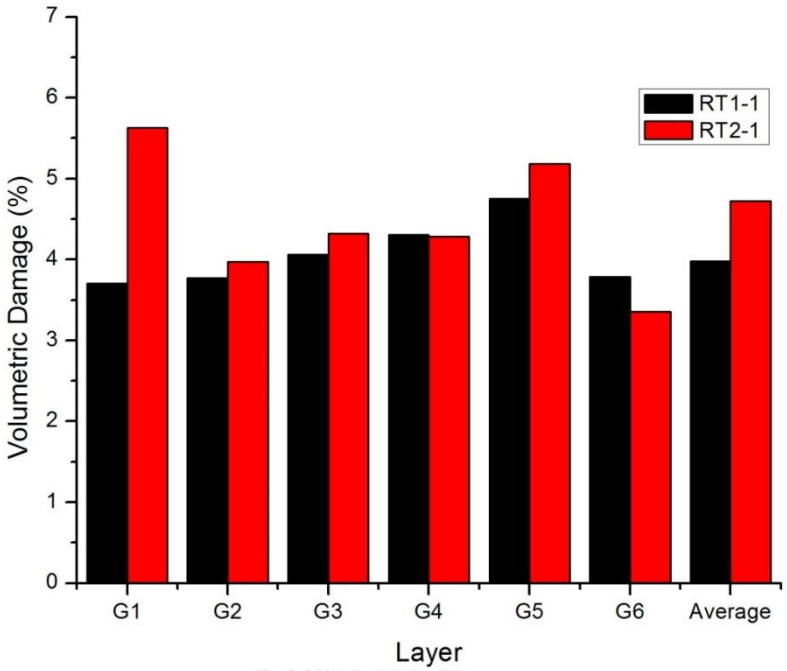

Figure 4 23 Volumetric Damage distribution in all glass layer of RT1-1 and RT2-1 model.

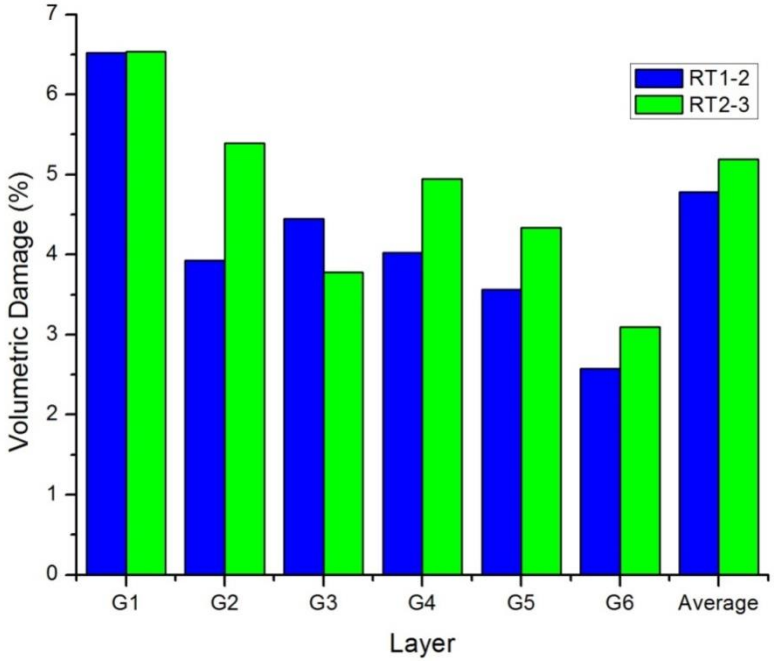

Figure 4.24 Volumetric Damage distribution in all glass layer of RT1-2 and RT2-3 model

4.3.3 Results of RT3 series with the total thickness of 58.8 mm

In this section, to further lower down the target thickness, we decided to use the top two layers with 19- and 15-mm thick glass, while the thickness of G3-G6 were 6 mm and 3 mm to reduce the wave propagation. According to RT1 and RT2 series, the high difference in glass thickness between the adjacent layers could backscatter the stress wave and sometimes lower the magnitude of stress wave propagation. Therefore, four configurations were considered in this RT3 series: (i) RT3-1 (19-15-6-6-6-3), (ii) RT3-2 (15-19-6-6-6-3) (iii) RT3-3 (15-6-19-6-6-3) and (iv) RT3-4 (15-6-6-19-6-3). The effect of thick (19-mm) glass position on the damage propagation was also studied in this section. The IE and VD for all RT3 model series were then analyzed in the following sections.

4.3.3.1 Energy comparisons

1. Internal Energy

The IE of all layers was showed in Figure 4.25 (a-b) and Table 4.28. Similar to the previous sections, the IE was highest in G1 in all configurations and drastically decreased in the below layers. However, among all RT3 series, only slight variation of IE in G1 was observed (Figure 4.25), which in turn suggested that the 15-mm and 19-mm G1 could accumulate about the same amount of IE energy from the impact. In our previous sections, the thick glass layer never positioned in G3 or G4, thus the noticeable variation in IE was observed mainly in G1 and G2. Interestingly, in this section, some apparent variations in IE were observed down to G6 in RT3-3 and G4 in RT3-4.

Table 4.28 Internal energy in all glass layers and PVB interlayers of all design configurations used in the study of RT3 series

Model name		Internal Energy (J)					
		RT2-1	RT2-3	RT3-1	RT3-2	RT3-3	RT3-4
Glass layer	G1	292.28	312.10	**301.18**	278.52	267.07	278.98
	G2	8.89	9.11	11.88	**19.60**	17.88	21.31
	G3	4.91	5.40	4.58	5.94	**10.73**	5.76
	G4	4.10	4.74	4.78	2.94	4.15	**10.07**
	G5	3.26	2.38	2.85	2.07	3.24	3.32
	G6	1.00	0.82	1.04	0.66	10.73	1.66
PVB layer	P1	4.54	4.74	**4.69**	8.91	8.78	10.33
	P2	0.82	0.92	0.83	**0.63**	2.43	3.00
	P3	0.68	0.68	0.70	0.54	**0.84**	1.20
	P4	0.49	0.51	0.48	0.30	0.52	**0.90**
	P5	0.36	0.34	0.38	0.24	0.45	0.72

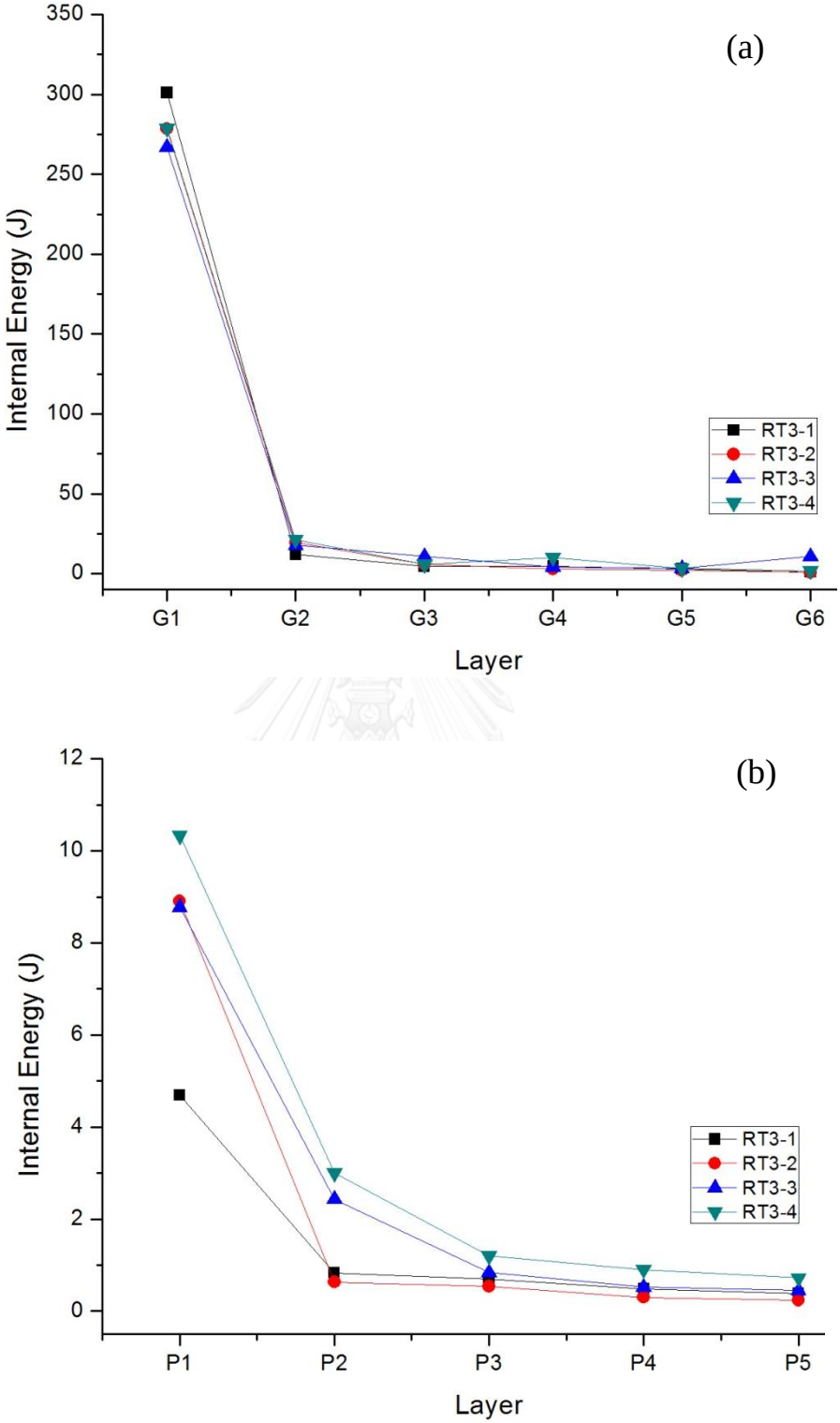

Figure 4.25 Internal Energy distributions in (a) G1 to G6 and (b) P1 to P5 of all configurations in RT3 series

RT3-1 and RT3-2 showed similar IE distribution with only slightly difference of the VD in G1 and G2, thus suggesting that the switching between 19-mm and 15-mm glass layers in G1 and G2 did not significantly change the pattern of stress wave propagation. On the contrary, RT3-3 and RT3-4 showed different IE distribution from RT3-1 and RT3-2. If considering only IE in G3, the highest IE was observed in RT3-3 (15-6-19-6-6-3), while for IE in G4, the highest IE was observed in RT3-4 (15-6-6-19-6-3). The result thus revealed that because of the high difference in the 19-mm and 6-mm adjacent glass layers, the IE seemed to accumulate in the thicker layer from the backscatter of stress wave due to the low IE absorption capacity in the 6-mm glass as discussed earlier.

The higher bullet penetration depth in both RT3-3 and RT3-4 also led to more IE transferred to the layers below G2. As the result, the higher IE value was observed in G3 and G4 of RT3-3 and RT3-4 models, respectively. From Figure 4.26, the RT3-3 model showed very highest IE in G6 potentially due to the very low internal energy uptake in the G1-G3 layers. RT3-4 and RT3-3 also showed the higher IE in all PVB layers than those in RT3-1 and RT3-2. This was likely due to the deeper penetration of bullet and the higher IE distribution to the below layers, where the 19-mm glass located. Furthermore, the IEs in P1 and P2 were significantly increased as 19-mm glass layers moved toward G2-G4 layers.

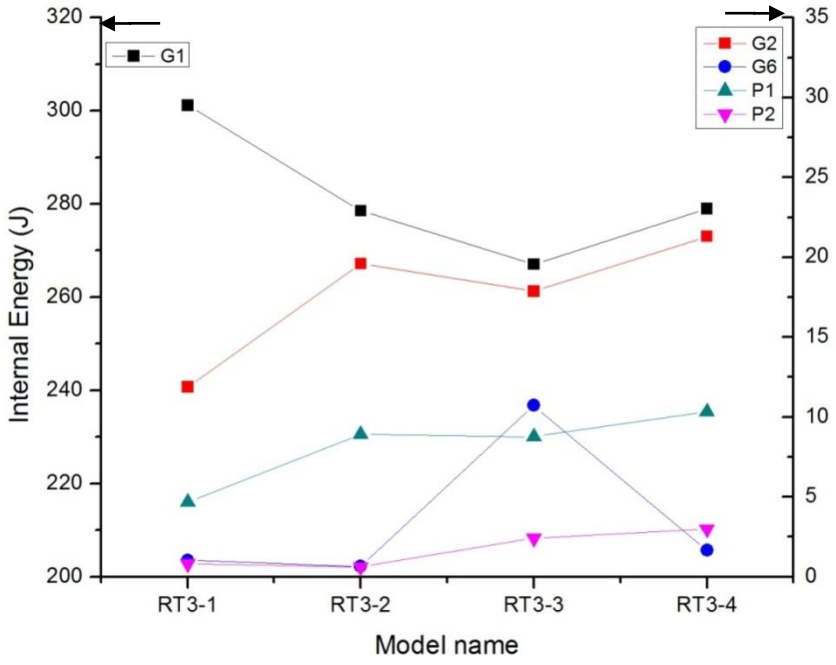

Figure 4.26 Internal Energy distributions in G1, G2, G6, P1 and P2 of all configurations in RT3 series.

2. Normalized Internal Energy

According to Table 4.29, the NormIE in G1 of all models were similar, except RT3-1 showed slightly lower value due to its higher volume of G1 compared to the other three models. RT3-3 and RT3-4 showed higher NormIE in G2 than those of RT3-1 and RT3-2 due to their low G2 thickness of 6 mm. with the low G2 thickness, the IE was accumulated with much higher energy density than using the 15-mm or 19-mm thick glass as in RT3-1 and RT3-2, respectively. Considering NormIE in P1, the significantly lower NormIE in P1 was observed in RT3-1. This arose from the 19-mm G1 of RT3-1 absorbed higher IE and only transferred lower IE to P1 below compared to the other RT3 models; other PVB layers did not show any significant difference in NormIE among the four models.

Table 4.29 Normalized Internal Energy in all glass layers and PVB interlayers of all configurations used in the study of RT3 series

Model name		Normalized Internal Energy (J/cm^3)			
		RT3-1	RT3-2	RT3-3	RT3-4
Glass layer	G1	0.87	1.02	0.98	1.02
	G2	0.04	0.06	0.16	0.19
	G3	0.04	0.05	0.03	0.05
	G4	0.04	0.03	0.04	0.03
	G5	0.03	0.02	0.03	0.03
	G6	0.02	0.01	0.20	0.03
PVB layer	P1	0.34	0.64	0.63	0.74
	P2	0.06	0.05	0.18	0.22
	P3	0.05	0.04	0.06	0.09
	P4	0.03	0.02	0.04	0.06
	P5	0.03	0.02	0.03	0.05

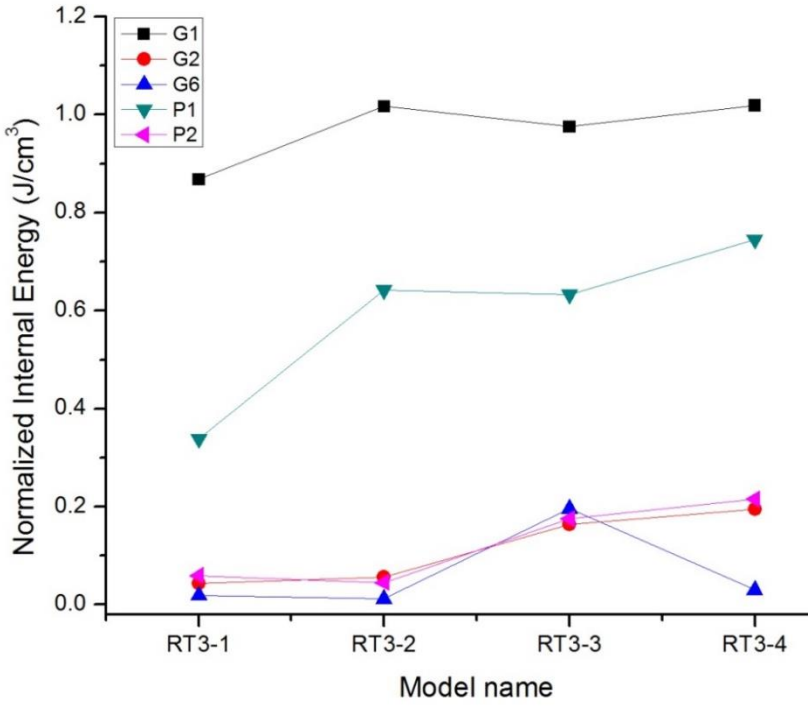

Figure 4.27 Normalized internal energy distributions in G1, G2, G6, P1 and P2 of all configurations in RT3 series

4.3.3.2 Volumetric Damage

The VD of all models in RT3 series was shown in Table 4.30 and Figure 4.28. Most models had relatively similar VD in G1 and G6, while the damage in G2 to G5 showed some interesting trend. The RT3-1 and RT3-2 models, the 19-mm layer in G1 and G2, had the highest damage in G4 and G3, respectively. Both RT3-3 and RT3-4 with the 19-mm layer placed in G3 and G4 had the highest damage in G2 due to the high bullet penetration. This trend thus suggested that the damage in RT3-1 and RT3-2 models mainly caused by the stress propagation, while in RT3-3 and RT3-4 caused by the bullet penetration.

In Table 4.30, the VD in G6 and average VD of RT3-1, RT3-3 and RT3-4 models were higher than those of standard models, thus suggesting that they might not pass the ballistic test. The highest VD in G6 was also observed in RT3-4 model, which also suggesting that using the 19-mm glass below G2 layers might not be as useful and this configuration might not be suitable for the bullet protection armor. Only RT3-2 showed the much lower VD in G6 than STD1 and STD2 models, as a result of the high G3 damage (the layer below the 19-mm glass) leading to the much lower VD in G6. Although RT3-2 might not pass the criteria due to high average VD and high VD in G3, the much lower VD in G6 highly encouraged us to select the RT3-2 model for the ballistic test.

Table 4.30 Percentage of Volumetric Damage of all glass layers in all configurations RT3 series

Model name	VD (%)						
	G1	G2	G3	G4	G5	G6	Average
STD1	4.18	**7.28**	2.30	**2.16**	2.72	**3.67**	**3.83**
STD2	4.25	**7.73**	2.64	**2.15**	2.81	**3.28**	**4.02**
RT2-1	**5.63**	3.97	4.33	4.29	5.18	**3.36**	4.73
RT3-1	**5.43**	3.84	5.91	7.29	5.09	4.08	5.14
RT3-2	5.55	**4.63**	9.10	5.60	3.96	**2.57**	5.29
RT3-3	5.75	5.89	**3.38**	5.82	5.15	4.04	4.80
RT3-4	6.65	8.32	3.86	**3.37**	4.35	4.86	5.66

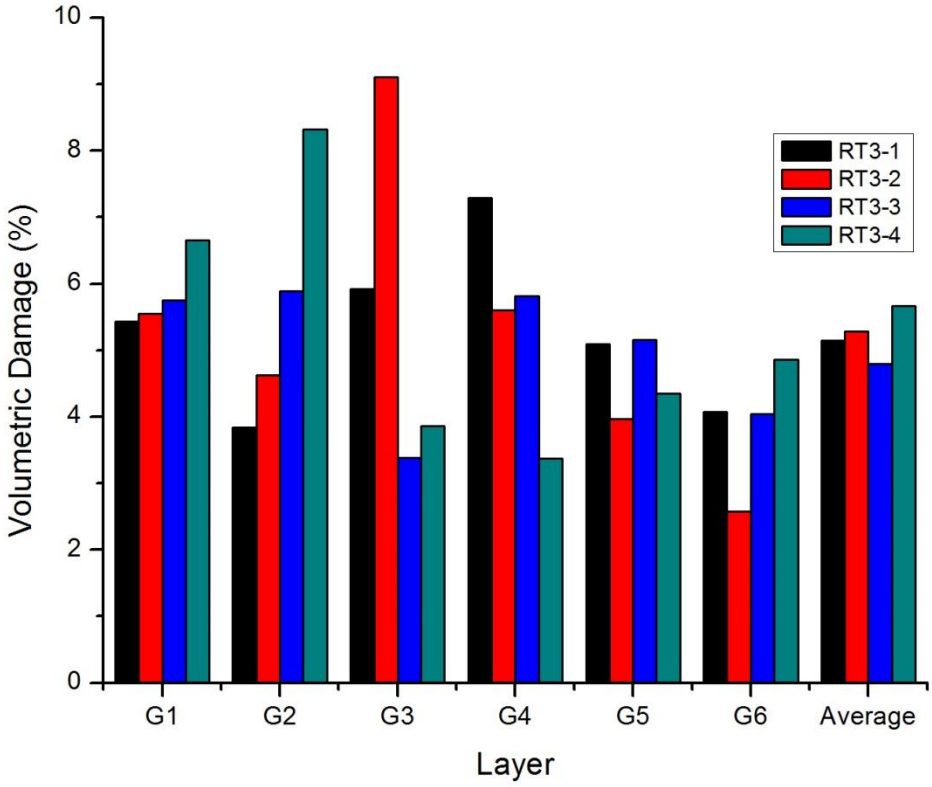

Figure 4.28 Volumetric damage in all glass layers of all configurations in RT3 series

4.3.3.3 Comparison with Experimental for RT1, RT2 and RT3 Series

According to FEA results of RT1, RT2 and RT3 series, the selected models for ballistic testing under NIJ standard level III were (i) RT1-1 (19-12-10-10-6-3), (ii) RT1-2 (19-10-10-10-6-3), (iii) RT2-1 (19-12-10-8-6-3), (iv) RT2-3 (19-10-10-8-6-3), (v) RT2-4 (10,19-10-8-6-3), and (vi) RT3-2 (15-19-6-6-6-3). The depth of penetration (DOP), layer that bullet stopped and crater diameter of all selected models compared with the experimental results were summarized in Table 4.31. The results revealed that the DOP and crater diameter results from FEA were underestimated in all models (except RT2-4 was overestimated and RT3-2 was correctly predicted). However, the layer that bullet stopped were matched with the experimental results in all models.

Table 4.31 Depth of penetration, the layer that bullet stopped and crater diameters of RT1, RT2 and RT3 series.

Model name	Depth of Penetration (mm)		Bullet stopped		Crater Diameter (mm)	
	FEA	Expt	FEA	Expt	FEA	Expt
RT1-1	10.45	16.71 ± 1.27	G1	G1	41.71 ± 8.92	48.65 ± 5.87
RT1-2	11.08	18.10 ± 0.70	G1	G1	50.45 ± 5.92	51.85 ± 3.33
RT2-1	13.72	20.23 ± 2.26	G1	G1/P1	36.28 ± 4.91	39.63 ± 3.17
RT2-3	13.51	18.11 ± 0.57	G1	G1	37.01 ± 5.51	53.83 ± 4.52
RT2-4	15.19	11.32 ± 0.08	G2	G2	33.24 ± 6.53	55.39 ± 3.48
RT3-2	15.72	15.36 ± 0.37	G1/P1	G1/P1	37.60 ± 1.22	36.47 ± 1.16

จุฬาลงกรณ์มหาวิทยาลัย
Chulalongkorn University

For RT1 series, both RT1-1 and RT1-2 models show the high G1 damage caused by the bullet impact. Both models also showed that the bullet could stop at the G1 layer. The crater diameter of RT1-2 was larger than RT1-1 model, which was in a very good agreement with our FEA results. The higher damage in G1 of RT1-2 than that of RT1-1 was also correlated well with the VD results in Section 4.3.1.2. Furthermore, the G6 of RT1-1 contained more cracks and some buckling on the back than RT1-2, which was also in a good agreement with our FEA results that showed the higher VD in G6 of RT1-1 than that of RT1-2. However, both RT1-1 and RT1-2 were successfully passed the ballistic test under NIJ standard level III.

For RT2 series, the crater diameter of RT2-1 was well predicted, while in RT2-3 and RT2-4 were much underestimated by FEA. The damage observation results were reported as medium-size fragments from the G6 of RT2-3 model. RT2-1 model demonstrated the ballistic damage on the rear plate as the tiny fragments, while RT2-4 showed the biggest crater diameter compared to other models in this testing with the medium to large size of glass fragments on the back of G6. As a result, no RT2 model series passed the ballistic test. According FEA results, our average VDs of all RT2

series were much higher than standard models. Therefore, our FEA model might slightly underestimated the VD in G6 of the models in this RT2 series.

For RT3 series, the RT3-1 and RT3-2 experimentally showed the opposite trend of DOP from FEA. RT3-2 was very well predicted by FEA in term of DOP, layer bullet stopped and crater size, while RT3-1 underestimated both DOP and crater size. The results of ballistic test on one of the RT3-2 samples showed some small glass fragment on the back of G6 with some clear cracks, while another sample show only glass dust with thinner cracks. Therefore, one sample of RT3-2 could pass the test, while the other sample failed. Nevertheless, the RT3-2 model could be used for further improvement in the next section.

Table 4.32 Ballistic damage of RT1-1 and RT1-2 model on the front side of G1 and the back side of G6.

Model Name	Front side	Back side	Bullet velocity (m/s)	NIJ level III result
RT1-1		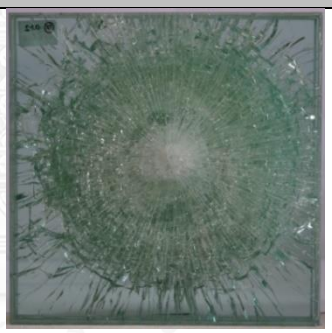	848.56	Pass [64]
RT1-2	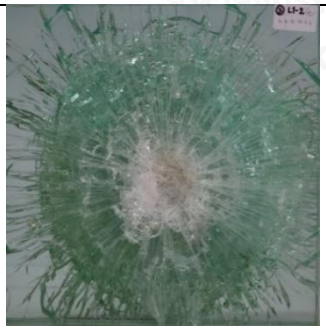	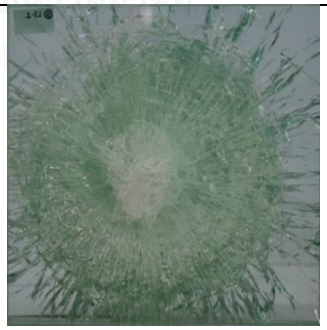	839.67	Pass [64]
RT2-1	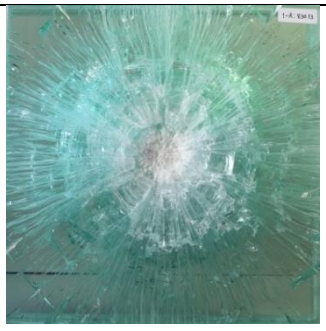		830.13 /835.4	Fail (2)

RT2-3		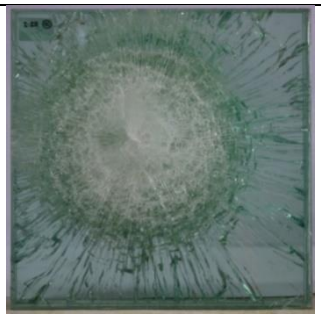	843.22	Fail [64]
RT2-4			840.49 /842.78	Fail (2)
RT3-2			844.96 /829.39	Pass (1) Fail (1)

จุฬาลงกรณ์มหาวิทยาลัย
Chulalongkorn University

4.3.4 Results of more design studies of RT3-2 Thick PVB insertion

According to Section 4.3.3, RT3-2 (15-19-6-6-6-3) had prone to the successful ballistic testing level III due to low VD6 estimated from FEA studies. The thin targets were damaged by both high impact together with the forward and backward stress propagation. Therefore, in this section, the 1.52-mm thick PVB was inserted into this target to slow down the stress wave propagation in both directions (as discussed before in Section 4.2.2) in order to improve the ballistic performance of RT3-2 model. According to Section 4.2.2 the thick PVB insertion was benefit while inserted in P1, P2, P3 or all layers; therefore in this study, four configurations were used in FEA studies:(i) RT3-2-1TP (15=19-6-6-6-3), (ii) RT3-2-2TP (15-19=6-6-6-3), (iii) RT3-2-3TP (15-19-6=6-6-3) and (iv) RT3-2-AllTP (15=19=6=6=6=3) (where "=" represented the position of thick PVB film).

4.3.4.1 Energy comparisons

1. Internal Energy

In Table 4.33 and Figure 4.29(a-b), the IE distribution in RT3-2, RT3-2-3TP and RT3-2-AllTP in G1 to G6 had the similar trend, with only slight variation in each layer; therefore, the thick PVB insertion did not cause the significant change in the internal energy dissipation in each glass layer. As compared to RT3-2 model, slightly lower IE in G1 was observed in the target after thick PVB insertion, and higher IE was observed on glass layer which was on top of the thick PVB as compared to RT3-2 model.

Considering IE in P1, all models with thick PVB showed higher IE in P1 as in the following order: RT3-2-1TP > RT3-2-AllTP > RT3-2-2TP > RT3-2-3TP > RT3-2. The slower wave propagation from the direct impact in thick P1 led to higher IE accumulation in the layer; therefore, the models with the thick PVB in P1 layers (RT3-2-1TP and RT3-2-AllTP) had difference in IE distribution in PVB layers. Other models had relatively the same as IE distribution as that of RT3-2.

Table 4.33 Internal energy in all glass and PVB interlayers of all configurations used in the study of RT3-2 thick PVB insertion.

Model name		Internal Energy (J)				
		RT3-2	**RT3-2-1TP**	**RT3-2-2TP**	**RT3-2-3TP**	**RT3-2-AllTP**
Glass layer	**G1**	278.52	**274.60**	271.13	277.09	267.26
	G2	19.60	18.33	**22.14**	19.57	22.68
	G3	5.94	3.67	4.09	**6.67**	4.65
	G4	2.94	3.85	2.82	3.17	**2.51**
	G5	2.07	2.04	2.95	2.63	1.55
	G6	0.66	1.11	1.23	0.75	0.79
PVB layer	**P1**	8.91	**13.96**	9.43	8.99	13.26
	P2	0.63	0.61	**0.86**	0.75	0.65
	P3	0.54	0.47	0.45	**0.88**	0.52
	P4	0.30	0.45	0.36	0.42	**0.42**
	P5	0.24	0.30	0.28	0.27	0.29

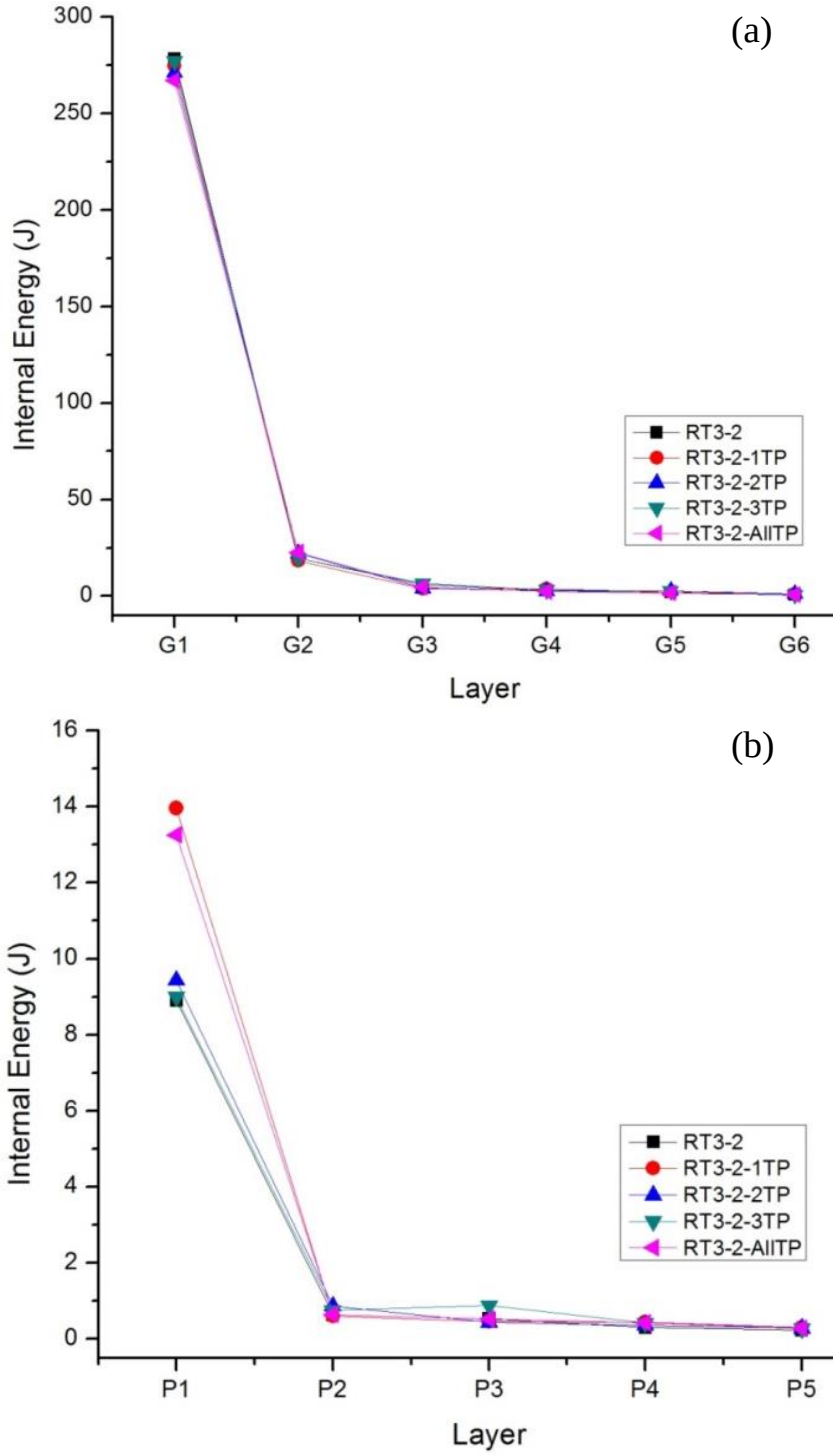

Figure 4.29 Internal energy distributions in (a) G1 to G6 and (b) P1 to P5 of all configurations of RT3-2 thick PVB insertion.

2. Normalized Internal Energy

Figure 4.30 showed the same NormIE distribution in glass layers as in IE, while slight deviation was observed in the NormIE in PVB layers. The thick PVB layers could lower the NormIE in the corresponding model, and as expected, the lowest NormIE of all PVB layers was observed in RT3-2-AllTP. This result implied that the thicker PVB insertion and ordering could affect the internal energy dissipation ability in the laminates.

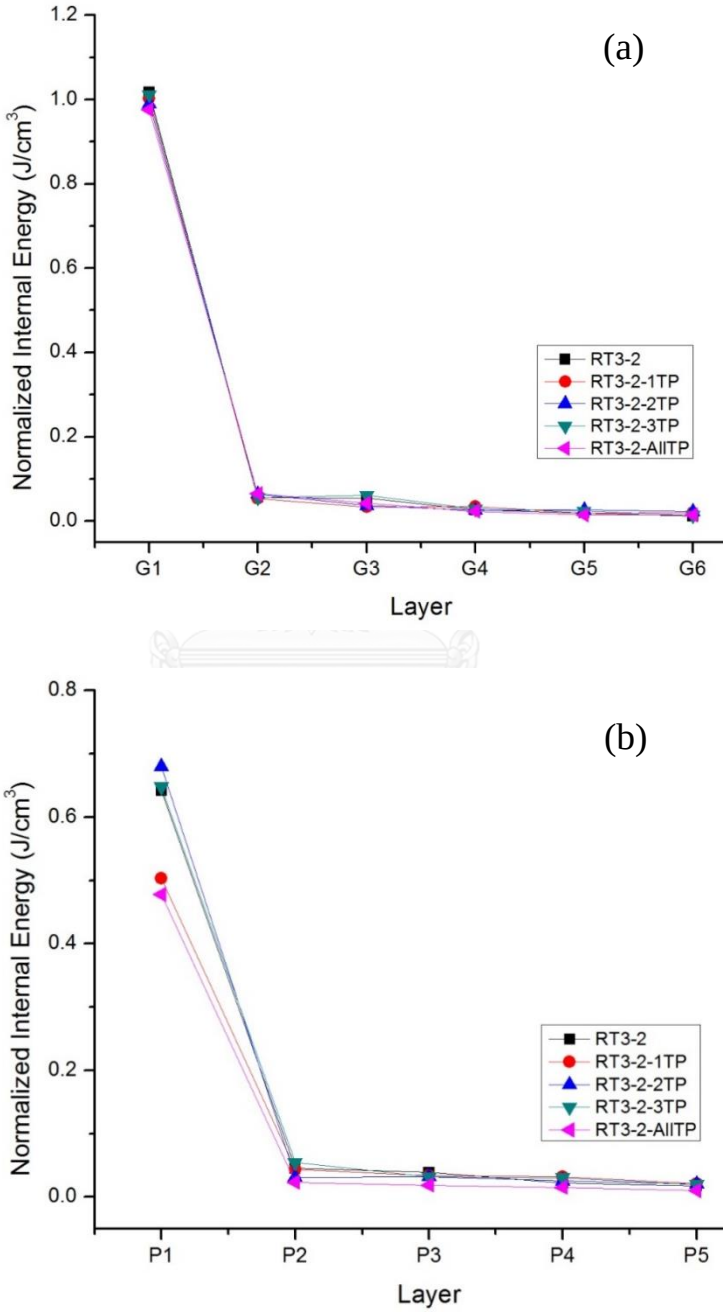

Figure 4.30 Normalized Internal Energy distributions in (a) G1 to G6 and (b) P1 to P5 of all configurations of RT3-2 thick PVB insertion

4.3.4.2 Volumetric Damage

The VD in the RT3-2-TP series was shown in Table 4.34 and Figure 4.31. As mentioned in Section 4.2.2, when thick PVB was inserted, the higher VD in the adjacent top glass layer was observed. The similar trend was also observed in this RT3-2-TP study. However, for this RT3-2-TP series, the insertion of PVB on the top layers (P1 and P2) could lower VD in G2-G3 layers but not in G4-G6. Therefore, for this thinner target, the thick PVB insertion in P1 and P2 (RT3-2-1TP and RT3-2-2TP models) could slow down IE from the impact causing higher VD in G1 and lower VD in G3 layer than RT3-2; however, the high magnitude stress wave could still propagate through the below layers causing higher VD in G6.

However, once the thick PVB were inserted in P3 or all layers (RT3-2-3TP and RT3-2-AllTP), the lower VD in G6 was observed. The highest VD of RT3-2-3TP was found in G3, which was similar to that of RT3-2. The RT3-2-AllTP had the highest VD in G1 and relatively high VD in G3; therefore, lower-magnitude and slower stress wave likely propagated to G6, causing lowest VD in G6 among other models in this series. This could imply that adding thick PVB could help slow down the stress wave dissipation within glass laminates; however, the suitable position of thick PVB insertion was dependent on the glass configurations. In conclusion, because the RT3-2-3TP and RT3-2-AllTP models showed the low average VD and the VD in G6 within the standard range, these two models were subsequently selected for the ballistic testing.

Table 4.34 Percentage of Volumetric Damage in all configurations of RT3-2 thick PVB insertion

Model name	%Volumetric Damage						
	G1	G2	G3	G4	G5	G6	Average
RT3-2	5.55	4.63	**9.10**	5.60	3.96	**2.57**	5.29
RT3-2-1TP	**7.11**	**3.82**	5.42	6.21	4.35	4.11	5.23
RT3-2-2TP	5.96	4.63	**6.19**	5.30	4.97	**4.50**	5.27
RT3-2-3TP	4.58	4.15	**9.30**	5.47	5.01	**3.28**	**5.02**
RT3-2-AllTP	**6.90**	4.55	6.29	4.40	2.67	**2.32**	5.04

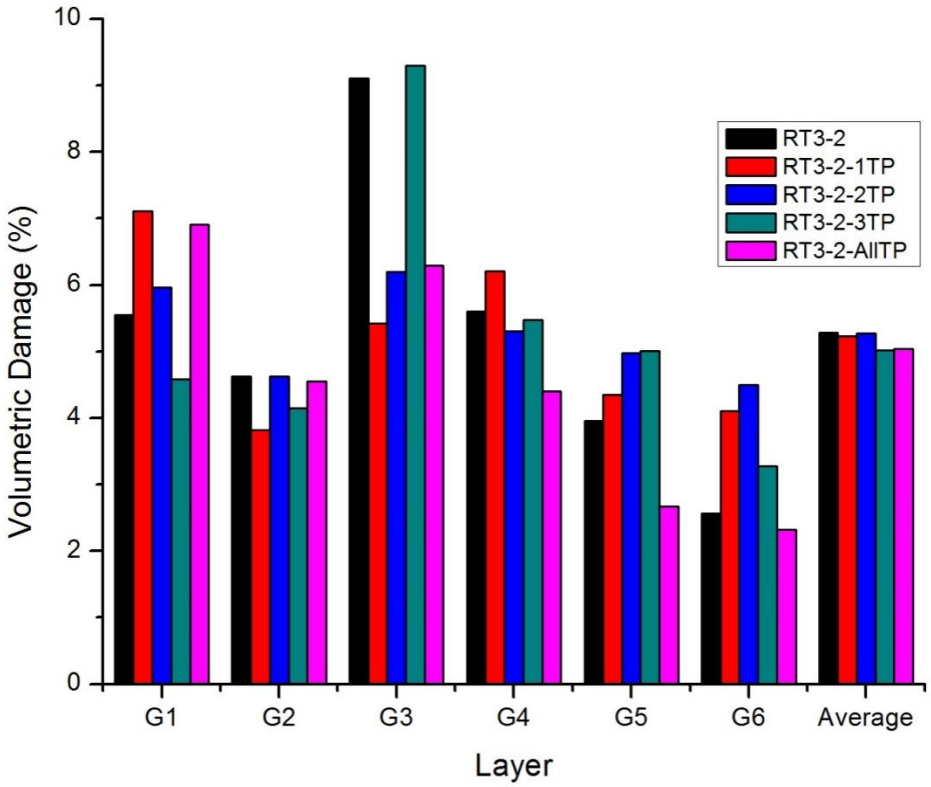

Figure 4.31 Volumetric damage in all glass layers of all configurations in RT3-2-TP series.

4.3.4.3 Comparison with Experimental

Table 4.35 showed both FEA and experimental results of DOP, the layer bullet stopped, and crater diameter for the RT3-2, RT3-2-3TP and RT3-2-AllTP. The FEA results of both models slightly underestimated the crater sizes. For DOP, RT3-2-3TP was slightly underestimated and RT3-2-AllTP was slightly overestimated from the experimental results. The RT3-2-3TP and RT3-2-AllTP in experiment showed the relatively similar ballistic protection performance.

Table 4.35 Depth of penetration, the layer that bullet stopped, and crater diameter of all configurations used in the RT3-2-TP series.

Model name	Depth of Penetration (mm)		Bullet stop		Crater Diameter (mm)	
	FEA	Expt	FEA	Expt	FEA	Expt
RT3-2	15.72	15.36 ± 0.37	G1/P1	G1/P1	37.60 ± 10.22	36.47 ± 1.16
RT3-2-3TP	12.90	15.03 ± 0.65	G1	G1/P1	41.86 ± 12.56	45.06 ± 1.80
RT3-2-AllTP	17.80	15.18 ± 0.58	G2	G1/P1	38.05 ± 9.66	42.23 ± 1.81

Table 4.36 Ballistic damage of RT3-2, RT3-2-3TP and RT3-2-AllTP model in the striking layer and back side of the rear plate.

Model Name	Front side	Back side	Bullet velocity (m/s)	NIJ level III result
RT3-2			844.96 /829.39	Pass (1) Fail (1)
RT3-2-3TP		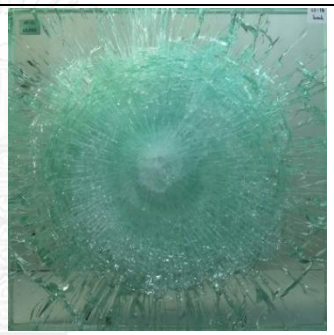	849.2 /849.52	Pass (2)
RT3-2-AllTP		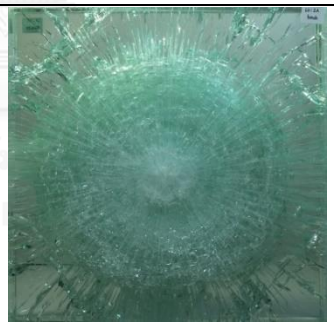	853.49 /851.31	Pass (2)

In Table 4.36 showed the front and back of RT3-2-TP target series after the ballistic testing under the NIJ standard level III. The RT3-2-3TP found no glass fragments or glass dust with only thin cracks on the back of G6. The RT3-2-AllTP showed the similar damage in G6 as RT3-2-3TP, but with the slightly smaller crater diameter. Therefore, both RT3-2-3TP and RT3-2-AllTP passed the ballistic test. Thus, in this study RT3-2-3TP was the model with the lowest thickness of 59.6 mm that could pass the ballistic test under the NIJ standard level III.

In summary, all selected configurations from RT1, RT2, RT3 and RT3-2-TP are listed in Table 4.37. Four out of eight configurations passed the ballistic testing under the NIJ standard level III with the lower total thickness and weight of soda-lime glass/PVB laminated transparent armor. The overall FEA results of damage prediction of all selected designs showed that in case of crater diameter and DOP, the FEA and experimental results were in the reasonable agreement. Furthermore, in most cases of using the VD in G6 and average VD for the prediction, the low VD in G6 together with low average VD within the range of standard models usually resulted in passing the ballistic test.

Some discrepancy of damage analysis between FEA and experimental results could be due to the limitation of the element size in our FEA setup. By using finer element size, the better stress and damage propagation could be obtained with the much higher computational time required. According to our results, the VD in G6 and average VD compared to standard models could be very helpful criteria for the design selections. However, for the better damage prediction, the meshing and some complex parameters in material models should be adjusted in more details to obtain the closest output to the experimental, while the higher performance of workstation to increase the computational capability should be taken into account.

From this study, we finally obtained the lightest-weight soda-lime glass/PVB laminated transparent armor under NIJ standard level III, which was RT3-2-3TP, with 13.62% in total weight reduction and 13.13% in total thickness reduction compared to the commercial STD2 model.

จุฬาลงกรณ์มหาวิทยาลัย
Chulalongkorn University

Table 4.37 All selected models for the ballistic testing under the NIJ standard level III.

Order assembly	Model Name							
	RT1-1	***RT1-2***	***RT2-1***	***RT2-3***	***RT2-4***	***RT3-2***	***RT3-2-3TP***	***RT3-2-AllTP***
G1	19	19	19	19	10	15	15	15
P1	0.76	0.76	0.76	0.76	0.76	0.76	0.76	**1.52**
G2	12	10	12	10	19	19	19	19
P2	0.76	0.76	0.76	0.76	0.76	0.76	0.76	**1.52**
G3	10	10	10	10	10	6	6	6
P3	0.76	0.76	0.76	0.76	0.76	0.76	1.52	**1.52**
G4	8	10	6	8	8	6	6	6
P4	0.76	0.76	0.76	0.76	0.76	0.76	0.76	**1.52**
G5	6	6	6	6	6	6	6	6
P5	0.76	0.76	0.76	0.76	0.76	0.76	0.76	**1.52**
G6	3	3	3	3	3	3	3	3
Total Thickness (mm)	**61.8**	**61.8**	**59.8**	**59.8**	**59.8**	**58.8**	**59.56**	**62.6**
%Reduced Thickness	**9.86**	**9.86**	**12.78**	**12.78**	**12.78**	**14.24**	**13.13**	**8.69**
Total Weight (kg)	**13.87**	**13.87**	**13.40**	**13.40**	**13.40**	**13.17**	**13.25**	**13.55**
%Reduced Weight	**9.58**	**9.58**	**12.65**	**12.65**	**12.65**	**14.15**	**13.62**	**11.67**
VD in G6	**3.79**	**2.58**	**3.83**	**3.10**	**3.03**	**2.57**	**3.28**	**2.32**
Average VD	**3.98**	**4.78**	**5.11**	**5.19**	**4.97**	**5.29**	**5.02**	**5.04**
VD in G6 of STD1	***3.67***							
VD in G6 of STD2	***3.28***							
Average VD of STD1	***3.83***							
Average VD of STD2	***4.02***							
Testing Results	**Pass**	**Pass**	**Fail**	**Fail**	**Fail**	**Fail**	**Pass**	**Pass**

CHAPTER 5

CONCLUSIONS AND RECOMMENDATIONS

5.1 Conclusions

In this study, ANSYS explicit STR® FEA software was used to design and estimate the ballistic performance for multiple configurations of soda-lime glass/PVB laminates. A model calibration was first performed to adjust the two significant parameters: (i) meshing and (ii) material models of the individual components. The most reasonable conditions identified for the T1, T2, STD1, STD2, A19 and B19 models are summarized in Table 5.1-5.2. These conditions showed reasonable Hertzian crack patterns and radial crack propagation as compared with the experimental results.

Table 5.1 Summary of the material models used for the soda-lime glass, PVB film and the 7.62 mm bullet.

Materials	Strength model	Equation of State	Failure model
Soda-lime glass	Johnson Holmquist 2	Polynomial	Johnson Holmquist 2
PVB interlayer	Johnson Cook	No	Principal Strain
Lead core	Johnson Cook	Shock linear	Johnson Cook
Copper alloy jacket			

จุฬาลงกรณ์มหาวิทยาลัย
Chulalongkorn University

Table 5.2 Summary of the modified parameters in the material models for soda-lime glass and the PVB film.

Materials	Parameters		Value
Soda-lime glass	JH-70	Hydrodynamic Tensile Limit/ T-Value (MPa)	-70
PVB interlayer	PVBJC4	Strain Rate Constant	0.0843
		Thermal Softening Exponent	0

The volumetric damage (VD) in the G6 layer and the average VD for the whole target, both from FEA, were compared with those of the STD1 and STD2 models and it was found that they could be used to judge the ballistic performance of the new configurations of lighter-weight soda-lime glass/PVB laminated transparent armor. From the effect of the striking layer glass thickness study, the A19 and A15 models had an average VD and VD in the G6 layer, that were within the acceptable range. The G1 layer of A15 (15-mm thick) had the highest internal energy (IE) absorption per unit

volume; while the G1 layer of A19 (19-mm thick) absorbed the highest IE but had the second highest IE per unit volume. Therefore, the striking glass thickness of 19 or 15 mm showed the highest performance in the A-series and passed the ballistic testing under the NIJ standard level III.

The effect of the PVB films thickness and ordering within the glass laminates structure were also investigated by FEA in the modified A15 model. The PVB film has the important role in adhesion between glass layers, after the damage propagation throughout the laminates system in the IE dissipation reduction by slow down the stress wave and crack propagations. However, for A15 configurations, only thick PVB insertion in P1, P2 and P3 could achieve the ballistic protection.

The configuration optimization was subsequently performed to reduce the total target thickness to 61.8, 59.8 and 58.8 mm, referred to as RT1, RT2 and RT3 series.

The RT1 series had a high tendency to pass the ballistic testing due to their relatively low average VD and VD in the G6 layer. Thus, both RT1-1 (19-12-10-8-6-3) and RT1-2 (19-10-10-10-6-3) passed the ballistic test under the NIJ standard level III.

The RT2 series adapted the glass configurations from the RT1 series by reducing the G4 layer thickness by 2 mm: RT2-1 (19-12-10-6-6-3) and RT2-3 (19-10-10-8-6-3). The results showed that this design concept could not pass the ballistic testing. Thus, this suggested that the RT1 configurations should not be used as a basic for further target thickness reduction. The switching of the G1 and G2 thickness for RT2-2 (12-19-10-8-6-3) and RT2-4 (10-19-10-8-6-3) did not help in the ballistic performance. Additionally, a much higher VD was observed, especially in RT2-2.

Therefore, in the RT3 series, the 19-mm and 15-mm thick glass layers were employed. Only RT3-2 (15-19-6-6-6-3) showed a much lower VD in the G6 layer, even though the average VD was higher than those of the standard models. One out of the two RT3-2 samples passed the ballistic testing under the NIJ level III standard. Finally, once the thick PVB film was inserted in P3 and all PVB layers of the RT3-2 configuration, it was found that the RT3-2-3TP and RT3-2-AllTP models successfully passed NIJ level III ballistic protection with a total target thickness reduction to 59.56 mm.

5.2 Recommendations for future work

Further material model parameter calibration should be performed to obtain more accurate or encompassing material characteristics under high-velocity impact loading. Due to the limitations of the available material data, an expanded literature review should be conducted or experiments should be designed to obtain the required data for both soda-lime glass and PVB material models. The FEA will be able to more accurately describe the damage propagation and energy accumulation in the target and will be an even more powerful tool for armor design optimization.

REFERENCES

[1] Grujicic, M., Bell, W. C. and Pandurangan, B. Design and material selection guidelines and strategies for transparent armor systems. Materials & Design 34(0) (2012): 808-819.

[2] Grujicic, M., Pandurangan, B. and d'Entremont, B. The role of adhesive in the ballistic/structural performance of ceramic/polymer–matrix composite hybrid armor. Materials & Design 41(0) (2012): 380-393.

[3] Jantharat, P. DEVELOPMENT AND PRODUCTION OF TRANSPARENT BULLET-PROOF ARMOR FOR LEVEL 3 PROTECTION UNDER NIJ STANDARD. Master of Science, Department of Materials Science chulalongkorn university. 2013.

[4] Chaichuenchob, C. BEHAVIORS OF CRACK DEVELOPMENT ON TRANSPARENT BULLET-PROOF ARMOR. Master of Science Program in Ceramic Technology, Department of Materials Science Chulalongkorn University. 2013.

[5] Antoine, G. O. and Batra, R. C. Optimization of transparent laminates for specific energy dissipation under low velocity impact using genetic algorithm. Composite Structures 124((2015): 29-34.

[6] Jalham, I. S. The Effect of Glass Plate Thickness and Type and Thickness of the Bonding Interlayer on the Mechanical Behavior of Laminated Glass. New Journal of Glass and Ceramics 01(02) (2011): 40-48.

[7] Grujicic, M., Pandurangan, B. and Coutris, N. A computational investigation of the multi-hit ballistic-protection performance of laminated transparent-armor systems. Journal of Materials Engineering and Performance 21(6) (2012): 837-848.

[8] Justice, N. I. o., Ballistic resistant protective materials 1985.

[9] Chaichuenchob, C., Aungkavattana, P. and Kochawattana, S. (2014). Crack evolution from ballistic threats in laminated glass. Key Engineering Materials. 608**:** 316-321.

[10] Kılıç, N., et al. Ballistic behavior of high hardness perforated armor plates against 7.62 mm armor piercing projectile. Materials & Design 63(0) (2014): 427-438.

[11] Ceralink, I. (2006). Transparent Ceramic Armor, Polaris Mediaworks

[12] LTD., G. (2015). Soda-lime glass sheet, Glasstime LTD.

[13] Tim J. Holmquist, Gordon R. Johnson, Dennis E. Grady and Jr., C. M. L. a. E. S. H. HIGH STRAIN RATE PROPERTIES AND CONSTITUTIVE MODELING OF GLASS. 15th International Symposium on Ballistics (21-24 May 1995): 1-15.

[14] Properties of Soda-lime-silica float glass[online] Avialable from: http://www. pilkington.com/resources/propertiesofsodalimesilicafloatglassats129 [2014,18 June]

[15] Soda-Lime Glass[online]. Available from: http://www.makeitfrom.com/material-data/?for=Soda-Lime-Glass [2015,January 18]

[16] Dorogoy, A., Rittel, D. and Brill, A. Experimentation and modeling of inclined ballistic impact in thick polycarbonate plates. International Journal of Impact Engineering 38(10) (2011): 804-814.

[17] Xinology Co., L. (1989). PVB film Xinology Co., Ltd.

[18] Dupont PV5200[online]. Available from: http://www2.dupont.com/ [2014,January 20]

[19] DuPont™ Butacite®polyvinyl butyral interlayer[online]. Available from: http://www2.dupont.com/Building_Innovations/en_CN/assets/downloads/BUTACITE-12pg-LoRes.pdf [2015,December 12]

[20] Bless, S. and Chen, T. Impact damage in layered glass. International Journal of Fracture 162(1-2) (2009): 151-158.

[21] O.C. Zienkiewicz, R. L. T., J.Z. Zhu. The finite element method-its basis and fundamentals Oxford, UK: Elsevier Butterworth-Heinemann, 2005.

[22] Inc., C. D. (2005). AUTODYN Explicit Software for Nonlinear Dynamics. Theory Manual Revision 4.3. CA,U.S.A.

[23] Ong, C. W., Boey, C. W., Hixson, R. S. and Sinibaldi, J. O. Advanced layered personnel armor. International Journal of Impact Engineering 38(5) (2011): 369-383.

[24] Holmquist, T. J. and Johnson, G. R. Response of boron carbide subjected to high-velocity impact. JOURNAL OF APPLIED PHYSICS 91(9) (2002): 5858-5866.

[25] D. S. Cronin, K. B. a. C. K. Implementation and Validation of the Johnson-Holmquist Ceramic Material Model in LS-Dyna. 4th European LS-DYNA Users Conference, Material I (May 2003): D-I 47-60.

[26] M. Richards, R. C. a. S. H. Ballistic Performance Assessment of Glass Laminates Through Experimental and Numerical Investigation. 18th International Symposium and Exhibition on Ballistics (1999):

[27] Grujicic, M., et al. A simple ballistic material model for soda-lime glass. International Journal of Impact Engineering 36(3) (2009): 386-401.

[28] T.J. Holmquist, G. R. J. Response of boron carbide subjected to high-velocity impact. International Journal of Impact Engineering 35((2007): 742-752.

[29] Hazell, P. J., Edwards, M. R., Longstaff, H. and Erskine, J. Penetration of a glass-faced transparent elastomeric resin by a lead–antimony-cored bullet. International Journal of Impact Engineering 36(1) (2009): 147-153.

[30] Lai, X. S. a. K. C. Optimizing Transparent Armor Design Subject to Projectile Impact Conditions. Ceramic Science and Engineering Proceedings Vol. 29(6) (2008): 15-22.

[31] Kupchella, R., Stowe, D., Xiao, X., Algoso, A. and Cogar, J. Incorporation of Material Variability in the Johnson Cook Model. Procedia Engineering 103((2015): 318-325.

[32] Cook, G. R. J. a. W. H. (1983). A CONSTITUTIVE MODEL AND DATA FOR METALS SUBJECTED TO LARGE STRAIN, HIGH STRAIN RATES AND HIGH TEMPERATURES. 7th International Symposium on Ballistics.

[33] Yang, Z. and Zang, M. Dynamic property and constitutive model of polyvinyl butaral material at high strain rates. Polymers for Advanced Technologies (2014):

[34] Xu, J., Li, Y., Ge, D., Liu, B. and Zhu, M. Experimental investigation on constitutive behavior of PVB under impact loading. International Journal of Impact Engineering 38(2–3) (2011): 106-114.

[35] Timmel, M., Kolling, S., Osterrieder, P. and Du Bois, P. A. A finite element model for impact simulation with laminated glass. International Journal of Impact Engineering 34(8) (2007): 1465-1478.

[36] Bennison, T. A. a. S. J. Strength and Deformation Behavior of Laminated Glass. GLASS PROCESSING DAYS (2005): 116-119.

[37] Joseph M. Wells, S. D. XCT DIAGNOSTICS OF BALLISTIC IMPACT DAMAGE IN TRANSPARENT ARMOR TARGETS. Ceramic Engineering and Science Proceedings 33((2013): 133-143.

[38] Appleby-Thomas, G. J., Hazell, P. J. and Cleave, R. Penetration mechanisms in glass laminate/resin structures. Materials & Design 34(0) (2012): 541-551.

[39] Bobaru, F., Ha, Y. D. and Hu, W. Damage progression from impact in layered glass modeled with peridynamics. Central European Journal of Engineering 2(4) (2012): 551-561.

[40] Brajer, X., Hild, F. and Roux, S. On the dynamic fragmentation of glass: a meso-damage model. International Journal of Fracture 163(1-2) (2009): 121-131.

[41] Martin LARCHER, M. T., Norbert GEBBEKEN, George SOLOMOS. Simulation of laminated glass loaded by air blast waves. Applied Mechanics and Materials 82((2011): 69-74.

[42] Laboratory Services, F. S. C. Glass Fractures 2005[online]. Available from: https://www.fbi.gov/about-us/lab/forensic-science-communications/fsc/jan2005/index.htm/standards/2005standards7.htm [2015,16 October]

[43] Ceseracciu, L., Anglada, M. and Jiménez-Piqué, E. Hertzian cone crack propagation on polycrystalline materials: Role of R-curve and residual stresses. Acta Materialia 56(2) (2008): 265-273.

[44] Warren, P. D., Hills, D. A. and Dai, D. N. Mechanics of Hertzian cracking. Tribology International 28(6) (1995): 357-362.

[45] Jelagin, D. and Larsson, P.-L. Hertzian fracture at finite friction: A parametric study. Wear 265(5–6) (2008): 840-848.

[46] Grujicic, M., et al. An improved mechanical material model for ballistic soda-lime glass. Journal of Materials Engineering and Performance 18(8) (2009): 1012-1028.

[47] Tasdemirci, A. and Hall, I. W. The effects of plastic deformation on stress wave propagation in multi-layer materials. International Journal of Impact Engineering 34(11) (2007): 1797-1813.

[48] Center, N. R. Acoustic impedance[online]. Available from: https://www.nde-ed.org/EducationResources/CommunityCollege/Ultrasonics/Physics/signaltonoise.htm [2015,17 October 2015]

[49] Zhuang, S., Ravichandran, G. and Grady, D. E. An experimental investigation of shock wave propagation in periodically layered composites. Journal of the Mechanics and Physics of Solids 51(2) (2003): 245-265.

[50] Chen, X., Chandra, N. and Rajendran, A. M. Analytical solution to the plate impact problem of layered heterogeneous material systems. International Journal of Solids and Structures 41(16–17) (2004): 4635-4659.

[51] Woo, S.-C., Kim, J.-T., Kim, J.-Y. and Kim, T.-W. Correlation of fracture processes and damage mechanisms of armor structural materials under high strain rates with acoustic emission characteristics. International Journal of Impact Engineering 63(0) (2014): 29-42.

[52] Han, C. and Sun, C. T. A study of pre-stress effect on static and dynamic contact failure of brittle materials. International Journal of Impact Engineering 24(6–7) (2000): 597-611.

[53] Corporation, O. Acoustic Properties of Solids 2003.[online]. Available from: http://www.ondacorp.com/tecref_acoustictable.shtml [2015,17 October 2015]

[54] Corporation, O. Acoustic Properties of Plastics 2003.[online]. Available from: http://www.ondacorp.com/tecref_acoustictable.shtml [2015,17 October 2015]

[55] Chen, X. and Chandra, N. The effect of heterogeneity on plane wave propagation through layered composites. Composites Science and Technology 64(10–11) (2004): 1477-1493.

[56] Wilkins, M. L. (1969). Third Progress Report of Light Armor Program. Lawrence Livermore National Laboratory UCRL-50460.

[57] R. Velmurugana, G. B., M. Srinivasana, T.P. Mohanb and K. Kannyb (2013). Energy Dissipation of Nanocomposite Laminates During Impact Loading. IV International Symposium on Solid Mechanics - MecSol 2013 Porto Alegre - Brazil.

[58] Bazhenov, S. Dissipation of energy by bulletproof aramid fabric. Journal of Materials Science 32(15) (1997): 4167-4173.

[59] Evci, C. Thickness-dependent energy dissipation characteristics of laminated composites subjected to low velocity impact. Composite Structures 133((2015): 508-521.

[60] Tamuzh, P. P. O. a. V. P. ENERGY DISSIPATION IN A GLASS LAMINATE STRESSED IN CYCLIC TENSION-COMPRESSION Mekhanika Polimerov 4((1968): 655-661.

[61] Strassburger, E., Bauer, S. and Popko, G. Damage visualization and deformation measurement in glass laminates during projectile penetration. Defence Technology 10(2) (2014): 226-238.

[62] Skvortsov, V., Kepler, J. and Bozhevolnaya, E. Energy partition for ballistic penetration of sandwich panels. International Journal of Impact Engineering 28(7) (2003): 697-716.

[63] Wei, J., Shetty, M. S. and Dharani, L. R. Stress characteristics of a laminated architectural glazing subjected to blast loading. Computers & Structures 84(10–11) (2006): 699-707.

[64] Sujarinee Sinchai, T. W., Karn Serivalsatit , Rojana Pornprasertsuk Chapter 2 Transparent Armor Fabrication. 2014.

จุฬาลงกรณ์มหาวิทยาลัย
Chulalongkorn University

APPENDIX

จุฬาลงกรณ์มหาวิทยาลัย
Chulalongkorn University

VITA

Miss Yukolthorn Sriloy was born on September 21, 1988 in Bangkok, Thailand. She graduated Bachelor's Degree in Materials Science from the Department of Physics, Faculty of Science, Thammasat University. She continued a further study in Master's degree in the field of Ceramic Technology at Chulalongkorn University and graduated in 2015.

Academic Conference presentations

Y. Sriloy, R. McCuiston, and R. Pornprasertsuk, "Design and Optimization of Laminated Transparent Armor by Finite Element Analysis", The Fifth International Conference on Design and Analysis of Protective Structures (DAPS2015), Furama Riverfront Hotel, Singapore, May 19-21,2015 (Oral Presentation & Proceeding)

Y. Sriloy, P. Jantharat, S. Sinchai, R.McCuiston, and R. Pornprasertsuk, "Effect of Striking Glass and Polyvinyl butyral Film Thickness on Ballistic Performance of Laminated Transparent Armors by Finite Element Analysis", The 10th International Symposium in Science and Technology 2015 (ISST 2015), Bangkok, Thailand, August 31 - September 2, 2015 (Silver Poster Presentation Award)

Chulalongkorn University